The UCL Martian Thermosphere and Ionosphere Global Circulation Model: Development and Validation

TRACY MOFFAT

Submitted for the Degree of *Doctor of Philosophy*

Department of Physics and Astronomy

University College London

August 17, 2005

ProQuest LLC
789 East Eisenhower Parkway
P.O. Box 1346
Ann Arbor, MI 48106-1346

Acknowledgements

Throughout the course of this work many people have provided help and support to whom I owe thanks. Thanks have to go to my supervisor Alan Aylward for his eternal optimism that I would finish and his help with understanding the finer details of atmospheric physics. Thanks also to my two second supervisors; Ingo Mueller-Wodarg for putting up with my near constant coding queries in the beginning and George Millward for reassuring me when I was explaining my results. My family have always encouraged my love of science, especially astronomy, and I thank them for their support and love over the past years. I've made many friends while studying for my degrees, and thanks have to especially go to the following; to Alison and Tara who have shared the trials and delights of a PhD in Physics and the writing up process and to Tom and Andy with whom I have laughed and cried and who have given me support and advice when I most needed it. Lastly I thank my husband to be, without your love and support the past three years would have been so much harder.

Typeset using LaTeX

"Isis, Astarte, Diana, Hecate, Demeter, Kali, Innanna" - The Goddess chant

Do mo ghrá geal Eoghan, a cabhraigh liom an soothar seo a chur le céile

Abstract

Simulations of the Martian upper atmosphere have been produced from a self consistent three dimensional numerical model of the Martian thermosphere and ionosphere called MarTIM. This model has been developed at UCL to cover an altitude range of 60km - 250km+. A radiation scheme is included that allows the main sources of heat input, EUV/UV and IR absorption by CO_2 and CO, to be calculated. MarTIM self consistently calculates the composition of three of the main gases, CO_2, N_2 and O, which are mutually diffused. These are treated as the major gases in the model. The other species densities (the minor gases), CO, Ar, O_2 and NO, are based on diffusive equilibrium above the turbopause. The ionosphere is calculated from a simple photoionisation and charge exchange routine which yields a peak electron density of around $2 \cdot 10^5 cm^{-3}$ at 135km, for L_s=0, solar minimum conditions. The semi-diurnal (2,2) migrating tide has been simulated and the results are presented and discussed. Comparisons of the model output to the available measurements from Mars Global Surveyor and Mars Pathfinder demonstrate that the fundamental parameters are well modelled and point to opportunities for further development. The fixed lower boundary in the basic MarTIM was altered by using output from the Mars Climate Database as the lower boundary. The effects of this change at higher, thermospheric altitudes, has been calculated and reveals a significant dependence on this lower atmosphere input.

Contents

List of Figures

List of Tables

Chapter 1

Introduction

1.1 Introduction to Mars

Mars has been observed with the naked eye since ancient times. The earliest telescope observations began with Galileo in 1609. In the late 1600s Huygens observed white spots near the Martian pole (which we now know were the polar caps) and, through observations of features on the Martian surface, made the first estimate of the Martian rotation rate, 24 hours, [34]. The rotation rate was recalculated by Cassini a few years later and was revised to 24 hours, 40 minutes. Observations by Herschel, [38], resulted in estimates for Mars' obliquity and size and confirmation of the presence of polar caps. Dust storms were first seen by a French amateur astronomer, H. Flaugergues, in 1809 who recorded seeing "yellow clouds" on the surface on Mars, [42].

These early measurements of the rotation and size of the fourth planet from the Sun were accurate to within 1 or 2 percent and showed that Mars is smaller than the Earth, orbiting at an average distance of 1.52A.U with a period of 668 Earth days and a rotation rate of 24 hours 40 minutes.

It was known that Mars has a similar obliquity and rotation rate to Earth and therefore must experience daily and seasonal variations similar to those on Earth. It is now understood that the Martian seasons are more extreme compared to those on Earth due to the higher eccentricity of Mars' orbit (0.093 for Mars compared to 0.017 for Earth). At perihelion Mars receives about 40% more solar insolation than at aphelion. Winters on Mars are longer in the Southern Hemisphere than in the Northern Hemisphere, as demonstrated in table 1.1, and the Southern Hemisphere

summers are shorter, but hotter, than those in the Northern Hemisphere. The seasons are normally defined in terms of solar longitude (L_S). This is an angular measurement of the distance along a planet's orbit in the ecliptic as viewed from the Sun. $L_s = 0$ is defined as Northern Hemisphere spring equinox for Mars.

Season Lengths on Mars

L_s	Hemisphere-Season	Duration in Earth days
0	Northern Spring/Southern Autumn	194
90	Northern Summer/Southern Winter	178
180	Northern Autumn/Southern Spring	142
270	Northern Winter/Southern Summer	154

Table 1.1: The variable season lengths on Mars given in terms of Earth days

That Mars had a tenuous atmosphere was known from the early observations of clouds moving against the surface and occultation measurements, [38], [34], but the exact composition of the atmosphere was still causing debate into the early half of the 20th century. Ground based spectroscopy observations in the 1930s detected CO_2, but no traces of water vapour or oxygen. It was still assumed that, like Earth, the major component of the Martian atmosphere was N_2, which is difficult to detect using terrestrial spectroscopy, [21]. The first robotic fly-bys (the Mariner and Mars missions) of Mars in the late 1960s provided definitive measurements of the atmospheric composition and atmospheric pressure, showing a low pressure, CO_2 dominated Martian atmosphere. The Viking orbiter and lander program in 1976 was the most successful Mars mission of its time. Data on the atmospheric neutral and ion densities, pressure and temperature were collected, [76], [36]. Mars was not visited again for nearly two decades until the arrival of the Mars Global Surveyor and Pathfinder missions in 1997.

One-dimensional models of the Martian atmosphere, [9], have been used to examine the physical processes that determine parameters such as temperature in an effort to match to the data measured by the early missions. To better understand the dynamics and energetics of the Martian atmosphere, three-dimensional global circulation models (GCMs) were developed, [10], [29], [89]. One driver of the development of these models was the necessity to produce predictions of the atmospheric conditions for future Mars

mission arrivals. Orbiter missions, since 1997, use a technique known as aerobraking, [72], to achieve the correct orbit. The Martian atmospheric drag is used to slow the orbiters down. The amount of aerobraking obtained is determined by estimates from atmospheric models, and in turn each aerobraking event gathers more data on the density, temperature and pressure of the atmosphere at specific altitudes. This data is then used to validate the Martian atmosphere GCMs. The other main driver was to try and fully understand how circulation is driven on Mars. As Mars shares a similar sidereal day and axial tilt to Earth they share similar mean seasonal variations. By understanding the similarities and differences between these two planets atmospheres, a greater understanding of atmospheric physics is gained. Therefore, we can hope to enhance our understanding of all Mars-like planetary thermospheres and for instance, plan more accurately the aerobraking needs of future space missions. This is especially important in the context of recent mishaps such the Mars Climate Orbiter (1999), which was thought to have burned up in the Martian atmosphere.

1.2 Mars Modelling History

Building on the early work in the field there are now several models of the Martian thermosphere and lower atmosphere in existence, both three-dimensional global circulation models and one-dimensional models. This section will outline the main three-dimensional thermosphere and middle atmosphere models and explain, briefly, their history and current state of development.

1.2.1 National Centre for Atmospheric Research Martian Thermosphere GCM (NCAR MTGCM)

The NCAR Earth thermosphere GCM has been under development for several decades. This model was adapted for use as a Martian thermosphere model (MTGCM) around 1988, [9], [10], and the major processes for a CO_2 atmosphere were taken from work done previously on a Venus global circulation model, [11]. MTGCM is a finite difference, time-dependent, primitive equation model that self consistently and numerically solves for thermospheric neutral temperatures, neutral and ion densities and a three-dimensional wind field, [19]. It covers an altitude range of 70-300km and has various inputs that can be adjusted to vary the season, the solar flux and the maximum eddy

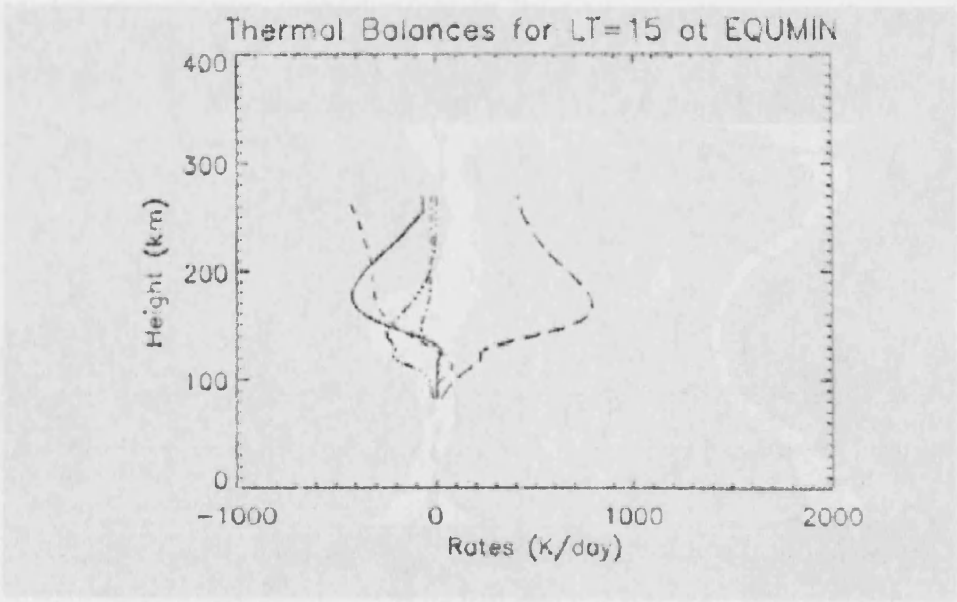

Figure 1.1: Heating and cooling rates from MTGCM. Shown for equinox, solar minimum at 15:00 hours. Where, UV/EUV heating = long dashed, Molecular Conduction = solid, Adiabatic Cooling = short dashed, Advection = dot-dash-dot and CO_2 cooling = dot-dot-dot-dash. [7]

diffusion coefficient. Tidal mode amplitudes and phases have also been included in MTGCM, [15]. Currently work is being done on coupling MTGCM to the lower Mars atmosphere model that has been developed at NASA-AMES, [19], so that the inflation/contraction of the lower atmosphere can be accounted for. Figures 1.1 and 1.2 show sample data from MTGCM, with solar forcing only and show a vertical profile of heating and cooling rates, plus the temperature structure across a pressure level, respectively.

1.2.2 Laboratoire de Meteorologie Dynamic-GCM

The LMD general circulation model started as a terrestrial GCM and was initially adapted to simulate the lower atmosphere of Mars using a new radiative transfer code, [40]. In 1999 the LMD and the Atmospheric, Oceanic and Planetary Physics group (AOPP), University of Oxford teamed up with Instituto de Astrofisica de Andalucia (IAA), Spain, to work with ESA on a Mars environment model, [29]. This model has now been extended up to 250km and is one of the first Martian GCMs to self-consistently couple the lower and upper atmosphere. The LMD-GCM is also a finite

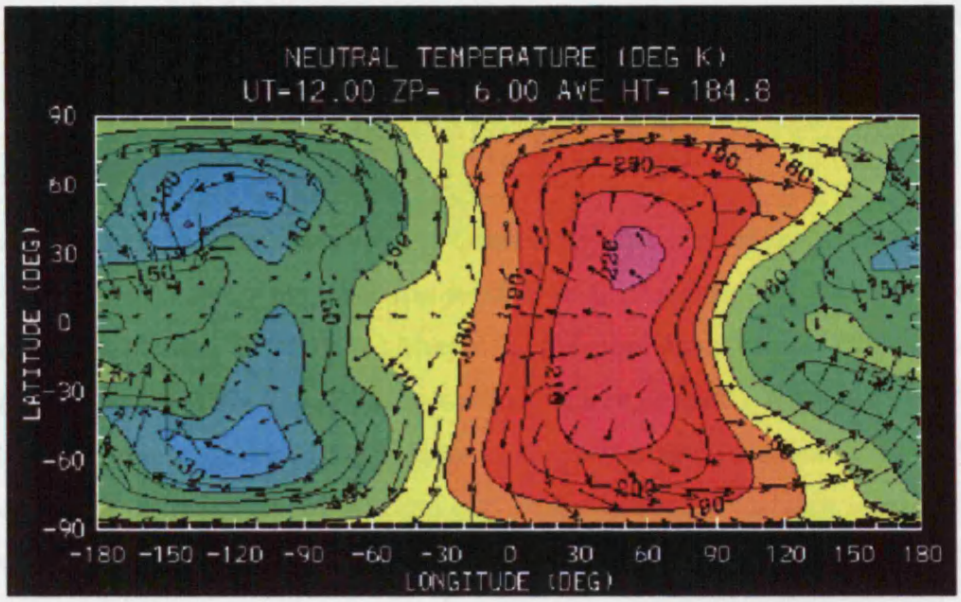

Figure 1.2: Temperature structure and horizontal winds across a pressure level (around 184km) from MTGCM. [7]

difference, time-dependent model which solves numerically the primitive equations of hydrodynamics on a sphere.

1.2.3 Mars Climate Database

The Mars Climate Database (MCD) is based on output from multi-annual integrations of two General Circulation Models (GCMs) which were developed jointly at Laboratoire de Météorologie Dynamique, Paris, and the University of Oxford, with support from the European Space Agency and the Particle Physics and Astronomy Research Council. The LMD GCM is a finite difference model as described in the section above, the Oxford GCM uses a semi-spectral technique involving a decomposition of the horizontal parameter fields into spherical harmonics, [51]. The use of both techniques is thought to allow for a better assessment of model errors. The MCD stores means and standard deviations of variables on a regular 5° (72×36) horizontal grid with 32 sigma levels in the vertical going up to 120 km altitude, where sigma is a terrain-following coordinate and is equal to the pressure at a given level divided by the surface pressure. Output is accumulated over multi-annual experiments for various dust scenarios (low to high). Fields are stored at 12 times of day for each season, with the year split into 12 seasons to give a comprehensive representation of both the annual and diurnal

cycles. It was developed initially to help describe the climate and surface environment of Mars and work is ongoing to raise the upper altitude limit.

1.2.4 Mart-ACC

The MAOAM (Martian Atmosphere: Observation and Modelling) is a German program, only a few years old, that has resulted in the development, from a terrestrial model, of a Martian GCM, called Mart-ACC (Martian Atmosphere - Circulation and Climate Model). It is a finite difference model with an altitude range of 0km to 130km. Mart-ACC uses a smoothed topography and a gravity wave parameterisation scheme. However, it assumes that the Martian atmosphere is dustless and that it is pure CO_2. Future work is expected to start to include dust features, the other constituent gases and increase the altitude range.

1.3 Mars' Atmospheric Structure: Modelling and Observation

The nature of the Martian atmosphere is discussed in this section with reference to observations and the UCL Martian Thermosphere and Ionosphere Model, hereafter known as MarTIM.

An example of the vertical temperature structure of the Martian upper atmosphere as represented by MarTIM is shown in figure 1.3. MarTIM was run under solar maximum and equinox conditions to produce this figure. The turbopause is the point in the atmosphere where the turbulent and molecular mixing of the atmospheric constituents is equal. The turbopause is at an altitude of around 125km on Mars, [75]. Below the turbopause, in the middle atmosphere, turbulent mixing dominates. This is where the gases in the atmosphere are thoroughly mixed and generally have the same temperature. Above the turbopause molecular mixing dominates. This is where the atmospheric gases begin to separate diffusively, rather than forming a homogeneous mixture. The species separate out due to their differing molecular masses. Diffusive separation is smothered below the turbopause due to high levels of mixing. The thermosphere begins at an altitude where the temperature starts to increase with height due to the EUV/UV heating. Eventually an altitude is reached where particles are

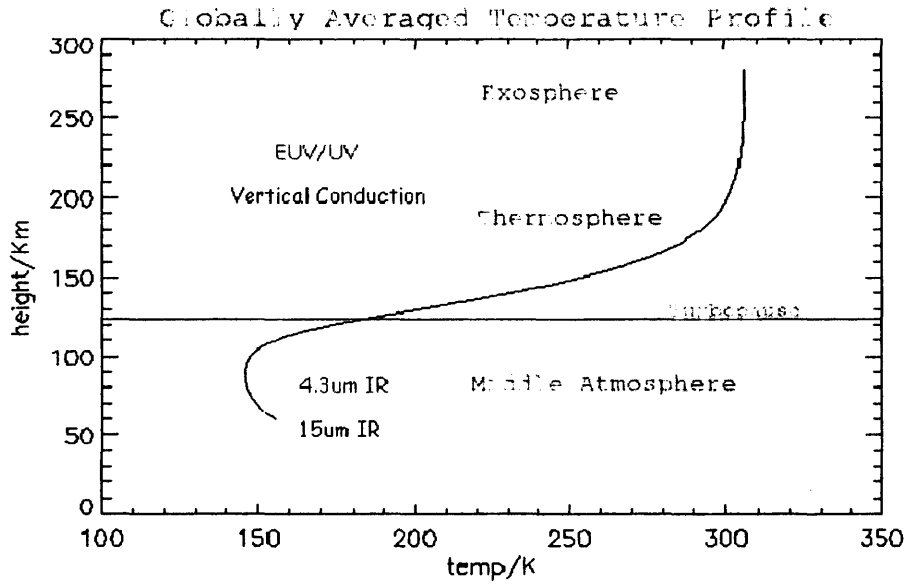

Figure 1.3: Globally averaged neutral temperature profile, for solar maximum and equinox conditions, showing the different regions in the thermosphere. Taken from MarTIM results.

on ballistic trajectories. This is termed the exosphere.

The atmosphere of Mars is nearly transparent to solar radiation, [34], with the exception of the EUV/UV wavelengths and some IR wavelengths. Consequently, its lower atmosphere temperature structure is controlled by thermal emission from the surface. However, as Mars does not have any oceans, the surface temperatures undergo wide seasonal and diurnal variations. Compared to Earth, the Martian atmosphere is cold, as is the surface. The lowest temperatures of around 150K are found near the poles and lead to the formation of polar caps formed from solid CO_2. The highest temperatures, around 275K, occur during the summer in the southern sub-tropical regions (when Mars is closest to the Sun). As a consequence of the surface temperature on Mars the surface emits most of its energy in the infrared range between 0.5μm and 50μm, [34]. As CO_2 is the main constituent of the Martian atmosphere, and as it has a vibration-rotation absorption band at 4.3μm, around 20% of the energy will be absorbed by the atmosphere. The remainder is emitted to space. Some of the radiation absorbed by the atmosphere is reradiated, this produces a modest greenhouse warming effect, of the order of 5K. Earth's atmospheric greenhouse effect produces a warming of around 35K, of this around 26% is due to CO_2. So although Mars atmosphere is mainly CO_2 its low density means that the greenhouse warming due to CO_2 on Earth

Conditions on Mars for the Lander arrivals

Lander	L_s	SZA	F10.7
Viking 1	96	44	69
Pathfinder	143	135	70

Table 1.2: The different season, solar zenith angle and solar flux conditions for Viking 1 and Pathfinder.

is larger by 30K. The surface pressure on Earth is higher than that on Mars (7.5 mbar) and so pressure broadening of the absorption lines occurs, resulting in more CO_2 absorption, [34], and more heating. This low surface pressure also means that liquid water is short-lived on the Martian surface.

The amount of heat input due to a single radiation band depends on the intensity of the solar radiation in that band reaching Mars, and how efficient the gases in the atmosphere are in absorbing it and converting it to kinetic energy. The amount absorbed at a given altitude depends on the composition of the atmosphere, the intensity of the radiation and the radiation attenuation.

Various direct measurements have been made of the vertical temperature structure on Mars. The two temperature profiles from the Viking 1 and the Pathfinder lander are shown in figure 1.4. The conditions at the time of the landings are shown in table 1.2, [7].

Evidence of vertically propagating waves, i.e. atmospheric gravity waves, [28], [16], have been found in the profiles. Global circulation models have already been able to successfully reproduce the general features of the Martian thermosphere, [9]. However, as the observed temperatures are lower than the initial model results, it has been necessary to assume that the efficiency of the conversion of solar EUV/UV radiation to heat is low. The values used are between 15% and 20% compared with 30% to 40% for Earth, [9]

As explained earlier, the heating of the thermosphere of Mars is dominated by EUV and UV absorption by most of the atmospheric constituents. In accordance with work done in other Mars GCMs, [9], the solar EUV radiation heating efficiency is set to 18% for all constituents in MarTIM. The solar EUV and UV fluxes vary over solar cycle and therefore the thermospheric temperatures vary. The modelled

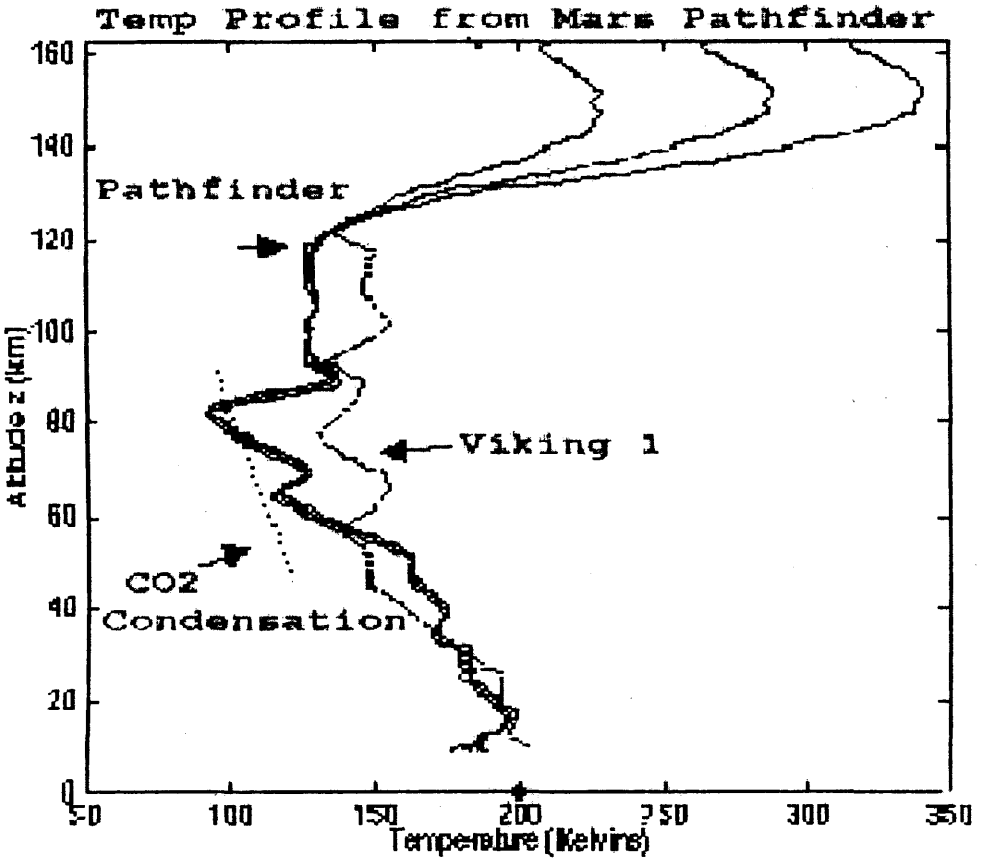

Figure 1.4: Temperature profiles from the Viking 1 Lander and the Pathfinder Lander. The CO_2 condensation region is labelled, [16].

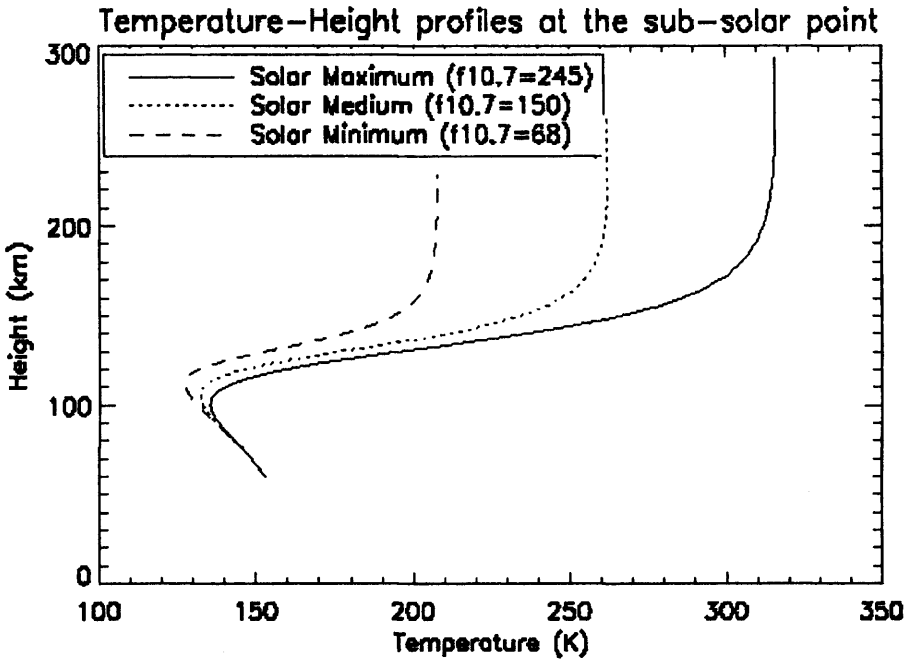

Figure 1.5: Neutral temperature profile from MarTIM, at the sub-solar point, for solar minimum, medium and maximum conditions at spring equinox in the northern hemisphere

increases in dayside temperatures in the thermosphere, according to MarTIM, from solar minimum conditions to solar maximum conditions are shown in figure 1.5. Solar activity is measured by the F10.7cm flux measured at Earth. The dominant heat transfer mechanism in the thermosphere is vertical molecular conduction. The heat is conducted downward into the lower atmosphere at which point the constituent densities are sufficiently large for radiative cooling to occur.

Atmospheric heating by absorption in the near infrared bands of CO_2 and CO is important above 50km, and is dominant in the middle atmosphere of Mars. This is accounted for in the heating scheme of MarTIM. Also in the Martian middle atmosphere the main infrared cooling mechanism is by the CO_2 15μm emission band. It is assumed that collisions between O and CO_2 affect this 15μm band, causing collisional relaxation. Hence, the O/CO_2 ratio is an important factor in determining the efficiency of the cooling. Above 80km, there is a departure from local thermodynamic equilibrium. This adds complexities to the calculation of the infrared heating or cooling rates and needs to be taken into account in that region of the thermosphere when calculating the terms in the energy equation.

1.4 Elemental and Isotopic Composition

The atmosphere of Mars is composed of many neutral gases. Due to a lack of thermospheric density measurements MarTIM does not include all of them in the make up of its neutral atmosphere. The constituents used in MarTIM are CO_2, N_2, O, O_2, Ar, NO and CO. The three main diffusing gases; CO_2, N_2 and O have volume mixing ratios of 0.95, 0.027 and 0.013 respectively at the turbopause. Above the turbopause, as the gases fall off with their own scale heights, O becomes the dominant species at higher altitudes. Density profiles of the neutral species from 115km to 200km were measured by the neutral mass spectrometers on the Viking landers and these profiles were taken as the basis for the densities used in MarTIM, [75]. The mixing ratio of O was not directly measured and was inferred from airglow data from Mariner 6, 7 and 9 and through modelling of the O_2^+ and CO_2^+ density profiles, [30]. This uncertainty has important implications for the O/CO_2 ratio needed to calculate IR cooling. The neutral density structures are controlled mainly by diffusion. The constituents are photolysed and ionised by UV radiation. In the actual Martian atmosphere the molecules also undergo photodissociation, e.g. $CO_2 + h\nu \rightarrow CO + O$, and recombination throughout the atmosphere. This aspect of atmospheric chemistry on Mars has not been included in MarTIM, for reasons discussed in chapter 2.

Photoionisation and ionic reactions occur above 80km, forming the ionosphere. Within MarTIM these reactions are calculated, generating ion and electron density distributions. The photochemical processes (photoionisation and ion-neutral reactions), rather than diffusion, are the main controller of the location of the ionospheric peak on Mars. Measurements from the Retarding Potential Analyser on the Viking missions, [36], established that the principal ion in the Martian ionosphere is not CO_2^+ but O_2^+, with a density of the order of $1{\cdot}10^5 cm^{-3}$ at the peak. This is a result of the two ion-molecule reactions shown in equations 1.1 and 1.2, which transform rapidly the CO_2^+ and O^+ ions into O_2^+.

$$CO_2^+ + O \rightarrow O_2^+ + CO \tag{1.1}$$

$$O^+ + CO_2 \rightarrow O_2^+ + CO \tag{1.2}$$

The Viking missions confirmed the presence of CO_2^+ and O_2^+ and measured the

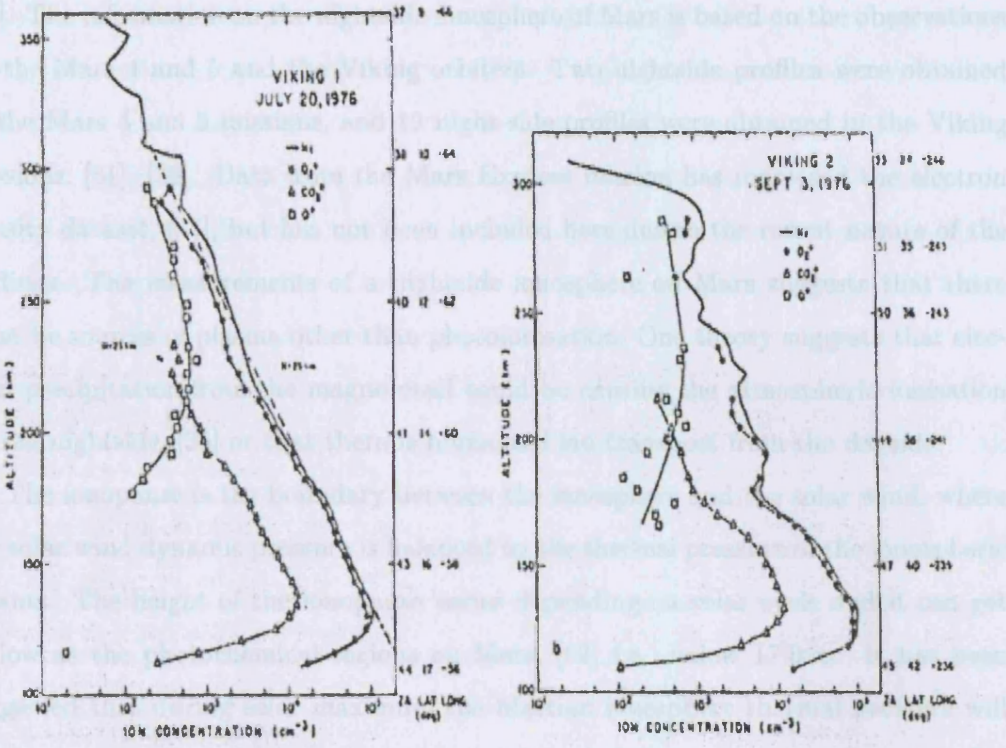

Figure 1.6: Ion density profiles from the Viking 1 and 2 Landers, [36].

electron and ion temperatures in the Martian ionosphere, [36]. Viking ion density data is shown in figure 1.6.

The main ionospheric peak is shown to be at around 135km. Photochemical processes dominate the ionospheric structure up to around 170km on Mars. According to theory diffusion takes over above this altitude, [62]. If diffusive equilibrium is assumed above 170km then O_2^+ densities should decrease with a scale height of around 120km. The observed profiles indicate a much smaller scale height of around 30km, [62]. It is clear then that the ionosphere on Mars is compressed. This is thought to be due to the direct interaction of the solar wind with the ionosphere, smothering the diffusive region in the ionosphere, [74]. The exact nature of the interaction between the solar wind and the Martian atmosphere is still not well known, and is limited by a lack of measurements in this region of the Martian atmosphere.

This direct interaction occurs because, unlike Earth, Mars does not have an intrinsic magnetic field so the ionosphere of Mars is not constrained by the magnetic field but rather by the neutral atmosphere dynamics. Observations of the nightside ionosphere, below 250km, on Mars are quite few, because the electron density is very low,

[92]. The information on the nightside ionosphere of Mars is based on the observations by the Mars 4 and 5 and the Viking orbiters. Two nightside profiles were obtained in the Mars 4 and 5 missions, and 19 night-side profiles were obtained in the Viking missions, [81], [36]. Data from the Mars Express mission has increased the electron density dataset, [83], but has not been included here due to the recent nature of the findings. The measurements of a nightside ionosphere on Mars suggests that there must be sources of plasma other than photoionisation. One theory suggests that electron precipitation from the magnetotail could be causing the atmospheric ionisation on the nightside, [35] or that there is horizontal ion transport from the dayside.

The ionopause is the boundary between the ionosphere and the solar wind, where the solar wind dynamic pressure is balanced by the thermal pressure of the ionospheric plasma. The height of the ionopause varies depending on solar cycle and it can get as low as the photochemical regions on Mars, [62] i.e. below 170km. It has been suggested that during solar maximum the Martian ionosphere thermal pressure will be strong enough to hold off the incident solar wind dynamic pressure at altitudes above the photochemical region, [91], hence the diffusive region of the ionosphere should be detectable.

There is evidence that Mars did once have an intrinsic magnetic field as there are patches of magnetised crust that have field strengths up to 1500nT in the southern hemisphere, [62]. The magnetic field can reconnect with the solar magnetic field and create 'mini-magnetospheres', [46]. Electrons trapped here may be hotter than those outside this region. This would affect those chemical reactions that are dependent on the electron temperature and hence cause differences in the ionospheric structure and dynamics. Recent results have shown that these magnetic hotspots also affect the height of the ionopause, [74]. Mars Express is making relevant measurements that will help to understand this region on the Martian ionosphere better.

1.5 Tides on Mars

As the Martian atmosphere is a rotating fluid, it is expected that the atmosphere can support a variety of wave motions. Waves are an important mechanism for transporting energy and momentum within the atmosphere. Tides are global oscillations of pressure, density, temperature and winds that are forced by thermal heating from the

ground level. The tides are at sub-harmonics of a solar day. They can propagate up through the atmosphere into regions where they begin to dissipate and then deposit their energy and momentum into the mean flow. Therefore, thermally driven tides on Mars are thought to have an important effect on the atmospheric structure and dynamics. It is thought that the semi-diurnal (2,2) migrating tide is a dominant mode in the thermosphere, [13]. The diurnal mode is predicted to break at 45km, [93], below MarTIMs fixed lower boundary of 60km

Mars Global Surveyor aerobraking data shows evidence of non-migrating tides affecting the density structure of the thermosphere (altitudes of 130-150km). All these modes need to be eventually included in MarTIM to ensure that the model is as realistic as possible.

Adapting classical tidal theory, [39], it is possible to reproduce the perturbations that would occur at the lower boundary of MarTIM. It is possible to do this because the Hough functions (which describe the latitudinal structure) are virtually identical for Earth and Mars due to their similar sidereal rotation rates. However, the equivalent depths of the tidal functions - the separation constant from Laplace's Tidal Equation - will differ as they depend on factors such as planetary radius and gravity. An estimate of the amplitude and phase of the semi-diurnal (2,2) migrating tide on Mars is available in existing literature, [13].

Perturbations, caused by the tides, are calculated for the height of the pressure level, meridional and zonal winds and temperature. In order to introduce these tidal perturbations to MarTIM they are added to the existing values at the lower boundary. The model intrinsically keeps the motions self-consistent above the lower boundary.

The details of classical tidal theory and its application to the Martian atmosphere will be dealt with in chapter 5.

1.6 The Modern Era of Observation of the Martian Upper Atmosphere

Earlier in this chapter we have seen that studies of the Martian upper atmosphere have been performed in-situ by instruments on board orbiters and landers, [34], since the late 1960s. After 1977 there was a period of nearly two decades before Mars was visited

again. The Pathfinder Lander (1997) was well publicised and, like the Viking missions before it, measured vertical profiles of density, pressure and temperature. Up until this time there was a very limited dataset for the upper atmosphere. It was very localised and did not include important parameters such as thermospheric wind speeds. Also in 1997 the first of several orbiters made it to Mars; Mars Global Surveyor (MGS). MGS measured in-situ upper atmospheric densities during its two aerobraking phases and ionospheric densities via radio occultations. These measurements represented a large increase in data on the upper atmosphere of Mars. This allowed studies to be undertaken, examining how the upper atmosphere varies with latitude, local time, season and dust storms. The first phase of aerobraking coincided with a planetwide dust storm, [6]. Another two orbiters have joined MGS at Mars in recent years; NASA's Mars Odyssey (1999) and ESA's Mars Express (2003). These have both contributed to the data gathered on the Martian upper atmosphere, although to date, there have been no direct measurements of wind velocities in the thermosphere. The Japanese orbiter, Nozomi, was scheduled to reach Mars orbit at the same time as Mars Express and was to have made measurements of the Martian upper atmosphere. Unfortunately the mission failed due to a series of mishaps and it was sent away from Mars, to avoid contaminating the planet.

The thermospheric datasets that now exist can be used to constrain and validate the MarTIM output for various conditions. The lower boundary in MarTIM has no connection to the lower atmosphere, so it cannot account for effects that dust storms have on the atmosphere. Therefore all model runs will be considered "clear" and the greater emphasis will be given to those datasets taken in "clear" conditions. The recent aerobraking datasets are not vertical profiles and so the determination of wind velocities is not straightforward. Work on deriving velocities from aerobraking data has been done, [90], but it is not yet a commonplace technique. Therefore, the majority of validation will be for parameters such as ion and neutral density and temperature.

Chapter 2

Model Detail

2.1 Introduction

To start to model an atmosphere knowledge of the relative gas abundances, temperature structure and pressure is needed. The dynamics in a three-dimensional model can be accounted for by considering each individual molecule with its mass, charge and velocity and working out all their interactions using equations such as Newton's laws of motion and chemistry. This would take far too much computer time so an alternative approach is taken. The whole upper atmosphere is treated like a fluid, and the collisions between molecules are frequent enough to allow this. The mean free path of a molecule, the distance it travels before colliding, is much shorter than the smallest macroscopic length scale, which is the pressure scale height, H, e.g. in the lower thermosphere the scale height is around 8km, the mean free path of a molecule is around 0.4m, much smaller than the scale height. For timescales of the order of seconds and above there are many molecular and atomic collisions. For a volume H^3 there are a huge number of atoms and molecules, so for macroscopic scales the atmosphere can be viewed as a continuous fluid. Equations can then be solved that describe the fluid, its dynamics, energetics and its composition. The dynamics describe the wind motions, the energetics describes the energy distribution and the continuity and diffusion equations describe the gas composition distribution in the atmosphere. Because of the non-linear nature of the equations, they have to be solved in a numerical fashion.

MarTIM is a three-dimensional numerical model of the dynamics and energetics of

the Martian upper atmosphere (thermosphere) and ionosphere. The lower boundary of the model is set to 0.883Pa, which is equivalent to about 60km in altitude. This is in accordance with the work done on an older Mars thermosphere model at UCL, [77], which assumes that this height is above the dust storms that can cover the planet.

MarTIM divides the atmosphere by latitude, longitude and pressure level, forming cells. These have variable resolution in the three spatial dimensions. In each cell, the relevant equations are solved, at a time t, and the boundary conditions of one feed into its neighbours, at time $t+\Delta t$, so a dynamic grid is built up and updated at each step of the model run. Each step of the model corresponds to a fixed time spacing (Δt), which can be altered at the start of a model run. The normal setting is 10 seconds.

The thermosphere modelled by MarTIM is described by seven constituents - CO_2, N_2, O, Ar, NO, O_2 and CO. The major constituents, CO_2, N_2 and O are mutually diffused. Up to the turbopause (around 125km), the number densities of the constituents are high enough that they are turbulently mixed. Above this, they are molecularly mixed. These gases are chosen as the "major" species because at the turbopause they are the dominant species. At the turbopause, the density of Ar is comparable to O. Ar is not chosen as a major species because it is chemically inert and O has an important role in IR cooling. CO also has comparable density to O at the turbopause and, although it has a minor role in infrared heating, it was decided that the role of O in the IR heat balance was greater . The number of major gases chosen was restricted to three due to the method of calculating diffusion, where the number of terms in the diffusion equation increase by n!, where n is the number of species involved, resulting in increased complexity. The minor constituents are calculated empirically, falling off with their own scale height above the turbopause.

In the thermosphere a radiation scheme is used that deals with solar radiation penetration in the EUV/UV range from 2-1725Å. In the middle atmosphere infrared heating is also important. This is due to CO_2 with a small proportion due to CO. The strongly absorbing fundamental bands for CO_2 and CO are the 4.3μm and 4.7μm bands respectively. As mentioned in chapter 1, CO_2 also provides the main cooling in this part of the atmosphere due to thermal emission in the 15μm band.

2.2 Fundamental Equations

2.2.1 Momentum

The dry adiabatic lapse rate describes the drop in temperature a parcel of air would experience if it was raised or lowered adiabatically. It is given by equation 2.1.

$$\Gamma_D = -\frac{dT}{dz} = \frac{g}{c_p}, \tag{2.1}$$

where c_p is the specific heat capacity at constant pressure, T the temperature and z the vertical co-ordinate. The adiabatic lapse rate on Mars, near the surface, is around 4.5Kkm^{-1}, [90]. The atmospheric lapse rate is defined as the vertical temperature gradient and is not normally perfectly adiabatic. If an air parcel is raised and the atmospheric lapse rate is greater than the adiabatic lapse rate, the parcel will have a higher temperature than the surrounding atmosphere and continue to rise. This condition is unstable. If the atmospheric lapse rate is less than the adiabatic lapse rate then the parcel will experience a force which tries to return it to its original position. This force is known as the buoyancy force and this condition is stable. The final condition is one of neutral stability, where both lapse rates are equal. Wherever the parcel of air is moved to under this condition it will be stable.

The forces at work in the atmosphere control the movement of the gases and thus determine the resultant winds. Application of Newton's second law to the atmosphere yields the momentum equation 2.2, [32], in a rotating reference frame.

$$\frac{d\vec{V}}{dt} = \vec{g} + \frac{1}{\rho}\nabla P - 2\vec{\Omega} \times \vec{V} + \frac{1}{\rho}\nabla \cdot \mu \nabla \vec{V}, \tag{2.2}$$

where V is the velocity, g the acceleration due to gravity, ρ the density, P the pressure, Ω the angular velocity of the planet and μ is the coefficient of viscosity. The first right hand term in equation 2.2 is the acceleration due to gravity. The second is the pressure gradient term, the main driving force for the neutral winds on Mars. In response to a pressure gradient, the fluid is forced to move down the gradient. The third term is the Coriolis force, which describes the motion in the non-inertial frame of a rotating planet. This acts perpendicular to the velocity vector of a cell in the rotating frame and changes its motion. It is balanced by the pressure gradient up to around 150km altitude, i.e. geostrophic balance breaks down above this height. It

doesn't initiate any winds - so does no work, just changes their direction. The fourth term occurs because of molecular and turbulent viscous drag. As different atmospheric layers move over each other, the horizontal wind gradients are reduced.

The left-hand side, which is the inertial term, is the Lagrangian derivative of the rate of change of wind velocity. The Lagrangian considers the changes that occur as one follows a fluid cell (i.e. along a trajectory). As the calculations for energy and momentum are done on the grid and not in a frame that follows the fluid, a conversion between Lagrangian co-ordinates and Eulerian co-ordinates is applied to the basic equations. The relationship between Lagrangian and Eulerian co-ordinates is given in equation 2.3, [32].

$$\frac{dA}{dt} = \frac{\partial A}{\partial t} + (V \cdot \nabla)A, \tag{2.3}$$

where A is any variable. If A is the velocity then the left hand side term gives the rates at which the velocity V is changing in a given part of the fluid. The first right hand side term gives the rate of change of velocity at a point in space that is momentarily occupied over time by the fluid. The second term is the non-linear advection term that is needed to account for the fact that a fixed point in space is occupied by multiple parts of the fluid due to its motion, i.e. that there is a transport of momentum. The advection term is believed to be important in the thermosphere, [32].

2.2.2 Equation of State

The equation of state for a "perfect gas" thermosphere takes the form of equation 2.4, [32].

$$P = \frac{\rho RT}{M} = \rho g H, \tag{2.4}$$

where P is the pressure, R is the gas constant for Mars (assuming a pure CO_2 atmosphere), M the mean molecular weight of the gas, T the neutral temperature, g the acceleration due to gravity and H the scale height ($=\frac{RT}{Mg}$). One scale height represents a decrease in pressure by a factor e. The scale height can also be represented as: $\frac{kT}{mg}$ where m is the mean molecular mass and k is the Boltzmann constant.

2.2.3 First Law of Thermodynamics

The energy conservation concept is described by the first law of thermodynamics. The change in energy in a system is equal to the net exchange of energy across the boundaries of the system. This is represented by equation 2.5, [32].

$$\frac{dT}{dt}c_p - \frac{1}{\rho}\frac{dP}{dt} = \dot{Q}, \tag{2.5}$$

where T is the temperature, ρ is the density, P is the pressure, c_p is the specific heat capacity of the gas at constant pressure and $\dot{Q}$ is the heat loss/gain per unit mass per unit time due to all the possible sinks and sources of energy. The first term on the left-hand side is the rate of change of internal energy of a perfect gas. The second term is the work done by the gas on its surroundings.

2.2.4 Hydrostatic Equilibrium

If an atmosphere is under hydrostatic equilibrium the acceleration due to gravity is balanced exactly by the vertical pressure gradient force and no vertical motions are present. In the thermosphere heat is being continually lost and gained which causes vertical motions. So the condition of hydrostatic equilibrium does not hold. However, by assuming the timescales for the vertical motions are long, a quasi-hydrostatic equilibrium state can exist. The assumption of hydrostatic equilibrium at any instant is then justified. This gives equation 2.6, [32].

$$\frac{\partial P}{\partial z} = -\rho g, \tag{2.6}$$

where P is the pressure, z the altitude, ρ the density and g the acceleration due to gravity.

2.2.5 Pressure Co-ordinate System

The model grid is fixed with respect to the surface of the planet, so a co-rotating non-inertial reference frame is produced. The equations of motion above have been written using the x, y, z and t co-ordinate system, where x is latitude, y longitude, z is the vertical direction and t is time. These equations can be simplified numerically by introducing pressure as the vertical co-ordinate. The Mars model extends 17 scale

heights vertically from $P_0 = 0.883$ Pa to $P_{16} = 9.9 \cdot 10^{-8}$ Pa. This corresponds to a height range of 60km to 200-350km depending on solar activity. The pressure at each height is determined by equation 2.7, [32].

$$P = P_0 e^{\frac{-z\alpha}{H}} = P_0 \cdot e^{-(n-1)\alpha}, \tag{2.7}$$

where P is the pressure, P_0 is the pressure at the lower boundary, z the altitude, H the scale height, n, a dimensionless variable, is the number of pressure levels, e.g. 17 pressure levels in the MarTIM, and α the fraction of pressure levels required. For example for half scale height resolution, $\alpha = 0.5$.

If scale height is assumed constant, the new vertical co-ordinate can be written as equation 2.8, [32].

$$z^* = -H\alpha^{-1} \ln(\frac{P}{P_0}), \tag{2.8}$$

where z^* is the new vertical co-ordinate and the other variables are as described above.

The use of pressure as a vertical co-ordinate simplifies the fundamental equations in the model. The transformation between z and p co-ordinates for a scalar S, in the x-direction is given by equation 2.9.

$$(\frac{\partial S}{\partial x})_p = (\frac{\partial S}{\partial x})_z + (\frac{\partial z}{\partial x})_p (\frac{\partial S}{\partial z}) \tag{2.9}$$

The geopotential Φ is defined as $d\Phi = gdz$. Transformed, this gives equation 2.10.

$$(\frac{\partial z}{\partial x})_p = \frac{1}{g}(\frac{\partial \Phi}{\partial x})_p \tag{2.10}$$

Substituting equation 2.10 and the hydrostatic equilibrium equation (2.6) into equation 2.9 gives equation 2.11:

$$(\frac{\partial S}{\partial x})_z = (\frac{\partial S}{\partial x})_p + \rho(\frac{\partial \Phi}{\partial x})_p (\frac{\partial S}{\partial P}) \tag{2.11}$$

The horizontal del operator in the "z" co-ordinate system, ∇_z, becomes equation 2.12

$$\nabla_z S = \nabla_p S + \rho \nabla_p \Phi \frac{\partial S}{\partial P} \tag{2.12}$$

Where ∇_p is the horizontal del operator in the pressure co-ordinate system. Equation 2.13 describes the scalar S in the vertical direction:

$$\frac{\partial S}{\partial z} = \frac{\partial S}{\partial P}\frac{\partial P}{\partial z} = -g\rho\frac{\partial S}{\partial P} \tag{2.13}$$

Substituting Φ for S in equation 2.13 gives:

$$\frac{\partial \Phi}{\partial P} = -\frac{1}{\rho} \tag{2.14}$$

Equation 2.14 is the hydrostatic equation for the pressure co-ordinate system and is equivalent to equation 2.6. The vertical velocity, which was defined in the z co-ordinate system as $V_z = \frac{dz}{dt}$, is defined in the pressure co-ordinate system as equation 2.15, [32].

$$\omega = \frac{dP}{dt} \tag{2.15}$$

Where ω is positive in a downward direction relative to an isobaric surface. The other fundamental equations can also be transformed into the pressure co-ordinate system and Eulerian frame of reference. This is shown in section 2.2.10.

2.2.6 Energy

The energy equation is a sum of all the sources and sinks of internal and kinetic energy in the atmosphere. The energy equation in Lagrangian co-ordinates is given by equation 2.16, [37].

$$\frac{d}{dt}(\epsilon + \phi) = \frac{1}{\rho}V \cdot \nabla P + Q_{EUV+IR} + \frac{1}{\rho}\frac{dP}{dt} + Q_{CO_2} + \frac{1}{\rho}\nabla(\mu\nabla)V + \frac{1}{\rho}\nabla(K_T + K_M)\nabla T + \frac{1}{\rho}\nabla^2 K_T \Gamma \tag{2.16}$$

Where ϵ is defined by $\epsilon = C_p T + 0.5V^2$ and represents the internal energy and kinetic energy of the atmosphere.

In equation 2.16 the terms on the right hand side, from left to right, are: internal kinetic energy, solar EUV+IR radiation input, internal potential energy, energy lost through CO_2 cooling, the viscous drag term (where $\mu = \mu_M + \mu_T$) and the two heat conduction terms. The subscripts T and M refer to the turbulent and molecular coefficients for viscosity and conduction respectively.

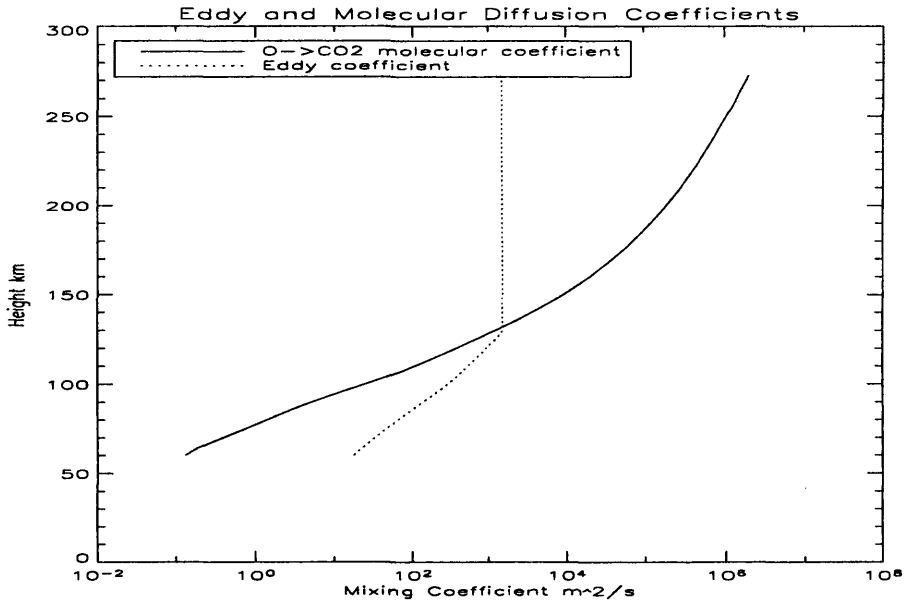

Figure 2.1: Eddy diffusion coefficient and molecular diffusion coefficient height profiles, taken from MarTIM results. Their crossing point defines the turbopause.

2.2.7 Inputs and Parameterisations

The eddy diffusion coefficient is set to a maximum value of $1500 m^2 s^{-1}$ at and above the turbopause, [10]. The eddy diffusion coefficient can be calculated below the turbopause using equation 2.17.

$$D_{eddy} = 1500(\frac{P}{P_t})^{-0.5}, \tag{2.17}$$

where D_{eddy} is the eddy diffusion coefficient, P_t is the pressure at the turbopause, $1.2 \cdot 10^{-4}$Pa, [10], and P the pressure at the level in question.

This eddy coefficient profile shape has been obtained from previous Mars modelling studies, [10], where this maximum value was shown to produce model thermospheric temperatures that fell within the constraints imposed by early missions, [9]. The eddy coefficient is an important value in generating a realistic heat balance in the Martian atmosphere. Figure 2.1 shows the eddy diffusion coefficient height profile as well as the molecular diffusion height profile and their crossing point defines the turbopause. They have been taken from MarTIM, for the subsolar point, at L_s=0 and solar minimum conditions.

K_M is the molecular heat conduction coefficient, [4], and for a pure CO_2 atmo-

sphere is given by equation 2.18. K_T is the turbulent heat conduction coefficient, [32], and is determined by equation 2.19.

$$K_M = 1.5T^{1.23} \tag{2.18}$$

$$K_T = C_p \cdot \rho \cdot D_{eddy} \tag{2.19}$$

Viscosity acts to remove velocity gradients in the atmosphere and also to dissipate heat between the atmospheric layers. In the thermosphere, above the turbopause, the mean free path of the molecules is relatively high and so molecular viscosity dominates. The coefficient of molecular viscosity, μ_M, is given by $1{\cdot}10^{-5}$, an approximation from [4]. Below the turbopause, the energy transfer is dominated by turbulence. The coefficient for turbulent viscosity is dependent on the turbulent heat conduction coefficient. It is given by equation 2.20.

$$\mu_T = \frac{2K_T}{C_p} \tag{2.20}$$

2.2.8 Heating and Cooling

Solar Heating

The solar heating, Q, is due to EUV/UV and IR absorption by the constituent gases in the atmosphere. The amount of heat from EUV and UV absorption is calculated in the following manner. The solar fluxes and absorption cross-sections are taken from Torr et al [87]. The fluxes and cross-sections have a wavelength resolution of 5nm and are converted to 2.5nm wavelength resolution by interpolation, for use in MarTIM. The absorption of solar flux is calculated in MarTIM using a "line of sight" method, which eliminates the need to use Chapman's grazing incidence function, [79].

The amount of EUV/UV absorption is given by the Lambert-Beer (L-B) exponential absorption law [78]. The heating rate is calculated by including the EUV/UV heating efficiency in the L-B absorption law (equation 2.21).

$$Q_j(z^*) = \int \sigma_j(\lambda) \cdot EUVFAC \cdot F(\lambda) \cdot e^{-\tau_j(z^*,\lambda)} d\lambda \tag{2.21}$$

Where τ_j is the optical depth at a height z^* for a species j, σ_j is the absorption cross-section of species j. $F(\lambda)$ is the incident solar flux. $EUVFAC$ is the absorption to heat efficiency i.e. the amount of absorbed radiation that gets converted to heat. In MarTIM it has been set to 18% for all gases, which is within the accepted range for Mars, [9], and assumed to be constant with height. This value is low compared to Earth where it is around 40%. Using larger values results in thermospheric temperatures on Mars that are too high compared to the data. The large intensity of observed UV airglow is evidence for the low $EUVFAC$ value on Mars.

However, there is also an additional solar contribution in the form of infrared heating in the middle atmosphere. The main absorbers of IR radiation are CO_2 and CO. CO_2 strongly absorbs in the 4.3μm and 2.7μm bands, CO absorbs strongly in the 4.7μm band. The infrared heating is not calculated in the same manner as the EUV/UV solar heating for two main reasons. To calculate the total absorption by CO_2 in the IR all the vibrational and rotational bands need to be considered, resulting in a vastly complicated equation. Additionally as altitude increases these vibrational bands experience a change from local thermodynamic equilibrium (LTE) to non-local thermodynamic (non-LTE) at around 85km on Mars, [55], resulting in more complications. There are many complex one-dimensional models to describe the infrared heating processes yet there is only a simple parameterisation in MarTIM that is scaled using the Chapman function. This parameterisation has been adapted from [57]. The rate of infrared heating is given by equation 2.22. A scaling factor is present due to the transition in the atmosphere from LTE to non-LTE.

$$Q_{IR}(z^*) = \frac{(k_{4.3\mu m}(z^*) + k_{2.7\mu m}(z^*)) \cdot [CO_2(z^*)] + k_{4.7\mu m}(z^*) \cdot [CO(z^*)]}{fac(z^*)} \tag{2.22}$$

Where k is the photoabsorption coefficient for the fundamental band (in s^{-1}), $[CO_2]$ and [CO] are the number densities at that pressure level and fac is the non-LTE factor. This factor is taken from [57] and is pressure dependent. Without this factor, the infrared heating rates would be unrealistically large at high altitudes. The importance of the CO_2 heating and cooling in the Martian atmosphere is discussed in more detail in chapter 4.

Heat Sinks

The main heat sink in the upper atmosphere is vertical molecular conduction. This transports energy down until the gas density becomes large enough for radiative cooling to occur. Below this, in the 60km to 130km region of MarTIM, non-LTE CO_2 cooling (see equation 4.1) is the dominant cooling mechanism. A parameterisation for the 15μm cooling does exist and has been obtained and implemented in MarTIM [60], [56]. In effect, it simplifies the non-LTE cooling problem to a two-band problem using the Curtis matrix method, [55]. Chapter 4 contains a more detailed discussion of the non-LTE theory used and alternatives.

2.2.9 Continuity

The continuity equation for a compressible fluid is given by equation 2.23, [32]. It expresses the conservation of mass. If a small volume, $\Delta x \Delta y \Delta z$, is considered with a density ρ the conservation of mass can be considered in a mathematical fashion. The inflow of mass per unit time into the x-face is given by $\rho V_x \Delta y \Delta z$, where V_x is the x component of the velocity. The outflow then becomes $[\rho V_x + \frac{\partial}{\partial x}(\rho V_x)\Delta x]\Delta y \Delta z$. So the rate of change of mass per unit volume in the x-direction becomes $+\frac{\partial \rho V_x}{\partial x}$.

$$\frac{\partial \rho}{\partial t} + \nabla \cdot \rho \vec{V} = 0 \tag{2.23}$$

2.2.10 Transformations

Converting the fundamental equations of the atmosphere into the pressure co-ordinate system and to the Eulerian reference frame (using equation 2.3) gives the main equations in the following form, [32]. The transformed momentum equation is shown in (2.24)

$$\frac{\partial \vec{V}}{\partial t} = -\vec{V} \cdot \nabla_p \vec{V} - \omega \frac{\partial \vec{V}}{\partial P} - \nabla_p \Phi - (2\Omega + \frac{V_y}{R\cos\theta})\vec{k} \times \vec{V}$$
$$+ g \frac{\partial}{\partial P} \frac{\mu}{H} P \frac{\partial \vec{V}}{\partial P} + \frac{1}{\rho} \mu \nabla_p^2 \vec{V}$$

, (2.24)

where $\vec{V}$ is the velocity, θ is the co-latitude, Φ is the geopotential, R the radius of Mars, μ the sum of the turbulent and molecular viscosity coefficients, $\vec{k}$ is the unit

vector in the vertical direction and ω is the vertical velocity in the pressure frame.

The energy equation in Eulerian space becomes equation 2.25:

$$\frac{\partial \epsilon}{\partial t} = Q_{EUV+IR} + Q_{CO_2} - V \cdot \nabla(\epsilon + gh) - \omega \frac{\partial(\epsilon + gh)}{\partial p} + V \cdot g \frac{\partial}{\partial p} \frac{\mu}{H} p \frac{\partial}{\partial p} V + \frac{1}{\rho}(K_T + K_m)\nabla^2 T + g \frac{\partial}{\partial p} \frac{(K_T + K_m)}{H} p \frac{\partial T}{\partial p} - g \frac{\partial}{\partial p} \frac{K_T g}{c_P}$$

, (2.25)

where ϵ is the sum of the kinetic energy plus the internal energy and h is the geopotential height. The other parameters are as defined for equation 2.16.

The transformed continuity equation becomes 2.26:

$$\frac{\partial \omega}{\partial P} + \nabla_p \vec{V} = 0 \tag{2.26}$$

2.3 Composition

Modelling a multiple gas atmosphere is complicated as the interactions between the individual species have to be accounted for. The method used in MarTIM is to evaluate self consistently the changes in composition of the atmosphere from the initial conditions. The input file for the neutral atmosphere used in MarTIM is taken from data derived from the Viking missions; [75], [31]. The input file contains a one-dimensional slice of pressure, height, temperature, and number densities for all the gases included in MarTIM. The number densities of the major constituents, CO_2, N_2 and O are mutually diffused using the diffusion equation, [32]. The major and minor gases are shown in figures 2.2 and 2.3 respectively.

As explained in chapter 1 there are two mixing methods in the thermosphere, turbulent and molecular diffusion. Below the turbopause, the density is relatively high and the gases have a short mean free path and collide frequently, so they are well mixed. Above the turbopause, the mean free path is longer and each gas behaves individually as it is diffused molecularly. This effect can be seen in figure 2.2 with the O density profile changing at around the turbopause height of 125km.

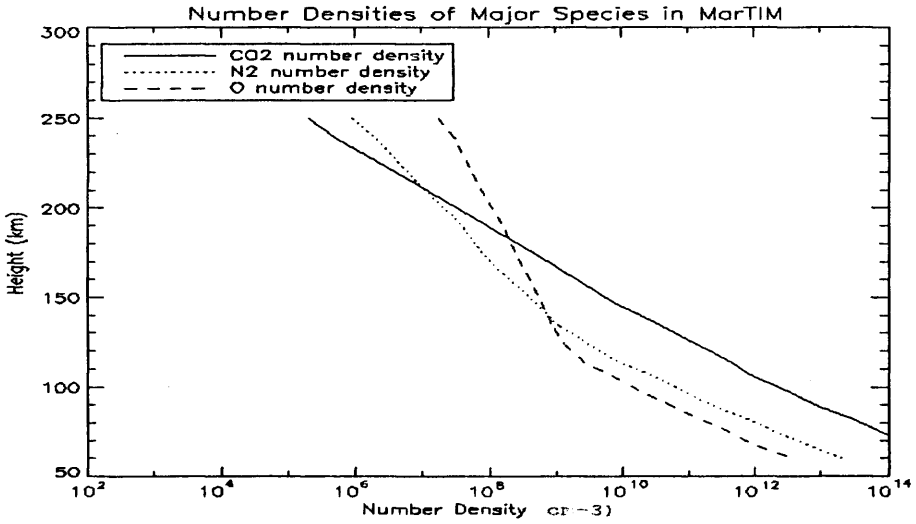

Figure 2.2: Number density of the major diffusing atmospheric species in the Martian thermosphere, for solar minimum and equinox conditions, in cm^{-3} from MarTIM input file

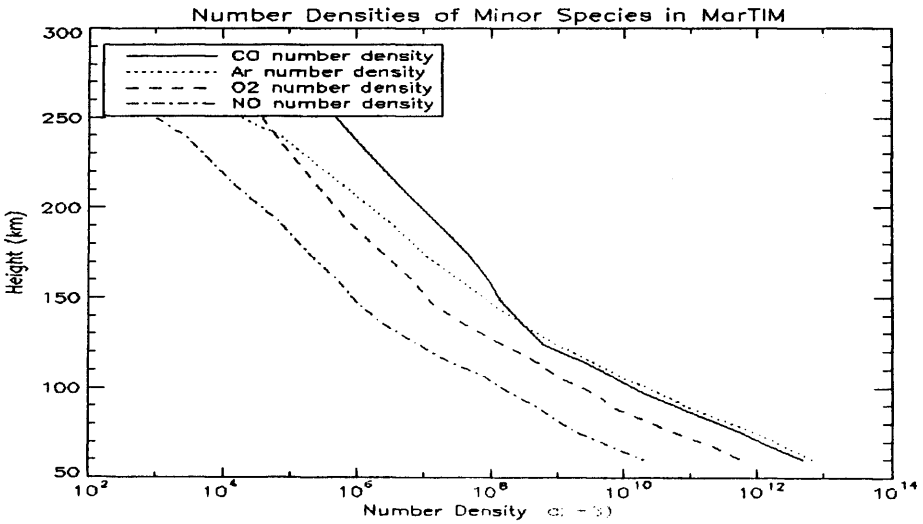

Figure 2.3: Number density of the minor atmospheric species in the Martian thermosphere, for solar minimum and equinox conditions, in cm^{-3} from MarTIM input file

Key values for calculating diffusion rates

Species n-m	s_{nm}	A_{nm}
O-N_2	0.774	$9.69e^{16}$
O-CO_2	0.5	$4.39e^{16}$
N_2-CO_2	0.752	$6.58e^{16}$

Table 2.1: A_{nm} and s_{nm} values for the diffusion rates of the major species in MarTIM

2.3.1 Diffusion

Circulation systems within the thermosphere create departures of composition from diffusive equilibrium, [32]. The diffusion equation calculates the rate of change of mean molecular weight for three major species over time. It is based on the work contained in [33]. The molecular diffusion coefficients are calculated using equation 2.27.

$$D_{nm} = (\frac{T}{T_s})^{x_{nm}} \cdot \frac{P_s}{P} \cdot r_{nm} \tag{2.27}$$

Where D_{nm} is the molecular diffusion coefficient for species n and m in units of cm^2s^{-1}. T, P are the temperature and pressure at the current pressure level, T_s, P_s are the temperature and pressure at the lower boundary. The exponent x_{nm} is equal to $s_{nm} + 1$, where s is a constant taken from [64], and is different for different n and m combinations. The last factor on the right hand side is given by equation 2.28.

$$r_{nm} = A_{nm} \cdot T_s^{x_{nm}} \cdot \frac{k}{10P_s} \tag{2.28}$$

Where k is the Boltzmann constant, A_{nm} is a constant specific for the species n and m and is taken from [64]. As we have seen the three diffusing gases in MarTIM are CO_2, N_2 and O. Table 2.1 shows the s and A values for these gases. It is assumed that the values for species n diffusing through species m is symmetric, so they would be the same values of s and A if the species were reversed.

The difference in the molecular diffusion velocities for species n and m is given by equations 2.29 and 2.30.

$$V_n - V_m = -D_{nm}[\frac{N^2}{n_n n_m}\nabla\frac{n_n}{N} + \frac{m_m - m_n}{M}\nabla ln(P)] \tag{2.29}$$

$$V_m - V_n = -D_{mn}[\frac{N^2}{n_n n_m}\nabla\frac{n_m}{N} + \frac{m_n - m_m}{M}\nabla ln(P)] \tag{2.30}$$

Where D_{nm} and D_{mn} are the molecular diffusion coefficients between species n and m, n_n and n_m are the number densities of the two species and m_n, m_m are the molecular weights of the two species. M is the mean molecular weight, N the total number density and P is the total gas pressure.

MarTIM also includes turbulent diffusion due to its lower boundary being below the turbopause level. To include the effect of turbulent diffusion in equations 2.29 and 2.30 the following terms shown in equations 2.31 and 2.32 have to be incorporated, [33].

$$-D_{eddy}\frac{N^2}{n_n n_m}\nabla\frac{n_n}{N} \tag{2.31}$$

$$-D_{eddy}\frac{N^2}{n_n n_m}\nabla\frac{n_m}{N} \tag{2.32}$$

Where D_{eddy} is the eddy diffusion coefficient defined in equation 2.17.

These two equations are combined with equation 2.33 and equation 2.23 to produce and expression for the temporal rate of change of molecular weight, shown in [33].

$$V = \frac{n_m V_m + n_n V_n}{N} \tag{2.33}$$

A three constituent equation has been developed, [32] and is used in other numerical global circulation models here at the Atmospherics Physics Laboratory, UCL, [37], including MarTIM. The problems in expanding the diffusion equation for more constituents has been mentioned earlier. The increased complexity that would arise in the diffusion equation would make it unsuitable for use in global circulation models.

2.3.2 Chemistry

To accurately predict the vertical profiles of the chemical species within the Martian atmosphere a photochemical model would need to be created. Most work on this has been done using one-dimensional models to estimate the globally averaged distribution of the chemical species, e.g. [65], [44], [71]. As more data is gathered about the exact composition of the Martian atmosphere, disagreements between the models and the

data increase. Calculating the abundance of gases such as CO_2 and CO using just standard gas phase chemistry yields lower than observed abundances, as stated in [45]. The main problem in the Martian atmosphere is the stability of CO_2. CO_2 photodissociates into CO and O and the timescales for the regeneration of CO_2, given by current theory, are too long for it to remain a dominant species. This cannot account therefore for the dominance of CO_2 in the Martian atmosphere by itself. It has been shown, [44], that an effective photochemistry scheme needs to allow for the presence of hydroxyls (OH, H_2O H) in the Martian atmosphere. These gases act as catalysts to speed up the production of CO_2. A three dimensional photochemical model has recently been developed, [50], which includes all the transport features which are absent in the one-dimensional models. They have shown that there are still problems in generating the correct abundances, and that dust and water ice chemistry has an effect. To have a realistic neutral-neutral chemistry scheme in a global circulation model the hydroxyl, dust and water ice abundances need to be included. There is evidence, [45], which suggests that even with the inclusion of a full three-dimensional photochemistry scheme the gas distribution would not match that expected. As the development of a full photochemical scheme for Mars would be a graduate project in itself, it has been decided that only simple ion-neutral chemistry will be present within MarTIM, and no other chemistry included at this stage of development.

2.3.3 The Ionosphere

Only neutral gas densities are read in at the start of a model simulation and the ion density profiles are calculated from the initial photoionisation and the subsequent production/loss charge exchange chemistry. Within MarTIM the ion production and loss rates are calculated at each time step. Initial ion density profiles due to photoionisation, calculated in the first time step, are adjusted at subsequent time steps, for each latitude-longitude point, by the production/loss reactions. The reaction rates are listed in table 2.2. After 30 model minutes the ion densities reach steady state. The Martian atmosphere is assumed electrically neutral, [63], so the electron density is set to be equal to the total ion density.

MarTIM ion production rate profiles for the subsolar point, solar minimum con-

Rate number	Reaction	Rate in cm^3s^{-1}
R1	$CO_2^+ + O \rightarrow CO + O_2^+$	$1.6 \cdot 10^{-10}$
R2	$CO_2^+ + O \rightarrow CO_2 + O^+$	$1.0 \cdot 10^{-10}$
R3	$O^+ + CO_2 \rightarrow O_2^+ + CO$	$1.2 \cdot 10^{-9}$
R4	$O_2^+ + e^- \rightarrow O + O$	$1.6 \cdot 10^{-7}(\frac{300}{T_e})^{0.55}$
R5	$CO_2^+ + e^- \rightarrow CO + O$	$1.4 \cdot 10^{-4}(\frac{1}{T_e})$
R6	$CO_2^+ + NO \rightarrow NO^+ + CO_2$	$1.2 \cdot 10^{-10}$
R7	$CO_2^+ + O_2 \rightarrow CO_2 + O_2^+$	$5.0 \cdot 10^{-11}$
R8	$N_2^+ + CO_2 \rightarrow N_2 + CO_2^+$	$8.0 \cdot 10^{-10}$
R9	$N_2^+ + O \rightarrow NO^+ + N$	$1.4 \cdot 10^{-10}$
R10	$N_2^+ + e^- \rightarrow N + N$	$3.5 \cdot 10^{-7}(\frac{300}{T_e})^{0.5})$
R11	$N_2^+ + CO \rightarrow N_2 + CO^+$	$7.4 \cdot 10^{-11}$
R12	$NO^+ + e^- \rightarrow N(2d) + O$	$1.08 \cdot 10^{-7}(\frac{1000}{T_e})^{1.2}$
R13	$O_2^+ + NO \rightarrow NO^+ + O_2$	$6.3 \cdot 10^{-10}$
R14	$CO^+ + CO_2 \rightarrow CO_2^+ + CO$	$1.1 \cdot 10^{-9}$
R15	$N_2^+ + O_2 - > O_2^+ + N_2$	$6.0 \cdot 10^{-11}$
R16	$O_2^+ + N_2 \rightarrow NO^+ + NO$	$1.0 \cdot 10^{-16}$
R17	$O^+ + NO \rightarrow NO^+ + O$	$8.0 \cdot 10^{-13}$
R18	$N_2^+ + O \rightarrow O^+ + N_2$	$9.8 \cdot 10^{-12}$
R19	$N_2^+ + NO \rightarrow NO^+ + N_2$	$4.1 \cdot 10^{-10}$
R20	$CO^+ + O \rightarrow O^+ + CO$	$1.4 \cdot 10^{-10}$
R21	$CO^+ + O_2 \rightarrow O_2^+ + CO$	$1.2 \cdot 10^{-10}$
R22	$O^+ + N_2 \rightarrow NO^+ + N$	$1.2 \cdot 10^{-12}(\frac{300}{T_e})^{0.41}$
R23	$CO^+ + NO \rightarrow NO^+ + CO$	$3.3 \cdot 10^{-10}$

Table 2.2: Reaction rates for Martin ionospheric chemistry

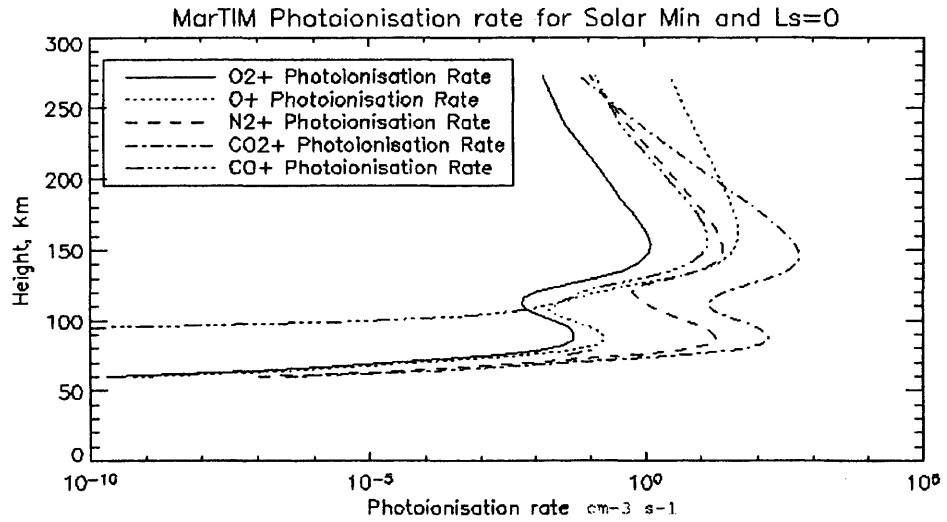

Figure 2.4: Photoionisation rates, from MarTIM, for solar minimum and equinox conditions at the subsolar point

ditions are shown in figure 2.4. MarTIM ion density profiles and an electron density profile, for the same conditions are shown in figure 2.5 and figure 2.6 respectively.

The magnitude of the lower peak of the ionosphere is controlled not only by X-rays and high energy photons but also by secondary electron ionisation. Work has been done on parameterising this secondary electron ionisation effect for use in global circulation models, [63]. Full details of how to calculate the amount of secondary ionisation can be found in [30]. The effect of including secondary ionisation in the ionospheric calculations is most noticeable in the densities in the lower ion and electron density peaks. This can be seen in results from MarTIM, shown in figure 2.7.

It has been assumed that photochemistry controls the ion density structures right to the top of the atmosphere within MarTIM and ion diffusion has not been included in the region above 170km, where it is predicted to take control of the ion distributions, [30]. As MarTIM does not include a method to account for the interaction of the solar wind with the ionosphere it is expected that the ion densities at high altitude will be larger than measured.

There is no inclusion of a nighttime source of ionisation in MarTIM, even though there is evidence that there is ionisation due to electrons being fed in from the magnetotail, [74]. As the production/loss ion reactions still occur on the nightside (with the exception of the photoionisation reactions obviously!) there is a low density iono-

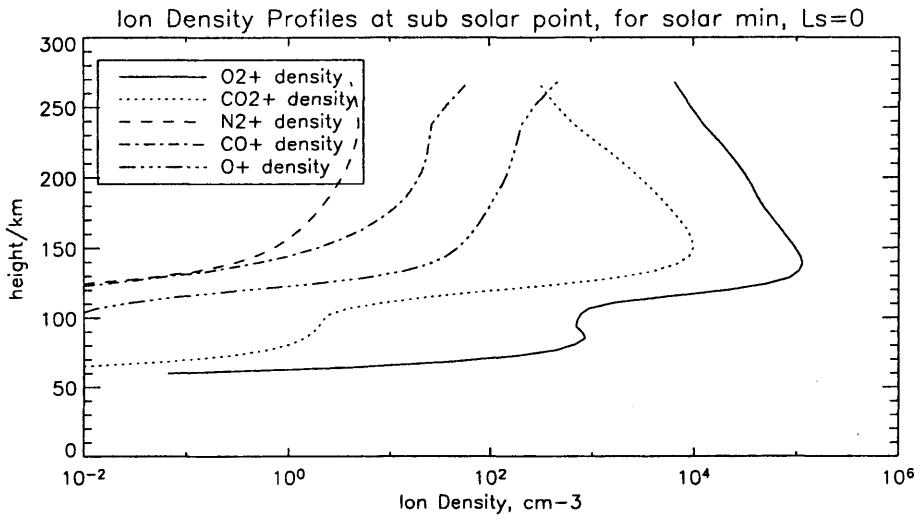

Figure 2.5: Ion density profiles, from MarTIM, for solar minimum and equinox conditions at the subsolar point

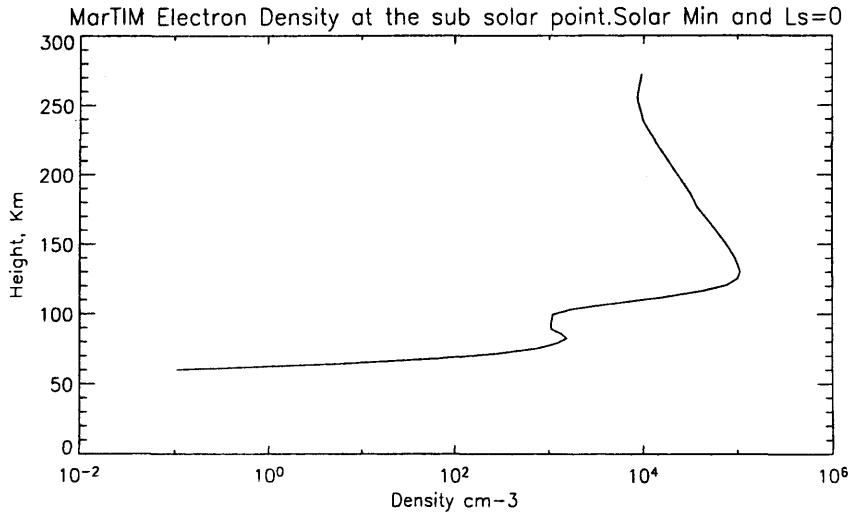

Figure 2.6: Electron density profile with no secondary ionisation, from MarTIM, for solar minimum and equinox conditions at the subsolar point

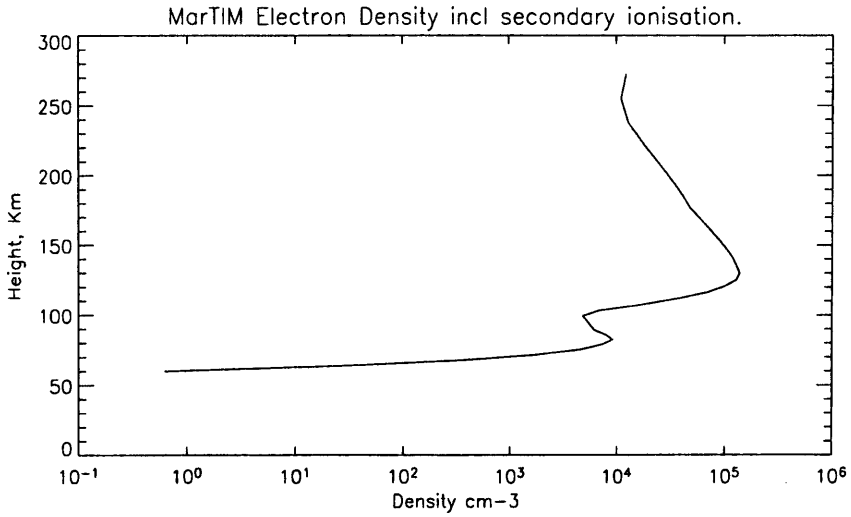

Figure 2.7: Electron density profile from MarTIM, with secondary ionisation included, for solar minimum and equinox conditions at the subsolar point.

sphere for a few hours after dusk, which is gradually neutralised by charge exchange in the atmosphere. This is shown in figure 2.8.

Further discussion of the ionospheric results produced by MarTIM can be found in Chapter 3.

2.4 Numerical Techniques

The equations of energy, momentum and continuity cannot be solved in an analytical fashion due to the non-linear terms included. MarTIM solves these equations numerically using a finite difference method.

The finite difference method generates solutions at a set of grid points. MarTIM represents the Martian thermosphere on a fixed global grid of height, latitude and longitude values.

The continuous momentum, energy and continuity equations are mapped onto the finite element grid by defining any function F, shown in equation 2.34.

$$F_i = F(x_i) \tag{2.34}$$

Where x_i represents a grid point as shown in equation 2.35

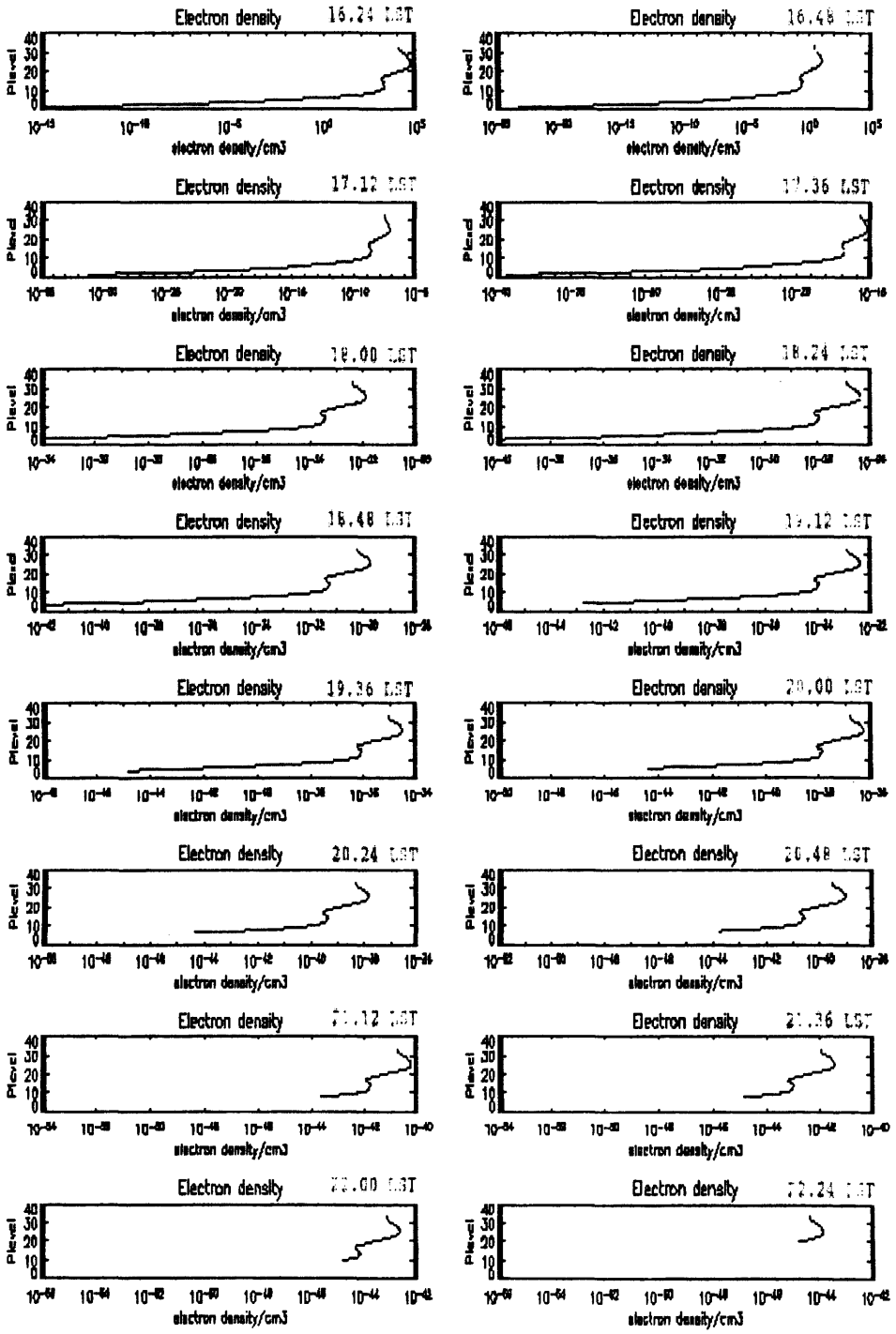

Figure 2.8: Electron density profiles from MarTIM, with secondary ionisation included, for solar minimum and equinox conditions, showing the effect of the onset of nighttime on the ionosphere.

$$x_i = x_1 + \sum_{m=1}^{i-1} \Delta x_n \tag{2.35}$$

Spatial derivatives can be defined at the gridpoints for the domain $x_1 \leq x \leq x_2$, and assuming that the function does not vary over the grid spacing, the first spatial derivative is given by equation 2.36.

$$\frac{\partial F}{\partial x} = \frac{F_{i+1} - F_{i-1}}{2\Delta} \tag{2.36}$$

Where $\Delta = x_i - x_{i-1} = x_{i+1} - x_i$ is the grid spacing.

The second spatial derivative is given by equation 2.37.

$$\frac{\partial^2 F}{\partial x^2} = \frac{F_{i+1} - 2F_i + F_{i-1}}{\Delta^2} \tag{2.37}$$

The accuracy of the use of these differentials in global circulation models has been found to be reasonable and is discussed in detail in [32].

2.4.1 Model Boundaries

The Upper Boundary

The velocities and temperatures at the upper boundary pressure level are set to the values from one level below. This is because it is assumed that there are no momentum or heat sources at the upper level of the model. It is also assumed that there is no vertical mass flux at the upper boundary. As a result the vertical velocity of the pressure level, ω, is set to zero at the upper boundary.

The Lower Boundary

The basic MarTIM model simulations are performed with a lower boundary set to a constant height(60km), pressure(0.883Pa), and temperature(154K). The wind velocities at this lower boundary pressure level were set to zero. The inclusion of the (2,2) migrating tide (chapter 5) and the Mars Climate Database Lower Boundary (chapter 6) introduced variations in the height, temperature and velocities at the lower pressure level. The mechanisms for altering the lower boundary pressure level are outlined in the respective chapters.

Smoothing Frequency

Direction	Temp and Winds	Composition
Horizontal	8	35
Vertical	10	26

Table 2.3: Smoothing frequency for MarTIM in terms of a model time step of 10 seconds

The Poles

The temperature, wind velocity and composition at the poles were initially dealt with using the method developed for the previous UCL Mars model, [77]. This method involved averaging the values of the nearest latitude circle (one cell away from the pole) and setting the polar values to this averaged value. In MarTIM, the polar regions were a source of numerical instability when using this calculation method. To help prevent the change in parameters being too great in the polar regions, the polar calculation was altered. The polar value now uses the average of the latitude circle two away from the pole. This method helped to stabilise the parameters at the pole and remove the numerical instability.

2.4.2 Smoothing and MarTIM Spatial and Temporal Resolution

Numerical models are prone to more general numerical instabilities, [32]. Instabilities in the model appear when a variable in adjacent grid points starts to slowly diverge across the grid boundary. These features are not physical but are amplified by the numerical method. A numerical smoothing algorithm is used every few time steps to eliminate these non-physical features. A trade off between computational time and accuracy has to be made so that the model simulation time is realistic. How often the smoothing is performed is established by trial and error, smoothing too often may result in losing small-scale structure in the model. Within MarTIM there are smoothing routines for both the horizontal and vertical variables representing wind, temperature and composition. The call rates are shown in table 2.3

The rates were found to be the optimum smoothing frequency after several tests were performed on MarTIM. The temporal and spatial resolution of the model also affected the smoothing frequency needed to achieve model stability. The longer the

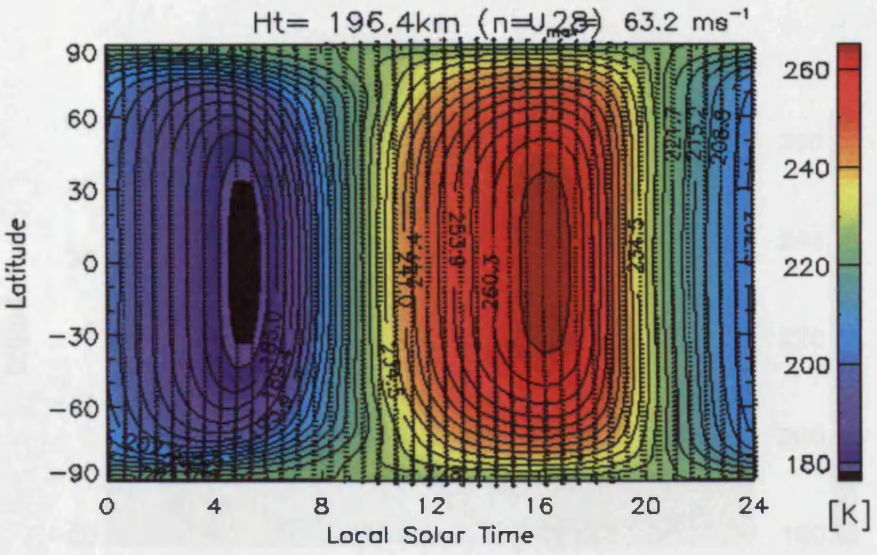

Figure 2.9: Temperature and horizontal winds across an upper atmosphere pressure level for solar minimum conditions and L_s=0, horizontal resolution is 2° latitude by 9° longitude

time step and the finer the spatial grid the more smoothing was needed to achieve stability. A lower limit latitude-longitude resolution was found to be 1° by 2° with a time step of 18 seconds and smoothing every timestep. This lower limit was set by the memory available and the model runtime. Model resolutions that took over 6 hours to simulate a "Mars day" were considered below the lower limit. The results shown in the figures below demonstrate that for a time step of 10 seconds, with the smoothing rates mentioned above, the magnitudes of the temperatures and wind speeds do not vary significantly.

It was discovered that the optimum resolution for MarTIM consisted of latitude-longitude grids of the order of 4° to 6° and a time step of 10 seconds. This meant model output was not biased towards either direction in terms of resolution and also provided reasonable run times for the model. Another advantage of this resolution is that smoothing levels needed for stability were not so high as to possibly dampen out any small scale structures that may occur. For chapters 3, 4 and 5 a 6° by 6° scheme is used, for chapter 6 a 5° by 5° scheme is used to match the Mars Climate Database version 3.1 horizontal resolution. Vertical resolution is also variable but it was decided to set this at a half scale height resolution until a need for high vertical resolution effects, such as gravity waves, was needed in MarTIM.

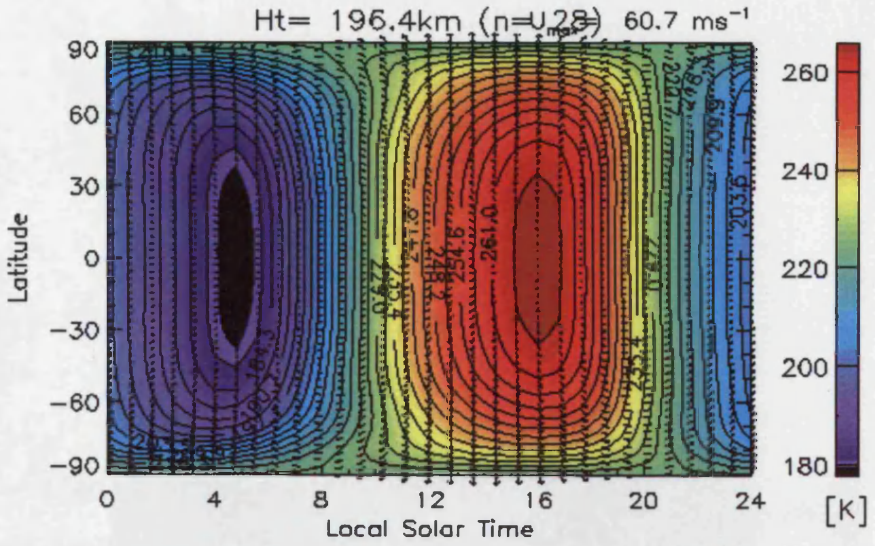

Figure 2.10: Temperature and horizontal winds across an upper atmosphere pressure level for solar minimum conditions and L_s=0, horizontal resolution is 3° latitude by 12° longitude

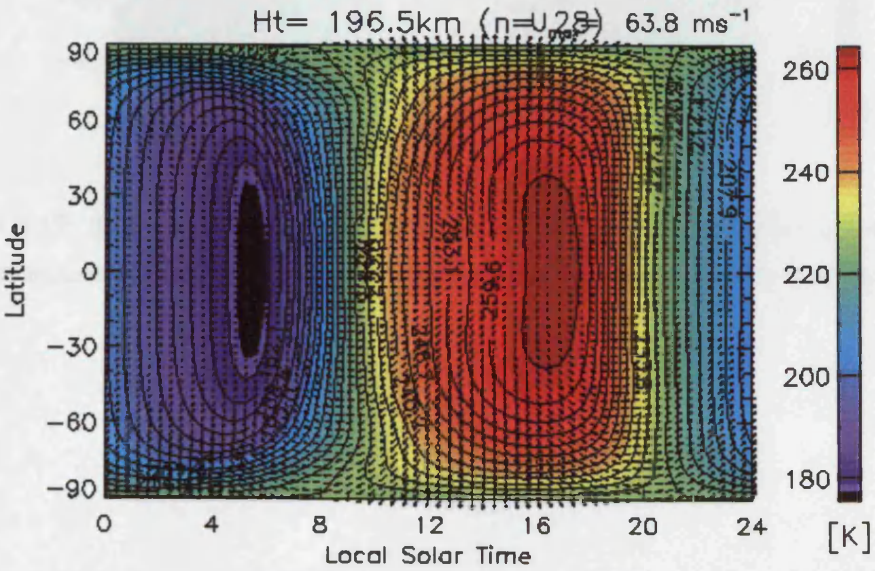

Figure 2.11: Temperature and horizontal winds across an upper atmosphere pressure level for solar minimum conditions and L_s=0, horizontal resolution is 5° latitude by 5° longitude

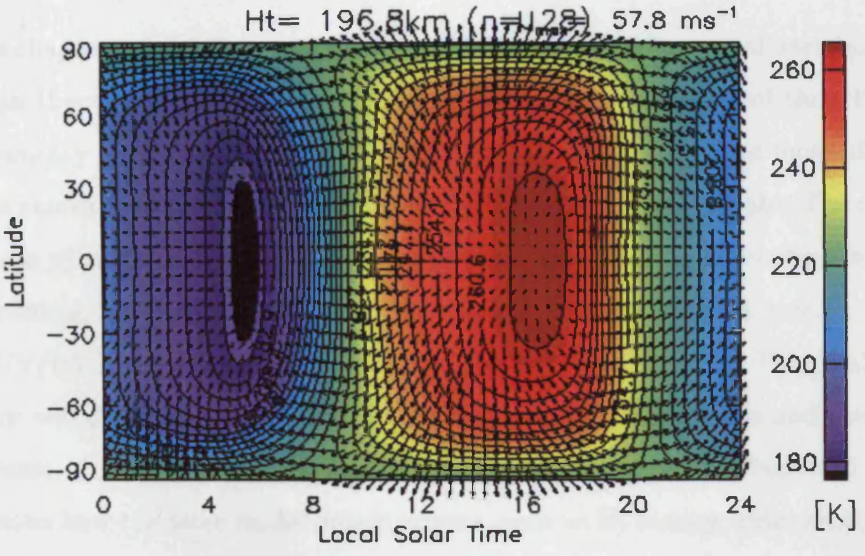

Figure 2.12: Temperature and horizontal winds across an upper atmosphere pressure level for solar minimum conditions and L_s=0, horizontal resolution is 6° latitude by 6° longitude

Chapter 3

Basic Model Simulations

In this chapter results demonstrating the basic diurnal and seasonal variations of the Martian thermosphere with in-situ EUV/UV forcing are shown and their behaviour and accuracy is discussed. MarTIM is run for four "Mars days" for most of the conditions shown here to ensure that the model had reached steady state. The exception to this is when the orbital effects are examined. MarTIM was run concurrently with incrementing L_s values to reproduce the seasonal variability over a year.

EUV/UV forcing is expected to control the upper atmosphere. The results in this chapter will demonstrate the basic background temperature, winds and composition structures. It will then be possible to use these results as a baseline from which to determine how the later model developments, such as IR forcing, tides and a variable lower boundary, affect MarTIM.

3.1 EUV/UV forcing: Energetics

The temperature in the Martian upper atmosphere is controlled by EUV/UV radiation flux absorption and the magnitude of the eddy diffusion coefficient. The measurements recorded in Mars' atmosphere by different satellite missions for a variety of seasons and solar conditions have been vital to constrain the model predictions of upper atmospheric temperatures. Table 3.1, adapted from [7], shows the conditions experienced by the various probes, and the temperatures recorded at thermospheric altitudes. The Mariner missions indirectly measured the temperature of the Martian atmosphere, but the altitudes to which these measurements may be assigned are not

Spacecraft	F10.7	L_s	SZA(°)	Temperature K(at altitude)
Viking L1	69.0	96.0	44.0	186 (200km, [8])
Viking L2	76.0	117.0	44.0	145 (150km, [8])
Mars Pathfinder	70.0	143.0	135.0	153 (160km, [28])
Mars Global Surveyor 1	93.0	256.0	73.5	220 (250km, [7])
Mars Global Surveyor 2	127.0	48.5	57.0	235 (180km, [7])

Table 3.1: Mars upper atmosphere measurements of temperature with corresponding altitude, solar activity, season and solar zenith angle.

clear from the literature and so have not been included in table 3.1.

As stated in chapter 1 the value chosen for the EUV efficiency is 18%. The eddy diffusion coefficient, which is set to a maximum of $1500 m^2 s^{-1}$ above the turbopause, [9], was decided upon after observing the effect of adjusting the coefficient on the thermospheric temperatures. Figure 3.1 show temperature profiles, at the subsolar point on the equator, for different eddy diffusion coefficient maximum values. The run conditions were for L_s=0 and solar minimum conditions.

For solar minimum conditions at equinox (L_s=0) the upper thermospheric temperature of Mars is expected to be around 220K-240K, [9]. Figure 3.1 shows that when the eddy diffusion coefficient is less than $1500 m^2 s^{-1}$ the exospheric temperatures are increased, and when it is more than $1500 m^2 s^{-1}$ the temperatures are reduced. This occurs because the eddy diffusion coefficient affects the magnitude of the total vertical conduction, see equation 2.19 and the last two terms in equation 2.16. As the eddy diffusion coefficient reduces, K_T does the same, so the magnitude of the vertical conduction terms are reduced, resulting in less heat being conducted away. The result of altering the maximum value of the eddy diffusion coefficient has resulted in thermospheric temperatures that are not too far away from the expected values for solar minimum. The $1500 m^2 s^{-1}$ value is chosen for MarTIM because it produces thermospheric temperatures that fall directly within the expected range mentioned above. In this way the choice of eddy diffusion coefficient is expected to reflect the correct heat balance.

Figure 3.2 shows the globally averaged heating and cooling rates for EUV/UV

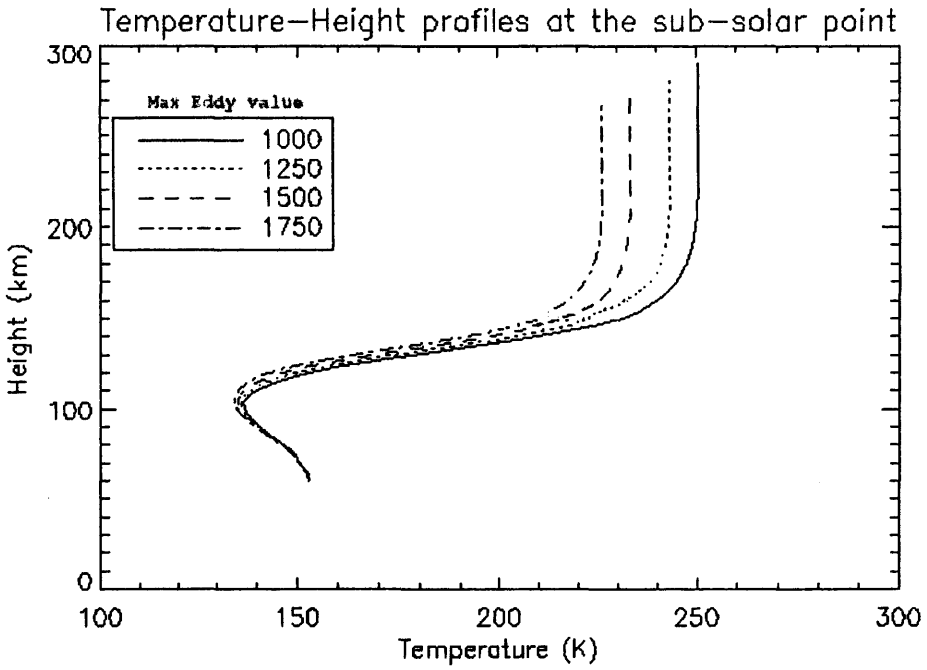

Figure 3.1: Temperature profiles with different eddy coefficients for L_s=0 and solar minimum conditions

forcing only.

Figure 3.2 shows that, globally averaged, the EUV/UV heating is balanced by the vertical conduction. Below around 130km there is a minimal amount of heating and cooling.

Figures 3.3 and 3.4 show the distribution of EUV/UV heating and vertical conduction around the equator in MarTIM as a function of local solar time and altitude. The peak EUV heating, corresponding to 570Kday^{-1}, occurs around noon, for solar medium conditions and L_s=0, at an altitude of 175km. Above this altitude the atmosphere is optically thin to EUV/UV radiation and the resulting distribution of heating is nearly uniform over the dayside, with a sharp cut off along the terminator. The distribution of vertical conduction is not as uniform as that of the EUV heating, with its peak of -550Kday^{-1} occurring just after 1600 LST. This corresponds to the temperature distribution that is shown in figure 3.5. The reason the peak temperature (225K in this case) is at 1600 LST and not noon is that on Mars it takes around 4 hours for a balance to be reached between the incoming radiation and the outgoing heat energy. A similar scenario exists on Earth.

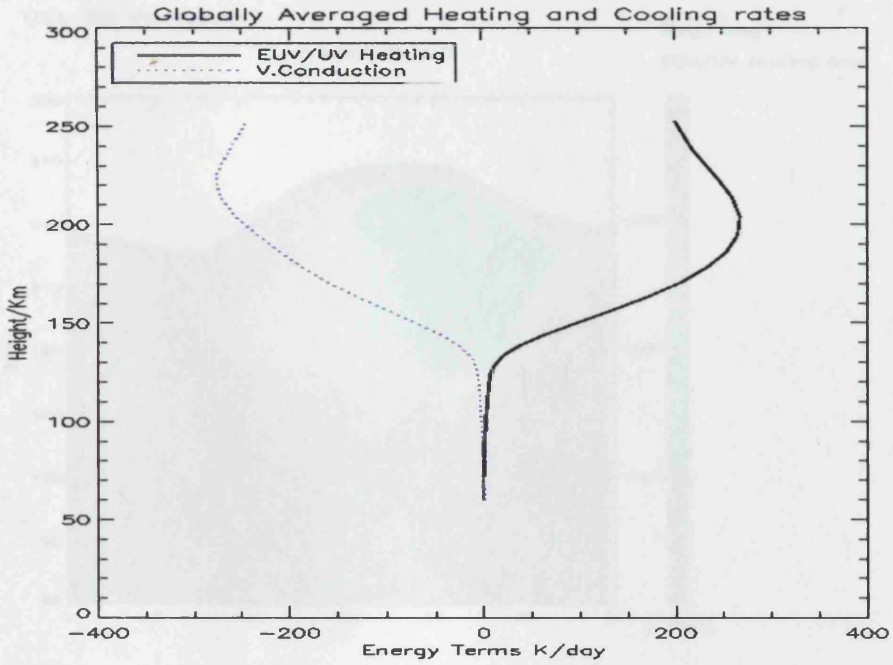

Figure 3.2: Globally averaged heating and cooling rates, from MarTIM, for L_s=0, solar minimum. EUV/UV forcing only

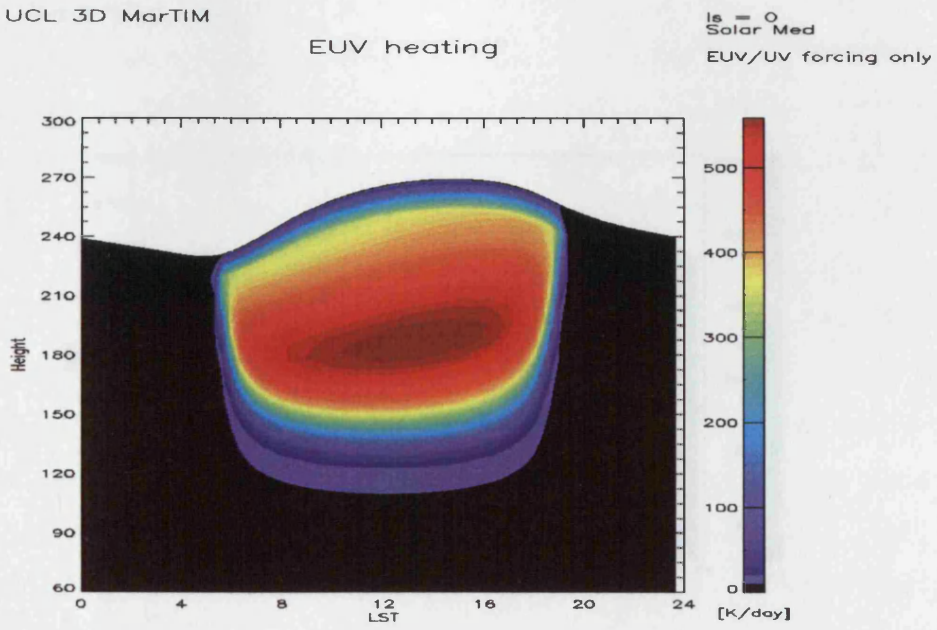

Figure 3.3: EUV solar heating rate, from MarTIM, for solar medium conditions, L_s=0, along the equator

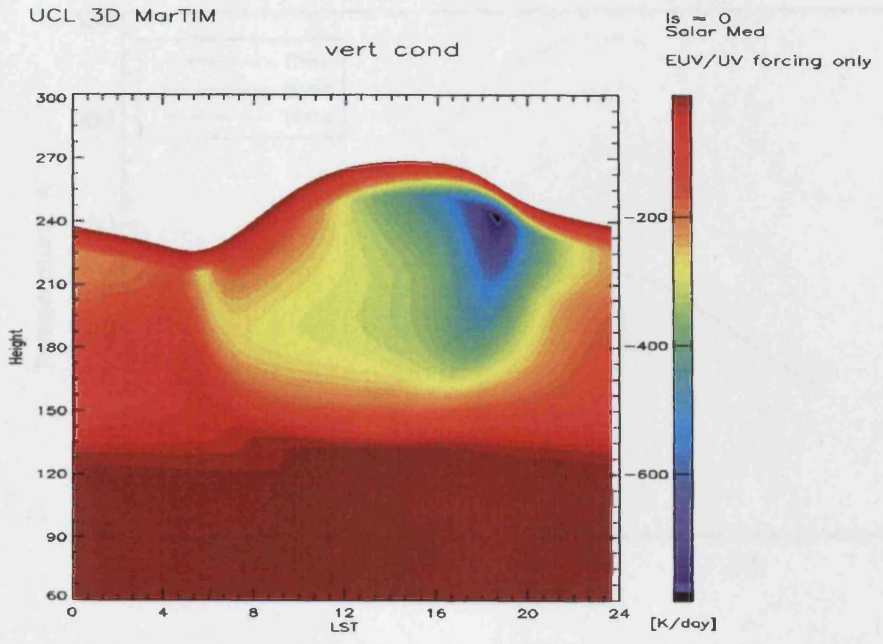

Figure 3.4: Vertical conduction, from MarTIM, for solar medium conditions, L_s=0, along the equator

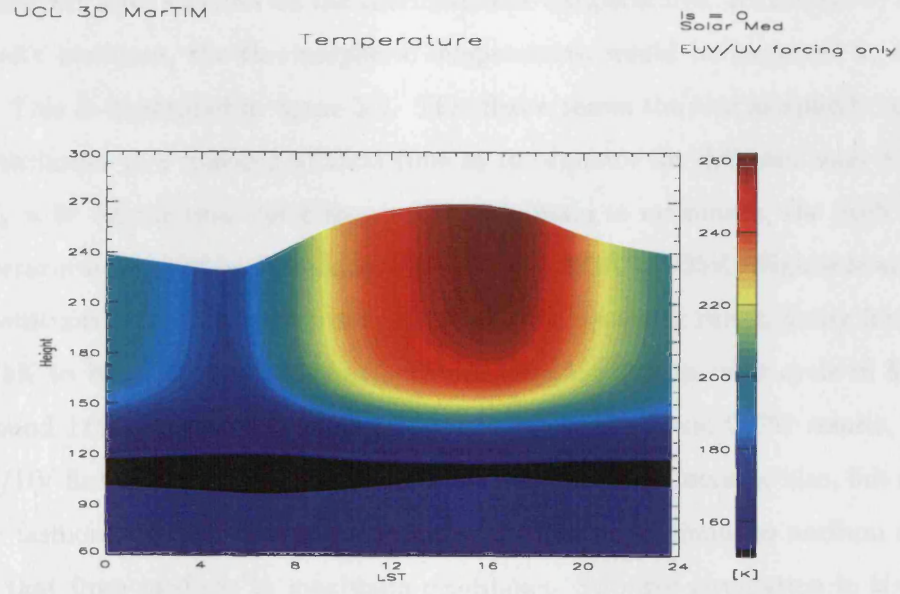

Figure 3.5: Temperature variation, from MarTIM, for solar medium conditions, L_s=0, along the equator

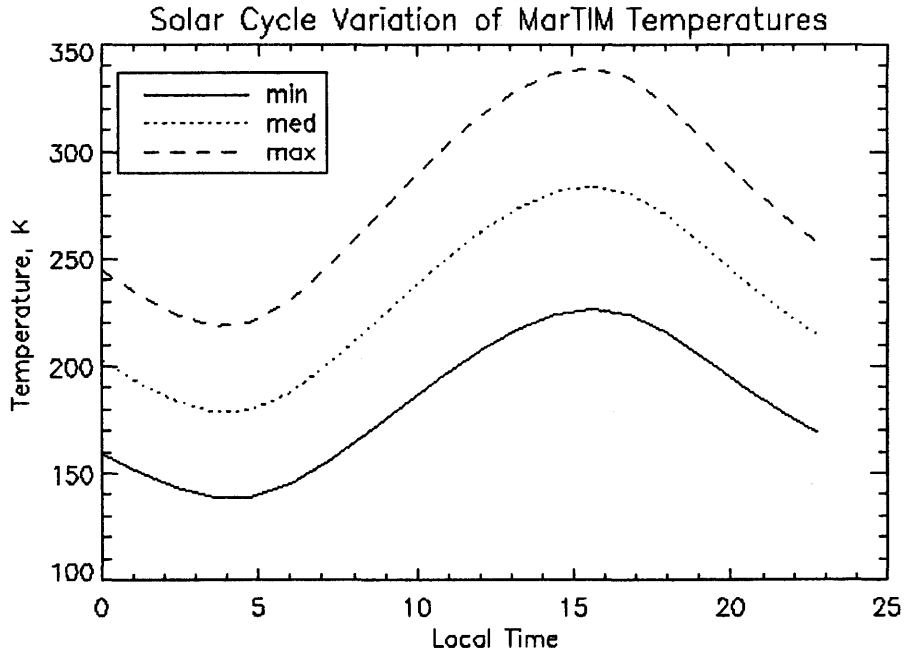

Figure 3.6: Thermospheric (pressure=$2.7 \cdot 10^{-7}$Pa) temperature variation, from MarTIM, L_s=0, for solar minimum, medium and maximum conditions, along the equator over a day.

Over the course of a solar cycle the EUV/UV flux intensity from the Sun varies and this will have an effect on the thermospheric temperatures. As the EUV/UV flux intensity increases, the thermospheric temperatures would be expected to increase also. This is illustrated in figure 3.6. This figure shows the thermospheric temperature variation as a function of local time at the equator for different solar activities for $L_s = 0$. As the solar cycle moves from minimum to maximum, the peak dayside temperatures respond by increasing from 220K to 280K to 335K. Nightside minimum temperatures also follow this trend, although over a smaller range, going from 135K to 175K to 220K. The dayside temperature variation due to solar cycle in MarTIM is around 115K, which is in good agreement with other basic GCM results, [9]. As EUV/UV fluxes increase over solar cycle, the temperatures increase also, but not in a linear fashion, i.e. the temperature increase from solar minimum to medium is larger than that from medium to maximum conditions. Stronger circulation in the atmosphere, resulting from increased radiative heating, would cool dayside temperatures, which also modifies the global winds.

The EUV/UV flux at Mars varies by 40%, [9], over the course of a Martian year

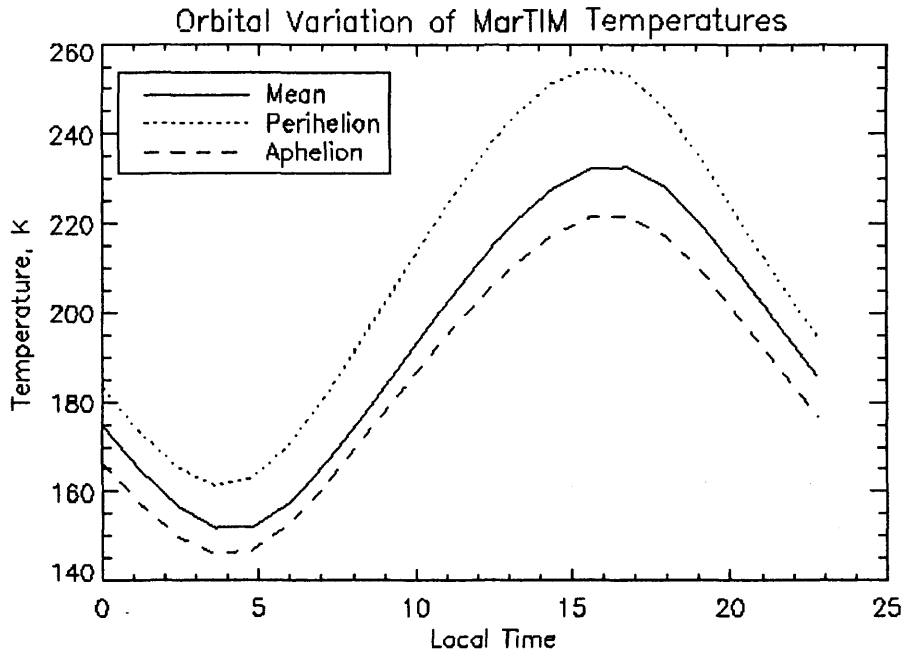

Figure 3.7: Thermospheric (pressure=$2.7 \cdot 10^{-7}$Pa) temperature variation, from MarTIM, for solar minimum conditions, for perihelion, aphelion and mean orbital positions, along the equator over a day.

due to the ellipticity of its orbit. It is thought that the low dayside middle atmosphere temperatures seen by the Viking 1 lander are due to a combination of solar minimum and aphelion conditions, [13]. To produce these results MarTIM was run in a continuous fashion, increasing the L_s every model day to reproduce the orbital effects. Figure 3.7 shows the MarTIM temperature response to orbital variation. The figure shows, for solar minimum conditions, the thermospheric temperatures as a function of local time, at the sub-solar point, for aphelion, perihelion and and average orbital position. Peak dayside temperatures due to orbital variation range from 215K to 230K to 250K, and the nightside minimum temperatures vary from 145 to 150K to 160K. This shows that, for MarTIM, there is a smaller variation in nightside temperature (15K) over a Mars year than for the dayside temperature (35K) due to orbital variation. It shows that the eccentricity of Mars' orbit cannot be ignored if temperatures are to be modelled in a realistic fashion.

Figures 3.8 and 3.9 below show the temperature distribution across an upper thermospheric pressure level for different seasons at solar minimum. It has already been

demonstrated that MarTIM produces a temperature variation due to Mars' eccentric orbit. This can be seen when comparing the aphelion (L_s = 90) and perihelion (L_s = 270) plots. The structures and temperature distributions are as expected, for northern hemisphere summer we see the hottest temperatures in the north, around 60°N latitude, the converse is true for the southern hemisphere summer season. For the two equinox plots it is useful to note that, although the general structures and distributions appear the same the bottom plot in figure 3.8 is slightly cooler. This is due to its position on Mars' orbit. The top plot in figure 3.8 shows the first equinox after perihelion and so the atmosphere is still relatively close to the Sun, by the time the second equinox comes around it has been further away from the Sun for longer.

3.2 EUV/UV forcing: Dynamics

The picture of the dynamics produced by MarTIM simulations with basic EUV/UV only forcing are described below. Seasonal and solar cycle variations resulting from these model runs are also discussed. The variations of the meridional and zonal winds across a high altitude pressure level are shown in figure 3.10, for solar minimum conditions and vernal equinox.

In figure 3.10 the effect of the Coriolis force on the winds can be seen. The heated air at the equator expands and then flows poleward where it sinks. These northward winds in the northern hemisphere, seen in the meridional plot, are affected by the Coriolis force which turns them eastward, the same happens to the southward winds in the southern hemisphere. Figure 3.10 thus shows that the meridional winds and zonal winds in MarTIM behave in a physically sound manner from the pressure and Coriolis point of view.

Figure 3.11 shows zonal mean plots for the meridional and zonal winds, from MarTIM, for solar minimum and L_s=0 conditions. The zonal mean meridional wind figure shows a strong southward wind in the southern hemisphere, matched by an equal magnitude northward wind in the northern hemisphere. This is expected for equinox conditions with the heating occurring at the equator and winds flowing away to the polar regions. Two opposite direction, smaller magnitude, wind structures are shown in the upper thermosphere, around pressure levels 29 to 33. This effect is due to the nightside equatorward winds being slightly stronger than the dayside poleward

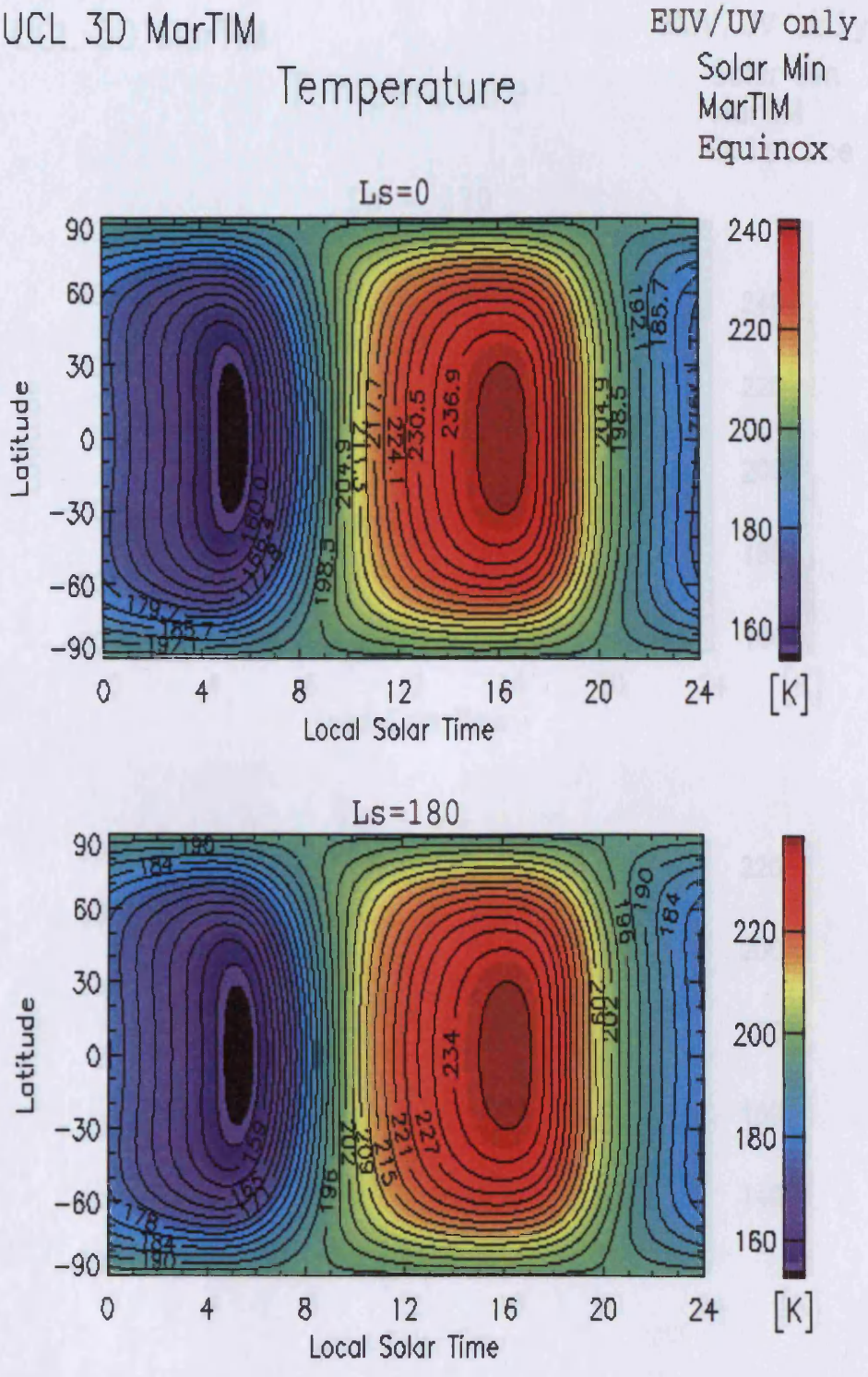

Figure 3.8: Temperature contour plots from MarTIM across an upper thermospheric pressure level (pressure=$2.7 \cdot 10^{-7}$Pa) for L_s=0 and L_s = 180 at solar minimum conditions, EUV/UV only forcing

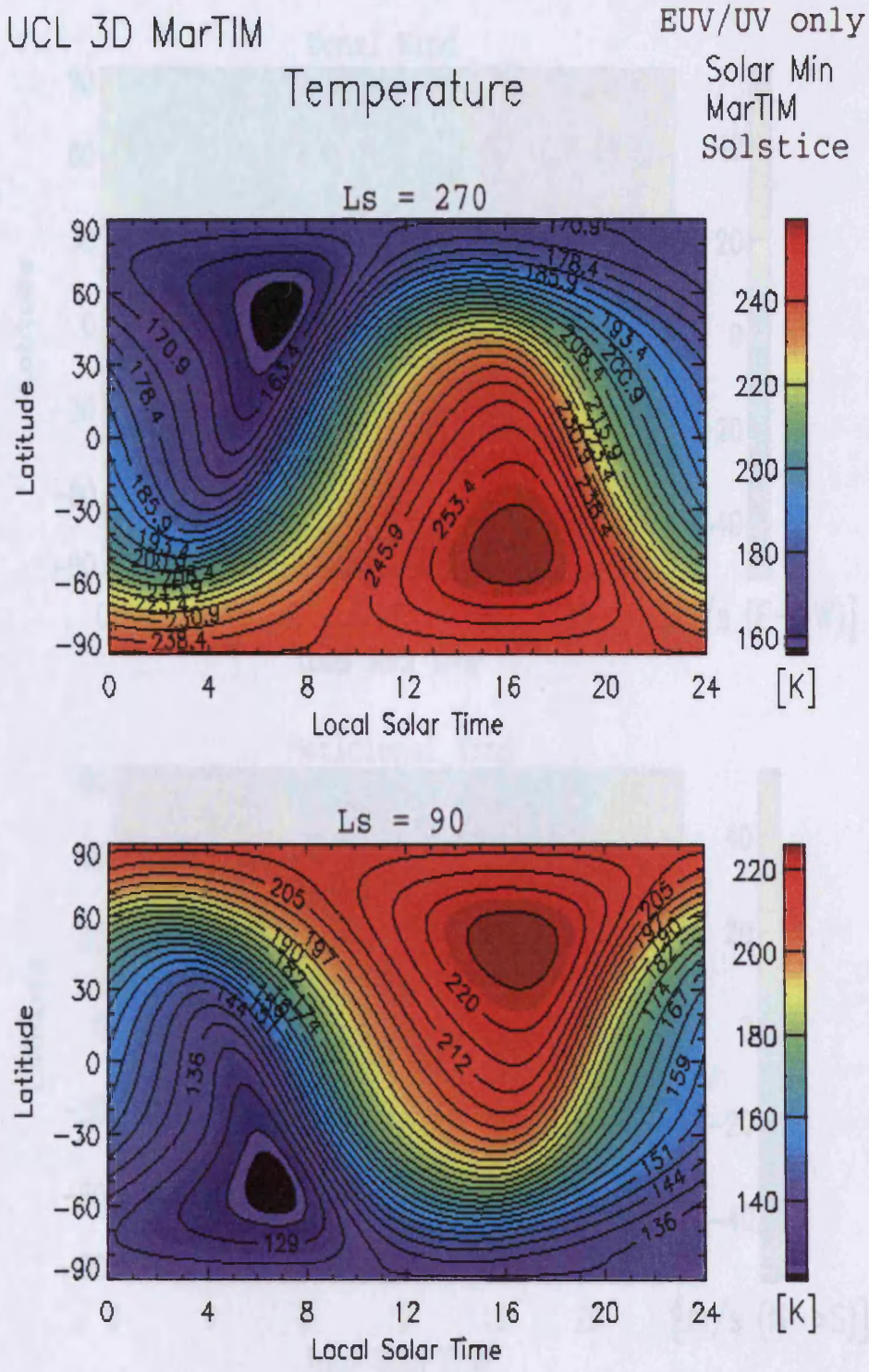

Figure 3.9: Temperature contour plots from MarTIM across an upper thermospheric pressure level (pressure=$2.7 \cdot 10^{-7}$Pa) for L_s=90 and L_s = 270 at solar minimum conditions, EUV/UV only forcing

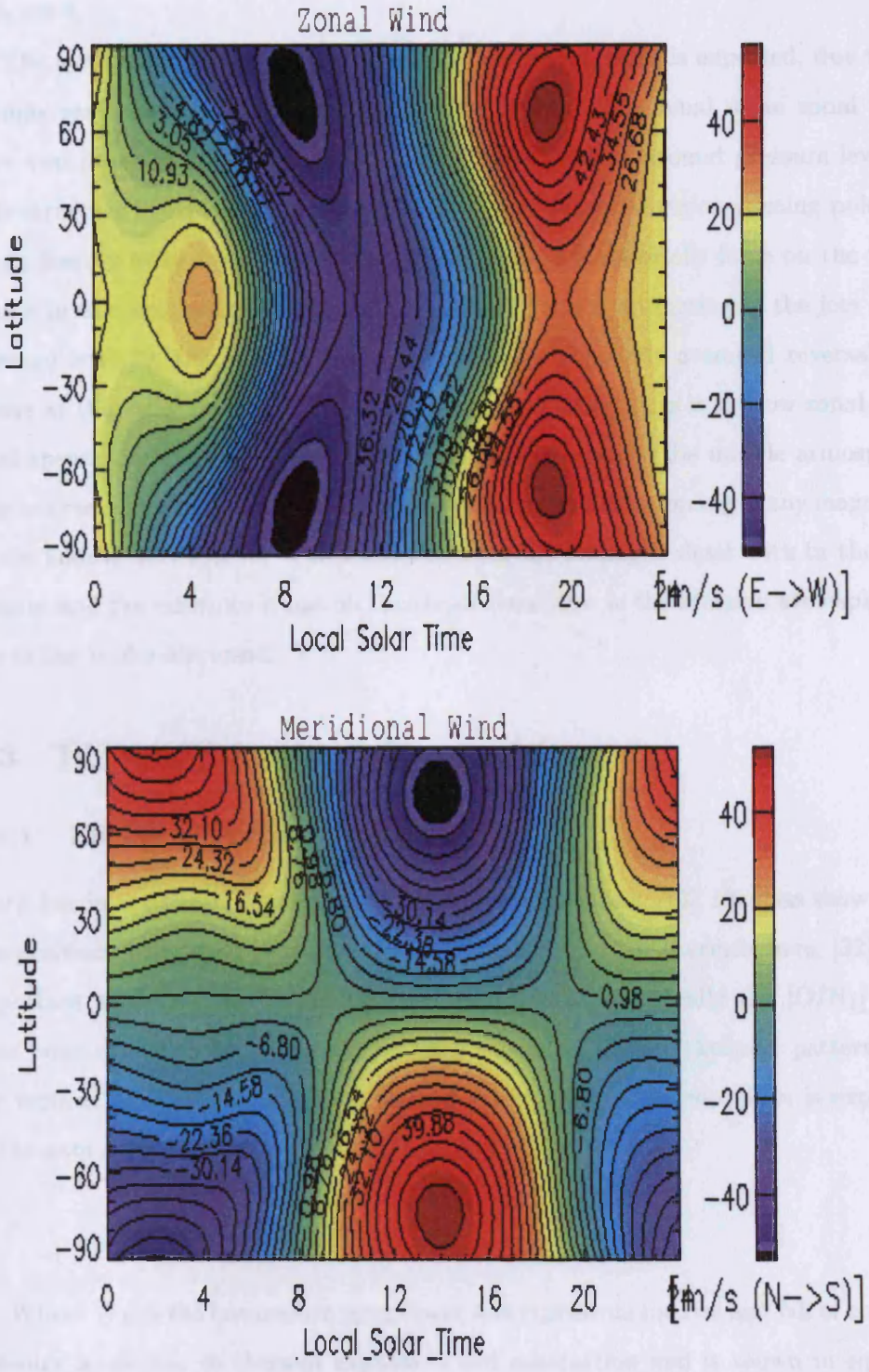

Figure 3.10: Zonal (top) and meridional (bottom) winds speeds across an upper thermospheric pressure level (pressure=$2.7 \cdot 10^{-7}$Pa), from MarTIM, for solar minimum conditions, L_s=0

winds in the top few pressure levels. This forms the structures seen in the top figure in figure 3.11.

The symmetric nature of the zonal mean wind structures is expected, due to the equinox season which causes symmetric solar forcing. The zonal mean zonal winds show two pronounced eastward wind flows, which peak at around pressure level 21. This structure is explained by the heating of the equatorial region causing poleward winds flowing away from the equator. The effect of the Coriolis force on the winds results in eastward winds in both hemispheres. There is a tapering of the jets above pressure level 29, this corresponds to the meridional zonally averaged reversal that occurs at this pressure level. One obvious feature of both plots is the low zonal mean wind speeds overall, and the extremely low wind speeds in the middle atmosphere. This is a result of the fact that for these model runs there is no forcing of any magnitude in the middle atmosphere. The addition of the IR forcing is dealt with in the next chapter and the influence it has on the mean zonal flow in the Martian atmosphere is one of the topics discussed.

3.3 EUV/UV forcing: Composition

3.3.1 Effects of Vertical Circulation

Work has been done on terrestrial global circulation models, [80], that has shown that composition changes are caused by global circulation in the thermosphere, [32]. The important thermospheric ratios in terrestrial models, specifically the $[O/N_2]$ ratio, have been shown to be influenced by the summer to winter transport patterns and the vertical divergence wind. The vertical velocity in the thermosphere is expressed as the sum of two components, see equation 3.1, [68].

$$V_z = W_B + W_D \tag{3.1}$$

Where W_B is the barometric component and represents the rise and fall of constant pressure levels due to thermal expansion and contraction and is shown in equation 3.2.

$$W_B = (\frac{\partial h}{\partial t})_P \tag{3.2}$$

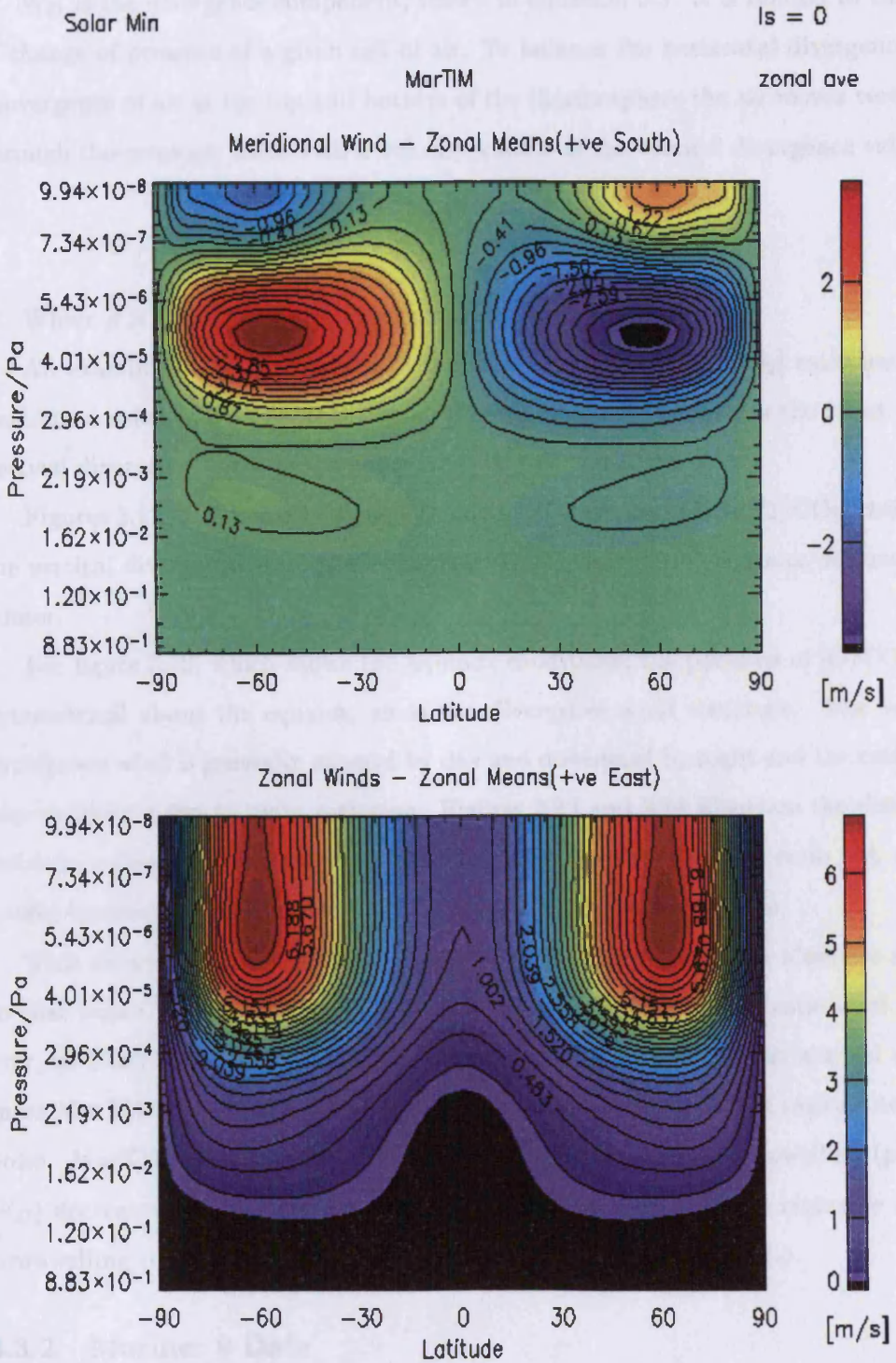

Figure 3.11: Zonal means for the zonal and meridional winds speeds, from MarTIM, for solar minimum conditions, L_s=0

Where h is the height from the surface and P the pressure.

W_D is the divergence component, shown in equation 3.3. It is related to the rate of change of pressure of a given cell of air. To balance the horizontal divergence and convergence of air at the top and bottom of the thermosphere the air moves vertically through the pressure levels with a velocity known as the vertical divergence velocity.

$$W_D = \frac{-1}{\rho g}\frac{dP}{dt} \tag{3.3}$$

Where ρ is the density and g the acceleration due to gravity.

An examination of the vertical divergence wind and the $[O/CO_2]$ ratio has been performed using MarTIM results from different seasons. These show the effect of the vertical divergence wind on the compositional ratio on Mars.

Figures 3.12, 3.13 and 3.14 show latitude-local time plots of the $[O/CO_2]$ ratio and the vertical divergence velocity for northern hemisphere spring equinox, summer and winter.

For figure 3.13, which shows the equinox conditions, the patterns of $[O/CO_2]$ are symmetrical about the equator, as is the divergence wind structure. The vertical divergence wind is generally upward by day and downward by night and the ratio plot also exhibits a day to night variation. Figures 3.12 and 3.14 illustrate the difference between equinox to solstice conditions on Mars for the $[O/CO_2]$ ratio. A strong winter/summer gradient exists with an expected local time variation.

This shows that the modelled global circulation distributions on Mars are similar to that found in terrestrial models, [80], albeit with a different gas ratio used. However, as Mars does not have an intrinsic magnetic field, and thus no auroral region, these MarTIM results do not show the same ratio variations in the regions near the poles. MarTIM shows that in the sunlit Martian thermosphere, upwelling (positive W_D) decreases the $[O/CO_2]$ ratio at a fixed pressure level. On the nightside mainly downwelling (negative W_D) occurs which increases the $[O/CO_2]$ ratio.

3.3.2 Mariner 9 Data

Data from Mariner 9, presented in [84], has been used to determine a variation in the fractional atomic abundance over latitude and local time. MarTIM simulations were produced for southern summer solstice and solar medium conditions, as suggested in

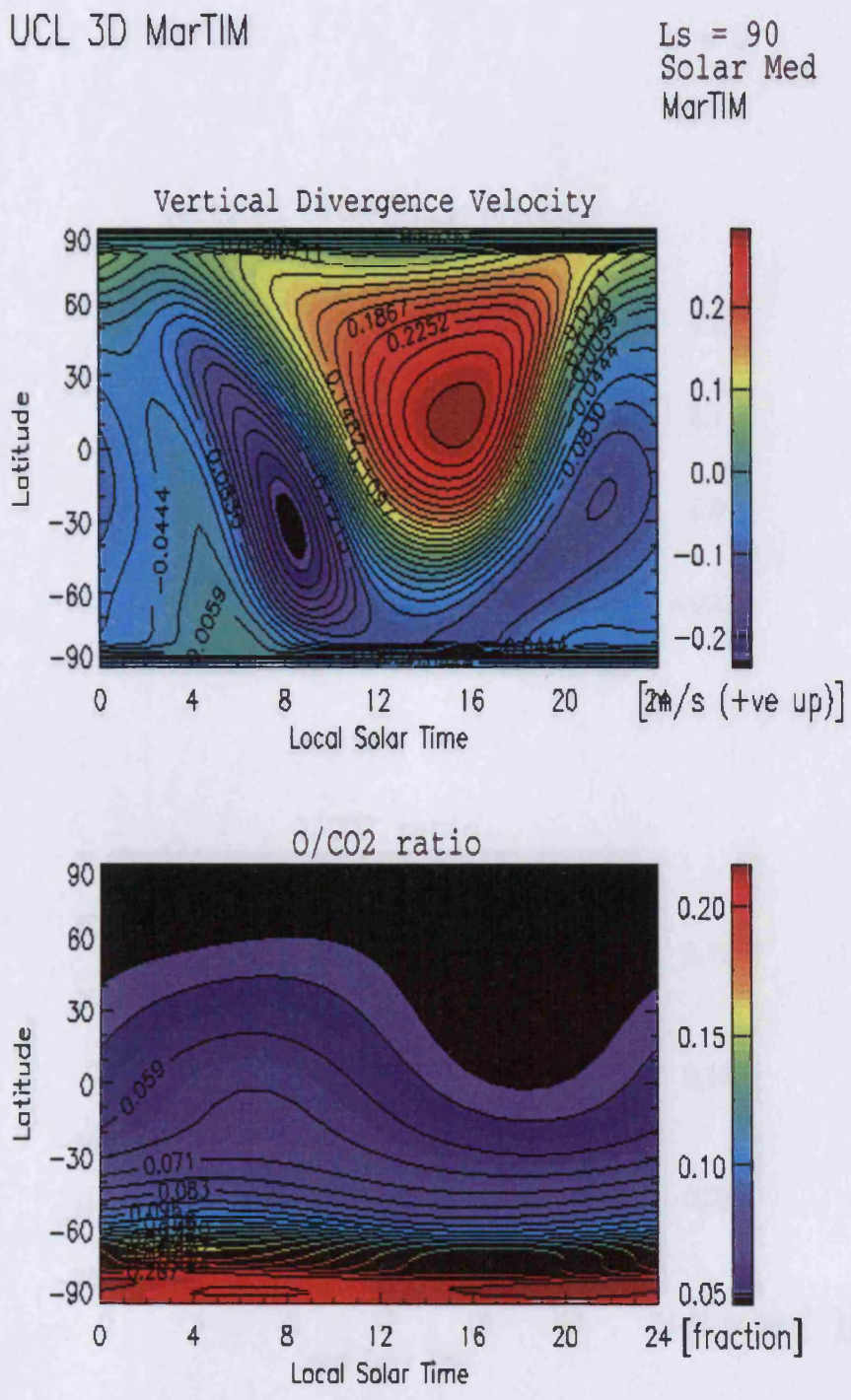

Figure 3.12: Vertical divergence wind and $[O/CO_2]$ ratio plot from MarTIM across a middle atmosphere pressure level (pressure=$4 \cdot 10^{-5}$Pa) for L_s=90, at solar medium conditions

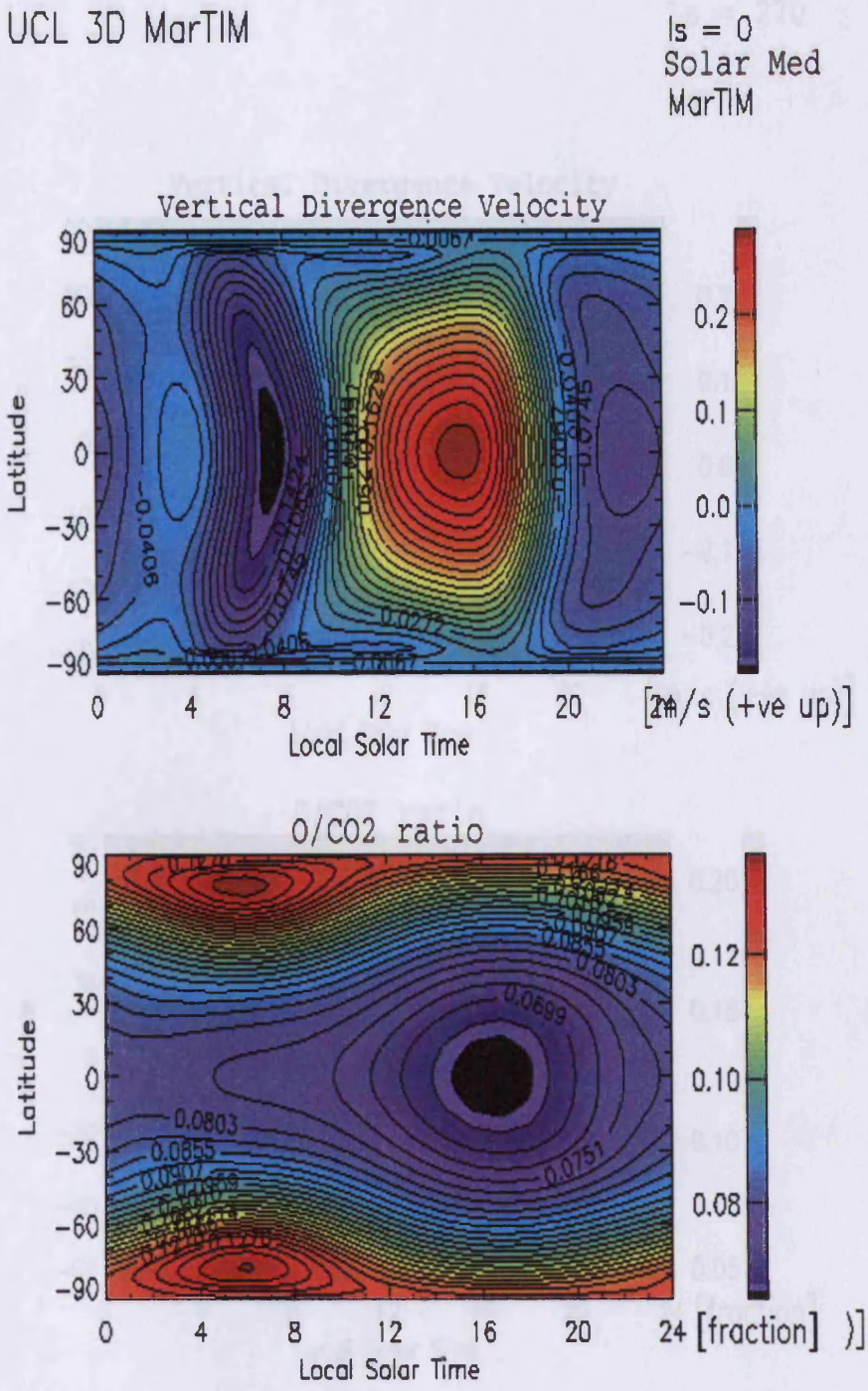

Figure 3.13: Vertical divergence wind and $[O/CO_2]$ ratio plot from MarTIM across a middle atmosphere pressure level (pressure=$4 \cdot 10^{-5}$Pa) for L_s=0, at solar medium conditions

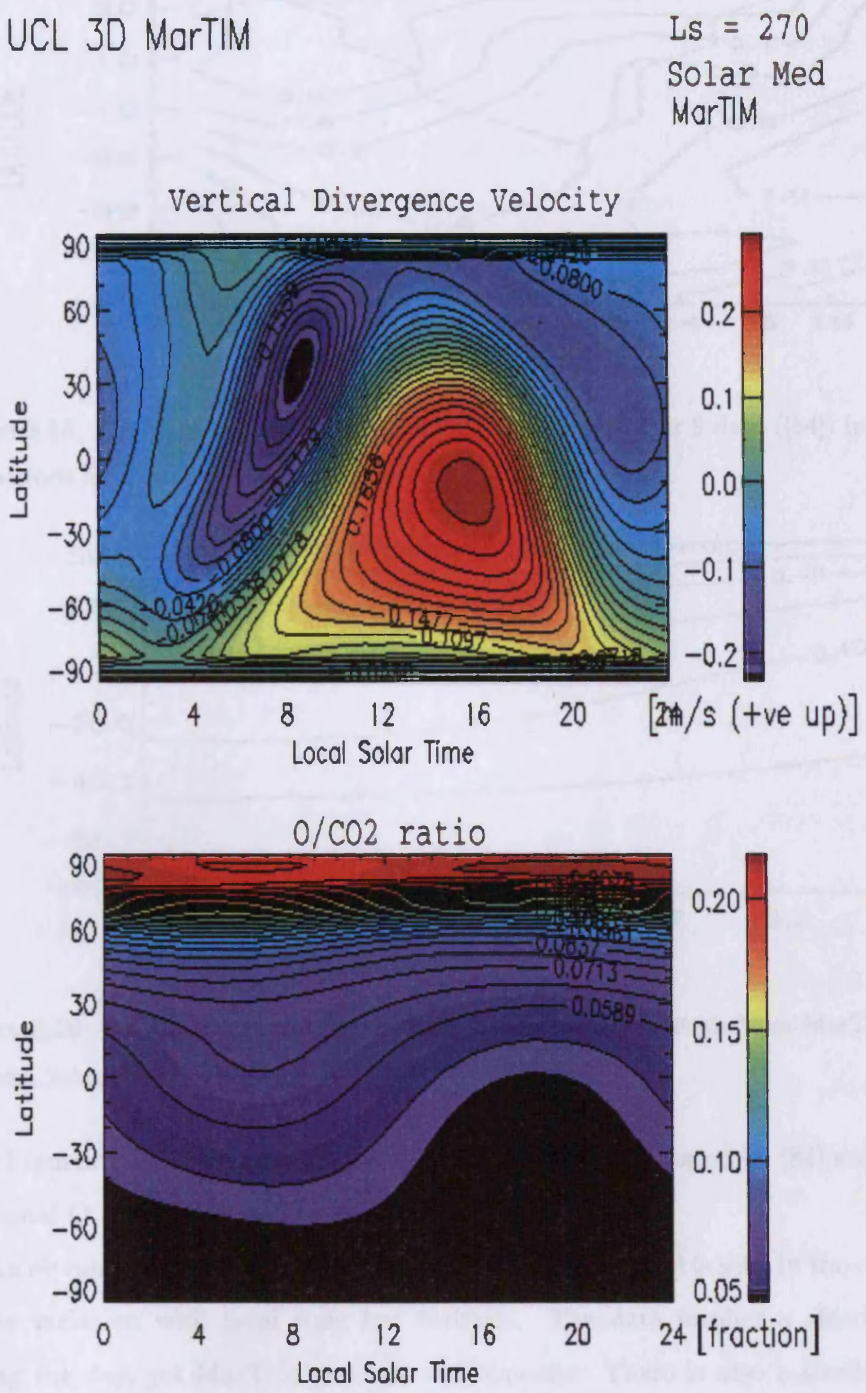

Figure 3.14: Vertical divergence wind and $[O/CO_2]$ ratio plot from MarTIM across a middle atmosphere pressure level (pressure=$4 \cdot 10^{-5}$Pa) for L_s=270, at solar medium conditions

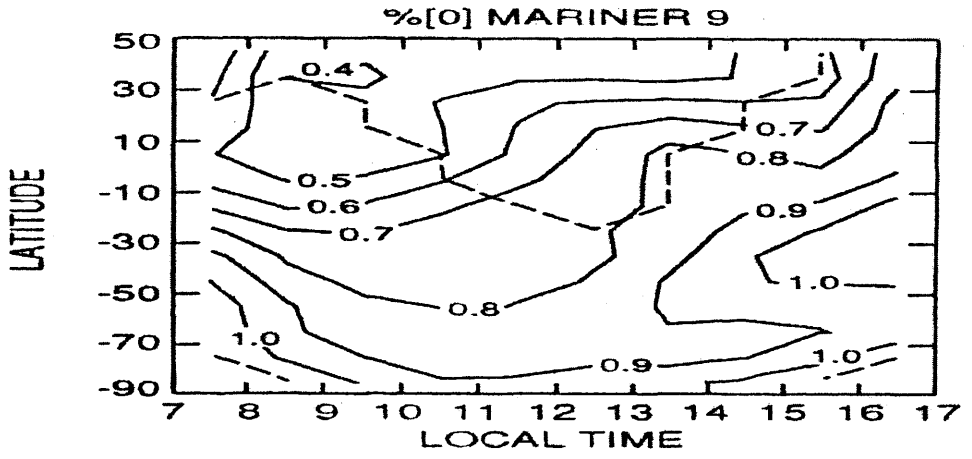

Figure 3.15: [O] fractional abundance plot derived from Mariner 9 data ([84]) in local time and latitude for the 1.2nbar pressure level.

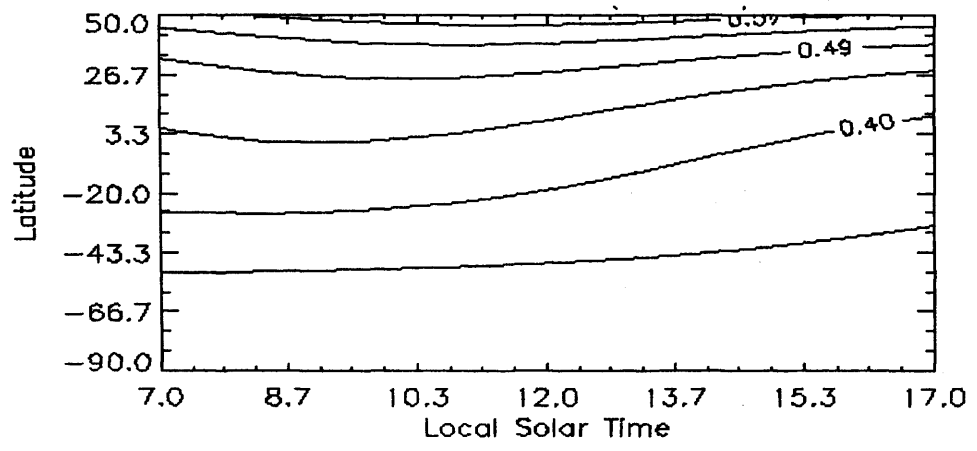

Figure 3.16: [O] fractional abundance plot in local time and latitude from MarTIM output, for the 1.2nbar pressure level.

[84]. Figures 3.15 and 3.16 show the Mariner 9 data as presented by [84] and MarTIM fractional O abundance, at the same altitude, respectively.

An obvious disagreement between the data and the model is seen in the comparison of the variation with local time and latitude. The data implies a steady increase during the day, yet MarTIM predicts the opposite. There is also a similar scenario when the latitudinal variation is compared, with MarTIM showing a north-south decrease in the fractional abundance, with the Mariner 9 data predicting an increase. However, the abundance ratios shown are of similar magnitudes. With EUV/UV solar forcing only, the zonal winds in MarTIM are producing the afternoon decrease

seen in the fractional abundance. Terrestrial modelling has shown that tidal effects and gravity waves affect the compositional distribution in the Earths thermosphere. As none of these features are present in the model simulation presented here, it is not expected that the structures would match well, but the similar magnitudes in fractional abundances between the model and data are expected. The effect of tides on the fractional abundance of O distribution will be examined in a later chapter.

3.4 Ionosphere Results

The nature of the ionospheric calculations have been described earlier in chapters 1 and 2. This section describes the results in detail and looks at the effects varying season and solar flux have on the ionospheric densities and structure.

As the figures in chapter 2 show, for solar minimum conditions, there is an ionospheric peak at around 130km, with a secondary layer at around 85km. There is negligible ionisation below 75km. Comparisons have been drawn between the ionosphere on Mars and the E-region that is found on Earth, [63], as the ionospheric peak occurs in a neutral background density of 10^{11} molecules/cm^3, similar to Earth. Under these conditions it is possible to model the ionospheric structure over latitude and longitude using the Chapman equations for photochemical equilibrium, [63]. This is permissible because under such conditions the time constants for photochemical processes (production and loss) are much shorter than for plasma diffusion, [63].

As has been shown in earlier sections, the Martian thermosphere is sensitive to changes in solar flux, and so we would expect some change in the ionosphere. This would be caused by the change in photoionisation rates and also by the production/loss reactions that are dependent on temperature. The effect of solar flux variation and hence photoionisation rates, is expected to be modest at 130km where the electron density peak occurs.

Figure 3.17 shows the wavelength dependent ionisation profiles for CO_2 at the subsolar point. (L_s=0, solar minimum). As the first reaction rate in table 2.2 shows, the conversion of CO_2^+ to O^+ is rapid, so the CO_2^+ profiles can be treated as O^+ profiles. Figure 3.17 shows that the main CO_2^+ peak is produced by photons with wavelengths $\lambda < 300\mathring{A}$, and the secondary peak by photons at $\lambda < 60\mathring{A}$.

Figure 3.18 below shows the variation of the electron density profiles for solar

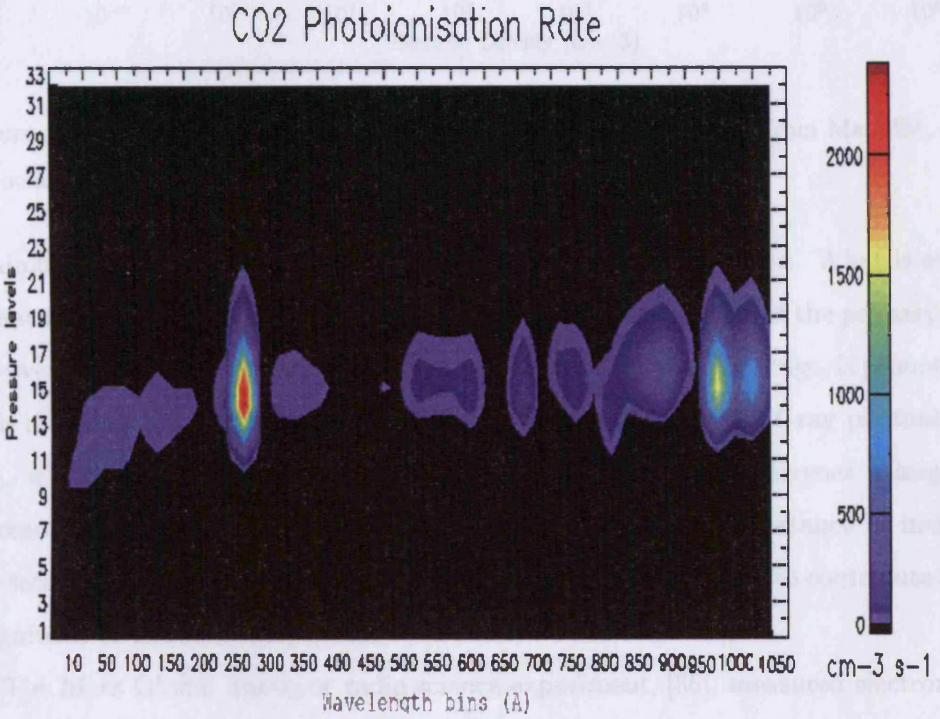

Figure 3.17: Wavelength dependent ionisation profiles for CO_2 at the subsolar point, using MarTIM wavelength bins in $\AA$. For solar minimum conditions, L_s=0

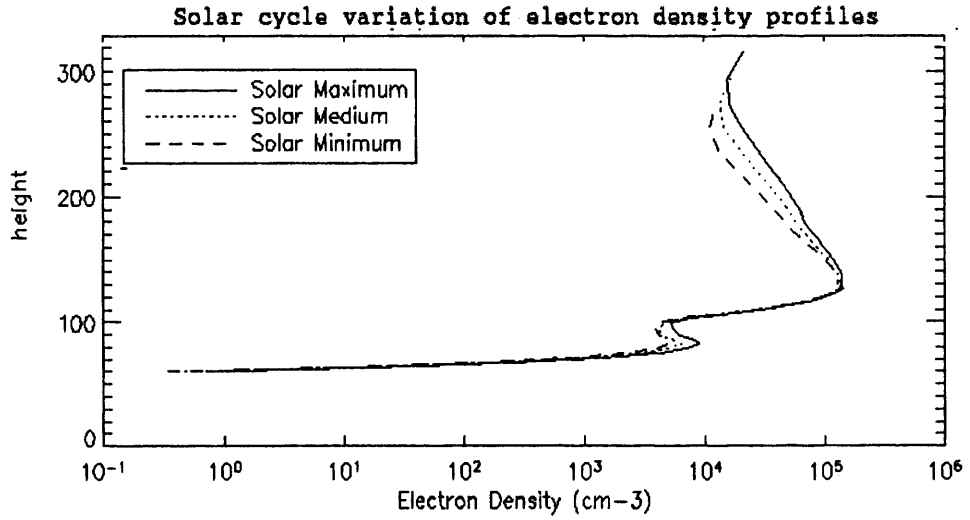

Figure 3.18: Variations over a solar cycle in electron density profiles from MarTIM, at the sub-solar point, L_s=0

minimum, medium and maximum conditions at the sub-solar point. What is evident is that the variation in solar flux has little effect on the magnitude of the primary peak, however the increase with solar activity in the secondary peak, or ledge, is pronounced. This is due to the fact that secondary peak is caused mainly by X-ray photons, [12], [30], which occur in the section of the solar spectrum that undergoes a large flux increase during high activity periods. This also shows the importance of including the secondary ionisation effects in the ionosphere model as they also contribute to the magnitude of the secondary peak.

The Mars Global Surveyor radio science experiment, [85], measured electron density profiles over a range of solar zenith angles and seasons. Figures 3.19 and 3.20 show the period from 06 May 1999 - 09 May 1999 of daily mean radio science electron density profiles compared with MarTIM results for the same conditions.

These results are in good agreement in terms of the matching of the primary ionosphere peak in magnitude and altitude. However the fall off from the main peak to the secondary peak in the MGS data does not occur as quickly as it does in MarTIM. This could be due to other secondary electron ionisation effects that are not included in MarTIM's ionospheric calculations. As MarTIM has a simply generated ionosphere, and there is good agreement with the position and magnitude of the ionospheric peak compared to MGS data this matter will be left for future work. The other main

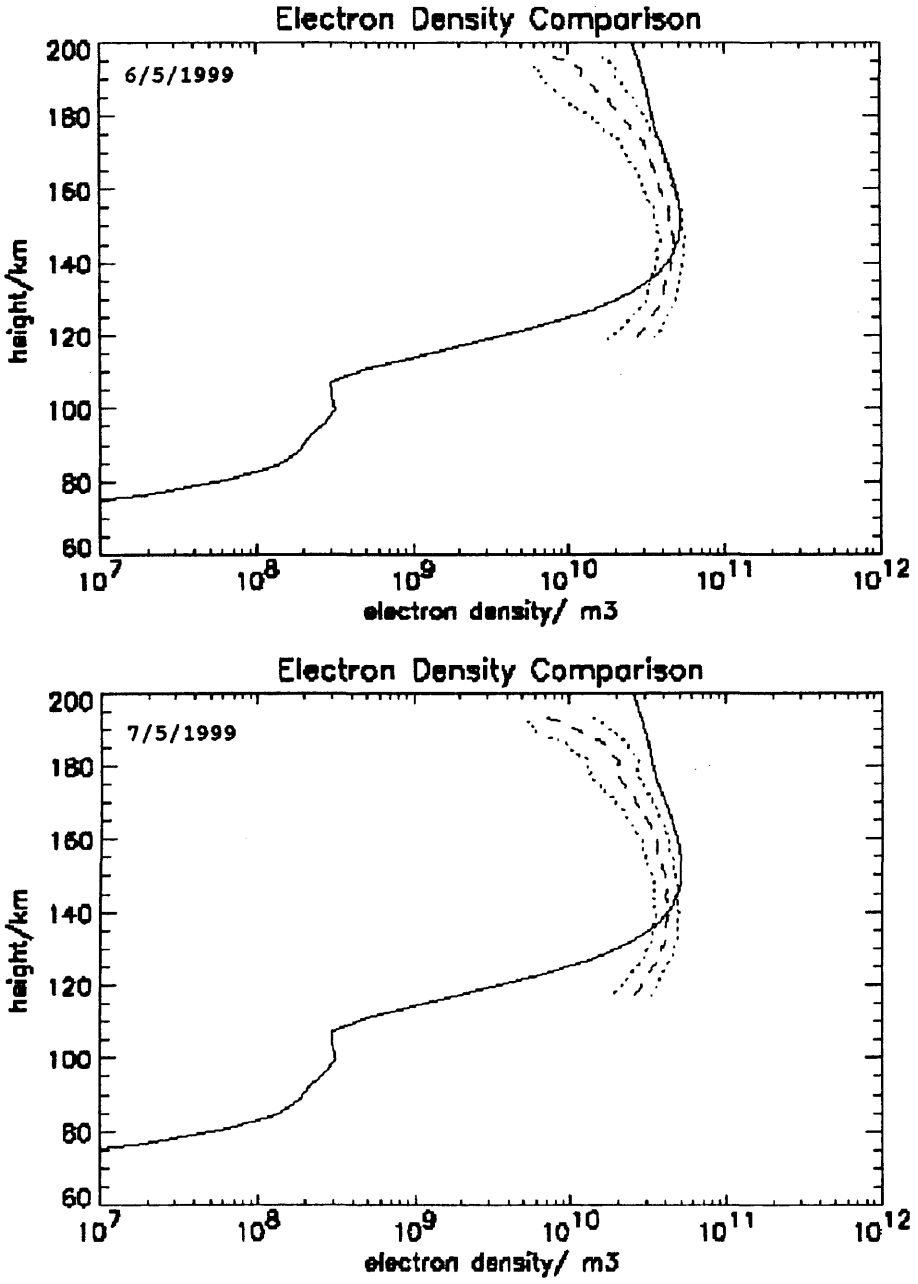

Figure 3.19: MarTIM electron density profile (solid line) compared to MGS radio science data (dashed line) with error bars (dotted lines) for the 6th and 7th May 1999

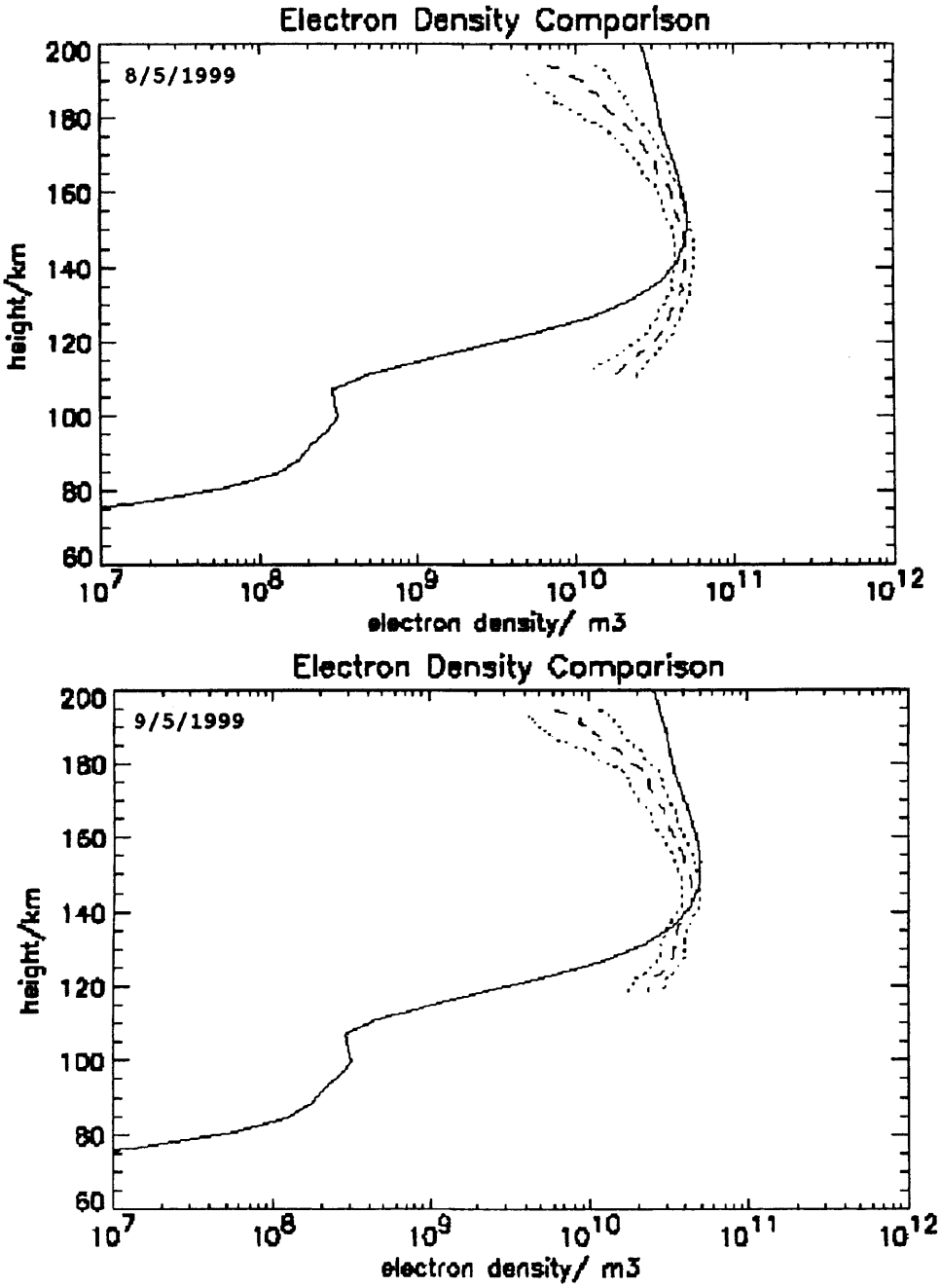

Figure 3.20: MarTIM electron density profile (solid line) compared to MGS radio science data (dashed lines) with error bars (dotted lines) for the 8th and 9th May 1999

discrepancy is at high altitudes where MarTIM overestimates the electron density compared to the MGS RS data. The reason for this could be linked to the assumptions in MarTIM that the ionosphere is in photochemical equilibrium at all altitudes and also that there is no solar wind interaction and thus no ion removal through the top layer, [74]. Future work on MarTIM will be able to determine whether including ion diffusion would bring the MarTIM predictions in line with the MGS RS data at high altitudes.

Chapter 4

The Infrared Energy Balance

The previous chapter has shown the basic model results due to EUV/UV only forcing, this chapter introduces the theory behind infrared heating and cooling in the Martian middle atmosphere. It then looks at the effect of introducing the infrared heating and cooling schemes into MarTIM in terms of the mean atmospheric structure.

4.1 The Non Local Thermodynamic Equilibrium Issue

In the Martian middle atmosphere the energy balance is controlled by CO_2 non-local thermodynamic equilibrium (non-LTE) effects, [54]. To accurately model what happens to the infrared heating and cooling rates an understanding of non-LTE is needed.

Carbon dioxide is a linear molecule, O-C-O. The bonds between the atoms are not rigid and can move in one of three modes: The bending mode, the asymmetric mode and the symmetric stretch mode, see figure 4.1.

These modes correspond to the 15μm, 4.3μm and 2.7μm bands. The bending mode, ν_2, is degenerate, very strong and coincides with the maximum of the Planck function at typical Martian thermosphere/middle atmosphere temperatures. Absorbed radiation can make the molecule change between vibrational modes. The CO_2 molecule also has rotational modes and combined with the vibrational modes means that there are hundreds of possible absorption bands. Calculating the photon absorption for all the bands needs a complicated equation and vast amounts of computer time. In terms of GCMs like MarTIM it is not feasible to implement such a

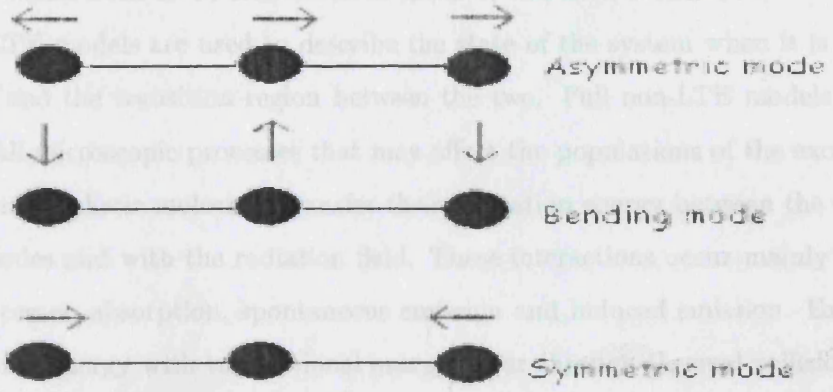

Figure 4.1: The modes of CO_2

calculation with computer time heavy code when a parameterisation will produce, to within a few percent, the same heating and cooling vertical profiles.

A planetary atmosphere is not in true thermodynamic equilibrium as it is not closed system. However, locally, it is possible to describe the kinetic energy of the molecules in the atmosphere and the internal energy distribution function of the atmosphere, using the local temperature. This state is known as local thermodynamic equilibrium (LTE). The radiating properties of atmospheric gas, its absorption coefficient k_ν, and the source function for the transitions at work, J_ν, depend solely on temperature. But, the radiation field can be quite different from the Planck function at the local temperature - this leads to the non-LTE scenario. As the radiation field is non local in nature, for non-LTE conditions the populations of excited states are controlled by photon exchange instead of collisions as in the LTE condition, [57], [60].

For each height in the atmosphere a kinetic temperature can be determined and a Boltzmann distribution can be defined for the energy levels of the modes. A vibrational or rotational temperature can be determined depending on the occupancy of the vibrational and rotational bands. If the vibrational temperature equals the kinetic temperature then the vibrational levels are said to be in LTE. If it was possible to determine the distribution temperature for each internal energy mode then the state of matter could be described completely - hence the purpose of non-LTE models.

For the Martian atmosphere, it is assumed for simplicity that the rotational levels are in LTE up to the exosphere. Therefore in MarTIM only the vibrational level

processes would need to be considered in terms of non-LTE conditions.

Non-LTE models are used to describe the state of the system when it is in LTE, non-LTE and the transition region between the two. Full non-LTE models have to consider all microscopic processes that may affect the populations of the excited levels. The atmospheric molecules transfer their excitation energy between the different energy modes and with the radiation field. These interactions occur mainly through three processes; absorption, spontaneous emission and induced emission. Exchanges of excitation energy with translational energy occur through thermal collisional processes. There is also a need to consider processes such as vibrational-vibrational transfers and photochemical reactions. Full non-LTE models effectively consist of a set of SEEs - statistical equilibrium equations - for every excited energy level and the processes that affect it. It is the parameterised version of these effects that are used within three dimensional global circulation models, [60], [58], [59].

4.1.1 Non-LTE Models

The ESA Non-LTE Model

Work on the ESA Martian Environment Models contract is being undertaken by a collaboration of several European groups, as mentioned in chapter 1. The work on the IR heating and cooling is being undertaken mainly by the IAA group, who have a history of non-LTE work in planetary atmospheres, [22]. The solution of the statistical equilibrium and radiative transfer equations are obtained using the Curtis matrix method, [55]. This is the simultaneous treatment of the statistical equilibrium equations (SEEs) and the radiative transfer equation (RTE). The RTE has to be in a "discrete" form, i.e. in terms of the altitude/pressure grid or optical depth, to obtain a matrix representation of the radiative terms in the SEEs. The elements of the Curtis matrix are the flux transmittances between atmospheric layers. It uses matrices of the size LD by LD, where L is the number of molecular levels and D is the number of pressure/altitude points in the model. This is a very time consuming calculation so work has been done to parameterise the results of the full calculations. It has been shown that, assuming there are only two vibrational levels instead of many, the cooling rate agrees well with the full non-LTE version, [60]. This is outlined in section 4.2. A full parameterisation for the IR non-LTE heating is not yet available and is currently

being worked on.

The Munich Non-LTE Model

The Max-Planck Institute for Solar System Research, in Germany, has a different approach to the non-LTE problem. The final version of their efforts to parameterise the non-LTE effects is to be used in the MAOAM GCM. The process used to solve the SEE and RTE is to iterate between the two. This approach uses the lambda iteration method, [48]. The apparent advantage over the Curtis matrix method is that it uses a smaller matrix, L by L. However, if the optical depth is large, this method can be slow to converge. Recently, [48], work has been done on accelerating the lambda iterative technique so that it would be suitable for use in general circulation models. Preliminary collaborative work has been undertaken, with MarTIM providing a reference atmosphere for the advanced lambda iterative code.

The advanced lambda iterative code has a faster run time compared to the original technique, yet if implemented fully into MarTIM, for realistic temporal and spatial resolution, the run time would become unfeasible e.g. increasing the time for one simulated Mars day to over 24 real hours. The techniques used in the ESA parametrised non-LTE cooling model have been adapted for use in MarTIM and presented in this thesis.

4.2 Infrared Cooling Parameterisation

Non-LTE conditions result in a reduction of the cooling rate values compared to LTE conditions alone. This is due to the number density of the emitting excited levels being smaller for non-LTE than LTE as the spontaneous emission to space adds to the collisional relaxation. This is an important effect in the Martian atmosphere, and depends non-linearly on the temperature structure.

IAA, [60], have produced a parameterisation of their full one-dimensional model for IR cooling that is accurate to within a few percent compared to the full model calculations. Using this parameterised version the computer run time is significantly reduced. The basis of this work is outlined below.

The reference atmosphere parameters that are important for IR cooling are height profiles of: pressure, temperature, number density and volume mixing ratios (vmr)

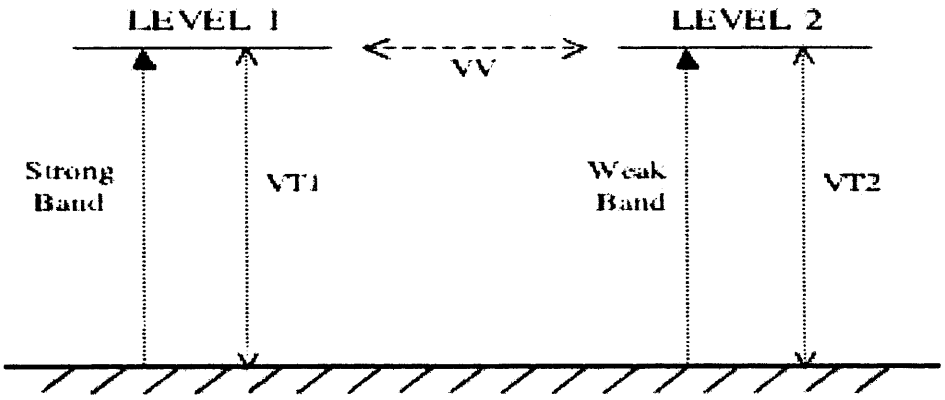

Figure 4.2: Non-LTE model simplification - using two excited vibrational states and the corresponding transitions, adapted from [60]

for CO_2 and CO. The model was simplified to only two excited vibrational states and their transitions, as shown in figure 4.2. This is equivalent to one strong band and one weak band.

The cooling equation is given in equation 4.1.

$$Q_{15\mu m}(z^*) = -hc\frac{\beta}{4}[\vec{v_1}A_1T_1(z^*,\infty)n_1^* + \vec{v_2}A_2T_2(z^*,\infty)n_2^*] \tag{4.1}$$

Where $n_{1,2}^*$ are the populations of the excited states, T the flux transmission to space, β the diffusivity factor (=1.8), A the Einstein coefficient and $\vec{v}$ the wavenumber of the band.

The populations of the excited states are calculated using equations, 4.2 and 4.3, [60].

$$n_2^* = \frac{l_1P_2 + \alpha_2P_1p_{21}}{l_1l_2 - p_{12}p_{21}} \tag{4.2}$$

$$n_1^* = \frac{P_1}{l_1} + \alpha_1\frac{n_2p_{12}}{l_1}n_2^* \tag{4.3}$$

Where P_n is the collisional production of state n from all V-T processes, p_{nm} is the collisional production of state n via V-V exchange from the (010) state of isotope m, l_n is the collisional loses of state n from all V-T and V-V processes in which it participates. α is a combination, of the Einstein spontaneous emission coefficients for the strong and weak bands, the velocity of light and the Planck constant, [60]. The

rate coefficients used in the parameterisation are listed in table 4.1 along with the reaction that causes them.

Type	Process	Rate Coeff
V-T	$CO_2(0,1,0) + CO_2 \rightarrow CO_2(0,0,0) + CO_2$	$4.2{\cdot}10^{-12}$ exp(-2990/T + 304000/T^2)
V-T	$CO_2(0,1,0) + CO \rightarrow CO_2(0,0,0) + CO$	$2.1{\cdot}10^{-12}$ exp(-2660/T + 223000/T^2)
V-T	$CO_2(0,1,0) + O \rightarrow CO_2(0,0,0) + O$	$3.0{\cdot}10^{-12}$
V-V	$CO_2(0,2,0) + CO_2 \rightarrow CO_2(0,1,0) + CO_2$	$2.49{\cdot}10^{-11}$

Table 4.1: Rate coefficients in cm^3s^{-1} with their reactions, adapted from [55]

Altering the V-T reaction value between CO_2 and O is equivalent to changing their ratio throughout the whole atmosphere, [60]. Accepted values are in the range $5.0{\cdot}10^{-12}cm^3s^{-1}$ to $8.0{\cdot}10^{-13}cm^3s^{-1}$, [60], [55]. Work on finding the heat balance has shown that altering this value changes the altitude where the strongest cooling occurs. This is shown in section 4.4 below.

4.3 Infrared Heating Parameterisation

Solar radiation is the main excitation mechanism for the vibrational levels of CO_2 and CO in the Martian atmosphere. To calculate fully the infrared heating rates the populations of the levels need to be found. Using a full one-dimensional calculation of the IR heating rates is not viable in a global circulation model, like MarTIM, due to the increased computer run time it would require. A parameterised version of the IR heating is used in MarTIM. This is a much simpler version than the IR cooling parameterisation that has been developed for the ESA non-LTE model, [54]. The photoabsorption coefficients for several fundamental bands of CO_2 and CO have been calculated, [55]. Using these values with the solar flux and CO_2 and CO densities at each pressure level, the infrared heating rate at the sub-solar point can be calculated, [55]. The IR heating rate calculations need to account for the non-LTE region in the atmosphere, mentioned in section 2.2.8. To account for this the LTE IR heating rate is adjusted by a pressure dependent conversion factor, [54]. It is assumed that the IR heating rate falls off from the sub-solar point using the Chapman grazing incidence

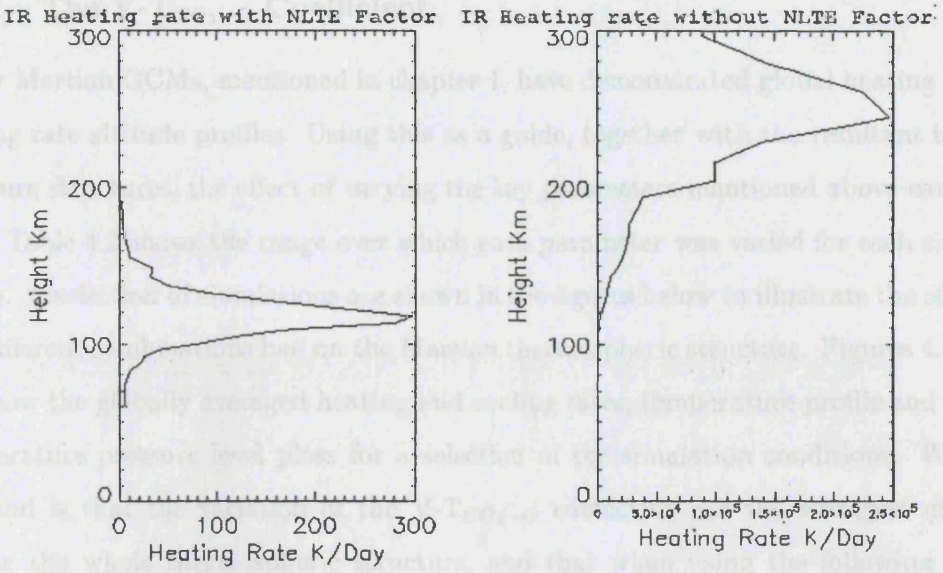

Figure 4.3: Infrared heating rates in K/day, at the sub-solar point, solar minimum conditions. Left hand plot shows the IR heating rate adjusted for non-LTE, the right hand plot shows the IR heating rate without the non-LTE adjustment, i.e. only LTE is considered.

function. There is no nighttime IR heating rate when using this technique.

Figure 4.3 shows a vertical profile of the IR heating rate at the sub-solar point with and without the Non-LTE conversion factor, showing that without the non-LTE conversion factor the infrared heating rate at high altitudes become unrealistic.

4.4 Heat Balance in the Martian Thermosphere

The heat balance in the thermosphere is essential in generating realistic global circulation and temperature structures. In MarTIM the heat balance is found by considering the EUV heating efficiency, the eddy diffusion coefficient and the V-T$_{CO_2-O}$ de-excitation rate coefficient, [10]. The next section explains the work done in finding the optimum balance values for MarTIM. Basic simulations are done for equinox conditions (L$_s$=0) with varying values for the eddy diffusion coefficient, $EUVFAC$ and V-T$_{CO_2-O}$ rate coefficient to see their effect on the thermospheric structures. This process is similar to that used to find the heat balance of other GCMs, [13].

4.4.1 The V-T_{CO_2-O} Coefficient

Other Martian GCMs, mentioned in chapter 1, have demonstrated global heating and cooling rate altitude profiles. Using this as a guide, together with the resultant temperature structures, the effect of varying the key parameters mentioned above can be seen. Table 4.2 shows the range over which each parameter was varied for each simulation. A selection of simulations are shown in the figures below to illustrate the effect the different combinations had on the Martian thermospheric structure. Figures 4.4 to 4.8 show the globally averaged heating and cooling rates, temperature profile and two temperature pressure level plots for a selection of the simulation conditions. What is found is that the variation of the V-T_{CO_2-O} coefficient has the strongest effect on the the whole thermospheric structure, and that when using the following values; eddy diffusion coefficient maximum = $1500 m^2 s^{-1}$, V-T_{CO_2-O} = $1 \cdot 10^{-13} cm^3 s^{-1}$, EUVFAC=18%, MarTIM generates profiles that agree generally with other models and limited measurements. The dumbbell type structure that is seen in the top temperature pressure level plots is explained in the section below.

V-T Coefficient ($cm^3 s^{-1}$)	$3 \cdot 10^{-12} \rightarrow 9 \cdot 10^{-14}$
Eddy Diffusion Coefficient ($m^2 s^{-1}$)	1800→700
EUVFAC (%)	20→16

Table 4.2: The range of simulation parameters used to explore heat balance in MarTIM atmosphere

Although the values for the eddy diffusion coefficient and the EUV heating efficiency are within the accepted ranges, the choice of MarTIM's V-T_{CO_2-O} coefficient is lower than is normally cited, [60]. There are several reasons for using such a low value in MarTIM. The CO_2 to O density ratio could be incorrect, as there have been no direct measurements of the O density on Mars, and so the input densities used in MarTIM may be incorrect. As stated earlier altering the V-T_{CO_2-O} coefficient is equivalent to altering the CO_2 to O ratio. Work was done with the Munich group whereby MarTIM provided the neutral atmosphere densities and they used their code to generate the IR cooling profiles. This work led to the assumption that high altitude

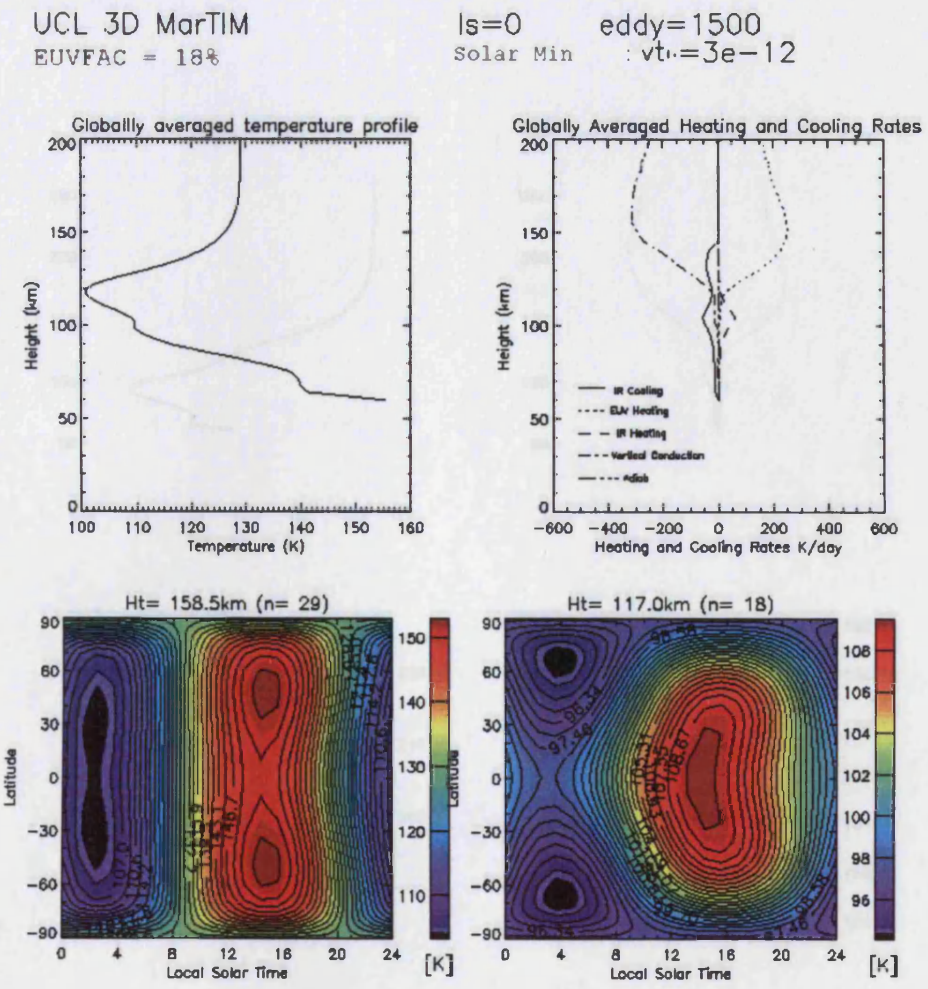

Figure 4.4: Figure shows globally averaged temperature and heating/cooling rate height profiles plus pressure level plots of the temperature near the top and middle of MarTIM. The parameters used in this simulation were set to: eddy diffusion coefficient=1500m^2s^{-1}, EUVFAC=18% and V-T=$3{\cdot}10^{-12}cm^3s^{-1}$

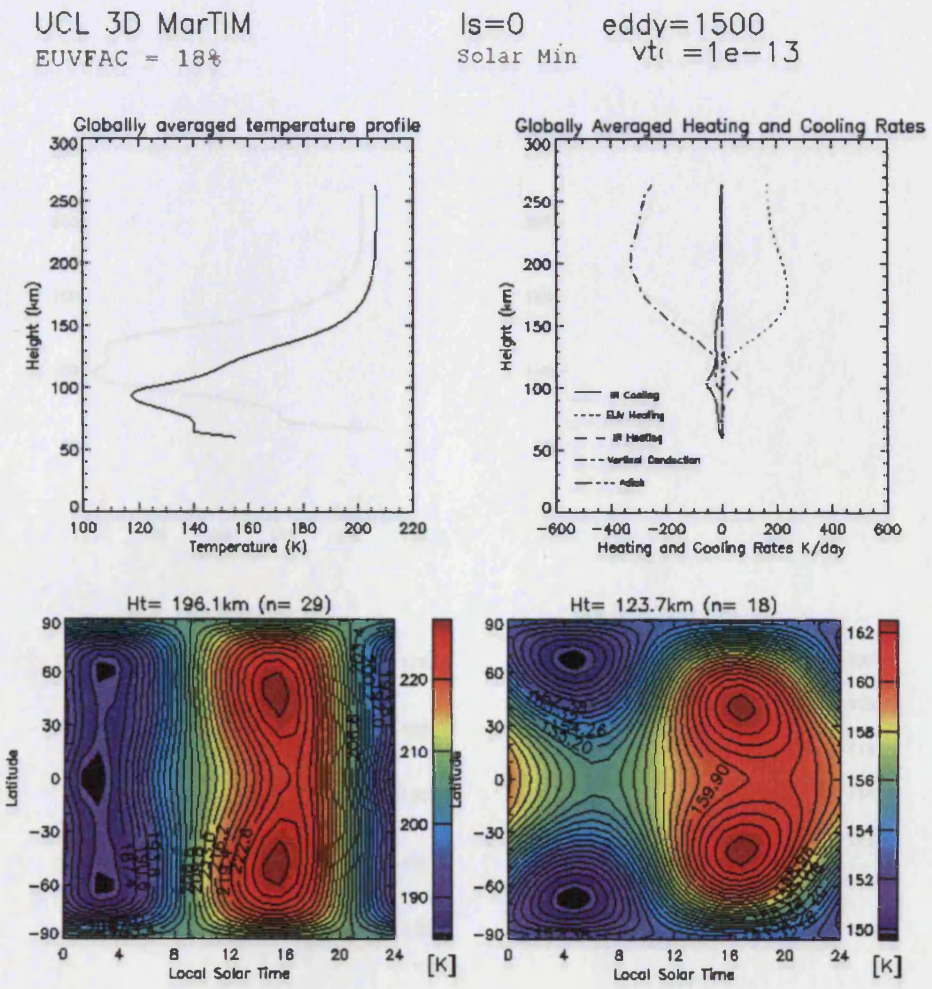

Figure 4.5: Figure shows globally averaged temperature and heating/cooling rate height profiles plus pressure level plots of the temperature near the top and middle of MarTIM. The parameters used in this simulation were set to: eddy diffusion coefficient=1500m^2s^{-1}, EUVFAC=18% and V-T=$1{\cdot}10^{-13}cm^3s^{-1}$

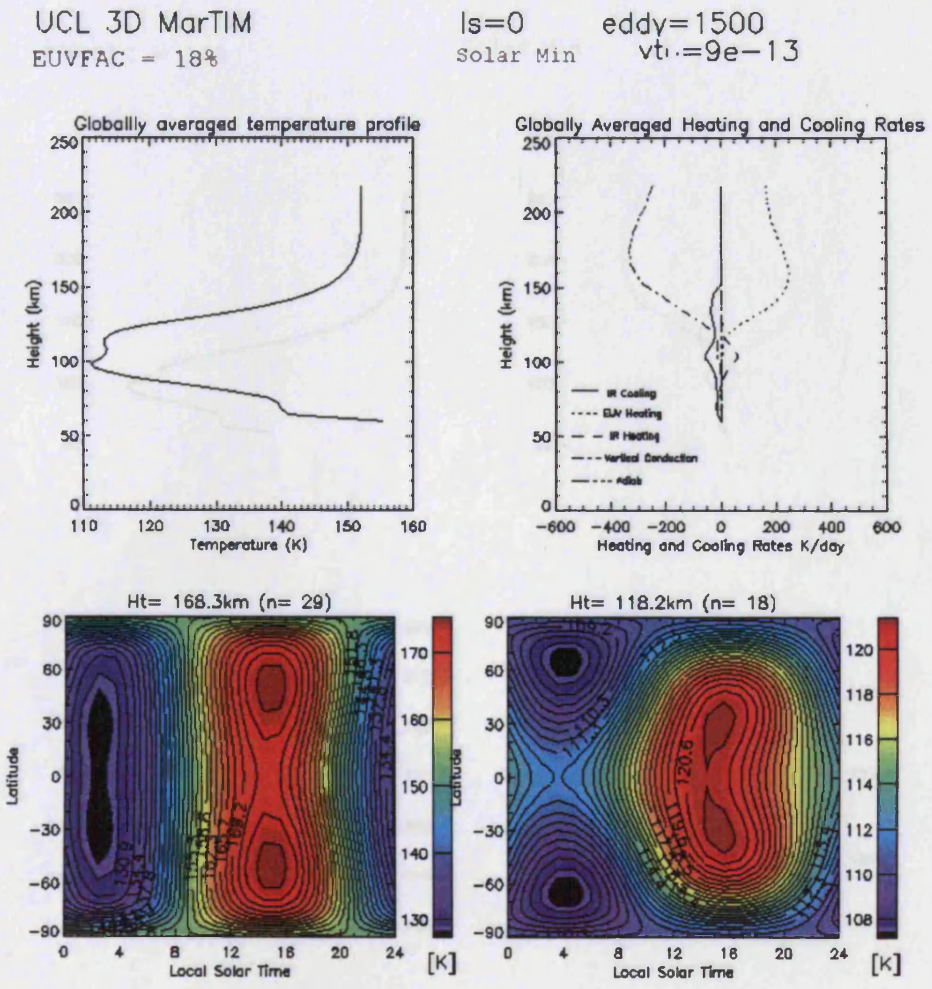

Figure 4.6: Figure shows globally averaged temperature and heating/cooling rate height profiles plus pressure level plots of the temperature near the top and middle of MarTIM. The parameters used in this simulation were set to: eddy diffusion coefficient=1500m^2s^{-1}, EUVFAC=18% and V-T=9·$10^{-13}cm^3s^{-1}$

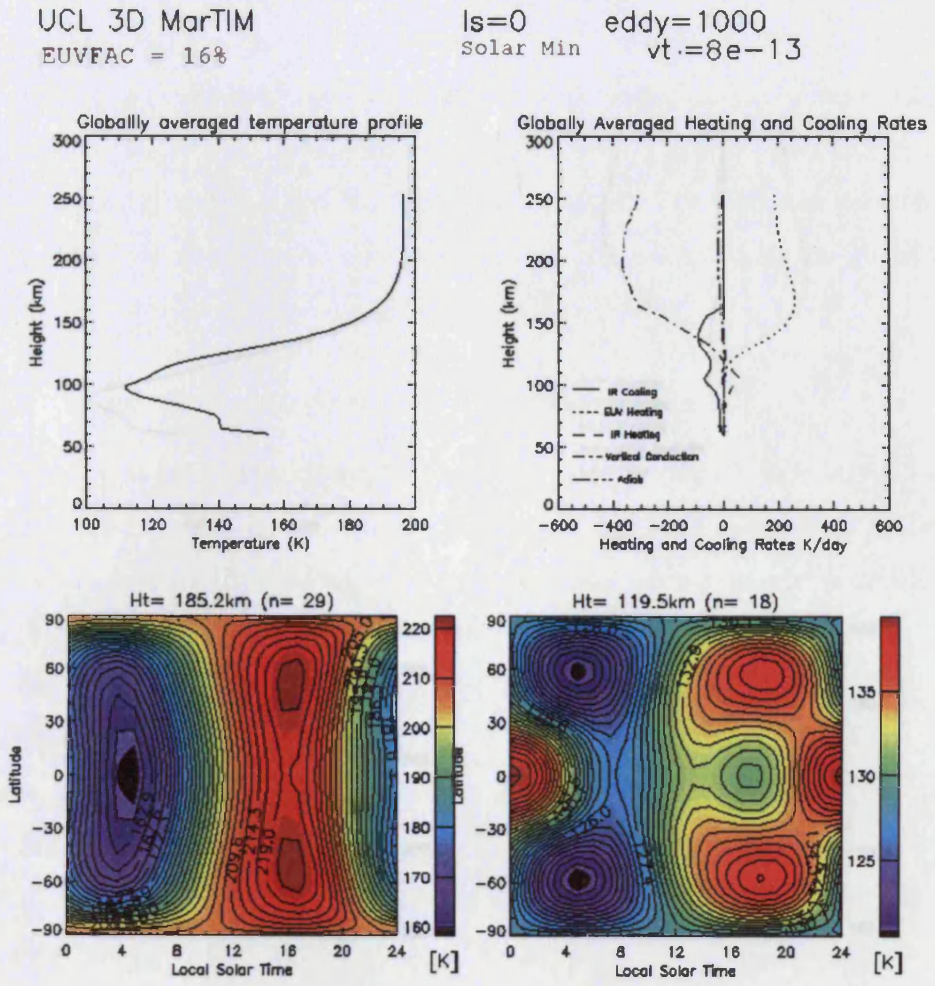

Figure 4.7: Figure shows globally averaged temperature and heating/cooling rate height profiles plus pressure level plots of the temperature near the top and middle of MarTIM The parameters used in this simulation were set to: eddy diffusion coefficient=1000m^2s^{-1}, EUVFAC=16% and V-T=$8{\cdot}10^{-13}cm^3s^{-1}$

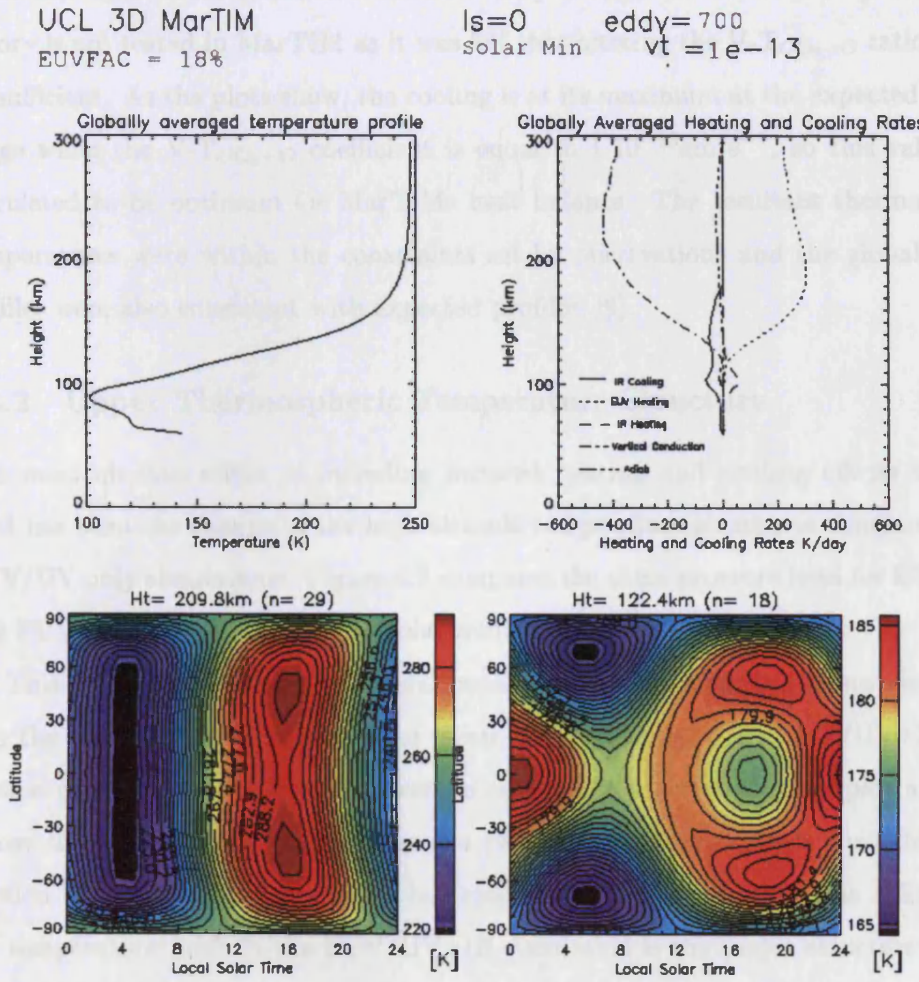

Figure 4.8: Figure shows globally averaged temperature and heating/cooling rate height profiles plus pressure level plots of the temperature near the top and middle of MarTIM The parameters used in this simulation were set to: eddy diffusion coefficient=700m^2s^{-1}, EUVFAC=18% and V-T=$1{\cdot}10^{-13}cm^3s^{-1}$

O density in MarTIM was larger than accepted, [47]. As a separate density dataset wasn't available, altering the CO_2-O ratio over height was thought to be an acceptable substitute. The suggestion that each of the gases may have its own turbopause has also been raised, [2]. If the O turbopause is lower than the accepted 125km level on Mars then this would result in a different CO_2-O ratio above the turbopause. This theory is not tested in MarTIM as it was felt that altering the V-T_{CO_2-O} ratio would be sufficient. As the plots show, the cooling is at its maximum at the expected 130km range when the V-T_{CO_2-O} coefficient is equal to $1{\cdot}10^{-13}cm^3s^{-1}$, so this value was calculated to be optimum for MarTIMs heat balance. The resultant thermospheric temperatures were within the constraints set by observations and the global height profiles were also consistent with expected profiles, [9].

4.4.2 Upper Thermospheric Temperature Structure

The most obvious effect of including infrared heating and cooling effects in MarTIM has been the change in the high altitude temperature structures compared with EUV/UV only simulations. Figure 4.9 compares the same pressure level for EUV/UV and EUV/UV+IR simulations for solar minimum, L_s=0.

This figure demonstrates a general cooling across the specific pressure level and also the whole atmosphere (note the mean lower altitude of the EUV/UV+IR simulation pressure level). The temperature range is 60K across the top plot and 90K across the bottom plot. Comparing the peak temperatures reveals that the introduction of IR heating and cooling has resulted in a drop of 30K. The splitting of the temperature peak in the EUV/UV+IR simulation is the major structure change and was unexpected and initially lead to the belief that significant CO_2 cooling was occurring at high altitudes. Figure 4.5 earlier shows that this is not the case. This temperature structure has been found in other models, [10], [19]. In MarTIM the introduction of the IR heating and cooling also causes a stronger dayside upwelling in the vertical winds along the equator (figure 4.10). This affects the divergent winds and acts to produce stronger adiabatic cooling on the equator, affecting the peak afternoon heating. These patterns can be seen in figure 4.10, which shows the vertical wind structures and the temperature structures for the same pressure level as 4.9, and again with EUV/UV+IR forcing.

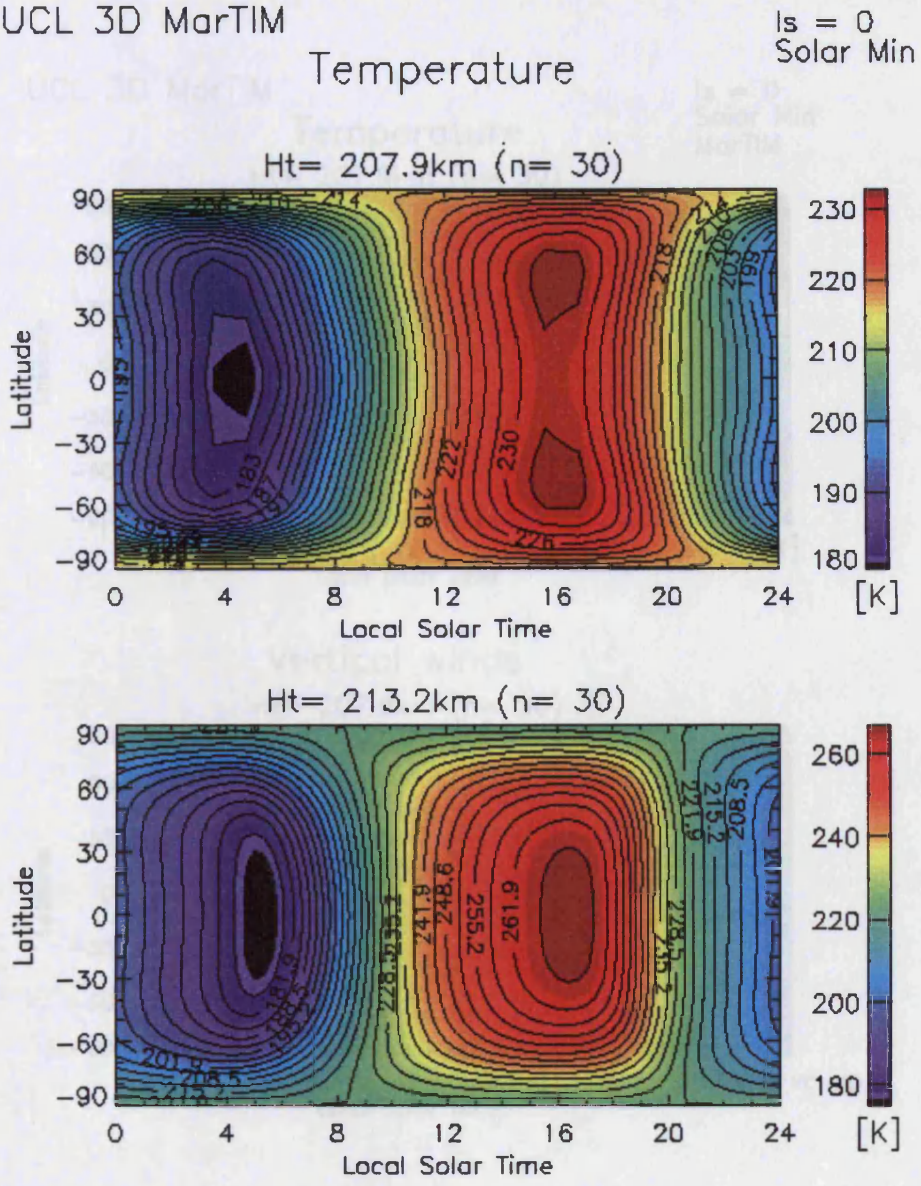

Figure 4.9: Pressure level 28 (pressure=$2.7 \cdot 10^{-7}$Pa) temperature plots for EUV/UV and IR forcing (top) and EUV/UV only forcing (bottom), for solar minimum, L_s=0

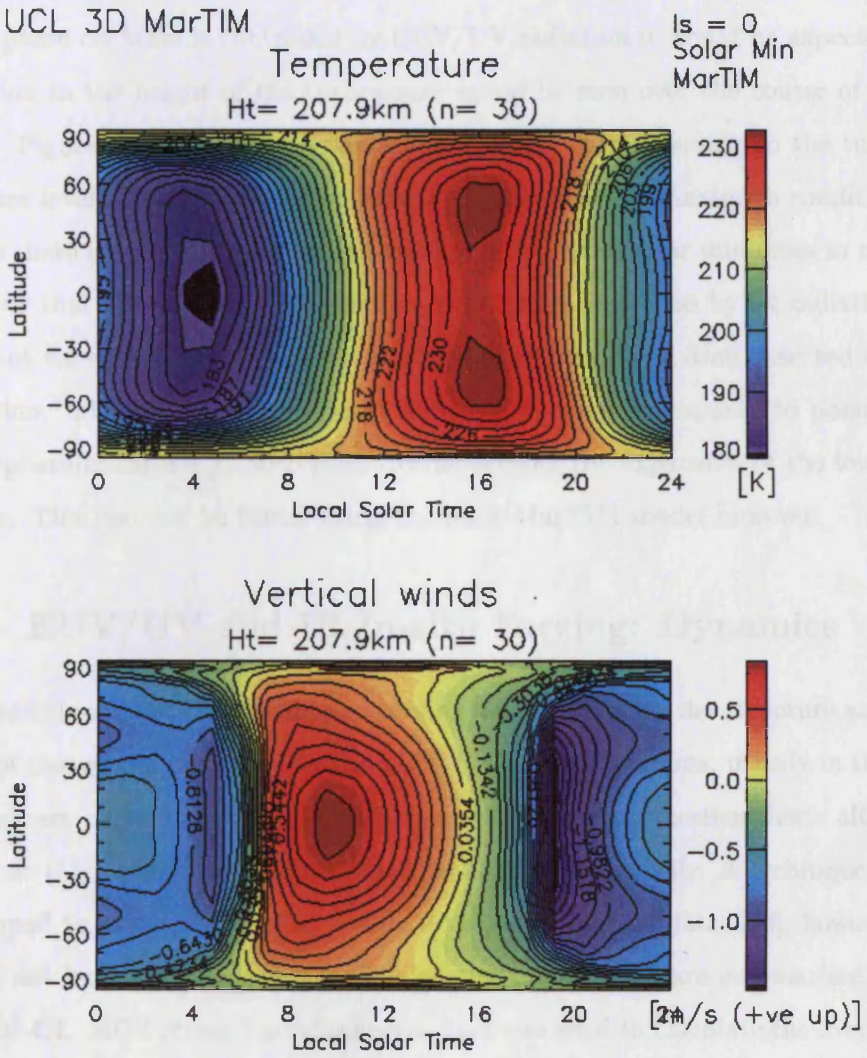

Figure 4.10: Pressure level plots of temperature (top) and total vertical wind (bottom) for EUV/UV and IR forcing, for solar minimum, L_s=0

4.5 EUV/UV and IR forcing: The Turbopause

The turbopause is the point in the atmosphere where the turbulent diffusion coefficient is equal to the molecular diffusion coefficient, see figure 2.1. As explained in chapter 2 the eddy diffusion coefficient is calculated by using $1.2{\cdot}10^{-4}$Pa as the pressure at the turbopause. This pressure corresponds to an average of 125km in height. If the middle atmosphere on Mars is controlled by EUV/UV radiation it would be expected that a variation in the height of the turbopause would be seen over the course of the solar cycle. Figure 4.11 shows the variation in altitude corresponding to the turbopause pressure level, for solar minimum, solar medium and solar maximum conditions.

As there is little variation in the average height from solar minimum to maximum it shows that the middle atmosphere in MarTIM is controlled by IR radiation which does not vary over the solar cycle compared to the large variation observed EUV/UV radiation. The turbopause would be expected to vary in response to possible lower atmosphere changes e.g. with dust storms causing the expansion of the lower atmosphere. This can not be tested using the basic MarTIM model however.

4.6 EUV/UV and IR In-situ Forcing: Dynamics

The introduction of IR heating and cooling has an effect on the structure and magnitude of the winds, compared to the EUV/UV only simulations, mainly in the middle atmosphere. There are no direct wind measurements for thermospheric altitudes on Mars, so it is difficult to validate MarTIM's winds empirically. A technique has been developed to derive zonal wind speeds from accelerometer data, [90], however as yet it has not been widely accepted. The results of this work are summarised in tables 4.3 and 4.4. MGS phase 2 accelerometer data was used to calculate the average zonal wind speeds in the northern and southern hemispheres over hundreds of orbits.

Figures 4.12 and 4.13 show the zonal winds for MGS phase 2 conditions stated in in tables 4.3 and 4.4, calculated by MarTIM. For figure 4.12 the zonal wind speeds in the altitude and latitude ranges stated in table 4.3 are around 20ms^{-1}, significantly less than the predicted 74ms^{-1}. For figure 4.13 a zonal wind speed of only 6ms^{-1} is shown, compared to the value of 34ms^{-1}. Assuming the wind magnitudes calculated from the accelerometer data are reliable MarTIM is showing considerably lower than

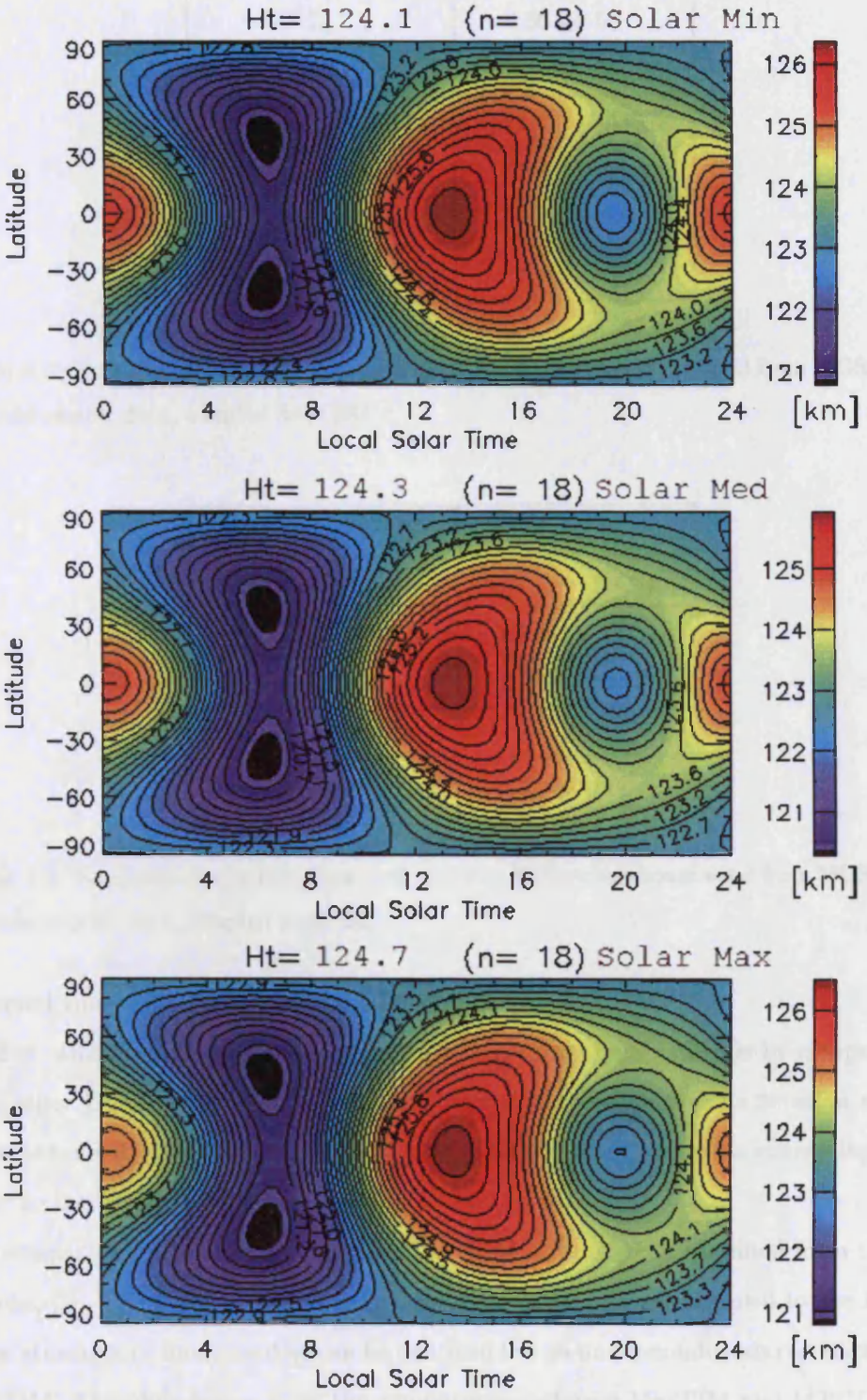

Figure 4.11: Altitude variation across the turbopause pressure level for solar minimum (top), medium (middle) and maximum (bottom) conditions

L_s	$30 \rightarrow 50$
Local Solar Time	16.7hrs $\rightarrow$ 15.6hrs
Periapsis Altitude	111km $\rightarrow$ 118km
Periapsis Latitude	60°N $\rightarrow$ 30°N
Number of orbits	149
Average Zonal Wind	$74 \pm 5 ms^{-1}$

Table 4.3: Northern Hemisphere data used to derive the average zonal wind from MGS phase 2 accelerometer data, adapted from [90]

L_s	$75 \rightarrow 85$
Local Solar Time	14.7hrs $\rightarrow$ 14.8hrs
Periapsis Altitude	104km $\rightarrow$ 114km
Periapsis Latitude	30°S $\rightarrow$ 60°S
Number of orbits	80
Average Zonal Wind	$34 \pm 7 ms^{-1}$

Table 4.4: Southern Hemisphere data used to derive the average zonal wind from MGS phase 2 accelerometer data, adapted from [90]

expected zonal wind speeds in the middle atmosphere.

The other form of wind speed validation that can be performed, is by comparisons with other GCMs run for the same conditions, if these comparisons revealed similar discrepancies it would point to the need for consideration of an extra energy input, in order to increase the wind magnitudes.

Comparisons have been made with MTGCM sample plots obtained from the literature, [7]. The plots are taken from before the MTGCM was coupled to the AMES lower atmosphere model and so can be assumed to run under conditions comparable to MarTIM. The plots below show the comparisons between MarTIM and MTGCM for solar minimum conditions and equinox. Figure 4.14 compares the vertical wind structure at the equator for MTGCM (top) and MarTIM (bottom), figure 4.15 compares

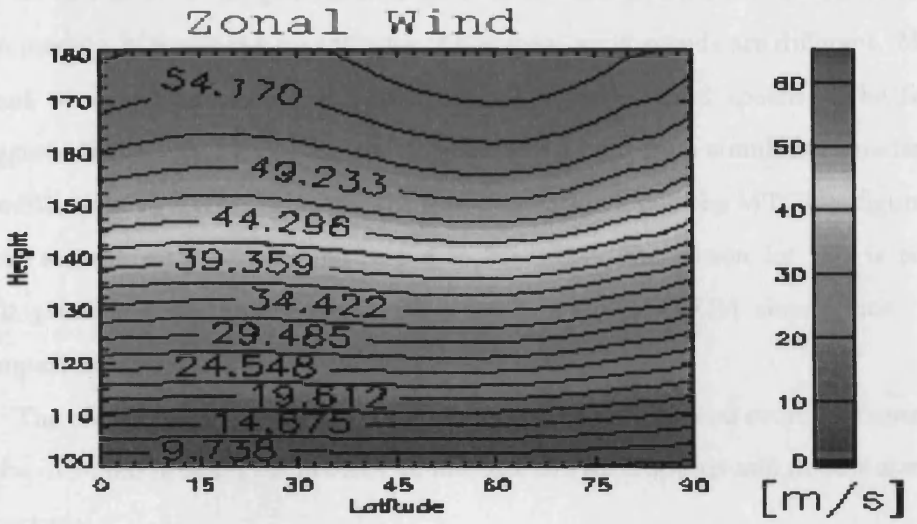

Figure 4.12: Northern Hemisphere zonal wind altitude plot from MarTIM, for L_s = 35, LST=1600 and MGS Phase 2 aerobraking conditions

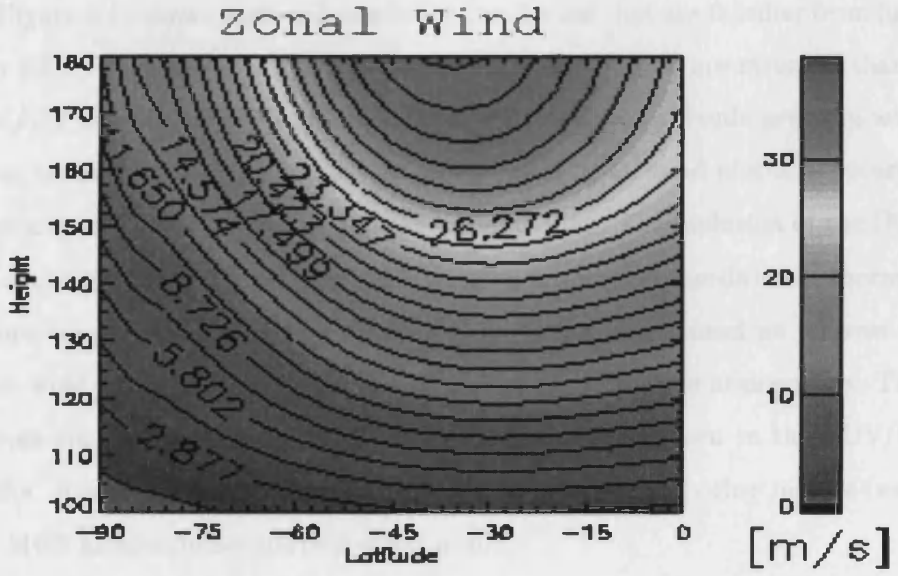

Figure 4.13: Southern Hemisphere zonal wind altitude plot from MarTIM, for L_s = 90, LST=1500 and MGS Phase 2 aerobraking conditions

the zonal wind structure at the equator for MTGCM (top) and MarTIM (bottom).

As can be seen the general structures in the atmosphere are similar between the two models, however the magnitudes of the zonal wind speeds are different. MarTIMs zonal wind speeds are about half of MTGCM zonal wind speeds. The literature suggests that the MTGCM figures in 4.15 and 4.14 are from simulations under similar conditions to MarTIM. However, the middle atmosphere in the MTGCM figures shows more structure than the same region in MarTIM. The reason for this is not clear, it is possible that tidal modes were present in the MTGCM simulations. Further comparisons with MTGCM are shown in chapter 5.

The comparisons done in this section imply that additional sources of energy need to be included in MarTIM in order to increase the wind speeds and middle atmosphere structure.

4.6.1 Zonal Mean Flow

The effects of introducing the IR heating and cooling on the zonal mean flow of the atmosphere are shown in figure 4.16. The simulations were for solar minimum, equinox (L_s=0) conditions.

Figure 4.16 shows eastward jets in the zonal wind that are familiar from figure 3.11 with EUV/UV heating only. The zonal jets in figure 4.16 are stronger than for the EUV/UV only simulations and also taper off at a lower altitude pressure level. This is due to the reversal seen in the meridional zonal mean wind plot now occurring at a lower altitude pressure level compared to figure 3.11. The inclusion of the IR heating and cooling in MarTIM has increased the zonal mean wind speeds in the thermospheric regions compared to EUV/UV heating only. It has also caused an increase in zonal mean winds speeds and zonal mean structure in the middle atmosphere. This helps address the problem of the low zonal mean wind speeds seen in the EUV/UV only results. However the mean speeds are still low compared to other models (see above) and MGS accelerometer derived zonal winds.

4.6.2 The Fixed Lower Boundary

As stated in chapter 2 MarTIM has a fixed lower boundary at which the horizontal winds are set to zero. The introduction of IR heating and cooling has demonstrated

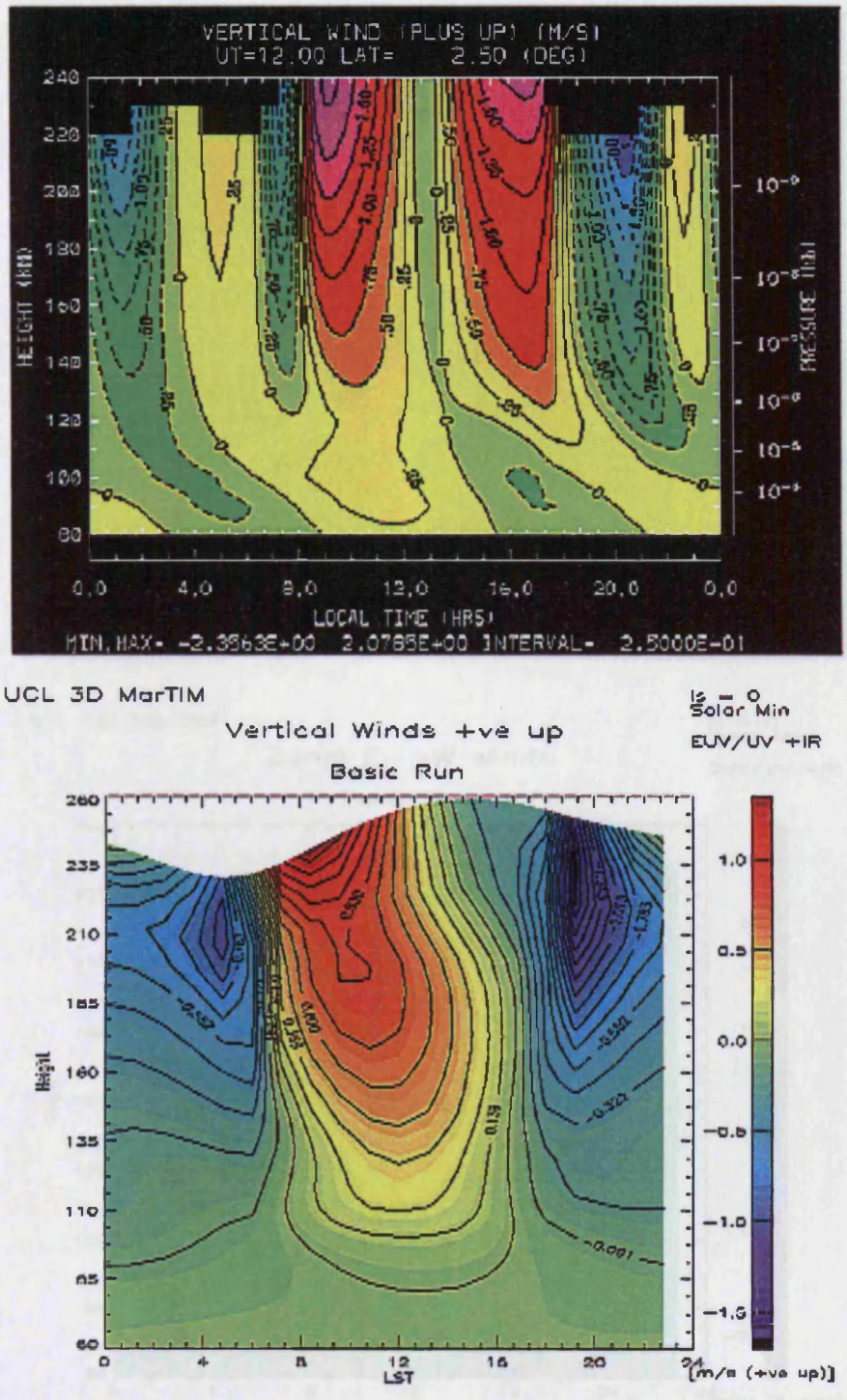

Figure 4.14: Vertical winds from MTGCM (top) and MarTIM (bottom) at 2.5°N latitude, local solar time vs height, solar minimum, L_s=0.

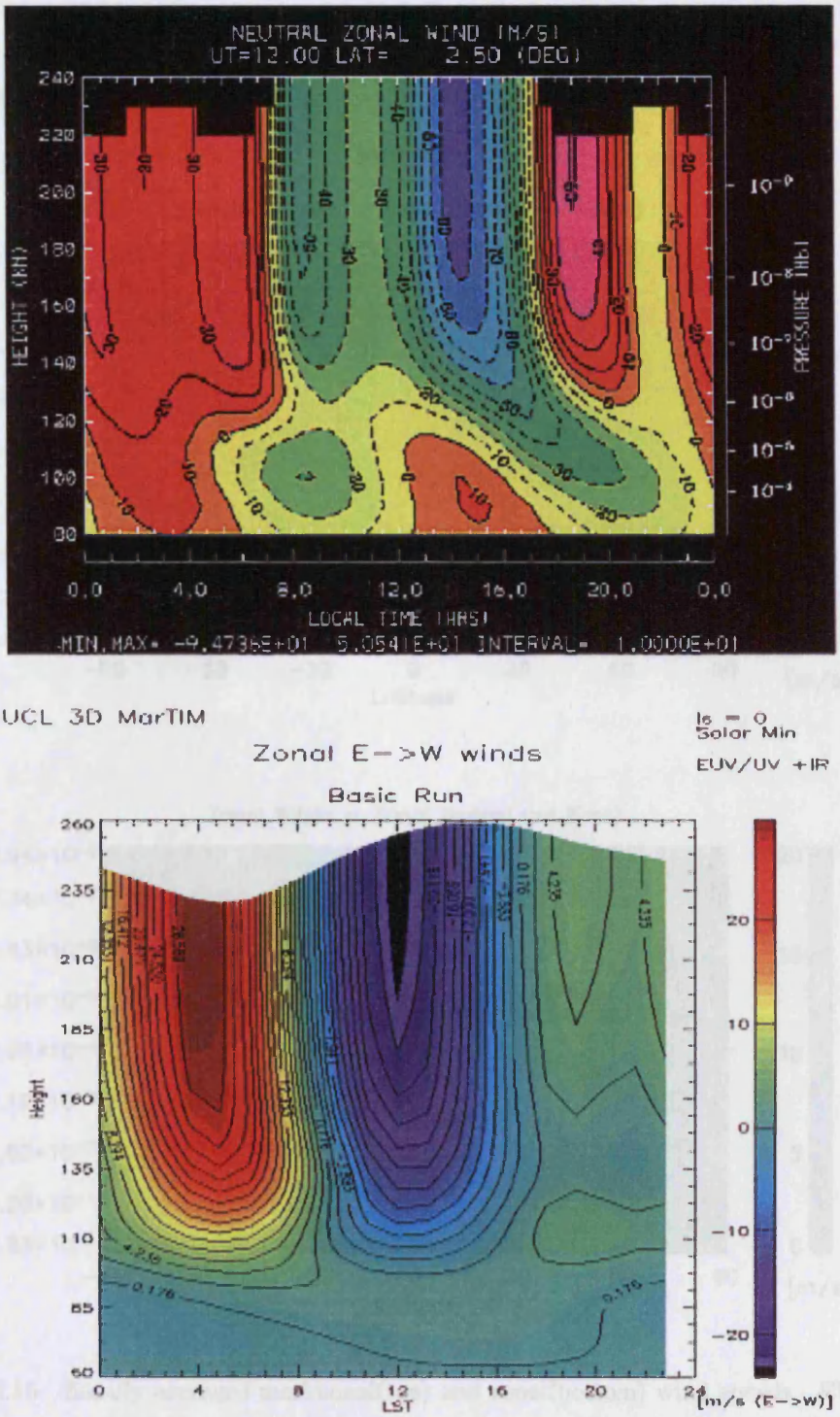

Figure 4.15: Zonal winds from MTGCM (top) and MarTIM (bottom) at 2.5°N, local solar time vs height, solar minimum, L_s=0

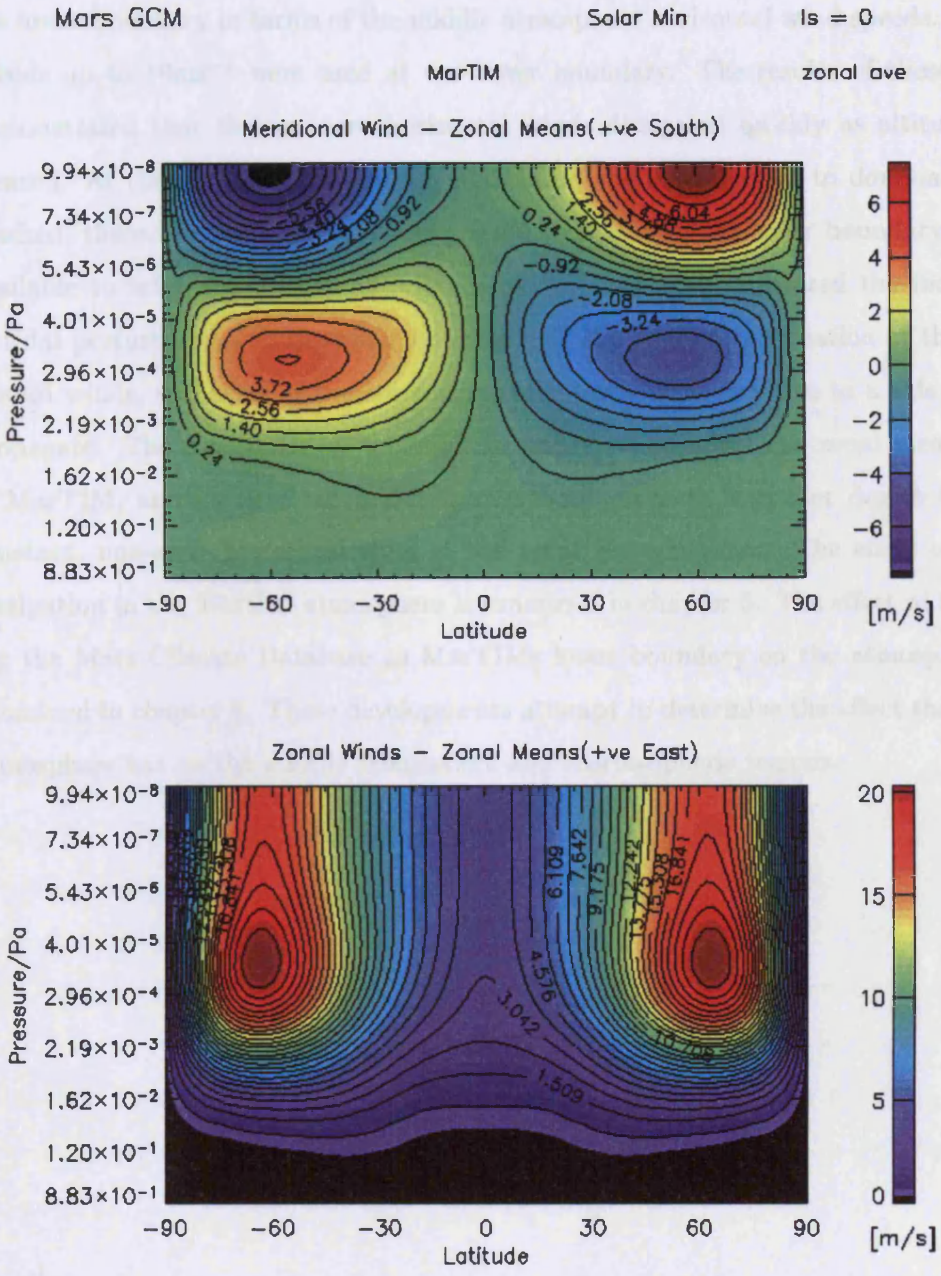

Figure 4.16: Zonally averaged meridional(top) and zonal(bottom) wind speeds - EUV/UV and IR forcing

that, although there is a slight increase in the middle atmosphere winds, the horizontal winds in this region remain low, as explained above. A series of tests were performed using MarTIM to examine the effect of constant, non-zero, horizontal winds across the lower boundary in terms of the middle atmosphere horizontal wind speeds. Wind speeds up to $10ms^{-1}$ were used at the lower boundary. The results of these tests demonstrated that the non-zero horizontal winds dissipated quickly as altitude increased. At the altitude at which the IR heating and cooling start to dominate was reached, there was little residual background wind due to the lower boundary input available to influence the overall wind pattern. This work motivated the inclusion of tidal perturbations at the lower boundary, as the oscillatory variation of the horizontal winds, and other parameters, across the lower boundary due to a tide would propagate. The dissipation of the tidal structure would affect the zonal mean flow in MarTIM, and increase the middle atmosphere winds to a greater degree than a constant, non-zero, horizontal wind at the lower boundary has. The effect of tidal dissipation in the Martian atmosphere is examined in chapter 5. The effect of including the Mars Climate Database as MarTIMs lower boundary on the atmosphere is examined in chapter 6. These developments attempt to determine the effect the lower atmosphere has on the middle atmosphere and thermospheric regions.

Chapter 5

Tidal Theory and Results

5.1 Introduction

In the course of the development of terrestrial atmosphere models a theoretical treatment of the response of a rotating atmosphere to periodic forcing due to solar heating has been undertaken, [17]. This theory is able to explain periodic structures seen in the terrestrial atmosphere, [69], [24]. These structures caused by this periodic forcing and its sub-harmonics are known as tides. Tidal theory was first developed by Laplace in the 1800's as applied to oceans. Laplace then applied his ocean tidal theory to the atmosphere. Assuming an atmosphere of uniform scale height, H, the oscillations were the same as for an ocean of uniform depth. Hough, [39], improved Laplace's tidal theory by introducing the spherical harmonic functions, known as Hough functions, which are solutions to the tidal equations. The global response of the atmosphere to tidal perturbations is described by the Hough altered Laplace Tidal Equation and is known as classical tidal theory. Here the assumptions and basic theory are outlined for the terrestrial atmosphere and the validity of applying this theory to Mars is discussed in section 5.4.

5.2 Classical Tidal Theory for the Terrestrial Atmosphere

It has been established that a range of perturbations of pressure, temperature, density and winds in the atmosphere can be described by classical tidal theory, [17]. In order to describe the response of the atmosphere to these perturbations in an analytical

fashion several assumptions have to be made. Four of these have been found to be the most important in terms of limitations to the applicability of the theory:

- Tides can be considered as linear perturbations on a mean atmospheric state
- Surface topography is ignored; the surface is assumed to resemble a smooth sphere
- Dissipative mechanisms and mean motions are ignored.
- Horizontal variation in the mean temperature and pressure are ignored.

Linear perturbations are applied to the momentum and energy equations and a pair of differential equations are generated, [17]. These are known as Laplace's Tidal Equation and the Vertical Structure Equation. The solution of these for any atmosphere can be broken down into vertical and horizontal eigenfunctions. The infinite set of eigenfunctions is the analytical solution of the two partial differential equations. In order to linearise the equations of energy and momentum, so as to practically apply the tidal perturbations, the geopotential, Φ, as shown in equation 2.10, is an essential parameter. It is a measure of the energy needed to move a particle vertically by dz through a gravitational field g.

Using the equation for hydrostatic equilibrium, equation 2.6, and equation 2.10, a relationship between the differentials of pressure and geopotential can be found, shown in equation 5.1.

$$\partial\Phi = -\frac{1}{\rho}\partial p \tag{5.1}$$

By including the log-pressure co-ordinate system (the definition for scale height as described in chapter 2) and the Coriolis parameter (equation 5.2, where Ω is the angular velocity of the planet), new linearised momentum equations can be found.

$$f = 2\Omega \sin\theta \tag{5.2}$$

These new momentum equations for an atmosphere under the tidal theory assumptions are given by equations 5.3 and 5.4. They describe the southward (U) and eastward (V) velocities in spherical co-ordinates, [79].

$$\frac{\partial U}{\partial t} - fV = -\frac{1}{R} \cdot \frac{\partial \Phi}{\partial \theta}$$

(5.3)

$$\frac{\partial V}{\partial t} + fU = -\frac{1}{R\cos(\theta)} \cdot \frac{\partial \Phi}{\partial \varphi}$$

, (5.4)

where φ is longitude, θ is latitude and f is the Coriolis force. The corresponding energy equation is shown in equation 5.5.

$$c_p(\frac{\partial T}{\partial t}) = \frac{1}{\rho}\frac{dp}{dt} + J, \tag{5.5}$$

where T is the temperature, ρ the density, p the pressure, c_p the specific heat capacity at constant pressure and J is the external heating per unit mass.

Under the linear assumption, a perturbation of the pressure, velocity and temperature can be expressed as: $a' = a_0 + a$. Where a' is any of the perturbation parameters, a_0 the unperturbed value and a the perturbation itself. Higher terms are neglected. If a is small compared with a_0 then this assumption is valid. Solutions of the form of equation 5.6 then need to be found.

$$a = a^{\sigma,s}(\theta, z) \cdot e^{i(\sigma t + s\varphi)}, \tag{5.6}$$

where, θ is the latitude, z the height, t the time, φ is the longitude, σ is the perturbation frequency i.e. $\frac{2\pi}{\sigma}$ equates for tides to 1 solar day, and s is the zonal (longitudinal) wavenumber $= 0, +1, +2, \cdots$. If $s = 1$ then this describes a diurnal tide, $s = 2$ a semi-diurnal tide, etc. In equation 5.6 the exponential term describes the phase and time dependence of the perturbation. The first term on the right hand side is a time and longitudinally independent amplitude. This expresses the height and latitudinal structure. Using equation 5.6 the partial time and longitude derivatives can be determined and applied to geopotential and wind velocities in 5.3 and 5.4 to replace the time and longitude derivatives, [69]. This results in equations 5.7 and 5.8.

$$U = -\frac{i}{R\sigma(1-\frac{f^2}{\sigma^2})} \cdot (\frac{sf}{\sigma\cos\theta} - \frac{\partial}{\partial\theta})\Phi \tag{5.7}$$

$$V = \frac{1}{R\sigma(1-\frac{f^2}{\sigma^2})} \cdot (\frac{f}{\sigma}\frac{\partial}{\partial\theta} - \frac{s}{\cos\theta})\Phi \tag{5.8}$$

The geopotential, Φ, is conventionally chosen as the parameter for the tidal perturbations, the other parameters are then given as functions of geopotential. However, any parameter could be chosen. The perturbation of Φ is given in the form of equation 5.9, in accordance with equation 5.6.

$$\Phi = \Phi(\theta, z) \cdot e^{i(\sigma t + s\varphi)} \tag{5.9}$$

Separating out the latitude and height variables of the amplitude term of equation 5.9 gives:

$$\Phi_s(\theta, z) = \sum_n \Phi^0_{s,n}\Theta_{s,n}(\theta)G_{s.n}(z), \tag{5.10}$$

where $\Phi_s(\theta, z)$ is $\Phi(\theta, z)$ for fixed s and n is the latitudinal wavenumber. $\Theta_{s,n}(\theta)$, $G_{s.n}(z)$ are the latitudinal and vertical structure components respectively. Introducing $\Phi^0_{s,n}$, as the amplitude of each individual mode of (s,n) with units of geopotential, means that $\Theta_{s,n}(\theta)$, $G_{s,n}(z)$ are unitless quantities.

Using the above definitions, and more complex calculations detailed in [15], the differential equations for $\Theta_{s,n}$ and $G_{s,n}$ are determined. These equations are 5.11 and 5.12.

$$i\omega H[\frac{1}{\rho}\frac{d}{dz^*}\rho\frac{d}{dz^*}G_n(z^*)] + \frac{i\omega\kappa}{h_n}G_n(z^*) = -\frac{1}{\rho}\frac{d}{dz^*}(\rho_0\kappa J_n) \tag{5.11}$$

$$\frac{d}{d\mu}[\frac{1-\mu^2}{\eta^2-\mu^2}\frac{d\Theta_n(\theta)}{d\mu}] - \frac{1}{\eta^2-\mu^2}[\frac{s}{\eta}\frac{\eta^2+\mu^2}{\eta^2-\mu^2} + \frac{s^2}{1-\mu^2}]\Theta_n(\theta) = -e_n\Theta_n(\theta) \tag{5.12}$$

With $\mu = \sin\theta$, $\eta = \frac{\sigma}{2\Omega}$ and $e_n = \frac{2\Omega a^2}{gh_n}$, with a being the planetary radius. Equation 5.11 is known as the Vertical Structure Equation and equation 5.12 is Laplace's Tidal Equation. Both equations define an eigenfunction-eigenvalue problem and h_n is the set of eigenvalues normally referred to as the equivalent depth. The equations above are written with fixed s, for simplicity.

Further work on the Vertical Structure Equation and tidal wavelengths are covered in other literature, [69], [15], [24]. These are not needed for MarTIM, as the model propagates the tide vertically in a numerical fashion.

5.3 Latitudinal Structure

The solution of Laplace's Tidal equation gives the latitudinal structure of the tidal perturbations. Hough's work on the Laplace Tidal Equation applied to shallow oceans meant that the eigenfunctions Θ_n became known as Hough modes. The analytical expression is given by equation 5.13.

$$\Theta_n^{\sigma,s}(\theta) = \sum_{m=s}^{\infty} C_{n,m}^{\sigma,s} P_{m,s}(\sin\theta), \tag{5.13}$$

where, $P_{m,s}(\sin\theta)$ are associated Legendre Polynomials of degree m and order s and $C_{n,m}^{\sigma,s}$ are the expansion coefficients for the polynomial series of a given Hough mode. Tables of these coefficients for the diurnal and semi-diurnal modes are available in the literature, [17]. The Hough modes are referred to by the pair of numbers (s,n), where s is the longitudinal wavenumber and n the latitudinal wave number. Positive values of n represent propagating waves, negative values represent trapped waves, [69].

Figure 5.1 shows the normalised latitudinal structures of the diurnal (1,1) and semi-diurnal (2,2) modes. The Hough modes are bounded at the poles, this is only the case if n is positive.

5.4 Martian Tides

Tides in the terrestrial atmosphere are well studied and have been shown to be well modelled using the above equations, [69], [15]. By understanding which parameters in the classical tidal theory vary from planet to planet it is possible to apply terrestrial tidal theory to Mars. The eigenvalue of equation 5.12, Laplace's tidal equation, can be written as equation 5.14, [53]. The parameters that determine the eigenvalues and eigenfunctions are those which are independent of the mass of the planet, the absolute rotation rate, the radius, etc. These are termed as s, the zonal wavenumber and η.

$$x_n = \frac{gh_n}{4R^2\Omega^2} \tag{5.14}$$

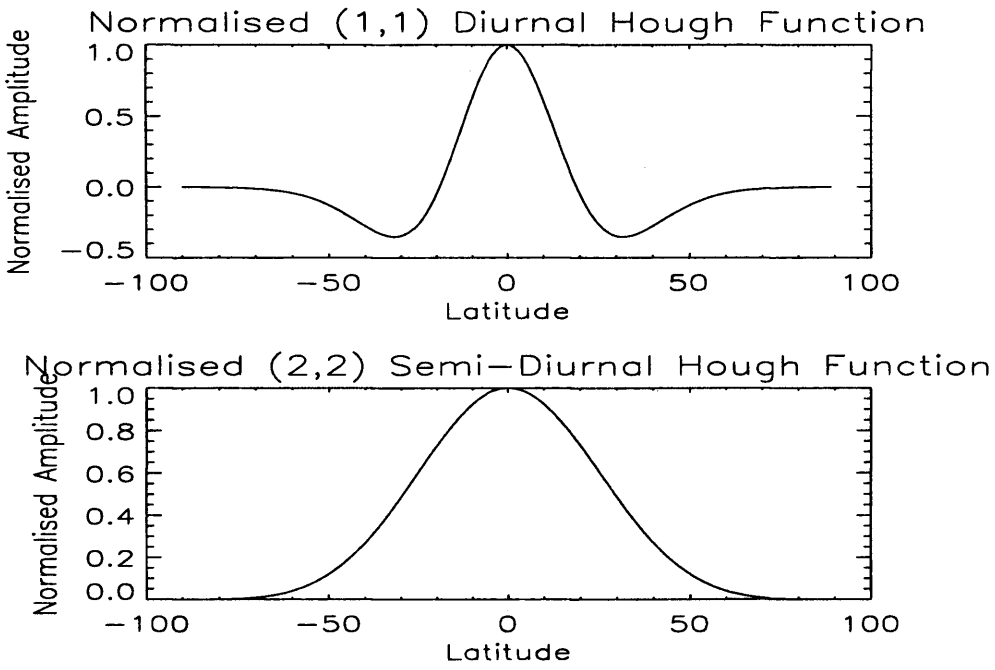

Figure 5.1: Normalised latitudinal structures of the diurnal (1,1) (top) and semi-diurnal (2,2) (bottom) Hough modes

Table 5.1, adapted from [53] shows the parameters for Earth and Mars that are associated with solving the Laplace tidal equation.

Parameter	Mars	Earth
Solar day	24hrs 39mins	24hrs
Sidereal day	24hrs 37mins	23hrs 56mins
η semi-diurnal	1.0	1.0
x_n semi-diurnal	0.0867, etc	0.0887, etc

Table 5.1: The parameters for Earth and Mars associated with the solution of Laplace's tidal equation

The values of η are the same for Earth and Mars. The Hough functions and the x_n's (the eigenvalues) are essentially the same for both planets. If the sidereal day and the solar day are assumed, for Mars, to be the same as for Earth then the Hough functions and x_n's are the same for both planets. The equivalent depths, h_n, of the tidal modes will be different for different planets and can be determined using equation

5.14 - assuming that the equivalent depths of the corresponding terrestrial mode are known. Values of h_n are listed in the literature, [17], for the terrestrial tidal modes (1,*) and (2,*), where * is 1 to 13. The determination of the geopotential amplitudes and phases appropriate at the lower boundary are described in the existing literature dealing with Martian tides, [93], [13].

5.4.1 Modelling Tides - A New Lower Boundary

In the basic model simulations shown in chapters 3 and 4, the MarTIM lower boundary pressure level at 0.883Pa was set to a fixed height of 60km. To simulate the tidal forcing due a tide propagating up from the lower atmosphere the parameters at the lower boundary are perturbed. It is necessary to perturb the geopotential height, horizontal winds and temperature simultaneously but also self consistently. Above the lower boundary the intrinsic dynamics of the model keep the parameters self-consistent. The perturbation equations are linked to classical tidal theory as seen in [24], which is outlined in earlier sections. The perturbation value of the geopotential height around 60km is given by equation 5.15.

$$\Delta z(\theta,t) = \sum_s \sum_n (Z^0_{s,n}\Theta_{n,s}(\theta)\cos(\sigma_s t + s\psi + \phi_{s,n})), \tag{5.15}$$

where, σ_s is the tidal frequency, $Z^0_{s,n}$ is the amplitude for mode (s,n), $\phi_{s,n}$ is the phase term for mode (s,n), $\Theta_{n,s}(\theta)$ are the normalised Hough functions. The horizontal wind equations are based on equations 5.7 and 5.8. They are given by equations 5.16 and 5.17:

$$U(\theta,t) = \frac{g}{R}\cdot\sum_s\sum_n \frac{-1}{\sigma_s(1-\frac{f^2}{\sigma_s^2})}\cdot Z^0_{s,n}\cdot[\frac{sf}{\sigma_s\cos\theta}\cdot\Theta_{n,s}(\theta) - \frac{\partial\Theta_{n,s}(\theta)}{\partial\theta}]\cdot\sin(\sigma_s t + s\psi + \phi_{s,n})) \tag{5.16}$$

$$V(\theta,t) = \frac{g}{R}\cdot\sum_s\sum_n \frac{1}{\sigma_s(1-\frac{f^2}{\sigma_s^2})}\cdot Z^0_{s,n}\cdot[\frac{f}{\sigma_s}\cdot\frac{\partial\Theta_{n,s}(\theta)}{\partial\theta} - \frac{s}{\cos\theta}\cdot\Theta_{n,s}(\theta)]\cdot\cos(\sigma_s t + s\psi + \phi_{s,n})), \tag{5.17}$$

where, as stated earlier in the chapter, f is the Coriolis parameter, R is the planetary radius and θ is the latitude.

The temperature perturbation equation, [23], is shown in equation 5.18

$$\Delta T(\theta,t) = \frac{-g}{R_{CO_2}} \cdot \sum_s \sum_n [\alpha Z^0_{s,n} \cdot \Theta_{n,s}(\theta) \sin(\sigma_s t + s\psi + \phi_{s,n})], \tag{5.18}$$

where α is given by equation 5.19, and R_{CO_2} is the gas constant for CO_2.

$$\alpha = (\frac{\kappa H}{h_n} - \frac{1}{4})^{-0.5} \tag{5.19}$$

In equation 5.19 κ is equal to $\frac{R_{CO_2}}{c_p}$, a value of $\frac{3}{13}$ for Mars.

5.4.2 The Semi-diurnal (2,2) Tide on Mars

The semi-diurnal (2,2) tide is thought to be one of the migrating tidal modes that dissipate at thermospheric altitudes on Mars, [13], [25]. The diurnal (1,1) tide was shown by [93] not to reach altitudes much above 45km. The approximate vertical wavelengths of the semi-diurnal tidal modes (2,3), (2,4) and (2,5) are shown in table 5.2.

Mode	(2,2)	(2,3)	(2,4)	(2,5)
Equivalent depths/km	5.479	2.572	1.330	0.966
λ_z/km	152.1	70.8	51.9	43.0

Table 5.2: The approximate vertical wavelengths for the (2,*) tidal modes.

The height at which tides break has been linked to dust loading in the lower Martian atmosphere, [93], [90]. As outlined in earlier chapters, MarTIM is not set up to include any features to account for the presence of dust in the lower atmosphere. It is known that during dust storms the opacity and heating rates in the lower atmosphere are altered and this could cause several effects in the thermosphere. Localised heating would cause localised expansion of the atmosphere, altering the altitude at which 0.883Pa is found. Also, other tidal modes might be enhanced and reach thermospheric altitudes before they dissipate, altering the momentum and energy distribution of the thermosphere. All simulations presented in this thesis are based on the assumption

that the Martian atmosphere is experiencing low dust conditions. The effects of dust storms on the thermosphere, through tides or other mechanisms, is left for future work.

Figures 5.2 and 5.3 show the (2,2) semi-diurnal perturbations at pressure level 1 of temperature, meridional winds, zonal winds and geopotential height.

The phases and amplitudes of the semi-diurnal tide on Mars are taken from [9]. The comparison for Earth and Mars semi-diurnal tidal inputs can be seen in table 5.3.

Tidal Inputs	Mars	Earth
Equivalent depths/km	5.4790	7.8519
Amplitudes/m	$2.3 \cdot 10^2$	2.7
Mean Phase(+hours westward of noon)	+2.4	+10.5

Table 5.3: The semi-diurnal tidal inputs for Earth and Mars, [9], where the phase refers to the tidal phase of the geopotential height perturbation.

5.5 Tidal Effects on the Winds: A Comparison

In chapter 3 a comparison between MTGCM results and MarTIM results found that the zonal wind speeds in MarTIM were half of those found in MTGCM. It was also noted that the MTGCM results contained more middle atmospheric structure than was expected from a basic Mars thermosphere model. To test whether the introduction of the (2,2) semi-diurnal tide increases the zonal wind velocities, or adds structure to the middle atmosphere, the comparison is repeated here. Figure 5.4 shows the vertical wind structure at the equator for a MarTIM simulation with the (2,2) tide, it is compared to figure 4.14 which shows MTGCM vertical winds. Figure 5.5 shows the zonal wind structure at the equator for the same conditions, it is compared to figure 4.15 which shows MTGCM zonal winds.

Figures 5.4 and 5.5 show greater middle atmospheric wind structure than appeared in basic MarTIM simulations shown in figures 4.15 and 4.14. The zonal winds in the (2,2) tide simulations are also slightly larger than those seen in the basic MarTIM simulations. In comparison to the MTGCM winds shown in figures 4.15 and 4.14

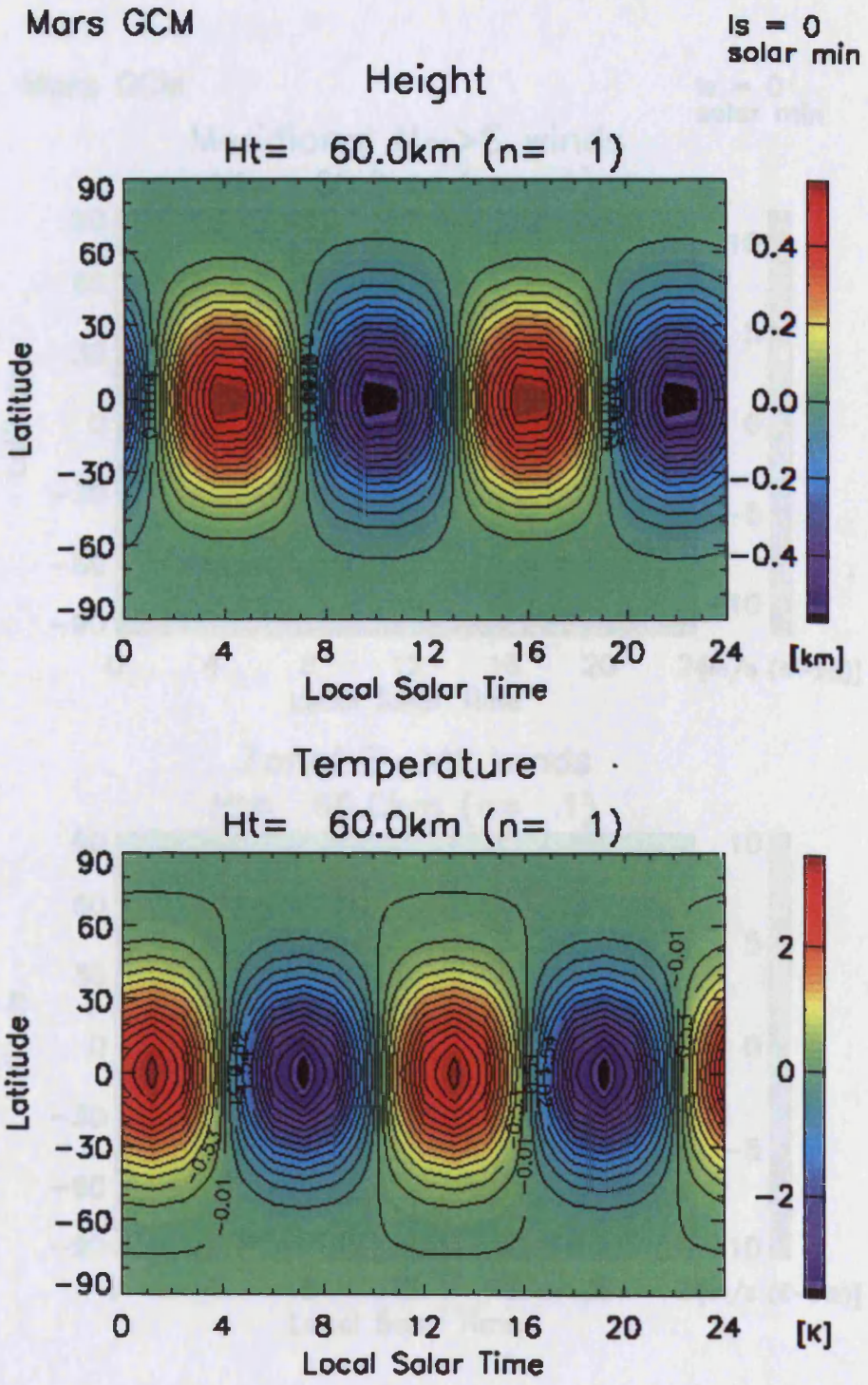

Figure 5.2: Semi-diurnal perturbation for geopotential height (top) and temperature (bottom) at the lower boundary. Difference plots for simulations with and without tides

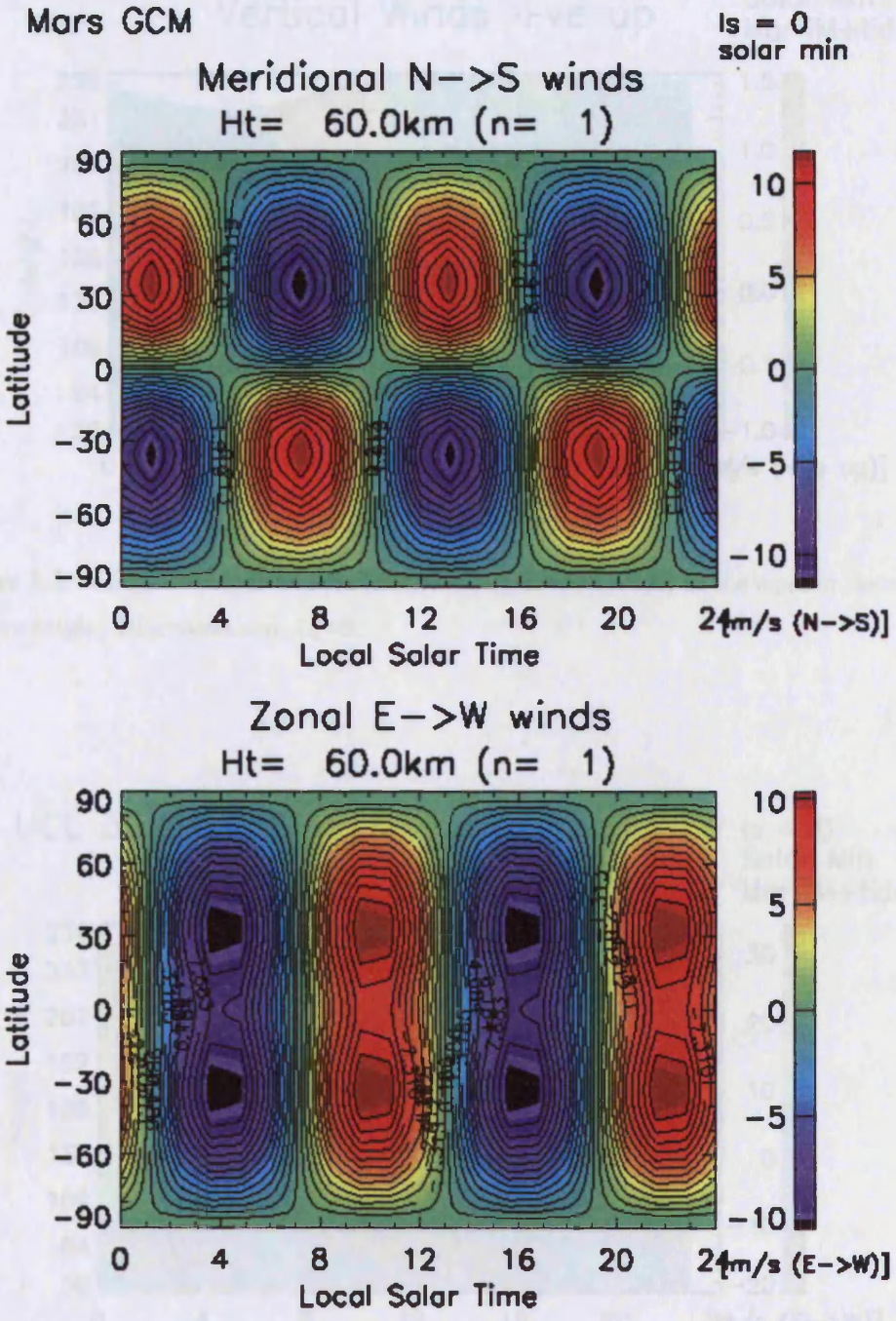

Figure 5.3: Semi-diurnal perturbation for meridional winds (top) and zonal winds (bottom) at the lower boundary. Difference plots for simulations with and without tides

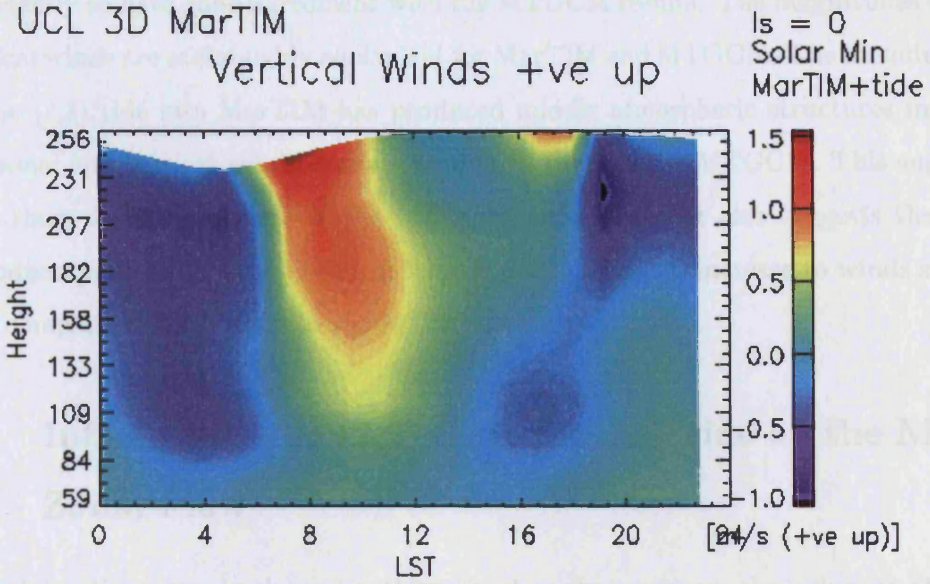

Figure 5.4: Vertical winds from MarTIM including the (2,2) tide, at the equator, local solar time vs height, solar minimum, L_s=0.

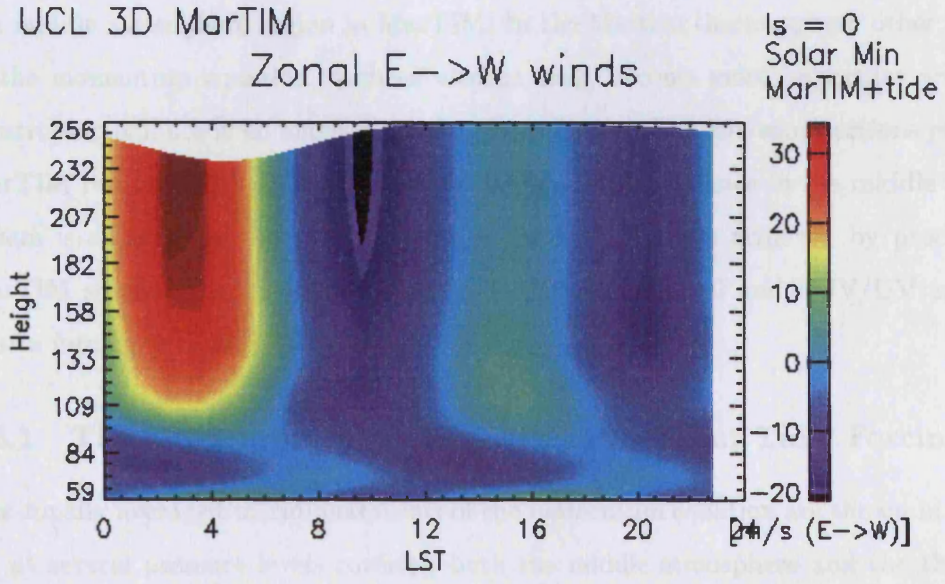

Figure 5.5: Zonal winds from MarTIM including the (2,2) tide, at the equator, local solar time vs height, solar minimum, L_s=0

the inclusion of the (2,2) tide in MarTIM has not increased the zonal wind speeds sufficiently to have good agreement with the MTGCM results. The magnitudes of the vertical winds are still roughly equivalent for MarTIM and MTGCM. The introduction of the (2,2) tide into MarTIM has produced middle atmospheric structures in both the zonal and vertical winds that are similar to those in the MTGCM. This suggests that there are tides present in the MTGCM simulations. It also suggests that the introduction of the (2,2) semi-diurnal tide is not sufficient to increase to winds speeds to a comparable magnitude to the MTGCM results.

5.6 Influence of the (2,2) Semi-diurnal Tide on the Mean Zonal Flow

Examining the terms in the momentum equation demonstrates the influence of tidal forcing on the middle atmosphere and thermosphere regions covered by MarTIM. A state of geostrophic balance is assumed if the atmosphere is in a state of equilibrium and in an altitude range where frictional forces become negligible. The geostrophic balance occurs when the significant terms in the momentum equation are the Coriolis force and the geopotential term (the pressure gradient term). This is true for the middle atmosphere region in MarTIM. In the Martian thermosphere other terms in the momentum equation, such as viscous drag, become more important and the geostrophic balance is no longer a good approximation. The following sections present MarTIM results which examine whether the geostrophic balance in the middle atmosphere is affected by the (2,2) tidal propagation. This was achieved by producing MarTIM simulations for solar minimum conditions for L_s=0 and EUV/UV and IR in-situ forcing with and without the (2,2) tide.

5.6.1 The Momentum Equation with and without Tidal Forcing

The zonally averaged meridional terms of the momentum equation are shown in figure 5.6 at several pressure levels covering both the middle atmosphere and the thermosphere and with varying latitude. In-situ forcing due to the solar EUV/UV and IR is present, but no tidal forcing. Figure 5.7 show the same parameters again with in-situ forcing but with the semi-diurnal (2,2) tidal forcing also present.

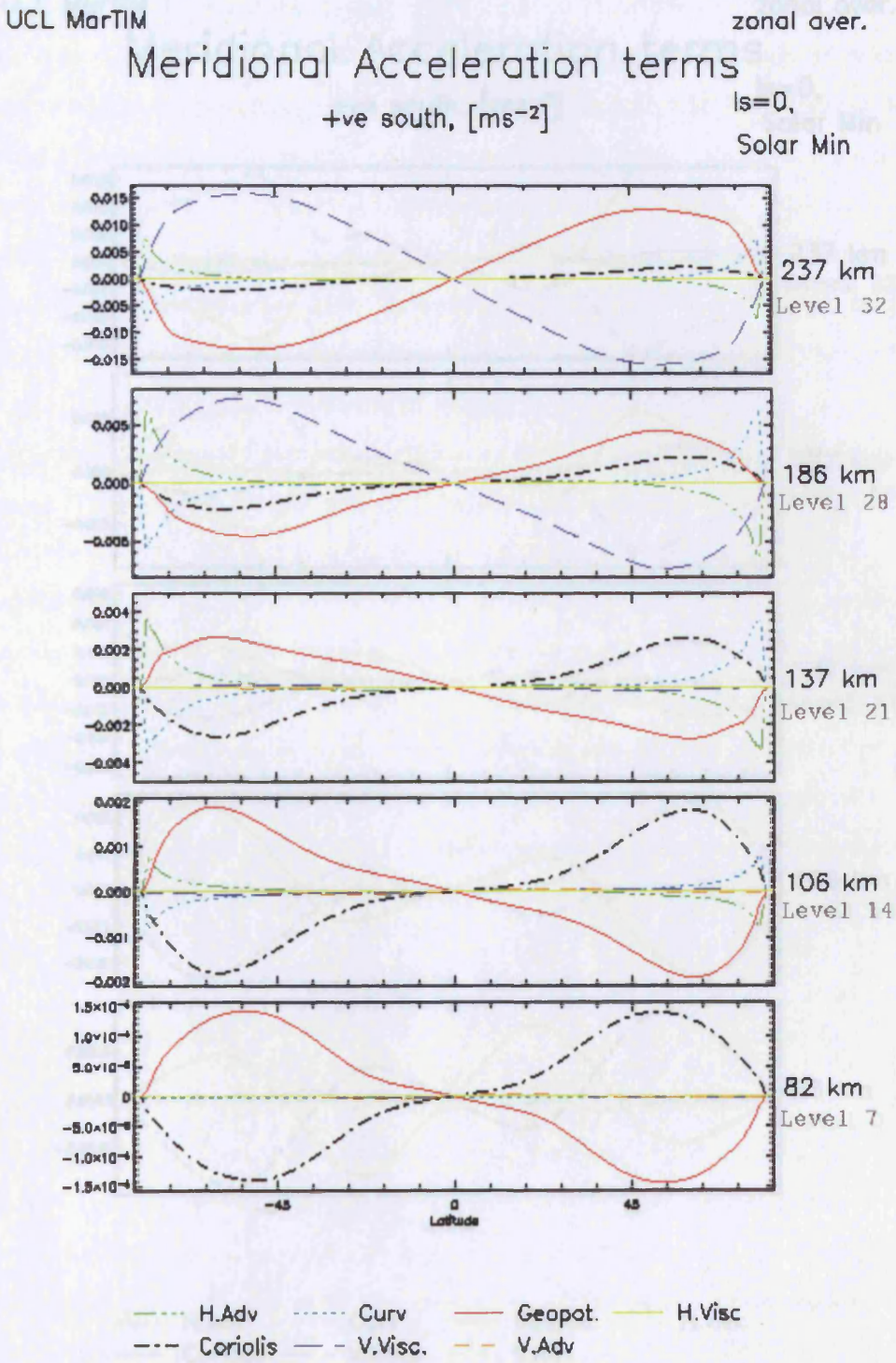

Figure 5.6: Zonally averaged meridional momentum terms at various pressure levels for EUV/UV/IR in-situ forcing only

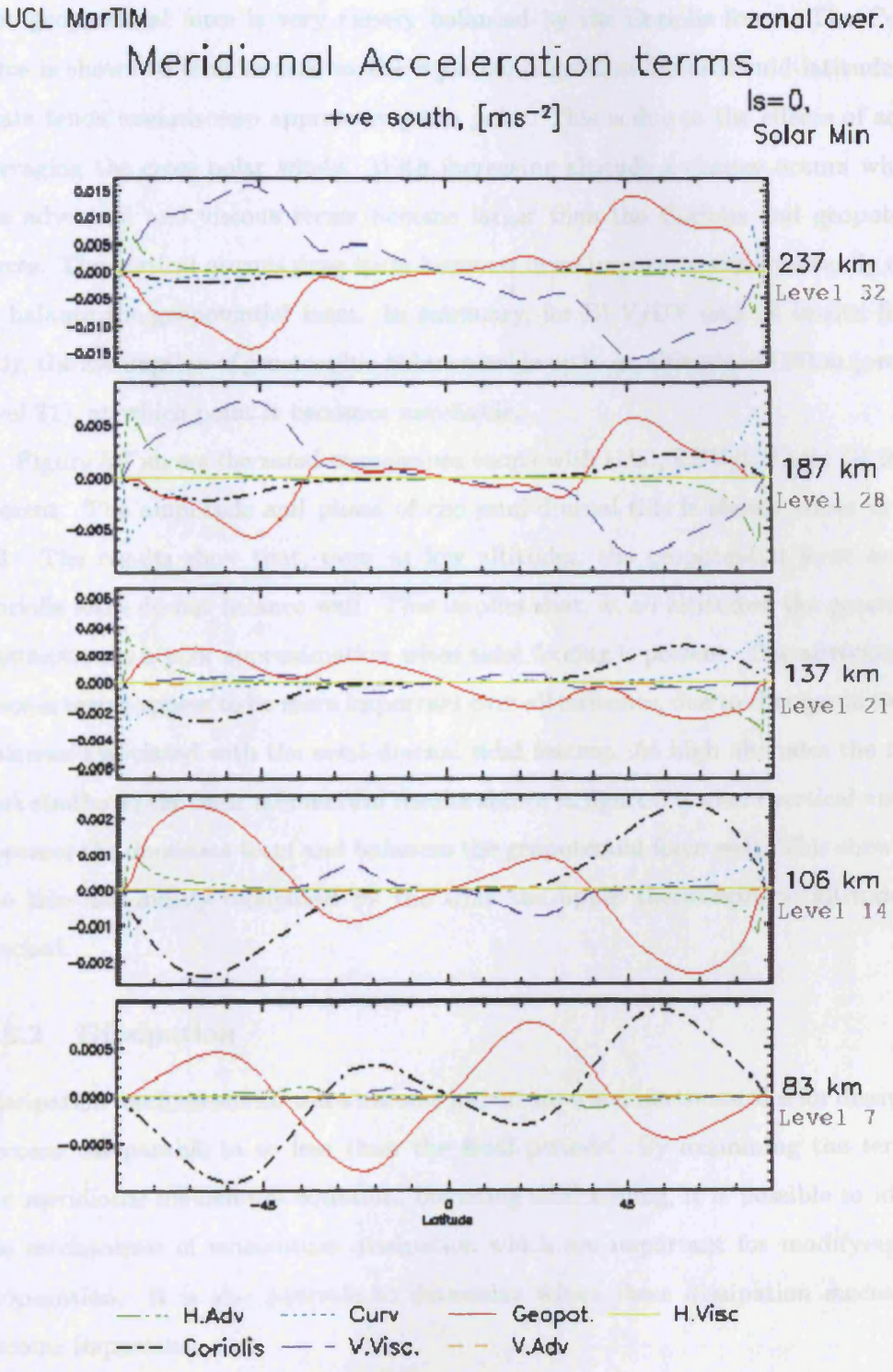

Figure 5.7: Zonally averaged meridional momentum terms at various pressure levels for EUV/UV/IR in-situ forcing and semi-diurnal tidal forcing

In figure 5.6 it can be seen that at low altitudes the geostrophic balance holds. The geopotential force is very closely balanced by the Coriolis force. The Coriolis force is shown to tend to zero at the equator, is greatest towards mid-latitudes and again tends towards zero approaching the poles. This is due to the effects of zonally averaging the cross polar winds. With increasing altitude a change occurs whereby the advection and viscous terms become larger than the Coriolis and geopotential forces. The vertical viscous drag term becomes more important and eventually comes to balance the geopotential term. In summary, for EUV/UV and IR in-situ forcing only, the assumption of geostrophic balance holds up to an altitude of 137km (pressure level 21), at which point it becomes unreliable.

Figure 5.7 shows the zonal momentum terms with tidal, EUV/UV and IR forcing present. The amplitude and phase of the semi-diurnal tide is shown above in table 5.3. The results show that, even at low altitudes, the geopotential force and the Coriolis force do not balance well. This implies that, at all altitudes, the geostrophic assumption is a poor approximation when tidal forcing is present. The advection and viscous terms appear to be more important over all latitudes, due to changes in the flow patterns associated with the semi-diurnal tidal forcing. At high altitudes the results look similar to the basic momentum results shown in figure 5.6 where vertical viscosity becomes the dominant term and balances the geopotential force well. This shows that the tide has mostly dissipated by the time the upper thermospheric altitudes are reached.

5.6.2 Dissipation

Dissipation mechanisms for tides become important when the timescales for dissipation become comparable to or less than the tidal periods. By examining the terms in the meridional momentum equation, including tidal forcing, it is possible to identify the mechanisms of momentum dissipation which are important for modifying tidal propagation. It is also possible to determine where these dissipation mechanisms become important.

An estimate of the timescales for dissipation, for a given tidal mode, due to terms in the momentum equation is given by dividing the momentum equation through by the velocity and inverting each term. The smaller the term in the momentum

equation at a given altitude, the larger the associated timescale for dissipation and the less important the term will be for dissipation above that height. For wind speeds of $70ms^{-1}$ and momentum terms of the order of $0.015ms^{-1}$ the dissipation timescale is of the order of 4600s.

5.6.3 Zonally Averaged Wind Structures

The zonally averaged meridional and zonal winds are shown, as a function of latitude and pressure level, in figure 5.8 for EUV/UV and IR in-situ forcing and in figure 5.9 for EUV/UV, IR and semi-diurnal tidal forcing.

Table 5.4 gives the average heights of the pressure levels for figures 5.8 and 5.9.

Pressure Level	Ht -basic	Ht-tides	Pressure Level	Ht-basic	Ht-tides
1	60.00km	60.00km	18	123.50km	123.83km
2	64.21km	64.21km	19	128.00km	128.38km
3	68.01km	68.02km	20	132.75km	133.16km
4	71.82km	71.87km	21	137.79km	138.22km
5	75.62km	75.68km	22	143.16km	143.62km
6	79.35km	79.41km	23	148.91km	149.39km
7	82.94km	83.02km	24	155.06km	155.57km
8	86.40km	86.49km	25	161.71km	162.23km
9	89.73km	89.84km	26	168.95km	169.49km
10	92.99km	93.12km	27	176.96km	177.52km
11	96.25km	96.41km	28	185.96km	186.54km
12	99.58km	99.76km	29	196.20km	196.80km
13	103.09km	103.28km	30	207.86km	208.48km
14	106.83km	107.05km	31	220.95km	221.61km
15	110.80km	111.04km	32	235.30km	236.00km
16	114.91km	115.19km	33	250.60km	251.33km
17	119.14km	119.45km	-	-	-

Table 5.4: The average heights of the pressure levels for EUV/UV and IR forcing simulation (basic) and EUV/UV, IR and tidal forcing simulations.

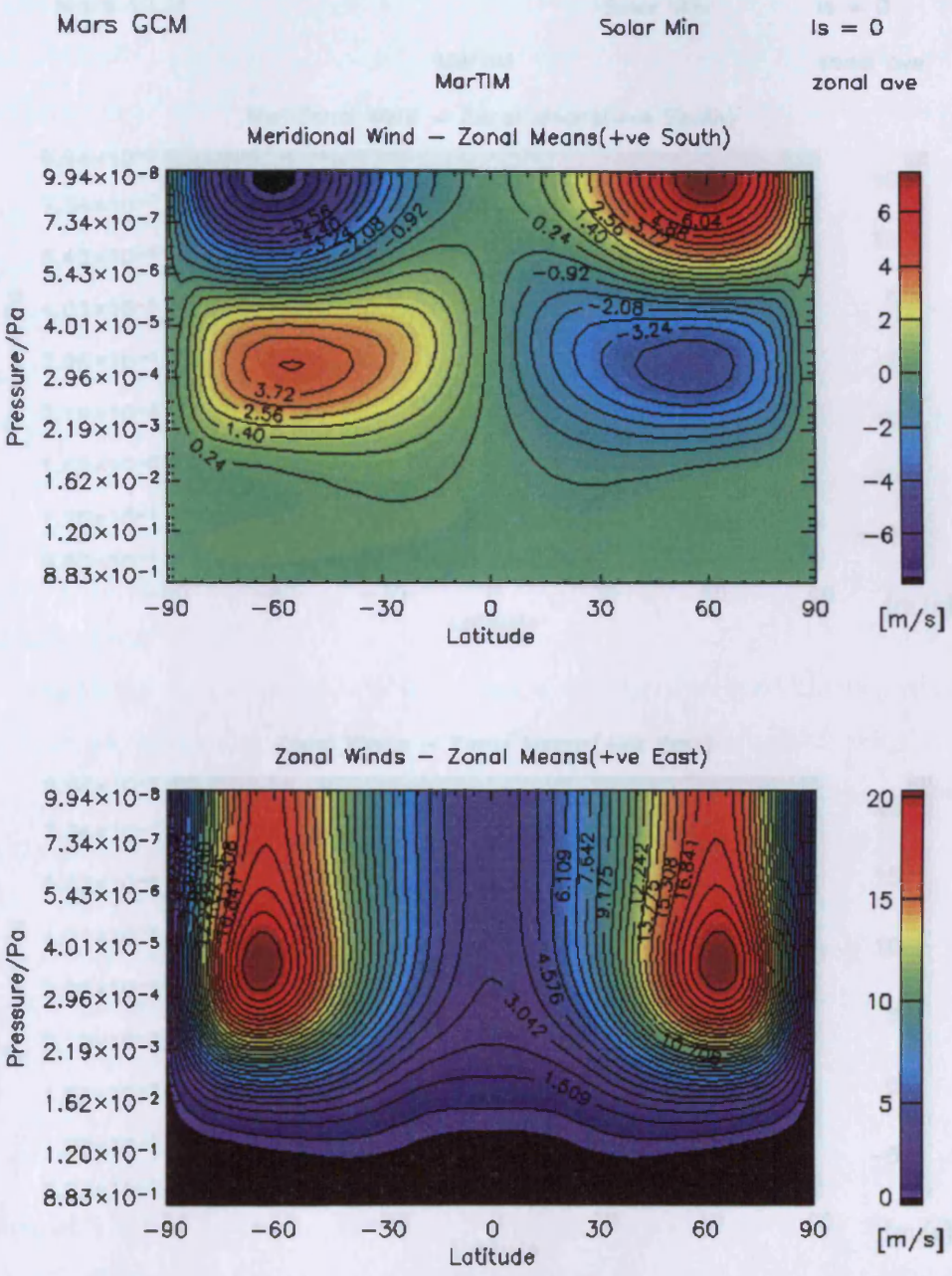

Figure 5.8: Zonally averaged meridional and zonal wind for EUV/UV/IR in-situ forcing

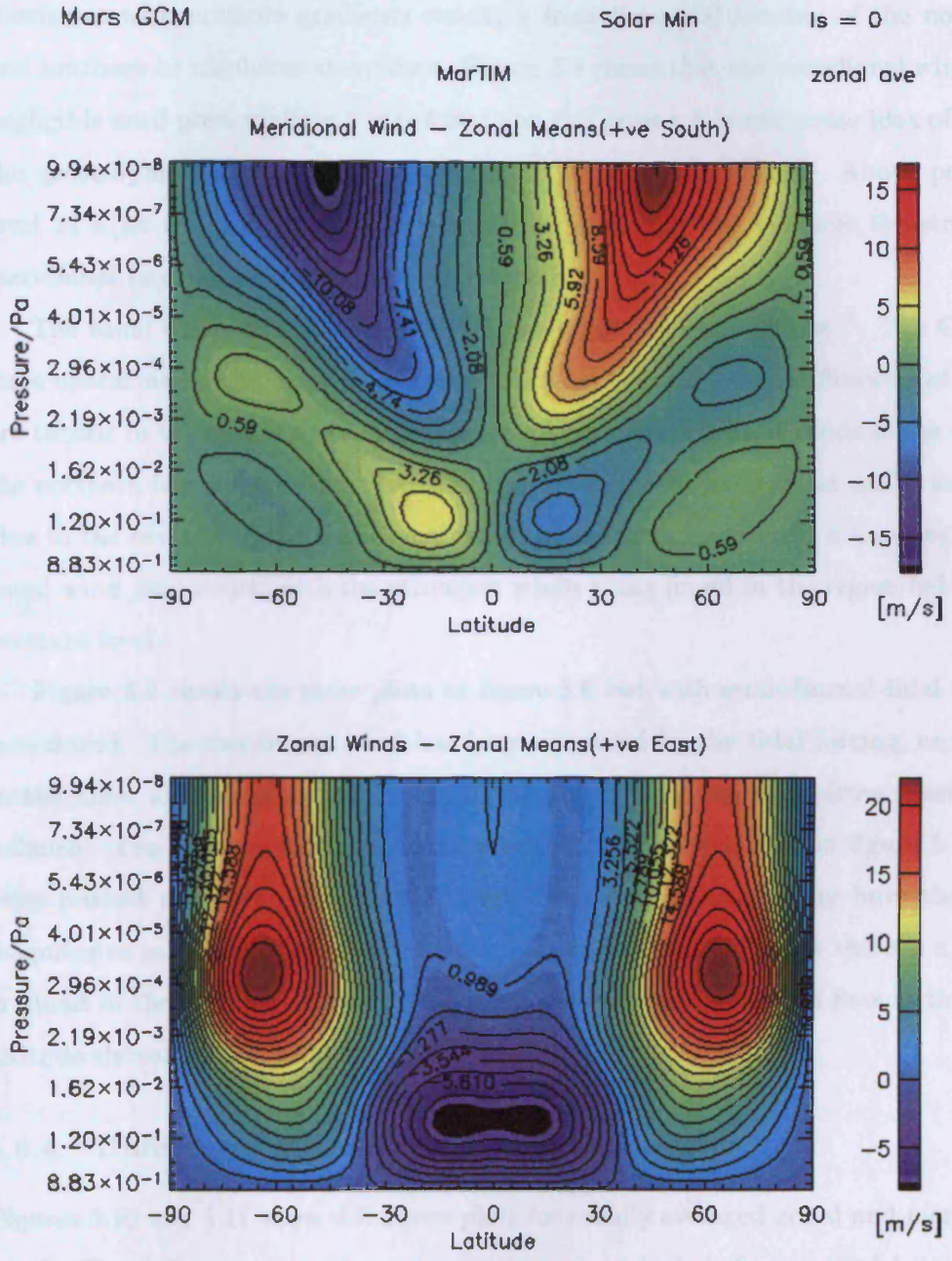

Figure 5.9: Zonally averaged meridional and zonal wind for EUV/UV/IR in-situ forcing and semi-diurnal tidal forcing

The meridional winds in figure 5.8 are small, with a maximum of $7ms^{-1}$. There are two closed jets situated between pressure levels 13-22. The southward jet is strongest at around -60° latitude, the northward jet is strongest at +60° latitude. This is consistent with pressure gradients resulting from the equal heating of the northern and southern hemispheres at equinox. Figure 5.9 shows that the meridional winds are negligible until pressure level 9 is reached and this gives a more accurate idea of where the geostrophic balance breaks down in the Martian atmosphere. Above pressure level 24 a jet reversal occurs, the jets become open and this is where the strongest meridional (zonally averaged) winds are found.

The zonal winds in figure 5.8 are also small, ranging from $0\text{-}20ms^{-1}$. The Coriolis force operating on the meridional winds produces the zonal winds. Southward winds are turned to the east in the southern hemisphere and northward winds to the east in the northern hemisphere- this results in the two eastward jets seen at ± 60 ° latitude. Due to the reversal in the meridional winds above pressure level 24 a tapering of the zonal wind jets occurs, with the strongest winds being found in the region below this pressure level.

Figure 5.9 shows the same plots as figure 5.8 but with semi-diurnal tidal forcing introduced. The meridional wind has been enhanced by the tidal forcing, especially in the lower altitude pressure levels, consistent with the departure from geostrophic balance. The two low altitude closed jets that were in evidence in figure 5.8 have been pushed down into the middle atmosphere and, although they have the same magnitudes as before, they have become bifurcated. At the equator there is a strong gradient in the meridional wind. This is associated with a westward flow at the same altitude shown on the zonal wind plot below.

5.6.4 Differences in the Zonally Averaged Flow

Figures 5.10 and 5.11 show difference plots for zonally averaged zonal and meridional winds. The difference plots show the zonally averaged winds from a model simulation with no tides, subtracted from a model simulation with the (2,2) tide present. These plots enable the effects on the mean zonal flow by tidal forcing to be isolated. The acceleration of the mean zonal flow is due to the molecular and eddy dissipation of the semi-diurnal propagating tide. Figure 5.10 shows that an equatorial westward flow

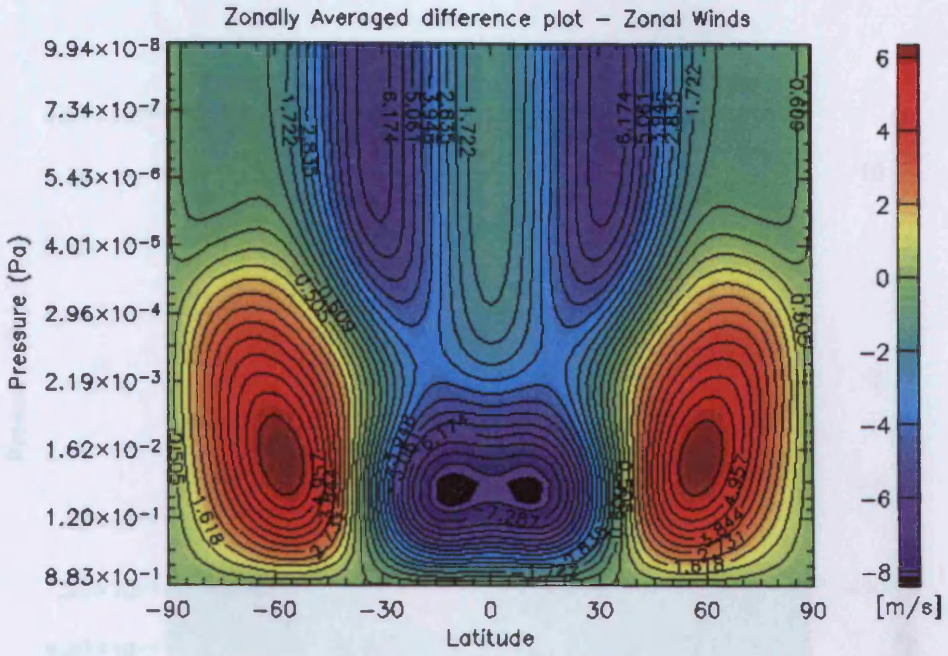

Figure 5.10: Zonally averaged zonal wind difference plot for a tide simulation minus a basic simulation

with maximum winds around 85km is present, with flanking weaker eastward jets around ±30° latitude. Figure 5.11 shows a multicellular structure between the lower boundary and around 100km, with strong northward and southward flows either side of the equator at ±30° latitude. Above 100km there are two strong flows, confined to ±60° latitude, which peak at ±30° latitude.

5.6.5 Tidal Amplitudes

The relationship between the tide dissipating and the changes in the mean zonal flow can be examined when comparing the tidal amplitudes and the difference zonal mean plots. The amplitude of the (2,2) semi-diurnal tide in the meridional winds is shown in figure 5.12.

Compared to figure 5.11 it shows that the greatest difference in the meridional winds occur above the altitude of the peak amplitude. This is where the tide is starting to be strongly dissipated. Figure 5.12 shows main peaks at ± 30° latitude and at pressure level 9, gradually tapering off to ± 60° latitude at pressure level 17. The strongest change in meridional winds occurs above these amplitude peaks. This

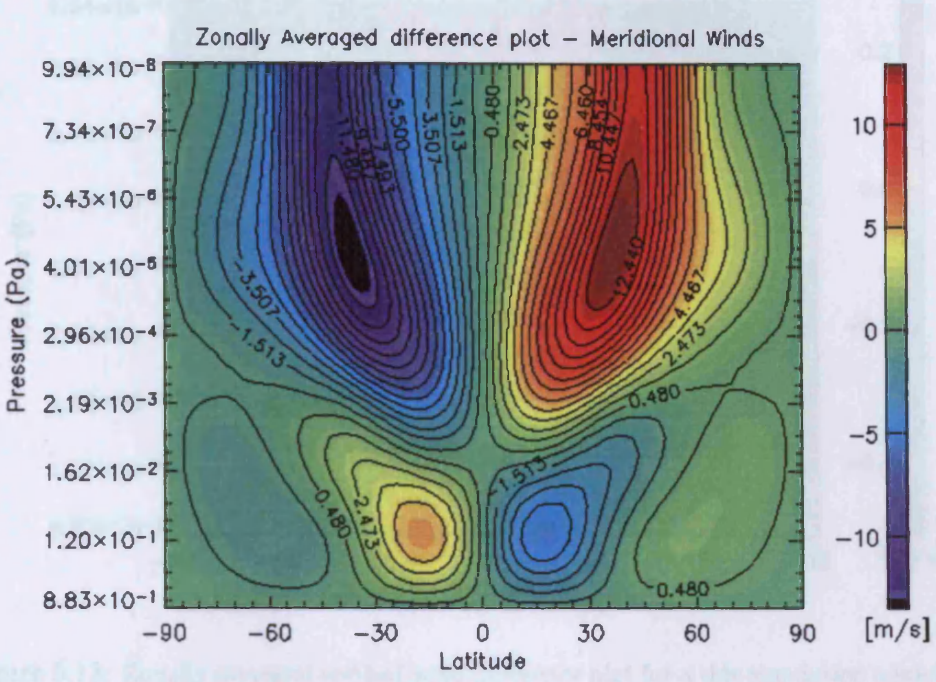

Figure 5.11: Zonally averaged meridional wind difference plot for a tide simulation minus a basic simulation

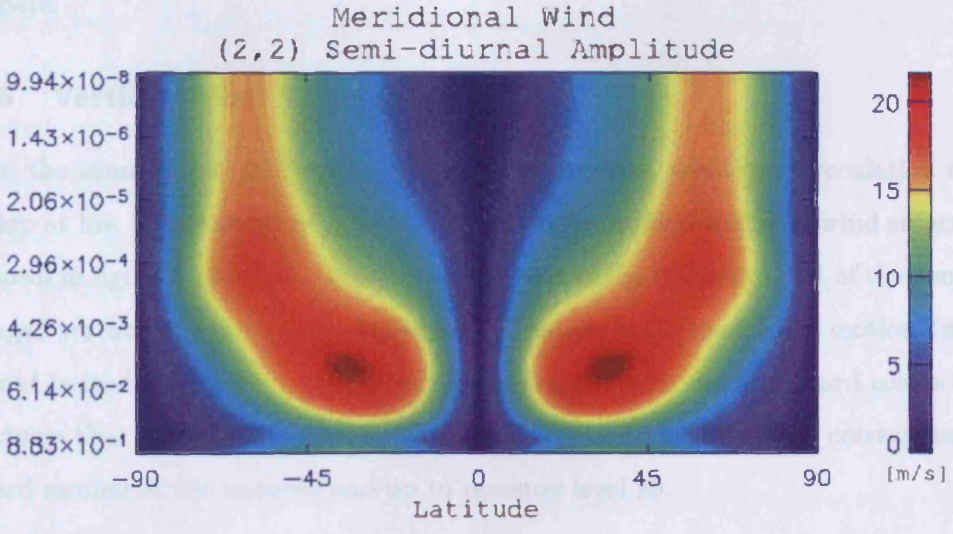

Figure 5.12: (2,2) semi-diurnal tidal amplitude from the meridional winds

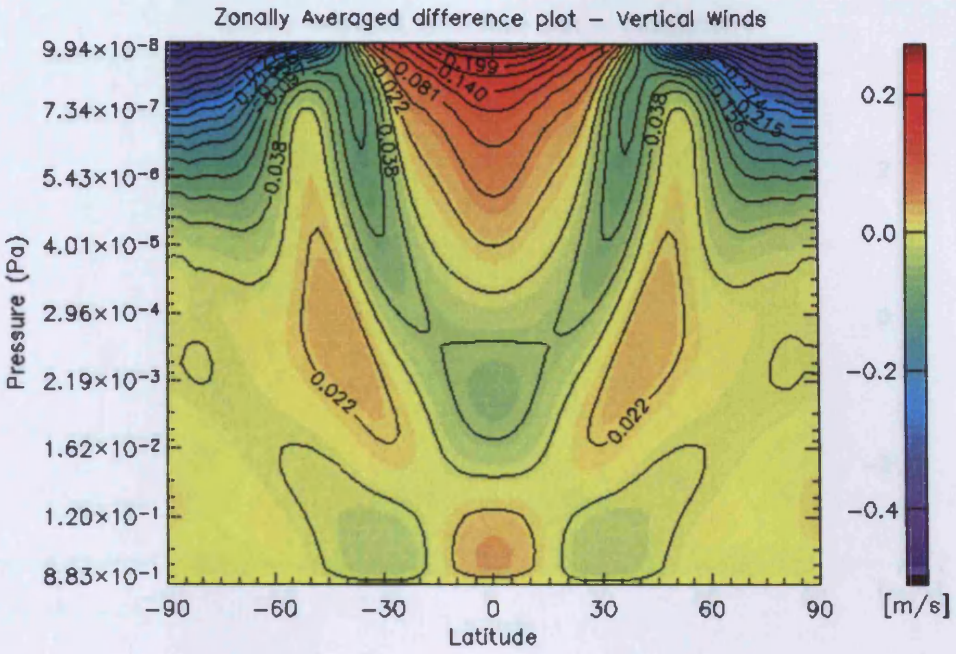

Figure 5.13: Zonally averaged vertical wind difference plot for a tide simulation minus a basic simulation

shows that the introduction of the (2,2) tide introduces a mean flow into MarTIM simulations. The zonally averaged meridional winds flow is greatest in magnitude above the tidal amplitude peak in the meridional winds, where the tide is starting to dissipate.

5.6.6 Vertical Wind Variations

When the semi-diurnal (2,2) tidal forcing is introduced, additional circulation cells develop at low latitudes associated with the changes in the meridional wind structure as shown in figure 5.11. These changes can be seen in the difference plot of the zonally averaged vertical wind structure, figure 5.13. Changes in the meridional motion due to the mid latitude poleward motions may be associated with the downward convection structures that occur at the pole and around $\pm 30°$ latitude and to the corresponding upward motion at the equator and up to pressure level 29.

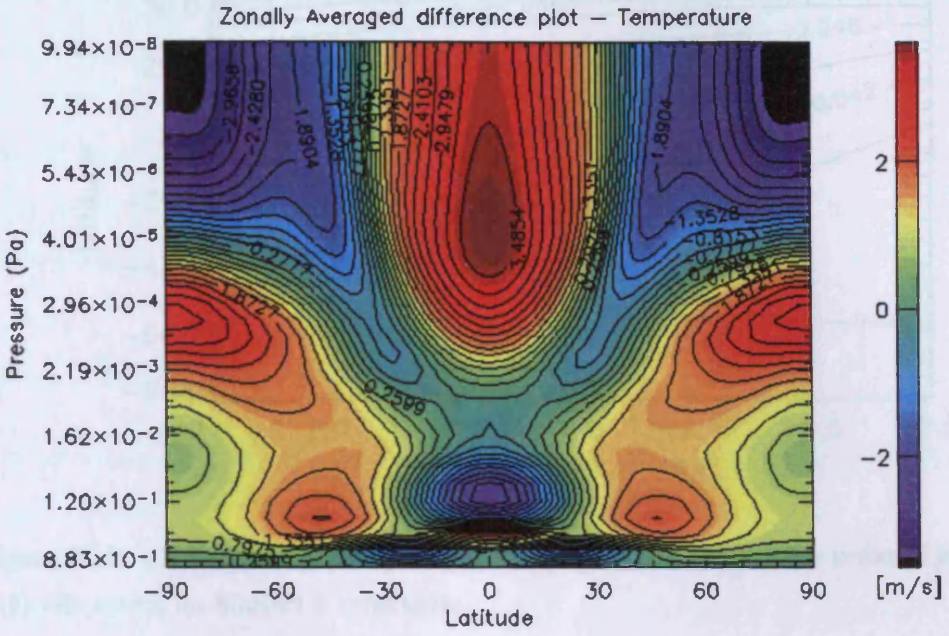

Figure 5.14: Zonally averaged temperature difference plot for with and without tides shown in terms of latitude and pressure level

5.6.7 Heating and Cooling due to the (2,2) Tide

Tidal forcing also produces changes in the zonally averaged temperature structure as well as the horizontal and vertical winds. Figure 5.14 shows a difference plot for the zonally averaged temperature. It shows that there are regions of cooling as well as heating and that the greatest structure changes occur in the lower half of the atmosphere, from pressure level 19 downwards. A pronounced vertical band of heating is seen that extends from the top pressure level down to pressure level 14 and is localised between ±30° latitude.

In the atmosphere the mean effect of the tidal influence is to cause heating between pressure levels 13 to 18 (at ±90° to ±70° latitude) and also between pressure levels 3 and 6 (at ±60° to ±40° latitude) and cooling mainly between pressure levels 21 to 33 (at ±90° to ±30° latitude) and pressure levels 3 to 7 (at ±30° latitude). Comparing figure 5.14 with figure 5.13 shows that this temperature structure may be, in part, related to the vertical wind changes. Upwelling winds would be expected to reduce the temperature through cooling via adiabatic expansion and the downwelling winds would, conversely, increase the temperature though compressional heating. Compar-

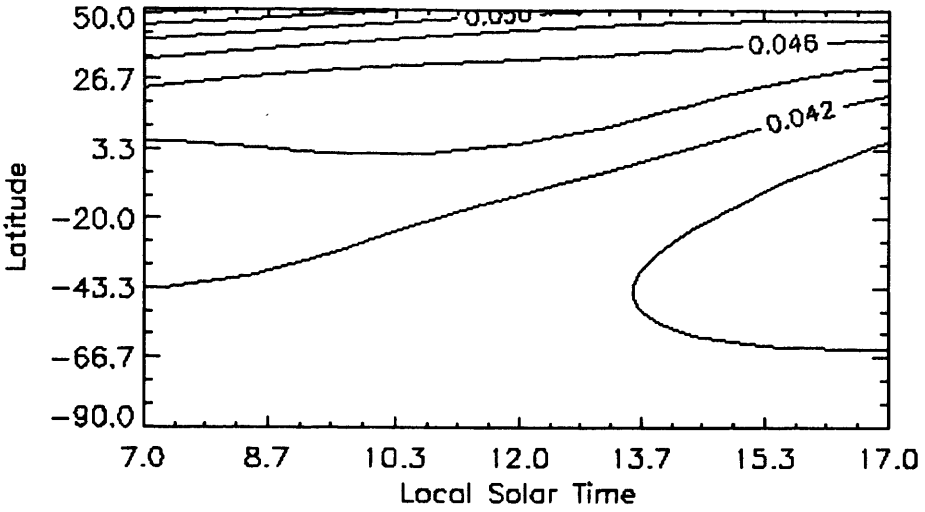

Figure 5.15: [O] fractional abundance from MarTIM across the 1.2nbar pressure level with (2,2) tide active, for Mariner 9 conditions

ing the position of the upwelling and downwelling structures in figure 5.13 to the heating and cooling structures in figure 5.14 a relationship can be seen. For example the downwelling "U" shape structure seen at $\pm 30°$ latitude in the vertical winds corresponds to the boundary of the heating "tongue" seen in the temperature plot.

However, the heating distribution at all latitudes can also be affected directly by a heating component due to dissipation of the tidal energy. The vertical and horizontal circulation in the atmosphere will add additional structure to any temperature changes caused by this dissipation process. So although similarities between the zonal mean difference vertical wind and temperature structures can be seen, it must be placed in the context of the other heating and cooling mechanisms at work in the Martian atmosphere.

5.7 Tidal Effects on Composition

In chapter 3 the fractional O abundance determined from Mariner 9 data was compared to basic MarTIM output and significant differences were found. This sections examines whether the incorporation of the (2,2) semi-diurnal tide has altered the fractional abundance distribution seen in MarTIM. Figure 5.15 shows the fractional abundance of atomic oxygen from MarTIM with the (2,2) tide active.

Although there is a difference when compared to the basic MarTIM fractional O

abundance output, the general pattern of the ratio still does not agree with the Mariner 9 data shown in figure 3.15. The figure demonstrates that while the semi-diurnal tide does have an effect on the gas distributions in MarTIM, it is not sufficient to resolve the differences between the data and the MarTIM simulations. This illustrates that more work needs to be undertaken on MarTIM to include other features that will address the distribution of momentum in the Martian thermosphere.

5.8 Tides Summary

The results in this chapter have shown that on Mars, the geostrophic balance becomes a poor approximation in the presence of (2,2) semi-diurnal tidal forcing. The upward propagation of the (2,2) semi-diurnal tide has been shown to be responsible for the input of considerable energy and momentum into the Martian thermosphere. This is highlighted when looking at the amplitude of the tide in the winds, where the greatest change occurs above the peak in amplitude of the tide. Strong mean zonal winds occur above the altitude at which the response to semi-diurnal forcing is greatest (where they are being strongly dissipated). The presence of tidal perturbations at the lower boundary has also resulted in an increase in the middle atmosphere winds. This shows that a small, varying ($\pm 10 \mathrm{ms}^{-1}$), wind perturbation introduced at the lower boundary has a greater effect on the middle atmosphere winds than a small, constant value, horizontal wind at lower boundary.

Chapter 6

New Lower Boundary

As described in chapter 2, the AOPP group at Oxford has been developing a lower atmosphere database for Mars that extends from the surface to around 120km. This is achieved by using the mean results from a finite difference GCM and a spectral GCM and called the Mars Climate Database, [52]. The main uses of the database are to study the weather effects in the Martian lower atmosphere, the role of dust storms and the effect of topography on the atmospheric structures and flows. The Mars Climate Database (MCD) version 3.1 extends to a mean altitude of 120km above the Martian surface, which provides an overlap of 60km with the lower range of MarTIM altitudes. The basic MarTIM does not include a lower atmosphere so by using the MCD as a lower boundary for MarTIM it is hoped to identify the effects of the lower atmosphere on the thermospheric flows and energy distribution. To this end, the MCD version 3.1, [51], has been used to provide a lower boundary input into MarTIM.

The MCD uses a sigma level pressure height scheme that is dependent on the surface pressure, see equation 6.1.

$$\sigma = \frac{P}{P_s} \tag{6.1}$$

Where P is the pressure at a certain height, P_s is the surface pressure and σ is the ratio of the two pressures. Table 6.1 shows the first few sigma values and equivalent heights above the surface.

The sigma level system differs from the pressure level system that MarTIM uses as it is dependent on the surface pressure. If the pressure level system used in MarTIM was extrapolated down to the surface some of the pressure levels would be below the surface because of the topographic features. Due to the differences in the pressure

Layer	σ	Approx height	Layer	σ	Approx height
1	0.999500	5m	16	0.021789	37km
2	0.998001	20m	17	0.011008	43km
3	0.995013	50m	18	$5.528 \cdot 10^{-3}$	48km
4	0.989086	115m	19	$2.767 \cdot 10^{-3}$	54km
5	0.977443	240m	20	$1.383 \cdot 10^{-3}$	60km
6	0.955004	490m	21	$6.910 \cdot 10^{-4}$	65km
7	0.913289	980m	22	$3.450 \cdot 10^{-4}$	71k
8	0.840606	1.8km	23	$1.722 \cdot 10^{-4}$	77km
9	0.726845	3.4km	24	$8.597 \cdot 10^{-5}$	82km
10	0.574642	7km	25	$4.291 \cdot 10^{-5}$	87km
11	0.407472	906km	26	$2.141 \cdot 10^{-5}$	92km
12	0.258882	14.2km	27	$1.069 \cdot 10^{-5}$	97km
13	0.150070	19.5km	28	$5.335 \cdot 10^{-6}$	101km
14	0.081573	25km	29	$2.663 \cdot 10^{-6}$	106km
15	0.042627	31km	30	$1.329 \cdot 10^{-6}$	110km

Table 6.1: Sigma level values and their equivalent height above the surface, adapted from [51]. The approximate height is determined by -10·ln(σ)km.

level schemes between MarTIM and MCD generating the lower boundary data to input into MarTIM is more complex than just choosing and inputting the closest MCD sigma level to 0.883Pa, which is the lower boundary pressure for MarTIM. A linear interpolation scheme was written that interpolated over the sigma levels in the 0.883Pa region and produced a longitude-latitude dataset that had a constant pressure of 0.883Pa. This interpolation was used to generate the basic input files of temperature, height, meridional and zonal winds for the lower boundary of MarTIM. The altitude range of the MCD sigma levels that are interpolated over to generate the constant 0.883Pa dataset is from around 55km to 66km.

This initial interpolation is performed for MCD conditions that are low dust and had the gravity wave parameterisation deactivated. These choices were made to ensure

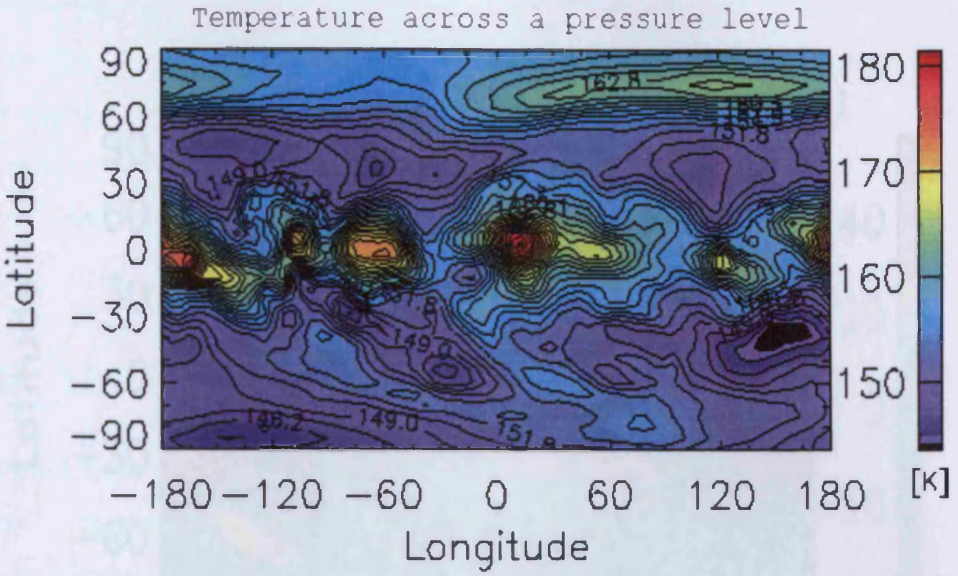

Figure 6.1: MCD temperature at MarTIM's lower boundary (pressure level 1) at 12:00UT

that any differences in MarTIM output would be due only to the lower boundary and hence, the lower atmosphere. It should be noted however that the low dust scenario in MCD was created to provide a strong lower limit for the amount of dust in the lower atmosphere and maybe too clear even for the relatively dust free seasons. However, for consistency with the rest of this thesis the low dust scenario has been used and the effects of it's use discussed at the relevant points in this chapter. For seasons L_s=270-330 major dust storms can occur on the Martian surface. As a result the perihelion conditions of the combined MarTIM+MCD model will not be investigated for these seasons to maintain the low dust assumption. The longitude-latitude resolution of MarTIM was set to match that of the MCD input files, 5° latitude by 5° longitude, thus eliminating the need for any further interpolations.

Figures 6.1 and 6.2 below illustrate the nature of the lower boundary data from the MCD. They show the height, temperature and meridional wind variation across a pressure level of 0.883Pa, $L_s = 0$, 12:00UT. In basic MarTIM the temperature and height were constant across the lower boundary and the horizontal winds were set to zero.

The MCD contains datasets that correspond to local times separated by two hours. A simple interpolation routine acts in the interface between the MCD and MarTIM

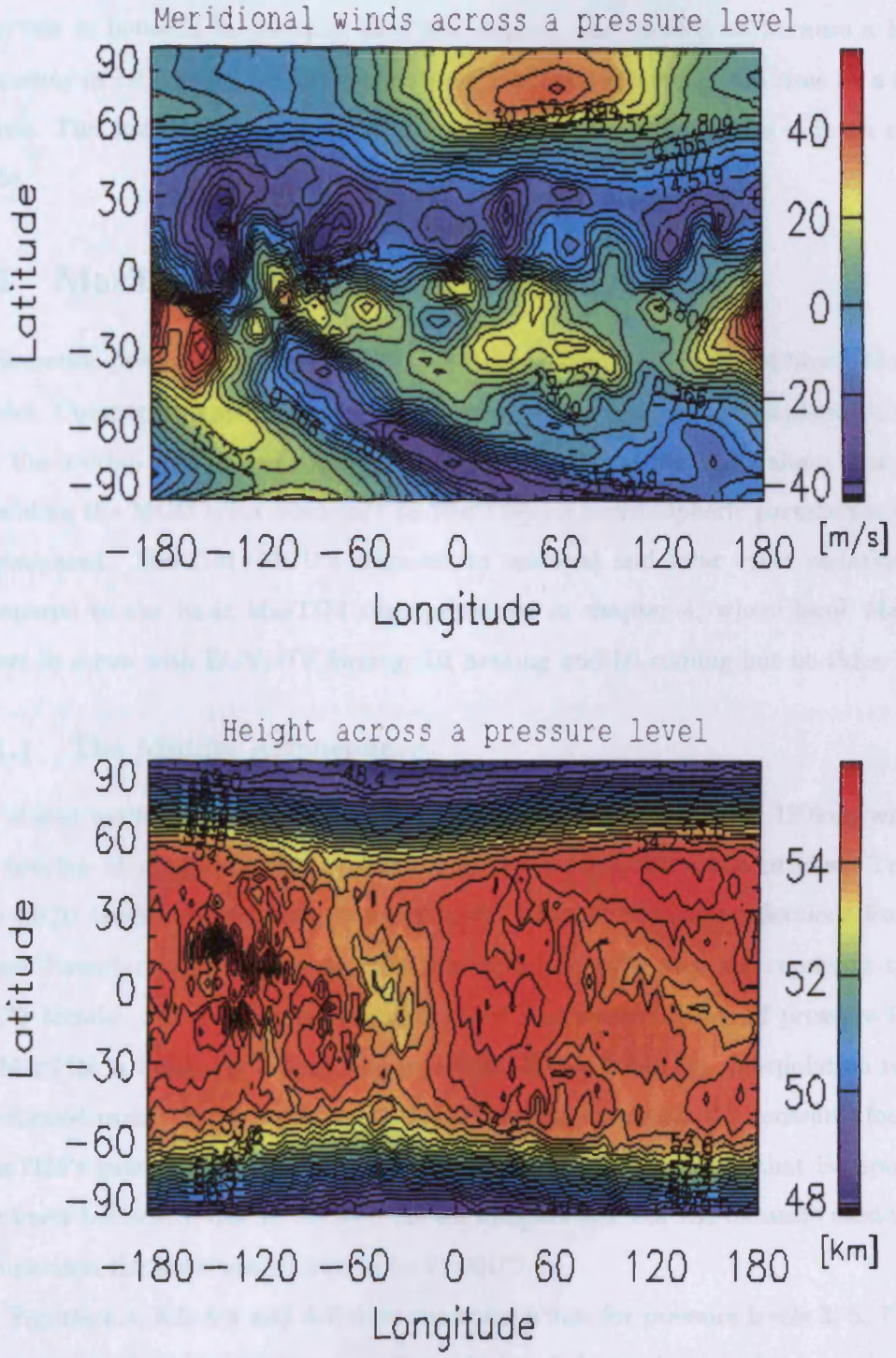

Figure 6.2: MCD height (bottom figure) and meridional winds (top figure) at MarTIM's lower boundary (pressure level 1) at 12:00UT

and enables the creation of datasets that are separated by one hour of local time. These are then read into MarTIM at the corresponding local time. The single hour intervals in between the reading of a new dataset was decided on because a higher frequency of calls to the MCD datasets would increase the model run time by a factor of ten. The combined MarTIM+MCD model is run for 4 days to let it reach steady state.

6.1 MarTIM+MCD: Basic Results

This section presents work investigating the basic nature of the coupled MarTIM+MCD model. Comparisons are presented for the zonal winds at middle atmosphere altitudes; i.e. the overlap region, and contrast MarTIM+MCD and the MCD alone. The effect of adding the MCD lower boundary to MarTIM on thermospheric parameters is also investigated. MarTIM+MCD's response to seasonal and solar cycle variations are compared to the basic MarTIM runs presented in chapter 4, where basic MarTIM refers to a run with EUV/UV forcing, IR heating and IR cooling but no tides.

6.1.1 The Middle Atmosphere

As stated earlier, the MCD's upper altitude limit is set to around 120km, which is an overlap of around 60km between MarTIM and MCD mean altitudes. The top few MCD levels are used as a "sponge layer", [52], to eliminate reflections from the upper boundary and is avoided in this comparison as it may not represent typical MCD trends. For solar minimum at $L_s = 0$, the mean altitude of pressure level 9 in MarTIM is below the upper altitude of the MCD. Using the interpolation routine mentioned earlier, datasets from the MCD were generated for the pressures found at MarTIM's pressure levels 3, 5, 7 and 9. The zonal wind pattern that is input into the lower boundary, due to MCD is shown in figure 6.3. For the datasets used in this comparison the time was chosen to be 12:00UT.

Figures 6.4, 6.5, 6.6 and 6.7 show the zonal winds for pressure levels 3, 5, 7 and 9 for both the MarTIM+MCD results (top plot) and the equivalent plot from the MCD (bottom plot).

MarTIM zonal wind structures across a pressure level are shown to depart from the MCD equivalent zonal wind structure plots as altitude increases. At pressure level 3,

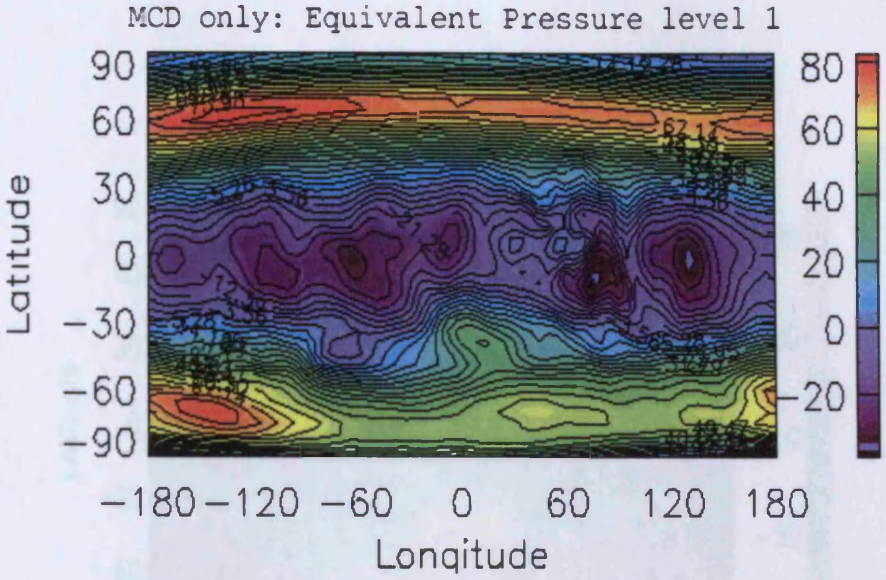

Figure 6.3: MCD zonal wind velocity that is input at MarTIM's lower boundary (pressure level 1) at 12:00UT

shown in figure 6.4, MarTIM's large scale zonal wind structures generally agree with the MCD. Both show a general eastward flow at high latitudes and westward flows around the equator. At pressure level 5, figure 6.5, the MarTIM starts to exhibit a different zonal wind structure compared to the MCD. There are still eastward flows at high latitudes similar to the MCD, but these form larger scale structures that join up at mid-latitudes, whereas the MCD shows predominantly westward flows at mid-latitudes. Pressure level 7, figure 6.6, shows large scale zonal winds structures in MarTIM that are similar to the MCD zonal wind structures. MCD shows eastward flows at -130°, +60° and +120° latitude, similar structures are present in the MarTIM plots, although they are much more dominant. Figure 6.7 at pressure level 9 is fairly similar to figure 6.6 in that the mid-latitude zonal wind structures are more dominant in the MarTIM plots. The structures seen in MarTIM are close to what is seen at higher altitude pressure levels in MarTIM.

These figures have shown that differences occur in the zonal wind structure between MCD and MarTIM+MCD as altitude increases. However a point to note is that the magnitudes of the winds are very similar for the MCD and MarTIM in the lower pressure levels but MarTIM's decrease as altitude increases. This shows that some the energy and momentum input at the lower boundary by MCD is dissipated slightly

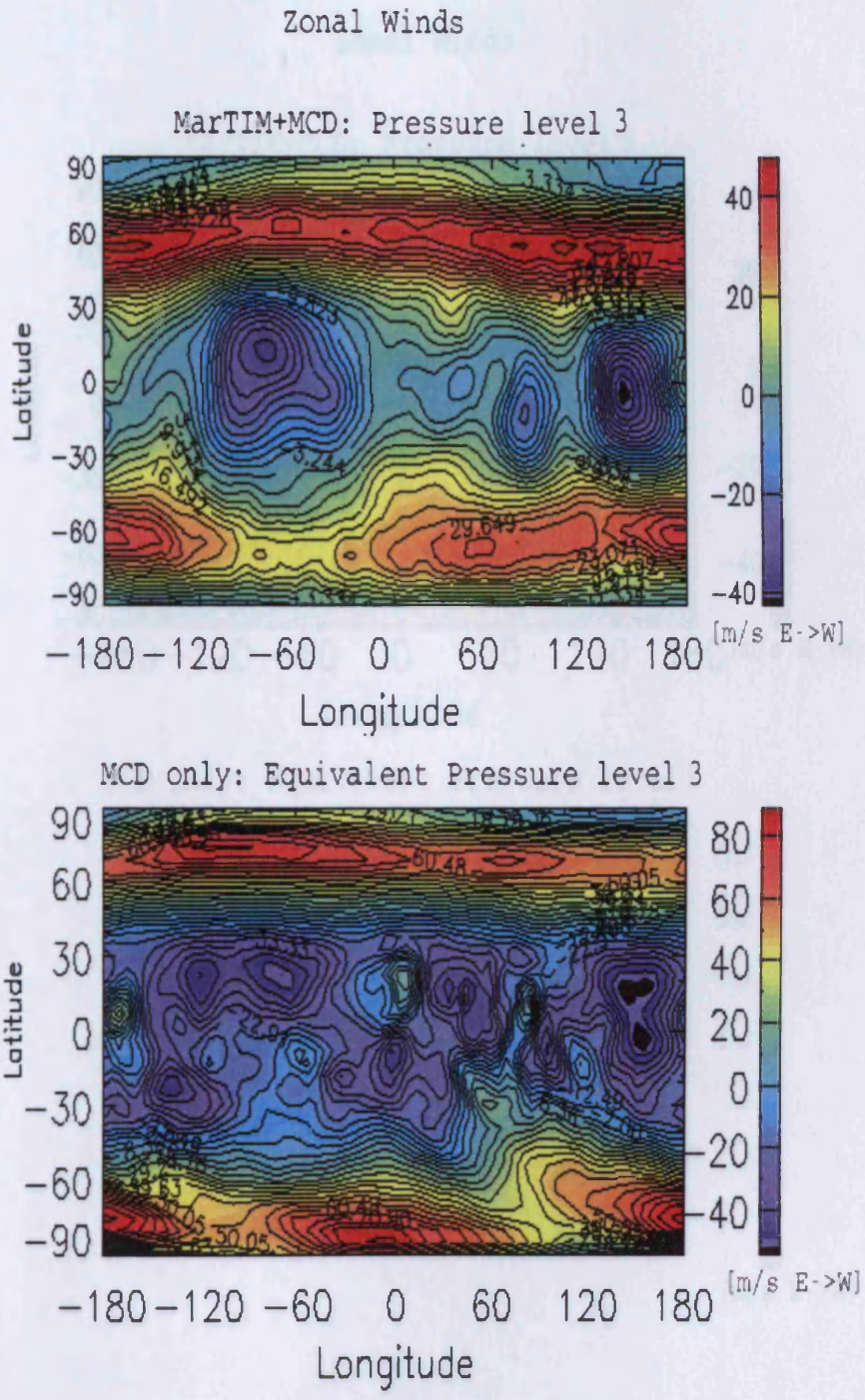

Figure 6.4: MarTIM+MCD zonal wind velocity (top) and the MCD zonal wind velocity (bottom) plotted across the equivalent MarTIM pressure level 3

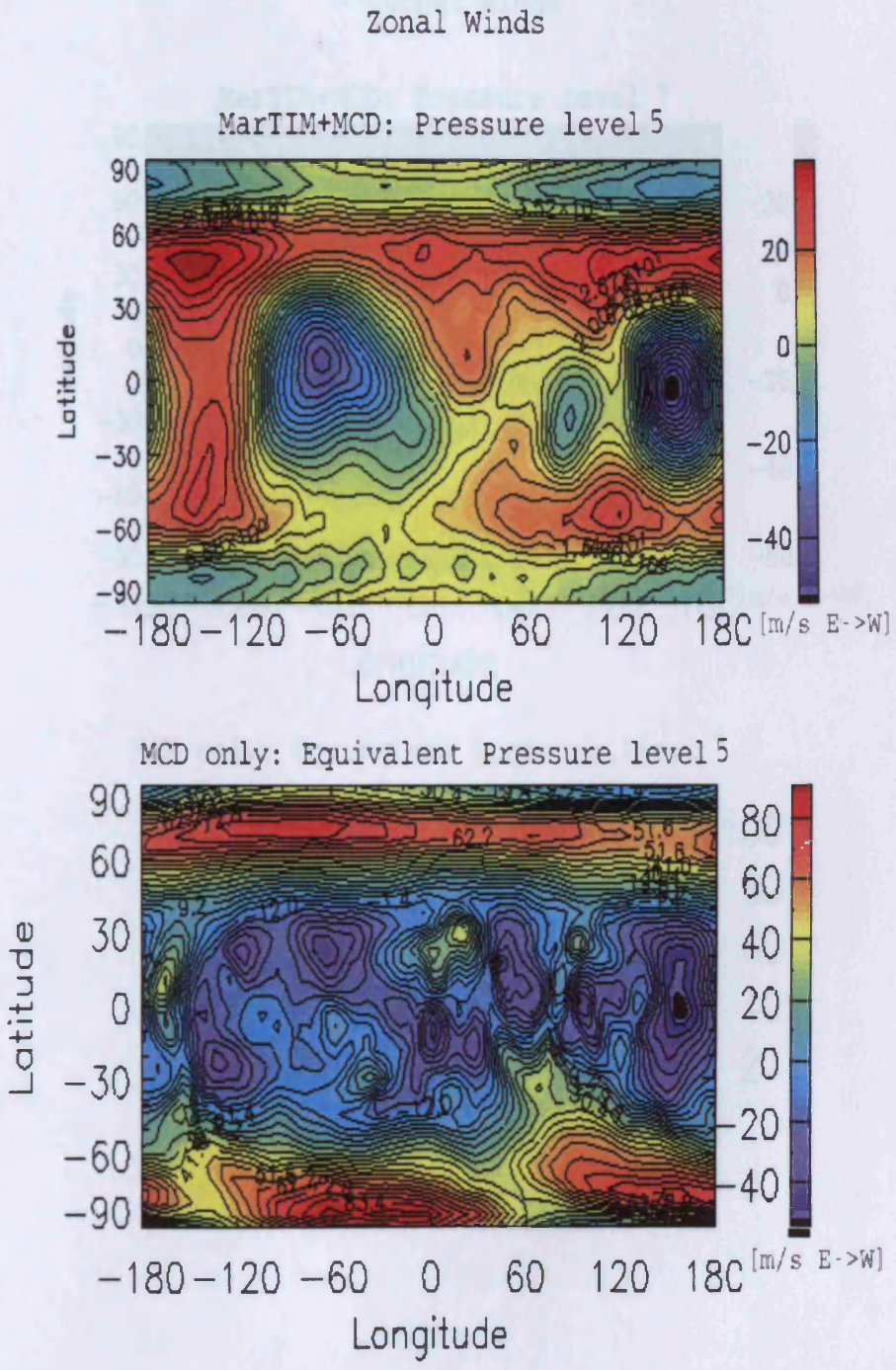

Figure 6.5: MarTIM+MCD zonal wind velocity (top) and the MCD zonal wind velocity (bottom) plotted across the equivalent MarTIM pressure level 5

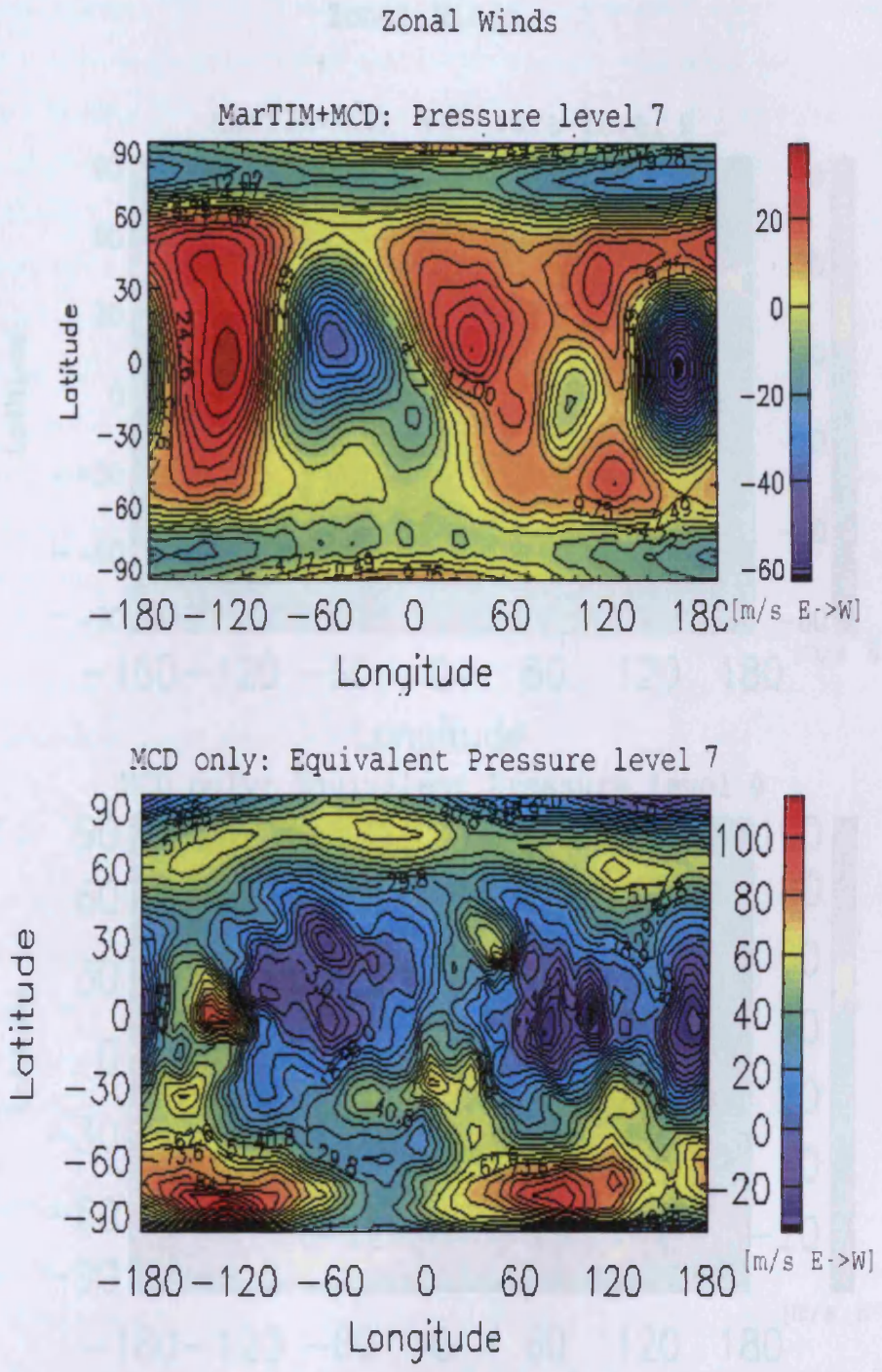

Figure 6.6: MarTIM+MCD zonal wind velocity (top) and the MCD zonal wind velocity (bottom) plotted across the equivalent MarTIM pressure level 7

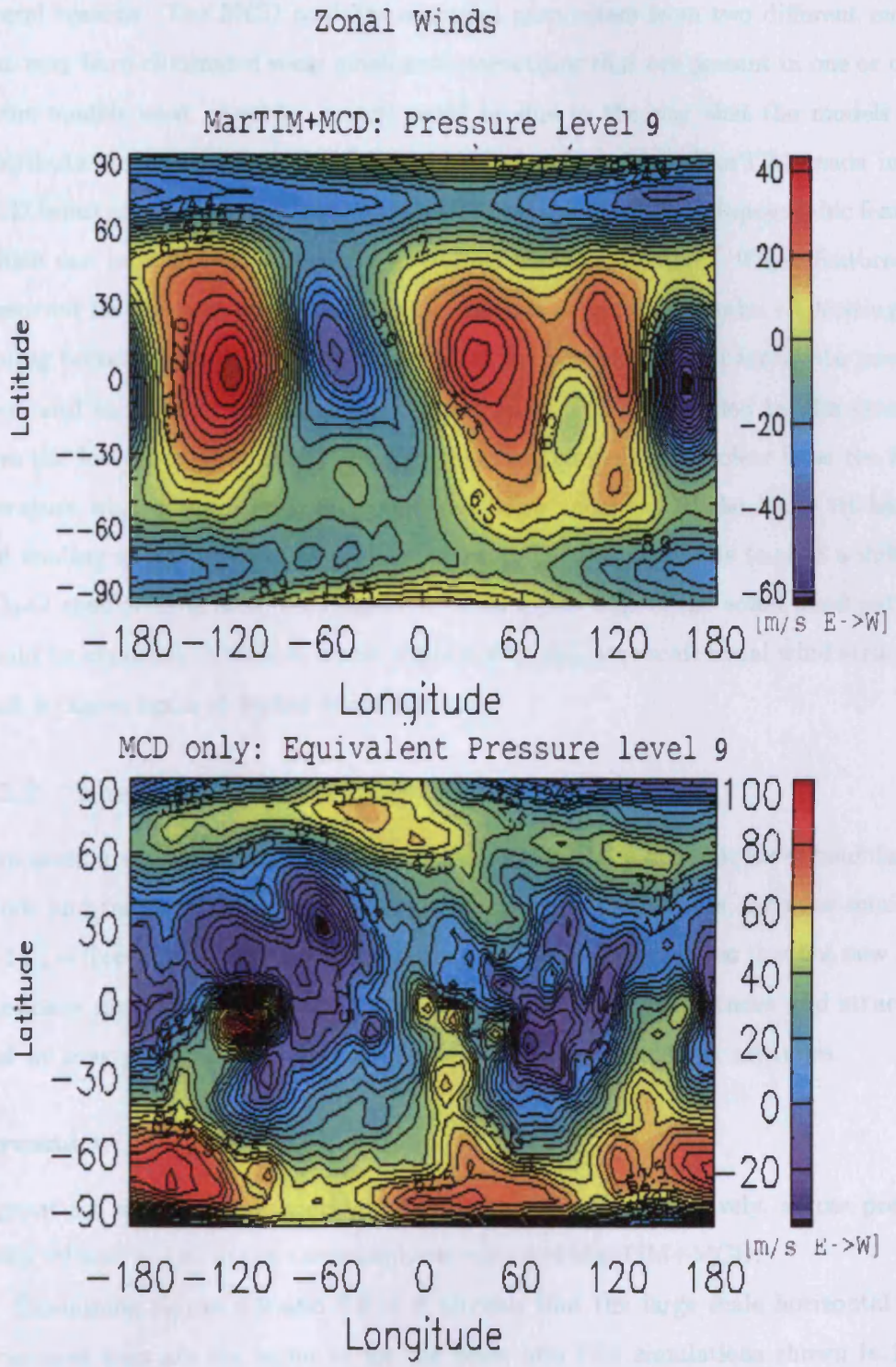

Figure 6.7: MarTIM+MCD zonal wind velocity (top) and the MCD zonal wind velocity (bottom) plotted across the equivalent MarTIM pressure level 9

in MarTIM+MCD. The differences in the large scale zonal structure could be due to several reasons. The MCD contains averaged parameters from two different models that may have eliminated some small scale structures that are present in one or other of the models used. Another reason could be due to the way that the models that contribute to MCD calculate infrared heating and cooling. MarTIM reads in the MCD input at pressure level one. This input contains artifacts of topographic features (which can be seen in the height and vertical wind parameters). These features are conserved for the bottom few pressure levels, but at higher altitudes IR heating and cooling becomes important. This would alter the height variation across the pressure level, and as a result the parameters would not only be controlled by the variation from the lower boundary input but also the IR forcing. It is not clear from the MCD literature what form of IR heating and cooling is included. If the MCD IR heating and cooling effects increase at a different altitude from MarTIMs (e.g. if a different CO_2-O coefficient is used, see chapter 4) then differences in the zonal wind patterns would be expected. This idea would explain why the large scale zonal wind structures start to agree again at higher altitudes.

6.1.2 Thermospheric Structures

This section examines the effects of the introduction of the dynamic lower boundary on winds and temperature structures at upper atmosphere altitudes, for solar minimum and $L_s = 0$ conditions. We have already seen in the previous section that the new lower boundary input introduces differences in the zonal wind magnitudes and structures and we may expect that there will also be an effect at the higher altitudes.

Dynamics

Figures 6.8 and 6.9 show meridional and zonal winds, respectively, across pressure levels 29 and 21 i.e. in the thermospheric region of MarTIM+MCD.

Examining figures 6.9 and 6.8 it is obvious that the large scale horizontal wind structures seen are the same as for the basic MarTIM simulations shown in figure 3.10. The presence of a lower boundary has introduced small scale features into the horizontal wind plots seen in figures 6.9 and 6.8. The main change in the horizontal winds with the introduction of the MCD lower boundary is the increase in the magni-

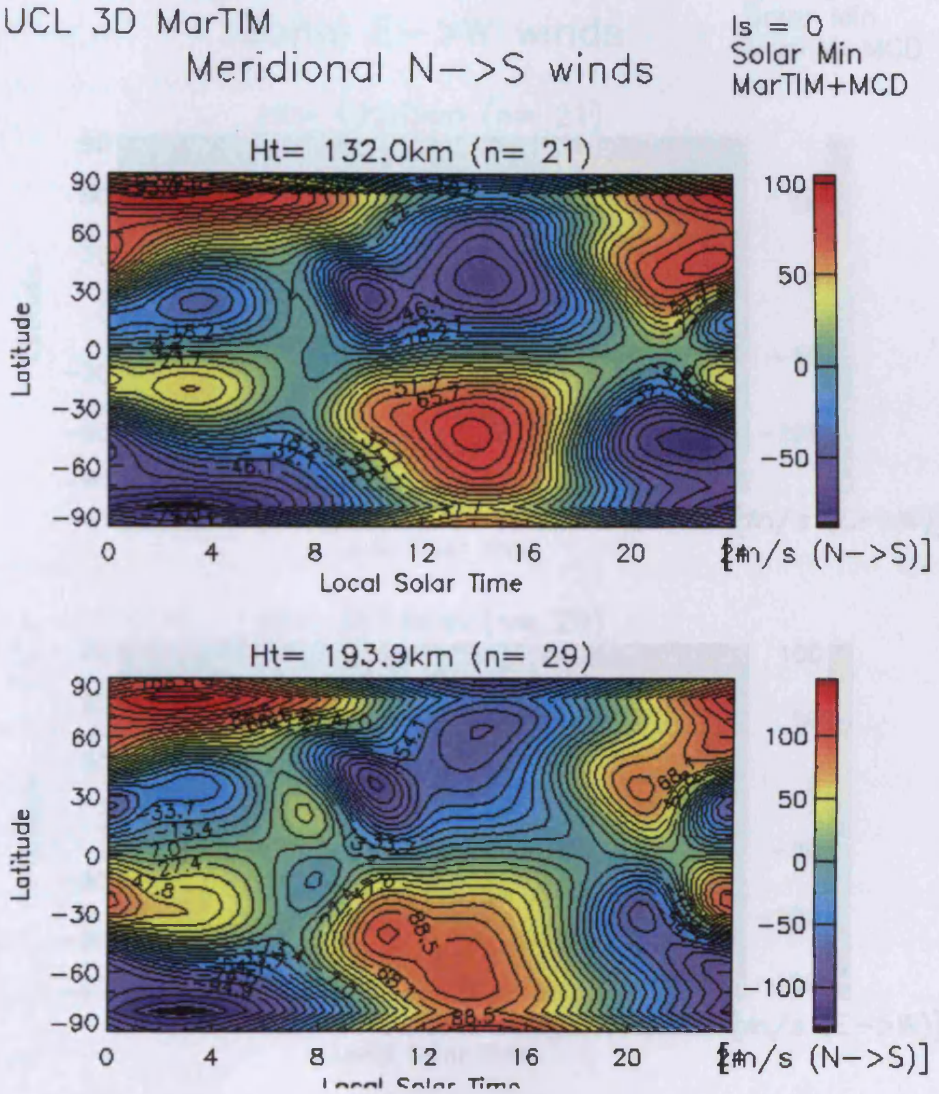

Figure 6.8: Meridional wind velocity plots, positive southward, across pressure levels at thermosphere mean altitudes for solar minimum and L_s=0 conditions at 12:00UT. MarTIM+MCD simulation.

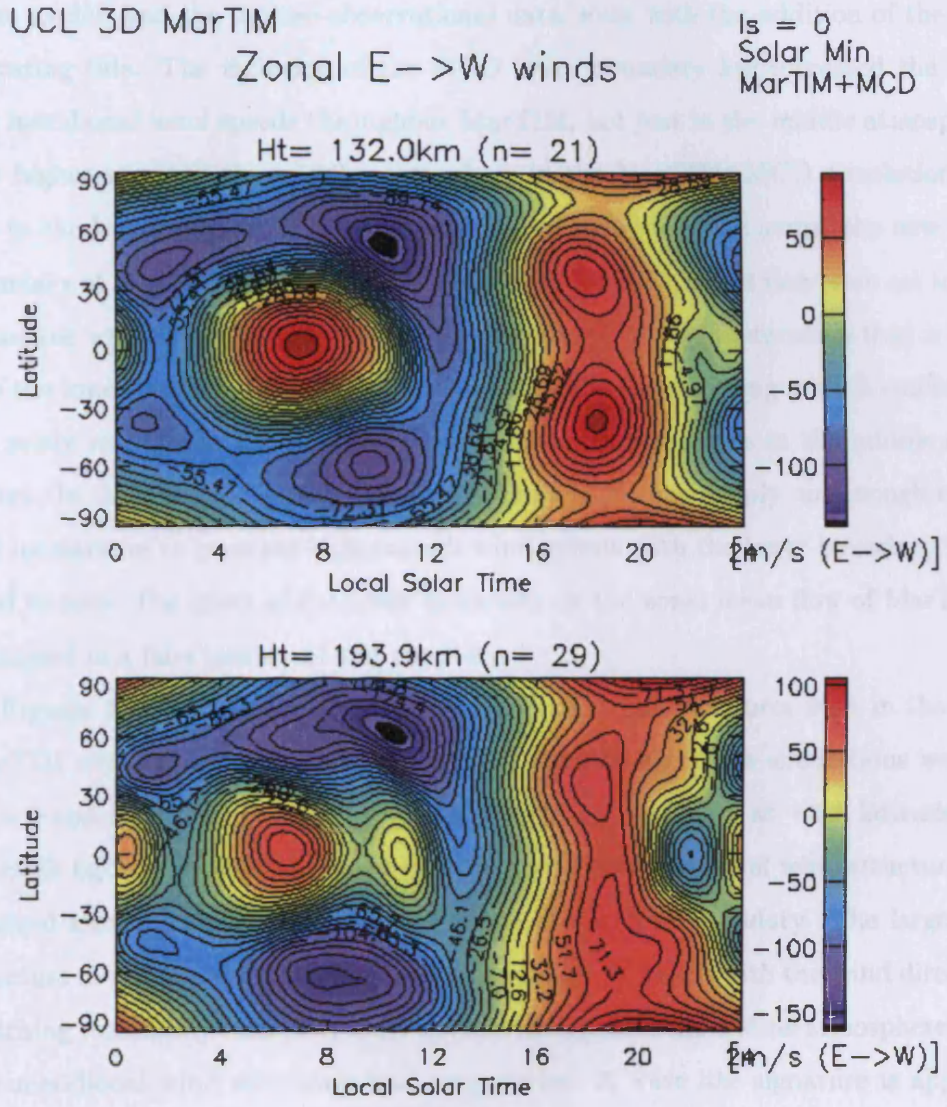

Figure 6.9: Zonal wind velocity plots, positive eastward, across pressure levels at thermosphere mean altitudes for solar minimum and L_s=0 conditions at 12:00UT. MarTIM+MCD simulation.

tudes of the winds. There has been an increase from $\pm 60 ms^{-1}$ to $\pm$ $140 ms^{-1}$ for the meridional winds at pressure level 29 and an increase from $\pm 60 ms^{-1}$ to $+100 ms^{-1}$ and $-160 ms^{-1}$ for the zonal winds at pressure level 29. The wind speeds for the middle atmosphere of MarTIM were, in initial comparisons, found to be too low compared with other models and the limited observational data, even with the addition of the (2,2) migrating tide. The inclusion of the MCD lower boundary has increased the zonal and meridional wind speeds throughout MarTIM, not just in the middle atmosphere. The higher winds in the middle atmosphere in the MarTIM+MCD simulations are due to the large winds that are now present and their variation across the new lower boundary of MarTIM, whereas in the basic MarTIM simulations they were set to zero across the whole lower boundary. The additional energy and momentum that is input into the lower boundary of MarTIM means that the solar heating and IR cooling are not solely responsible for generating the total horizontal winds in the middle atmosphere. In the basic model this was the case and there was simply not enough energy and momentum to generate high enough wind speeds with the lower boundary values fixed to zero. The effect of the lower boundary on the zonal mean flow of MarTIM is examined in a later section of this chapter.

Figures 6.10 and 6.11 compare the horizontal wind structures seen in the basic MarTIM simulations to the MarTIM+MCD simulations. Both simulations were for $L_s = 0$ and solar minimum, the plots show longitude vs height at $+20°$ latitude.

Both figure 6.10 and 6.11 show that the meridional and zonal wind structures are changed significantly by the inclusion of the MCD lower boundary. The large scale structure in the upper atmosphere is not changed very much, with the wind directions matching reasonably well. The most obvious change is in the middle atmosphere zonal and meridional wind structures and magnitudes. A wave like signature is apparent in the MarTIM+MCD middle atmosphere horizontal wind plots. This is most probably due to the tidal features, which are present in the MCD, propagating into the thermosphere via the lower boundary.

Energetics

The effect of the MCD lower boundary on the temperature structure of MarTIM is examined in this section. Figure 6.12 shows the temperature across pressure levels

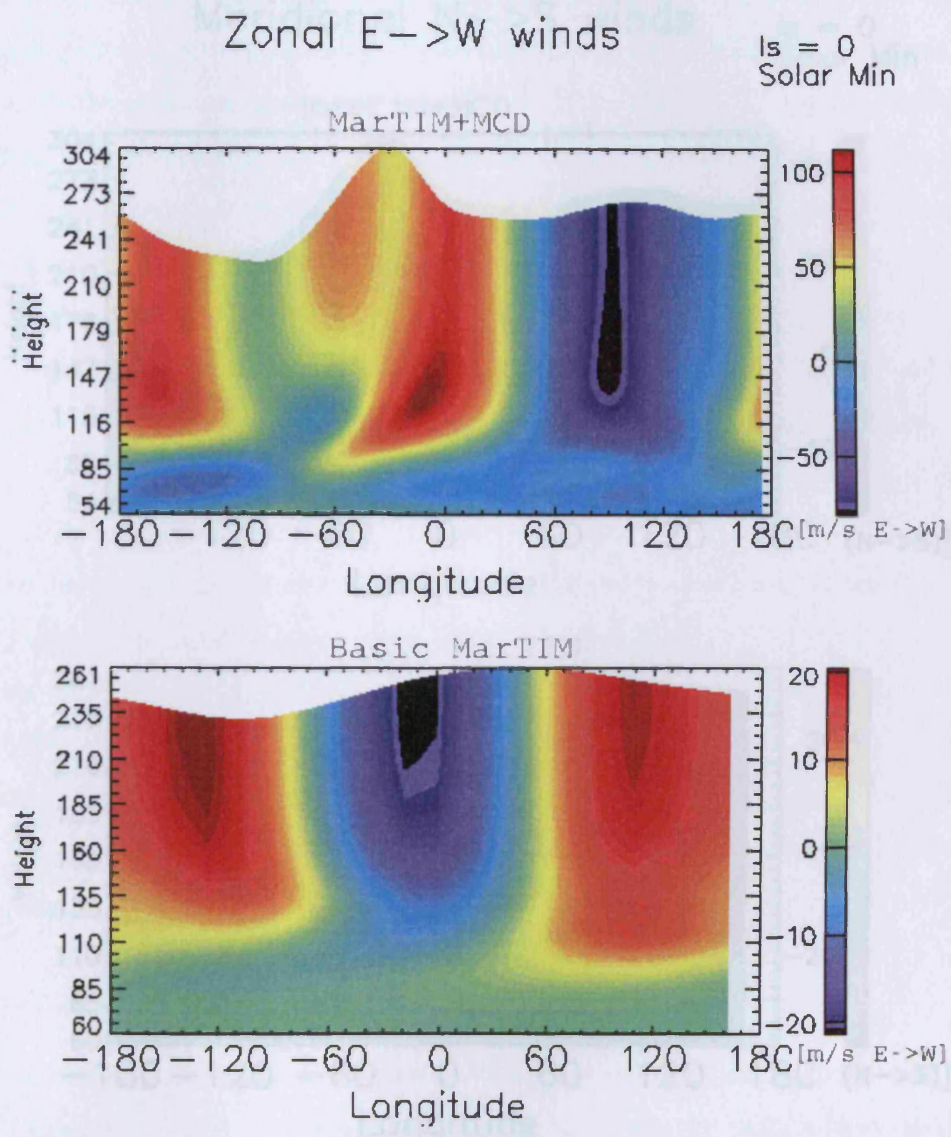

Figure 6.10: Longitude vs height plot of the zonal winds at 12:00UT +20° latitude for MarTIM+MCD (top) and basic MarTIM (bottom) for solar minimum and $L_s = 0$ conditions.

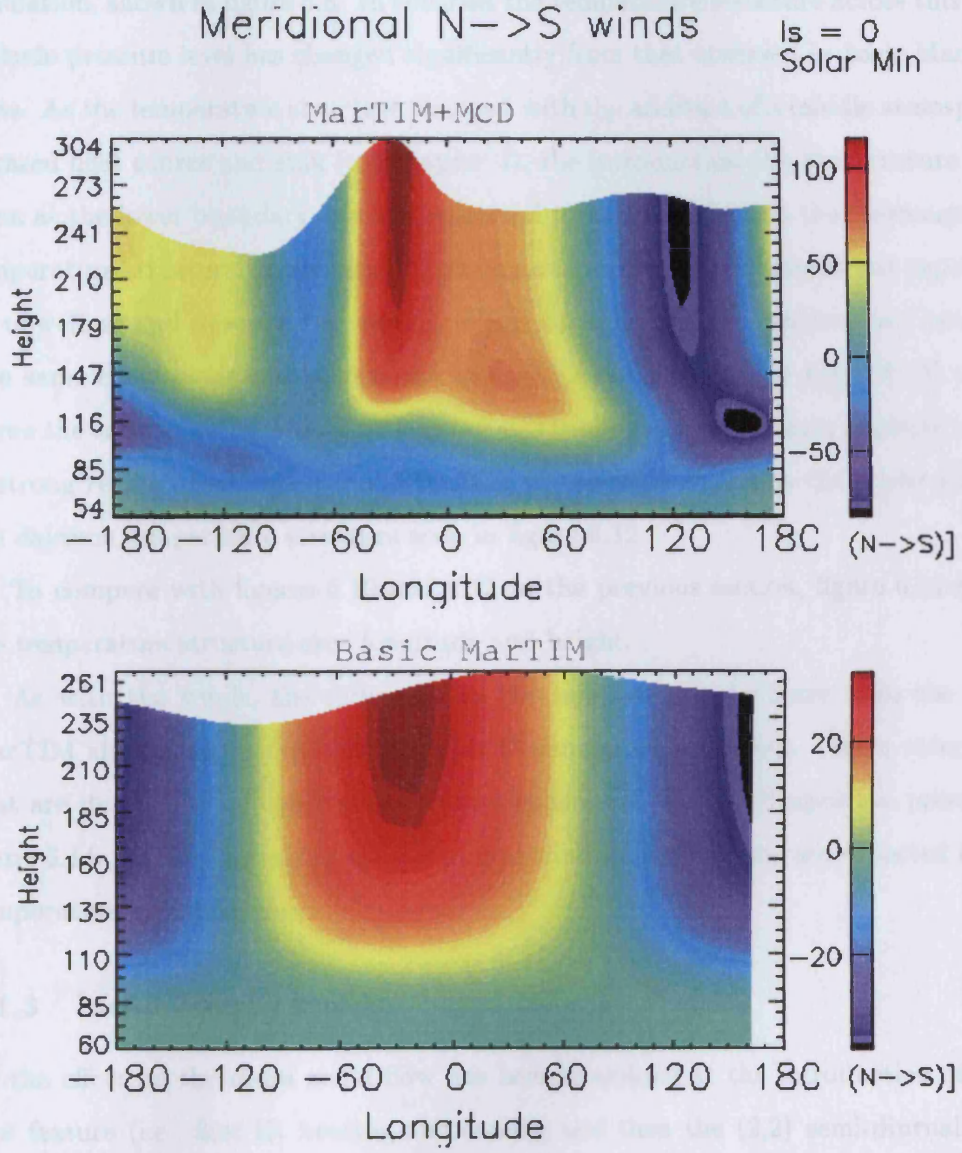

Figure 6.11: Longitude vs height plot of the meridional winds at 12:00UT +20° latitude for MarTIM+MCD (top) and basic MarTIM (bottom) for solar minimum and $L_s = 0$ conditions.

29 and 21 (corresponding to the thermospheric region of MarTIM+MCD) for solar minimum conditions and $L_s = 0$.

The average magnitude of the temperatures seen in the pressure level 29 plot in figure 6.12 are only slightly higher than for the same conditions in a basic MarTIM simulation, shown in figure 3.8. In contrast the temperature structure across this high altitude pressure level has changed significantly from that observed in basic MarTIM plots. As the temperature structure changed with the addition of a middle atmosphere infrared heat source and sink (see chapter 4), the introduction of a temperature variation at the lower boundary was also expected to have an effect on the thermospheric temperature structure. In chapter 4 the temperature structure observed was explained by upwelling and downwelling vertical winds causing adiabatic cooling and heating. The same conclusions can be reached here. This is backed up by figure 6.13, which shows the corresponding adiabatic heating and cooling across the same pressure levels. A strong region of adiabatic cooling occurs in the same region as the cooler spot in the daytime temperature structure seen in figure 6.12.

To compare with figures 6.10 and 6.11 in the previous section, figure 6.14 shows the temperature structure over longitude and height.

As with the winds, the difference in the temperature structure from the basic MarTIM simulation to the MarTIM+MCD simulation is evident. Again structures that are due to the influence of lower atmosphere via the MCD input are present in figure 6.14. As they appear in the horizontal wind structures they are expected in the temperature structure also.

6.1.3 Mean Zonal Flow

As the effect on the mean zonal flow has been examined at the introduction of each new feature (i.e. first IR heating and cooling and then the (2,2) semi-diurnal tide) the same is done here for the introduction of the MCD lower boundary. Figure 6.15 shows the zonal mean horizontal wind structures for MarTIM+MCD simulations. The conditions are for solar minimum and $L_s = 0$.

Overall the zonal means of the meridional and zonal wind speeds are much larger than seen in the basic simulations. Table 6.2 shows the maximum and minimum zonal mean wind speeds over all altitudes for the basic MarTIM simulation, with

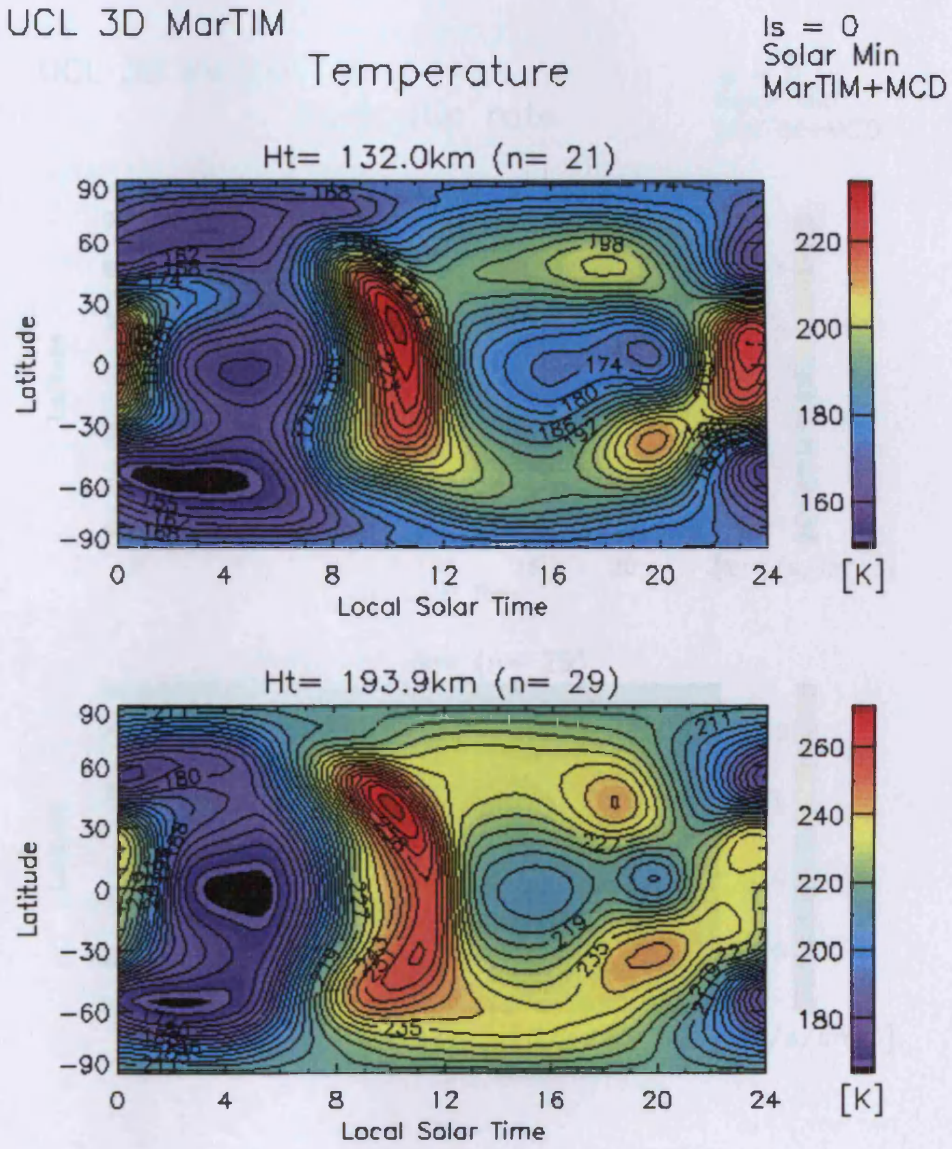

Figure 6.12: Temperature plots across pressure levels at upper and middle atmosphere mean altitudes for solar minimum and L_s=0 conditions at 12:00UT. Taken from MarTIM with MCD lower boundary.

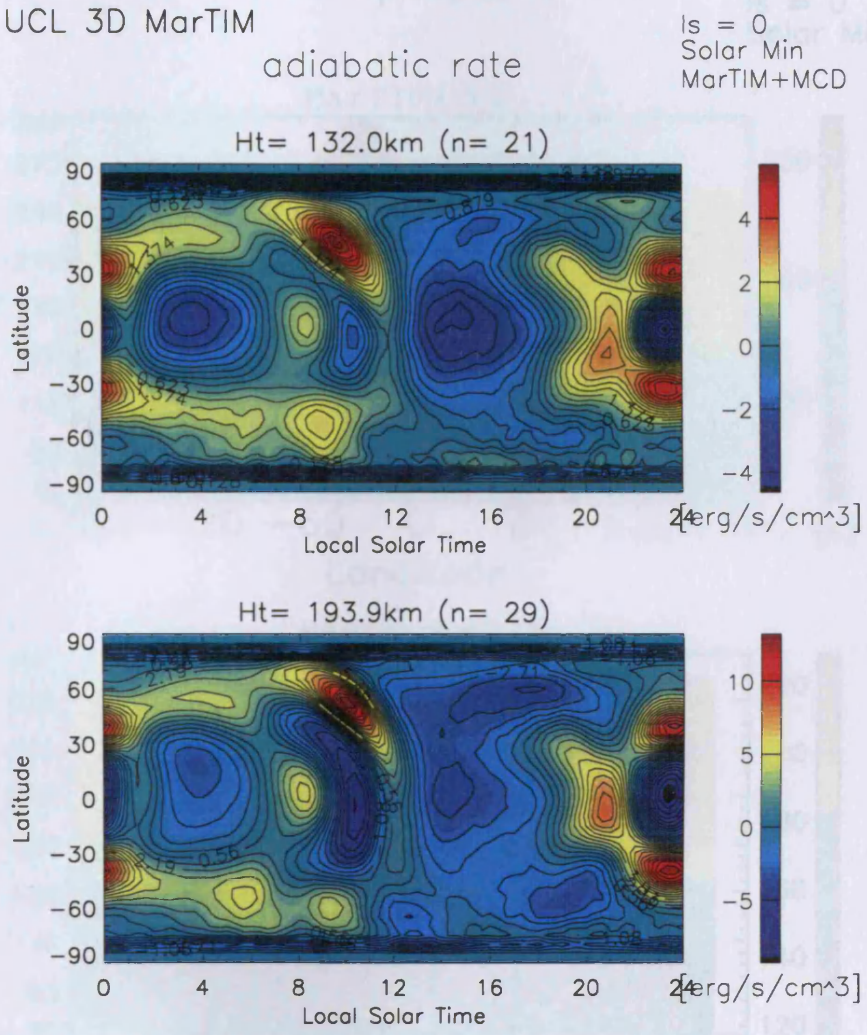

Figure 6.13: Adiabatic heating/cooling plots across pressure levels at upper and middle atmosphere mean altitudes for solar minimum and L_s=0 conditions at 12:00UT. Taken from MarTIM with MCD lower boundary.

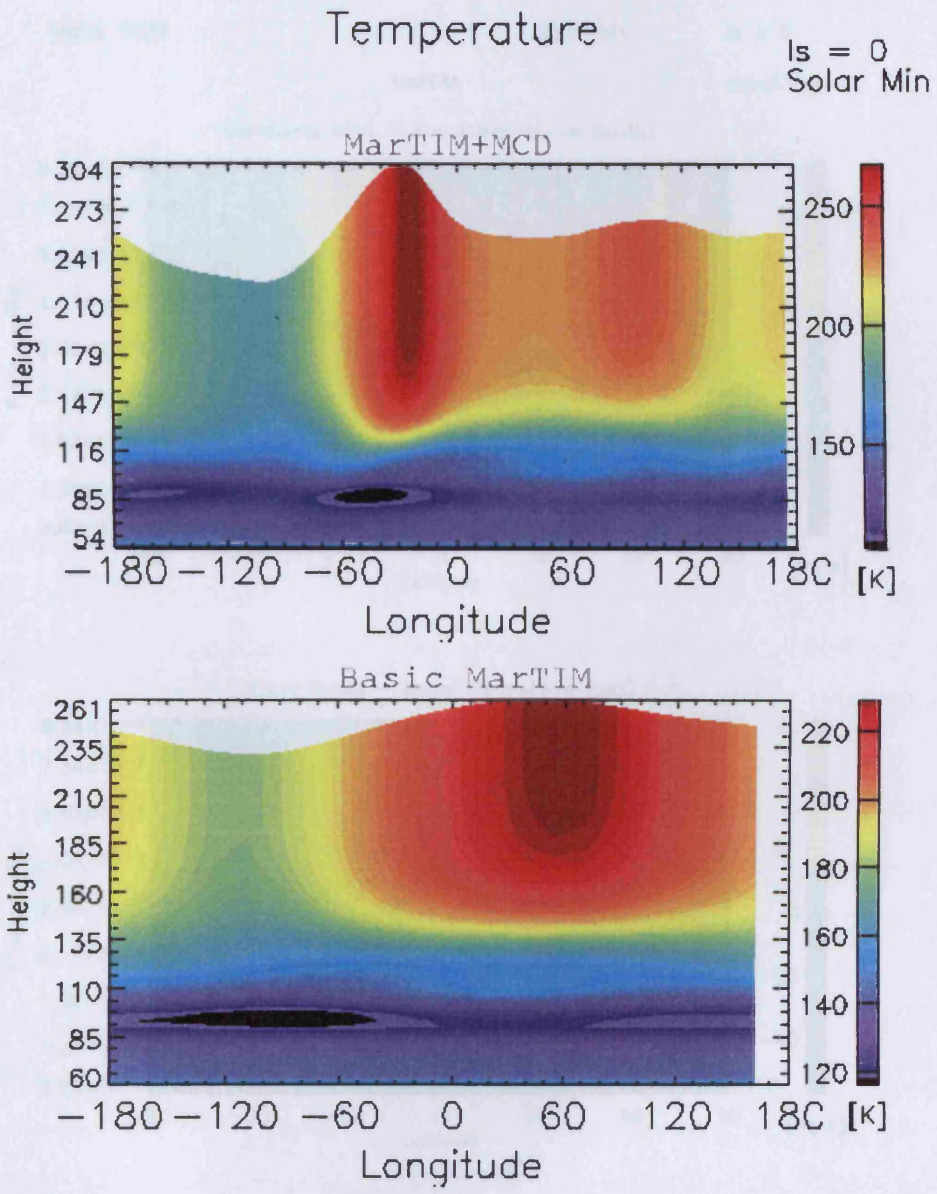

Figure 6.14: Longitude vs height plot of the temperature at 12:00UT +5° latitude for MarTIM+MCD (top) and basic MarTIM (bottom) for solar minimum and $L_s = 0$ conditions.

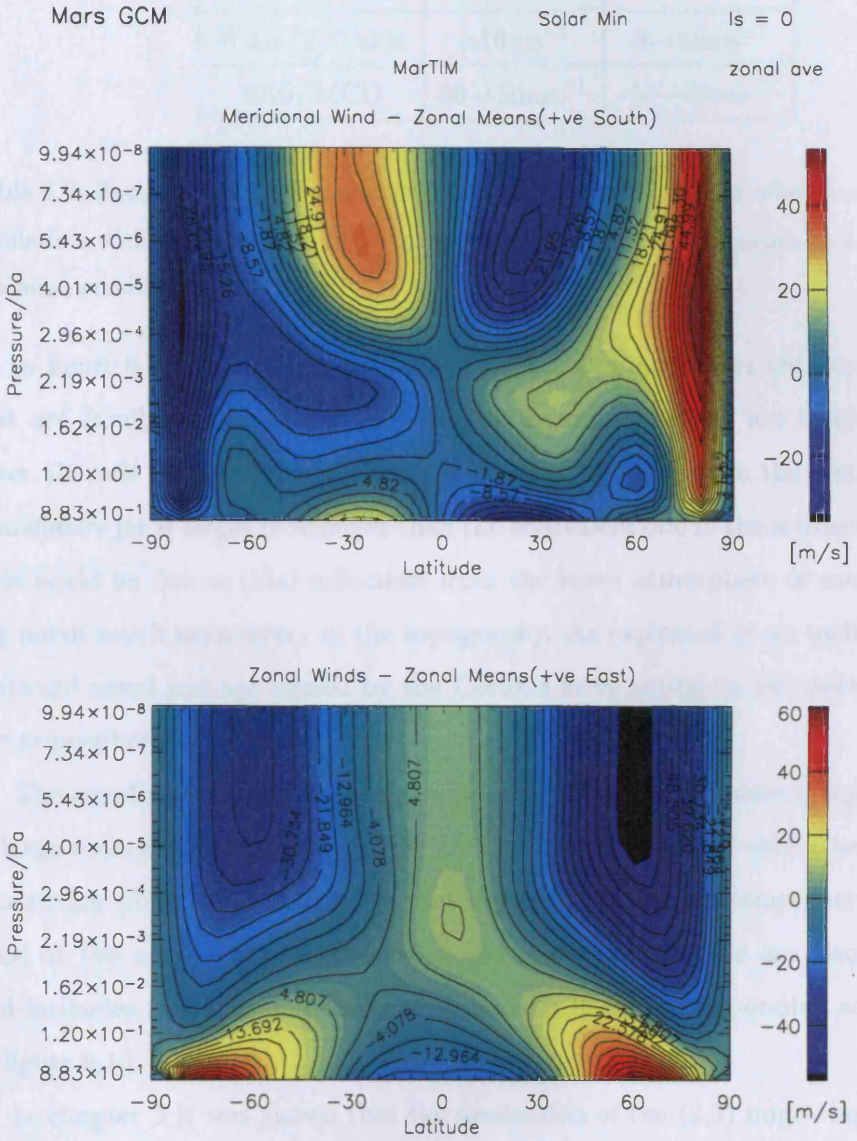

Figure 6.15: Zonally averaged meridional(top) and zonal (bottom) wind velocity plots from a MarTIM+MCD simulation, for L_s=0 and solar minimum conditions

tides simulation and a simulation with the MCD lower boundary.

Simulation	Meridional	Zonal
Basic	$\pm 7 ms^{-1}$	$0 \rightarrow 20 ms^{-1}$
With (2,2) tide	$\pm 16 ms^{-1}$	$-8 \rightarrow 22 ms^{-1}$
With MCD	$30 \rightarrow 50 ms^{-1}$	$-50 \rightarrow 60 ms^{-1}$

Table 6.2: Zonal mean meridional and zonal wind speeds over all altitudes for a basic MarTIM simulation, with tides and with MCD lower boundary. All simulations are for $L_s = 0$ and solar minimum conditions

In figure 6.15 the zonal mean plot of the zonal winds shows the two eastward jets that are familiar from figures 3.11 and 4.16, although they are constrained to the lower altitude pressure levels. There is a slight asymmetry in the jets, the northern hemisphere jet is larger is stronger than the equivalent one in the southern hemisphere. This could be due to tidal influences from the lower atmosphere or even remnants of the north south asymmetry in the topography. As explained in an earlier chapter the eastward zonal jets are caused by the Coriolis force acting on the poleward winds in the atmosphere.

The zonally averaged meridional wind plot in figure 6.15 shows a significant change in large scale structure in the middle atmosphere compared to earlier work. There are two strong polar wind structures that dominate the whole atmosphere - southward wind at the north pole, northward at the south pole. There are also structures at mid-latitudes that can be related to those seen in the corresponding zonal wind plot in figure 6.15.

In chapter 5 it was shown that the dissipation of the (2,2) migrating tide changed the meridional zonal mean structure in the middle atmosphere. Figure 6.15 shows that the introduction of the MCD lower boundary affects the structure right up to the thermosphere. The influence of the lower atmosphere (and the tides present there) introduced via MCD, are affecting the thermospheric structure.

In order to clearly demonstrate the effect of the MCD lower boundary on the mean zonal flow on MarTIM, difference plots have been generated. Figures 6.16 and 6.17 show zonally averaged difference plots for meridional and zonal wind velocities. The

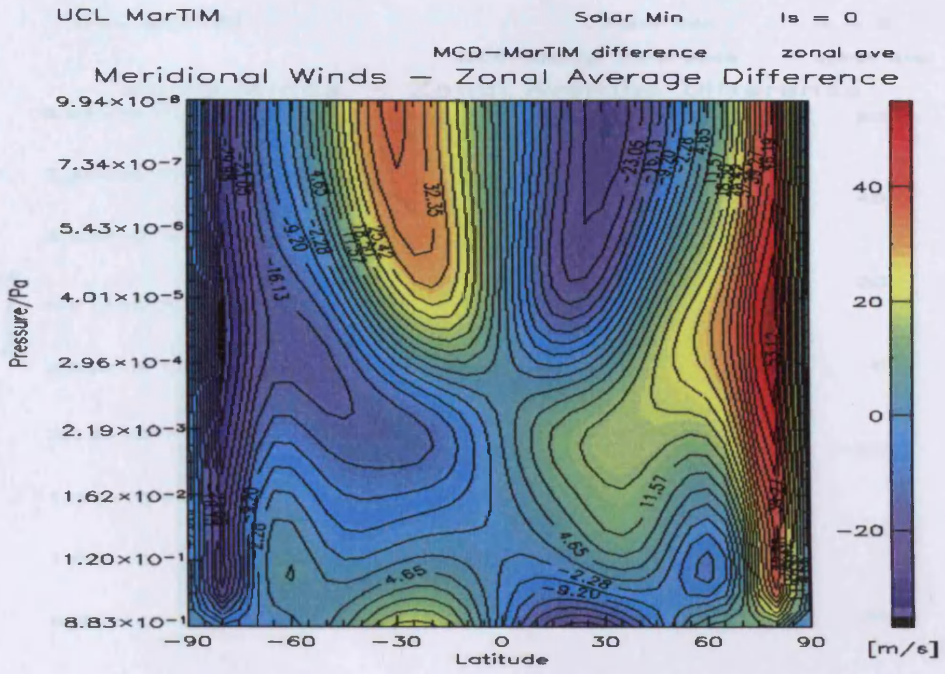

Figure 6.16: Zonally averaged meridional wind speed difference plot, for L_s=0 and solar minimum conditions

MarTIM results used are those with the MCD included and subtracted from a basic MarTIM simulation (EUV/UV/IR heating, no tides) for the same seasonal and solar conditions.

The difference plots shown in figures 6.16 and 6.17 underline the scale of the MCD lower boundary's effect on the mean zonal flow in MarTIM. Subtracting the basic zonal mean flows from the MarTIM+MCD flows has resulted in little change.

As stated before, the main motivation of incorporating the MCD as the lower boundary to MarTIM was to address the issue of the low horizontal wind speeds in the middle atmosphere. The evidence in this section has shown that higher wind speeds are generated in the middle atmosphere with the inclusion of the MCD lower boundary. This suggests that the original MarTIM lower boundary, where the horizontal winds in the lower boundary were set to zero and the height and pressure fixed, was naive. By having a fixed lower boundary, MarTIM had constrained the magnitudes of the middle atmosphere winds. The lower boundary work has also shown how features in the lower atmosphere, and on the surface, are able to produce influences, that when treated self-consistently, are able to propagate up into the thermosphere and

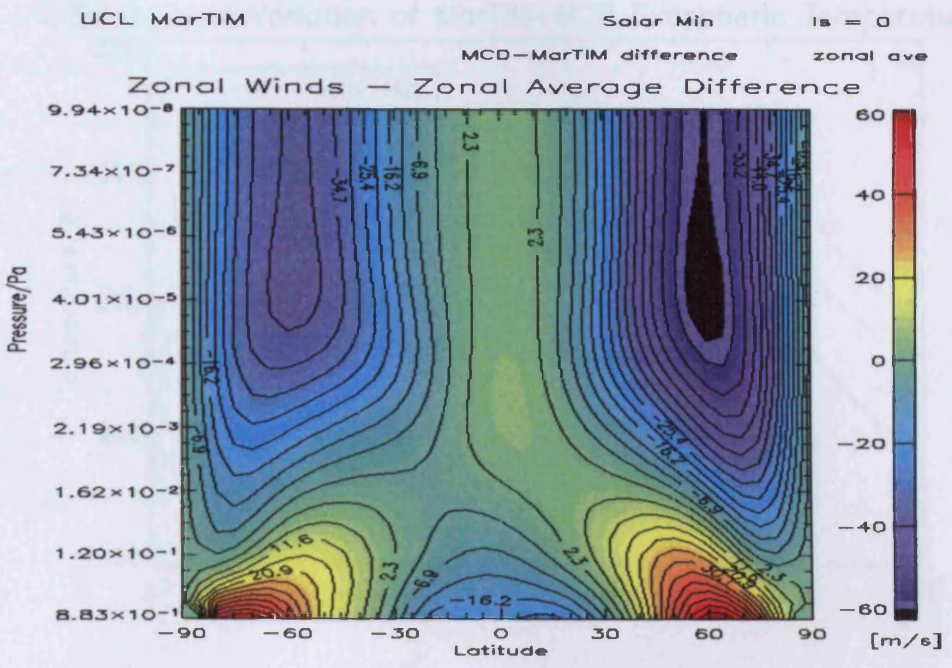

Figure 6.17: Zonally averaged zonal wind speed difference plot, for L_s=0 and solar minimum conditions

significantly change its structure. Further studies with different MCD dust scenarios should demonstrate greater responses in the thermosphere than shown here using the limiting low dust scenario. Increased dust loading would be expected to alter the strength of tides in the lower atmosphere and also the zonal mean gradients, which would feed into MarTIM via the lower boundary.

6.1.4 Seasonal and Solar Cycle Variations: MarTIM+MCD

The diurnal temperature variation over a solar cycle is examined in this section. Figure 6.18 shows the diurnal temperature variation over the course of a solar cycle from a MarTIM+MCD simulation.

Figure 3.6 showed the expected diurnal structure due to EUV/UV heating from a basic MarTIM equinox simulation. In comparison figure 6.18 shows a more complex diurnal structure for the MarTIM+MCD equinox simulation. Instead of the gradual increase in temperature at dawn there is a sudden increase, followed by a double peak. The trough between these peaks is at a temperature that is closer to the basic MarTIM exospheric temperatures. Figure 6.18 illustrates that, despite the strong zon-

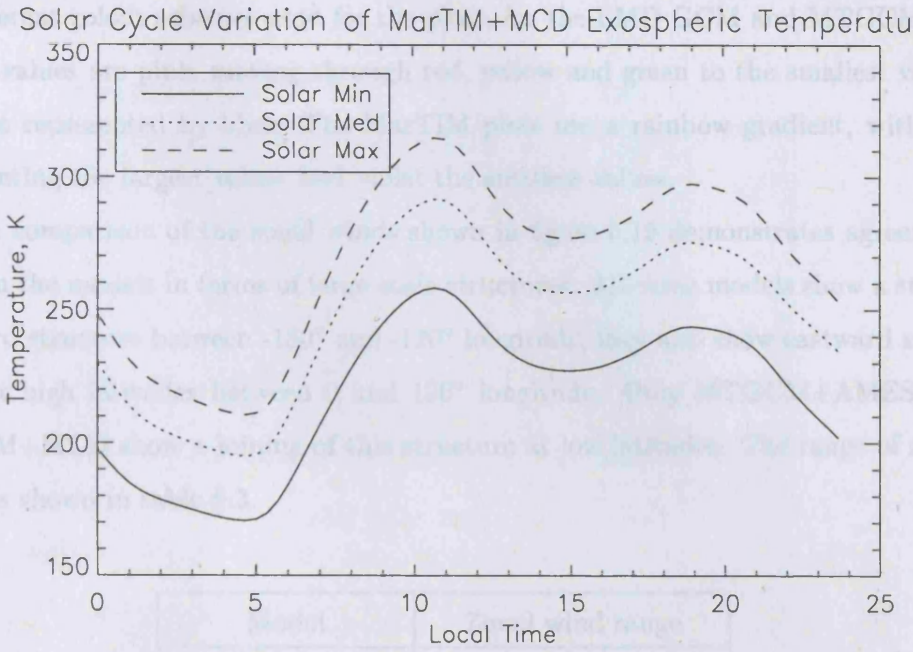

Figure 6.18: The effect of the solar cycle on exospheric temperatures for L_s=0, for MarTIM+MCD simulations, at the sub solar point, pressure=$2.7 \cdot 10^{-7}$Pa)

ally symmetric EUV/UV heating, the influences from the MCD lower boundary still have a profound effect on the temperature structure and magnitude at thermospheric altitudes.

6.2 Model Comparisons

In 2003 an intercomparison workshop was held in Granada, Spain. UCL was invited to provide MarTIM output for comparison with the LMD GCM and the MTGCM+AMES GCM. Each of the models was required to produce output for solar medium conditions and L_s=0. At that time MarTIM did not include the MCD lower boundary. However the MarTIM+MCD has been run for the workshop conditions and some of the results are presented in this section. The full intercomparison plots for the three models are shown in appendix A. This section illustrates the similarities and differences in structure and parameter magnitudes between the three GCMs, which all include lower atmosphere effects.

Figure 6.19 shows the zonal winds at 12:00UT in terms of longitude and latitude at an average height of 200km from MarTIM+MCD, MTGCM+AMES and LMD. There

are different colour schemes used for the plots, for the LMD GCM and MTGCM the largest values are pink, moving through red, yellow and green to the smallest values that are represented by blue. The MarTIM plots use a rainbow gradient, with red representing the largest values and violet the smallest values.

The comparison of the zonal winds shown in figure 6.19 demonstrates agreement between the models in terms of large scale structures. All three models show a strong eastward structure between -180° and -120° longitude, they also show eastward structures at high latitudes between 0 and 120° longitude. Only MTGCM+AMES and MarTIM+MCD show a joining of this structure at low latitudes. The range of zonal winds is shown in table 6.3.

Model	Zonal wind range
MarTIM+MCD	-150ms^{-1} →+100ms^{-1}
MTGCM+AMES	-240ms^{-1}→+160ms^{-1}
LMD GCM	-240ms^{-1}→+240ms^{-1}

Table 6.3: Zonal winds speed ranges at 200km for MarTIM+MCD, MTGCM+AMES and LMD GCM

The LMD GCM has the largest range of zonal winds of the three models. MTGCM+AMES and MarTIM+MCD zonal winds ranges are intermediate.

As there are differences in the wind speeds it is expected that there will be a difference in the distribution and magnitudes of the main sources and sinks of energy in the thermosphere/middle atmosphere region. Figure 6.20 shows the EUV heating distribution in the three models in terms of a longitude-altitude slice at the equator. Figure 6.21 shows the CO_2 cooling distribution in the same format.

Figure 6.20 demonstrates that the EUV heating distribution over local time is the same for all three models, with the peak occurring at noon local time. The main differences are in the magnitude of the heating rate and the altitude coverage. The LMD GCM and MarTIM+MCD agree well with maximum EUV heating rates of around 600K/day, MTGCM+AMES though has a heating rate of 1150K/day, considerably higher. In terms of altitude coverage the LMD GCM maximum heating is concentrated between 130km and 170km, MarTIM+MCD and MTGCM+AMES both cover

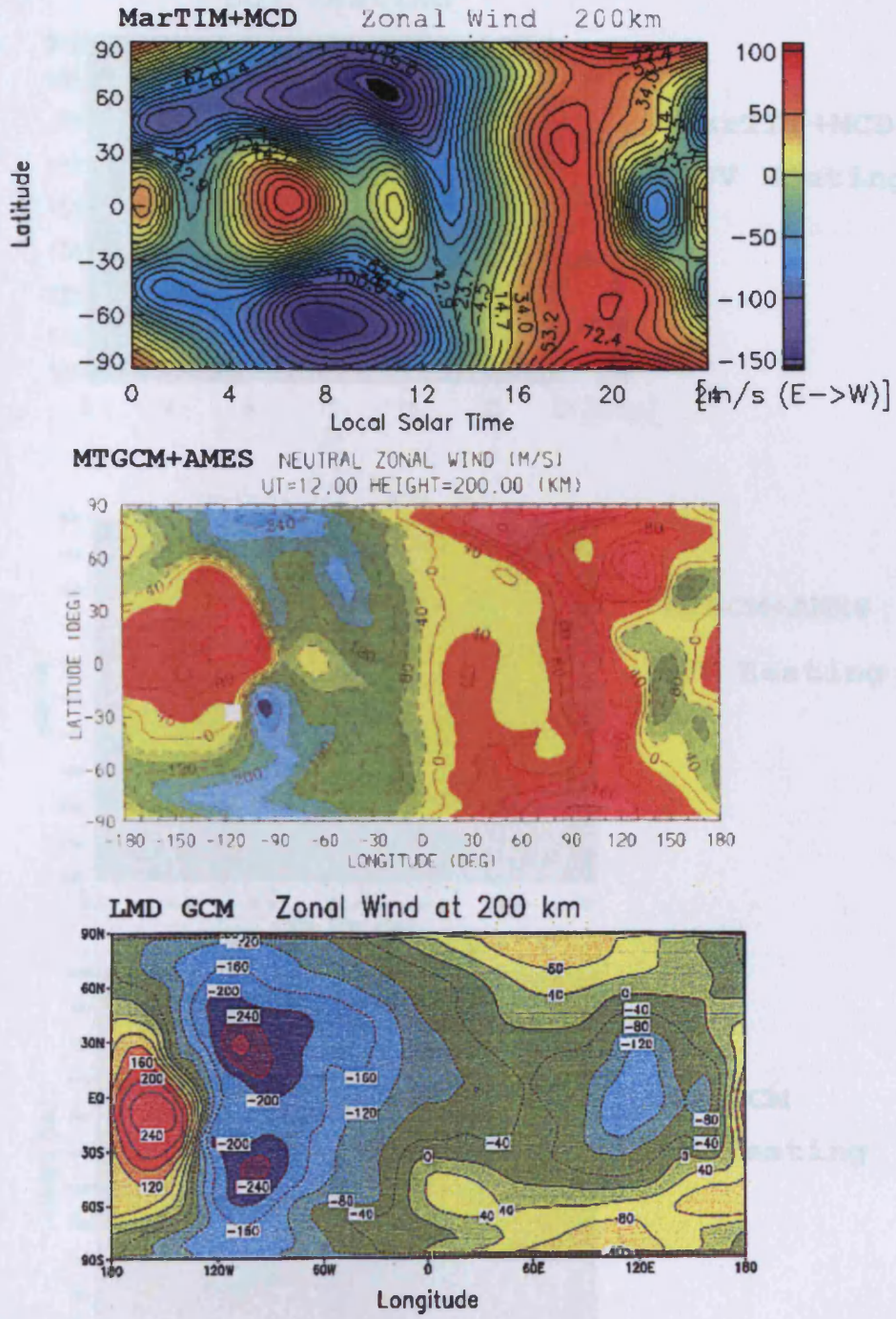

Figure 6.19: Zonal winds at 200km in terms of longitude and latitude. MarTIM (top), MTGCM+AMES (middle) and LMD GCM (bottom)

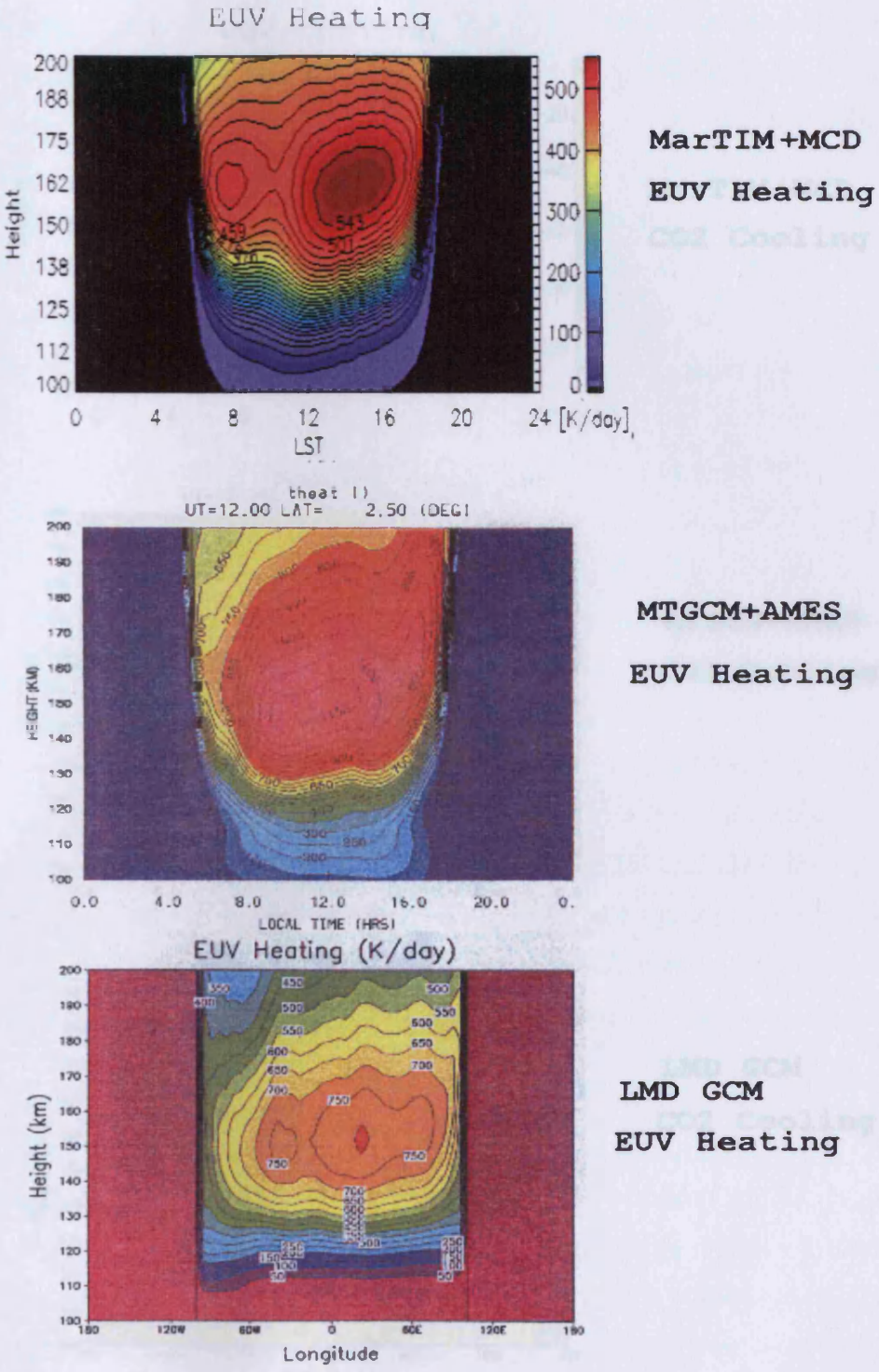

Figure 6.20: EUV heating in terms of altitude and longitude at the equator. MarTIM (top), MTGCM+AMES (middle) and LMD GCM (bottom)

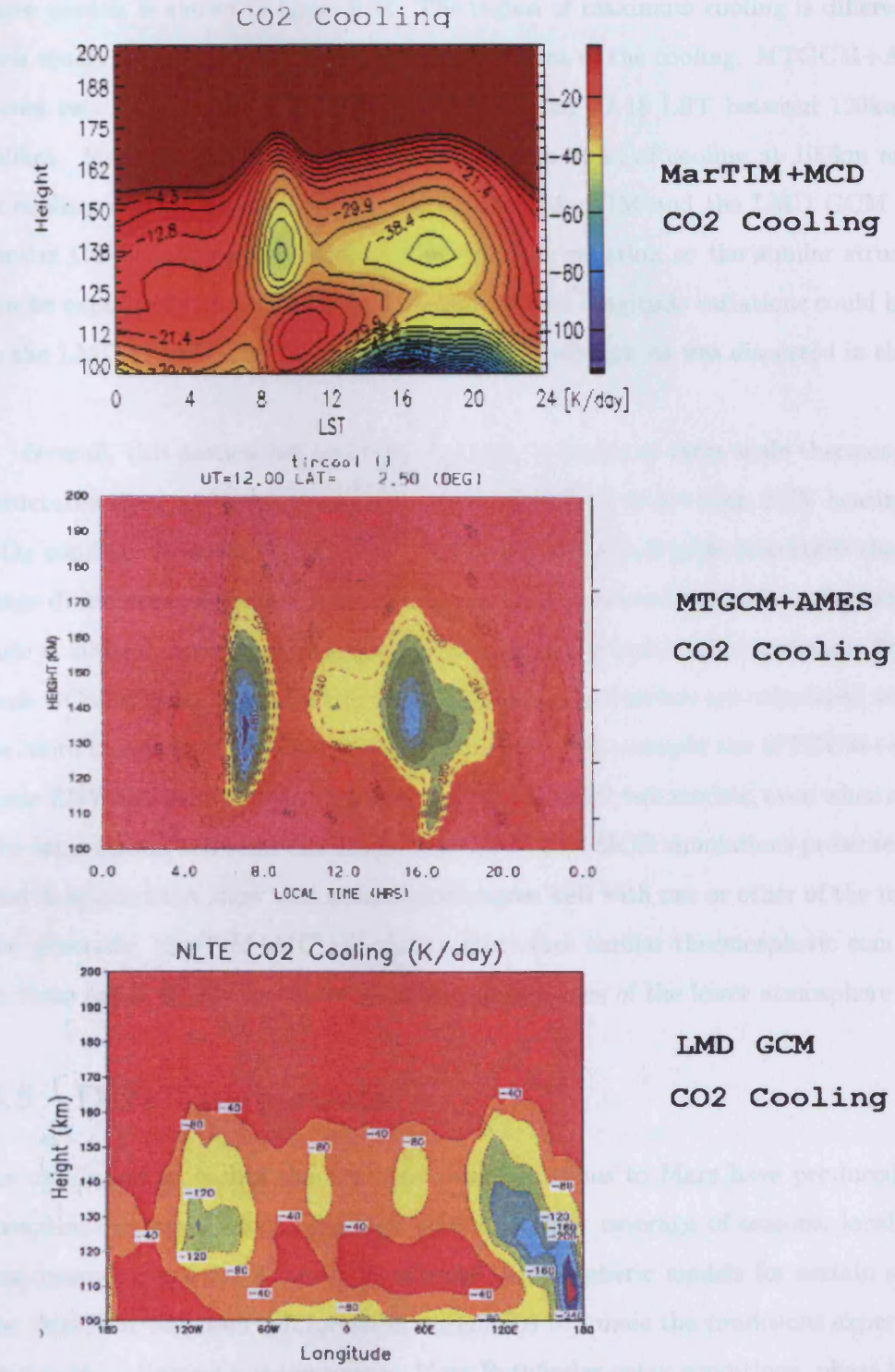

Figure 6.21: CO_2 cooling in terms of altitude and longitude at the equator. MarTIM (top), MTGCM+AMES (middle) and LMD GCM (bottom)

a wider range from 130km to 190km. The difference in CO_2 cooling rates between the three models is shown in figure 6.21. The region of maximum cooling is different for each model as are the longitude and altitude extent of the cooling. MTGCM+AMES shows two strong regions of cooling at 8 LST and 12-18 LST between 120km and 150km. MarTIM+MCD and LMD GCM show a band of cooling at 100km as well as cooling regions between 120km and 150km. MarTIM and the LMD GCM use a similar CO_2 cooling parameterisation in their formulation so the similar structures can be explained. The differences in magnitude and longitude variations could be due to the LMD GCM using a different V-T_{CO_2-O} coefficient as was discussed in chapter 4.

Overall, this section has underlined is that in terms of large scale thermospheric structures there are similarities between the three models for both EUV heating and CO_2 cooling. However, in terms of magnitudes and small scale structures there are large differences. Appendix A shows that for other parameters, such as the temperature at 200km, there is not even good agreement on the large scale structures. The way each GCM is formulated and how the fundamental parameters are calculated needs to be more transparent to allow proper comparison. For example the MTGCM+AMES solar EUV heating rate is so much higher than the other two models, even when run for the same season and solar conditions. The MarTIM+MCD simulations presented here and in appendix A show that some aspects agree well with one or other of the models. So, generally, MarTIM+MCD is able to reproduce similar thermospheric conditions to these other GCMs that have included the influence of the lower atmosphere.

6.3 Data Comparisons

As mentioned in earlier chapters, the recent missions to Mars have produced thermospheric datasets which, although limited in their coverage of seasons, local times and latitudes, provide a means to validate thermospheric models for certain scenarios. MarTIM has been run for various scenarios to mimic the conditions experienced during the following mission phases; Mars Pathfinder entry conditions, phase 2 aerobraking conditions for Mars Global Surveyor (MGS) and the derived winds from the MGS aerobraking sets, [90].

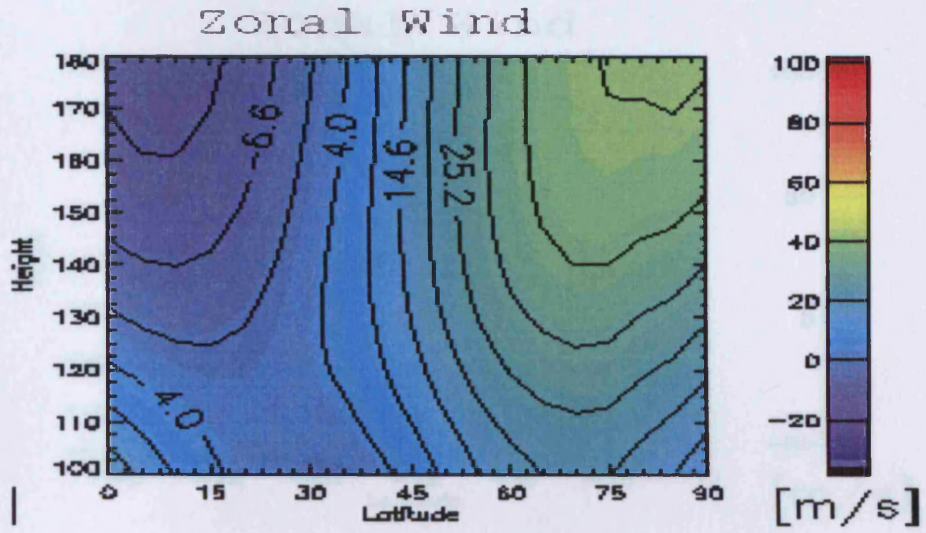

Figure 6.22: Northern Hemisphere zonal wind altitude plot from MarTIM+MCD, for L_s = 35, LST=1600 and MGS Phase 2 aerobraking conditions

6.3.1 Wind Validation

In chapter 4 MarTIM zonal winds were compared to the zonal wind values derived from MGS aerobraking data. It was found that the magnitudes in MarTIM were much smaller than observed in the data. Figures 6.22 and 6.23 show the zonal winds plotted for the conditions stated in tables 4.3 and 4.4 in chapter 4.

For figure 6.22 the wind in the region specified in table 4.3 is around 24ms^{-1}. This is actually smaller than the values predicted by the basic MarTIM simulations and still well below the data determined value of 74ms^{-1}. Figure 6.23 shows a wind of 18ms^{-1}, a three times increase compared to the basic MarTIM simulation, yet still not the right order of magnitude compared to the data. It appears that although including the MCD lower boundary have in certain circumstances, increased the wind speeds to provide better agreement with the data, there remain discrepancies overall. Deriving horizontal winds from the accelerometer data is a new technique and maybe subject to revision, hence focusing on the fine details of the comparison with this dataset is not a priority.

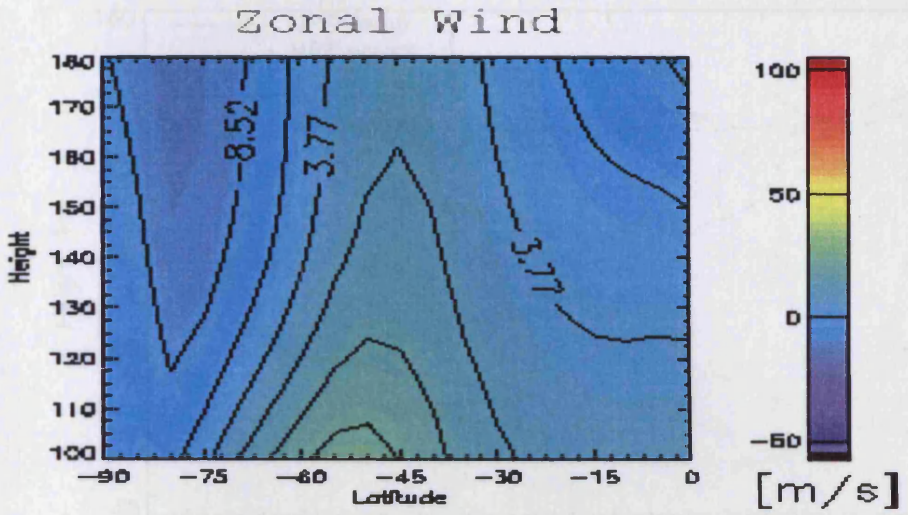

Figure 6.23: Southern Hemisphere zonal wind altitude plot from MarTIM+MCD, for L_s = 90, LST=1500 and MGS Phase 2 aerobraking conditions

6.3.2 Mars Pathfinder

The Mars Pathfinder mission provided a single profile dataset, containing the parameters of temperature, density and pressure for the following conditions: the probe entered the Martian atmosphere at 03:00 local Mars time, for solar minimum and L_s=143. A comparison of the Mars Pathfinder temperature profile and three MarTIM temperature profiles (basic MarTIM, with (2,2) tide, with MCD lower boundary) are shown in figure 6.24.

What figure 6.24 shows is that MarTIM, even with the MCD lower boundary, does not exhibit the same small scale structures seen in the Mars Pathfinder profile. There is a region of agreement around 90km in absolute value and at 130km the upper error bar of the Pathfinder data overlaps with the model results. This comparison has been done on the assumption that the Pathfinder probe did not experience any horizontal motion on its descent. It is not known how much horizontal variation there was during descent, as it is not possible to accurately model the exact Pathfinder conditions. It has also been suggested, [29], that the small scale structures in the Pathfinder temperature profile are due to gravity waves breaking in the middle Martian atmosphere. As there is not currently a gravity wave scheme in MarTIM it is expected that the MarTIM

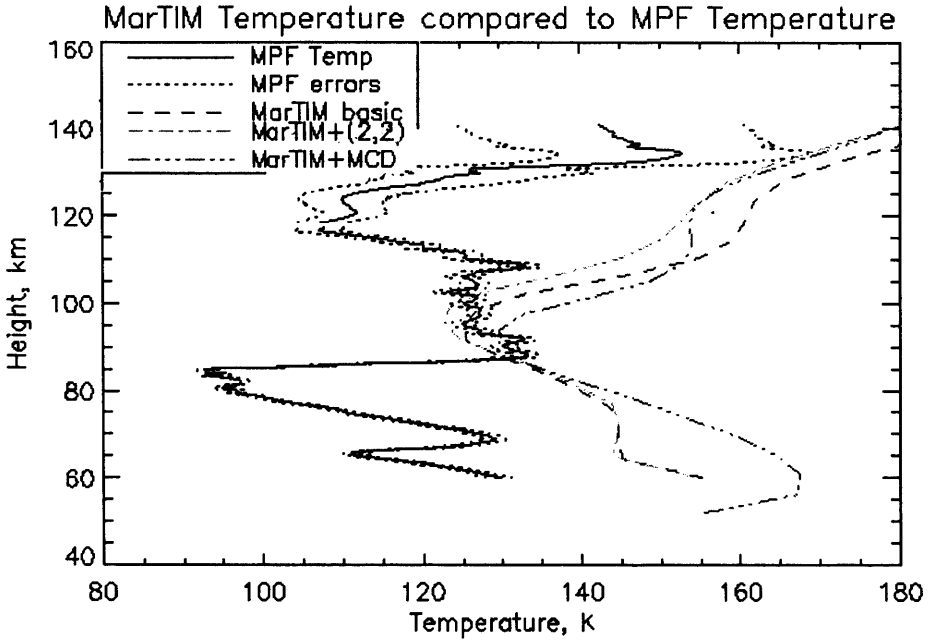

Figure 6.24: Plot showing a comparison between the Mars Pathfinder temperature profile and three MarTIM temperature profiles for the same conditions

profiles would not exhibit the same small scale structure.

6.3.3 Mars Global Surveyor

Mars Global Surveyor (MGS) provided the first large dataset of Mars atmospheric parameters while attaining orbit. The data from the accelerometer on MGS provided measurements of density, scale heights and temperatures over two distinct Martian seasons. Phase 1 of aerobraking lasted 7 months from L_s = 180 to 300. Phase 2 of the aerobraking lasted 5 months from L_s = 30 to 95, [5]. Phase 1 of the aerobraking coincided with the "Noachis" major dust storm on Mars. It has already been shown in the literature, [6], that the densities measured were considerably different to the expected values. As all the model simulations in this work are considered dust free the phase 1 dataset is not used for comparative purposes with MarTIM. Figure 6.25 shows the latitudinal and local time coverage of the aerobraking phases of MGS. Phase 2 has good latitudinal coverage and limited local time coverage, from 15-17 local solar time.

The MarTIM+MCD model has been run to simulate the conditions experienced by MGS during phase 2 of the aerobraking. Figure 6.26 compares MGS phase 2 ac-

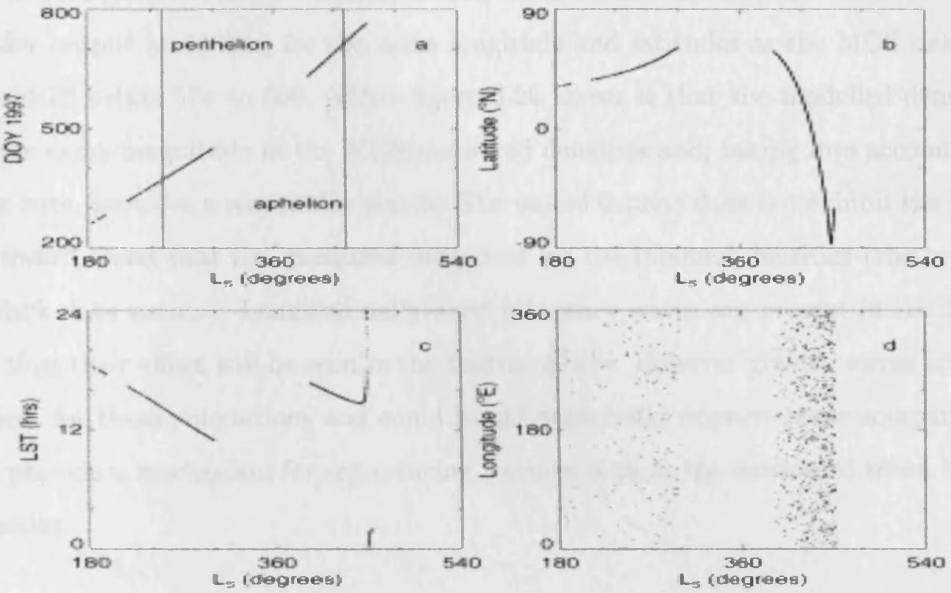

Figure 6.25: Image taken from, [90]. Parameters during aerobraking: (a)date in days since January 1, 1997. (b)latitude coverage, (c)Local Solar Time coverage and (d)longitude coverage. All plotted against L_s. Phase 1 aerobraking occurred before L_s=360 and phase 2 afterwards.

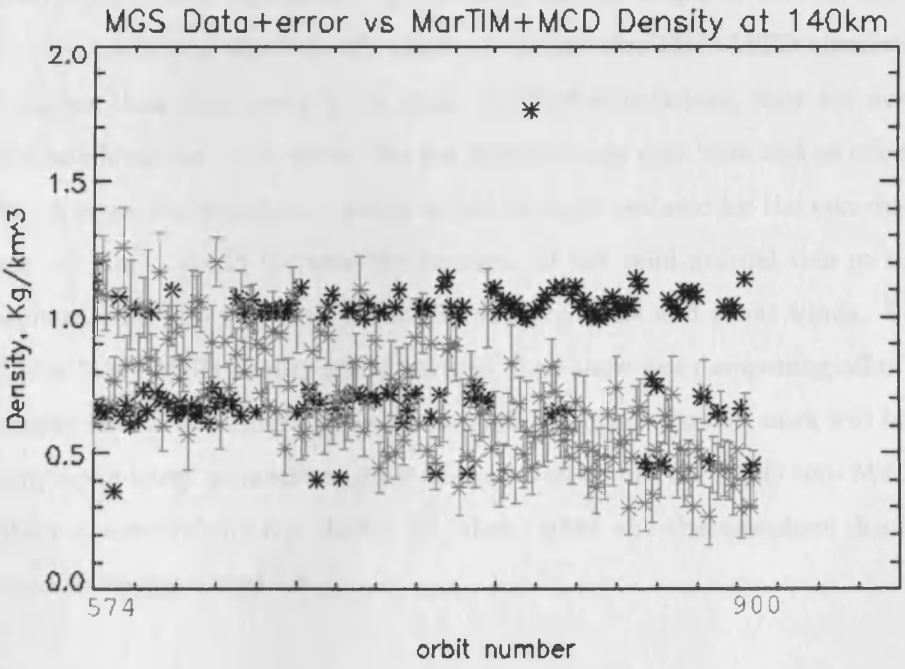

Figure 6.26: Plot showing a comparison between MGS density (red crosses) with errors (blue lines) and MarTIM+MCD modelled densities (black stars) at 140km

celerometer (inbound and outbound) density data, with error bars, and MarTIM+MCD density output at 140km, for the same longitude and latitudes as the MGS dataset, over MGS orbits 574 to 900. What figure 6.26 shows is that the modelled densities are the same magnitude as the MGS measured densities and, taking into account the error bars, provides a reasonable match. The model density does not exhibit the same downward trend that the measured data does for the inbound densities (the top set of black data points). Longitudinally fixed planetary waves are present in the MCD and thus their effect will be seen in the thermosphere. However gravity waves are not present for these simulations and could would potentially improve these comparisons and provide a mechanism for reproducing features such as the downward trend in the densities.

6.4 Summary

This chapter has shown how important the introduction of MCD lower atmosphere is in terms of modelling the middle and upper Martian atmosphere. The main unrealistic feature of the basic MarTIM simulations, shown in chapters 3 and 4, were the low magnitudes in middle atmosphere wind speeds compared to other models and data. The horizontal wind speeds observed in the MarTIM+MCD simulations are much higher than those seen in the basic MarTIM simulations, they are now of the order of hundreds ms^{-1}. However, the low dust scenario may have had an effect on the results. A more dusty scenario, which would be more realistic for the non dust storm seasons on Mars, would increase the strength of the semi-diurnal tide in the lower atmosphere, and also the zonal mean thermal gradients and zonal winds. The combined MarTIM+MCD results would perhaps then show less dampening off of the key parameters that is currently observed at higher altitudes. Further work will be needed to incorporate lower atmosphere dust storms effects from the MCD into MarTIM, as the phase 1 aerobraking has shown, [6], these affect the thermosphere dramatically and need to be accounted for.

Chapter 7

Conclusions and Future Work

7.1 Conclusions

Modelling of the Martian atmosphere has been motivated in recent years by the flurry of missions to Mars and the data they have gathered. As a result there are now several Martian atmosphere global circulation models in existence, each having been developed in a slightly different manner. The UCL Martian thermosphere and ionosphere global circulation model has been developed in several stages;

- Taking the core code containing the equations of energy, momentum and continuity from the Titan GCM, [70] and converting it to represent a basic Martian atmosphere
- Investigating the features in the Martian thermosphere caused by EUV/UV solar forcing
- Introducing IR heating and cooling and analysing the effects on the thermosphere
- Introducing the (2,2) semi-diurnal tide and determining its effects on the thermosphere
- Introducing a lower boundary that represents the lower atmosphere from the Mars Climate Database and hence looking at some of the effects of the lower atmosphere on the Martian thermosphere

This stage by stage development of MarTIM has enabled the effects introduced by each new feature to be easily identified and understood, e.g. the effect of introducing the IR heating and cooling on the mean zonal flow. It has been shown that the basic model behaves in a physical manner and that the introduction of features such as the (2,2) semi-diurnal tide and the MCD lower boundary are needed to generate model results that are comparable to other Martian thermospheric GCMs and to the limited datasets that are available. The (2,2) semi-diurnal tide increased the horizontal winds in the middle atmosphere of MarTIM, which were unrealistically low in the basic MarTIM simulations. It was however the introduction of the MCD lower boundary that had the greatest effect on the winds in the middle atmosphere. This also had a very significant effect on the thermospheric regions of Mars. This influence cannot be ignored if realistic data and model comparisons, and also predictions of atmospheric conditions, are to be made.

7.1.1 EUV/UV Solar Forcing Results

The diurnal and seasonal response of the Martian thermosphere and middle atmosphere to EUV/UV solar forcing was examined in the first section of this thesis. A clear relation of rising temperatures with increased solar flux was established. The high eccentricity of the Martian orbit results in a 40% variation in the EUV/UV flux reaching Mars over the course of a Martian year. Figure 3.7 demonstrated that MarTIM has realistic variation in thermospheric temperatures over the seasons, with temperatures at perihelion much higher than at aphelion.

The winds generated by the basic EUV/UV MarTIM simulations were also examined. As there are few direct thermospheric wind measurements it is difficult to judge what are satisfactory wind speeds in the thermospheric region, and so comparisons with other Martian GCMs is the main way of gauging their accuracy. The meridional and zonal wind structures generated by MarTIM for equinox conditions seem realistic. The effect of Coriolis force is easy to identify in the zonal mean plots shown in figure 3.11, with the northward and southward meridional winds turning under this influence and forming easterly jets in each hemisphere. However it was apparent that the very low meridional and zonal winds in the middle atmosphere, below the region of EUV/UV heating, needed to be addressed.

The effect on the relative abundances of the constituents due to the circulation patterns in MarTIM was examined by studying the seasonal variation of the $[O/CO_2]$ ratio and the vertical divergence wind. It was found that there was a similarity between the results of MarTIM and comparable Earth $[O/N_2]$ studies, in that the vertical divergence wind and the ratio distribution were linked and that there is a strong winter/summer gradient in the $[O/CO_2]$ ratio. The basic features found in [80] are also found in the Martian thermosphere, with regions of positive vertical divergence velocity corresponding to regions of decreasing $[O/CO_2]$ across a fixed pressure level. The comparable behaviour between these models for different planets is expected as Mars, in most respects, represents a "quiet" Earth scenario, that is it does not have magnetospheric type interactions. The biggest differences would be expected in the polar/auroral region, as Mars has no intrinsic magnetic field.

An initial comparison of Mariner 9 [O] fractional abundance data and MarTIM [O] fractional abundance was also undertaken. This comparison demonstrated a major difference between MarTIM and the data in the distribution of the [O] abundance across local time and latitude. MTGCM also showed this discrepancy in the literature, [84]. The direction of the composition gradient in MarTIM was the opposite of that in the data. Attempts to address this discrepancy in MarTIM were undertaken with the introduction of the tidal perturbations.

The Ionosphere

The simple photoionisation-charge exchange model used in MarTIM to generate an ionosphere predicted the correct major ions and ionospheric altitude structure. It also agreed reasonably well with MGS Radio Science data. The inclusion of an ionisation parameterisation for the secondaries improved the accuracy of the second lower ionospheric peak. Due to the simple nature of the ionospheric model there is no significant nighttime ionosphere in MarTIM. Also the ionospheric density at high altitudes appears to be overestimated when compared to MGS data. These will need to be addressed to improve the ionospheric model in MarTIM and are discussed in the future work section.

7.1.2 Basic Model Results

Chapter 4 dealt with the introduction of the IR heating and cooling schemes in MarTIM and the importance of having a good non-LTE parameterisation. Work on determining an optimum "heat balance" for MarTIM concluded that the key parameters needed were as follows: Eddy diffusion coefficient maximum=1500m^{2}s^{-1}, V-T$_{CO_2-O}$ coefficient = 1·10^{-13}cm^{3}s^{-1}, which is important in IR cooling and $EUVFAC$=18%, the EUV/UV absorption to heat efficiency. The introduction of the IR heating and cooling into the middle atmosphere changed the temperature structure for the whole model and altered the circulation patterns in the middle atmosphere. This resulted in vertical wind changes which affected the locations of adiabatic heating and cooling. Thus the IR heating and cooling schemes alter not just the middle atmosphere region where they dominate but also the thermosphere, as the changes in the model flows propagate into the thermosphere. The variation of altitude of the turbopause with solar cycle was found to be small, demonstrating that the IR heating and cooling control this variation rather than the EUV/UV heating. The IR radiation does not vary significantly over solar cycle, unlike the EUV/UV radiation.

The choice of the V-T$_{CO_2-O}$ coefficient used in the CO_2 IR cooling parameterisation in MarTIM is open to discussion as it is low compared to the accepted values, as stated in chapter 4. The V-T$_{CO_2-O}$ coefficient was altered in order to produce a comparable cooling profile to that found in the literature for the NCAR MTGCM, [9]. One has to bear in mind however, that the NCAR MTGCM IR cooling profile may itself be incorrect. One other possibility is that the O density profile used in MarTIM simulations is not accurate and further measurements of thermospheric abundances are needed. It is felt that more transparent intercomparison between the existing Martian thermospheric GCMs is also needed to understand how each achieves its IR heating and cooling profiles.

The introduction of the IR heating and cooling increased the horizontal wind speeds in the middle atmosphere by a small amount. Comparisons to data and other models suggested though that they were still too low. The comparisons with the accelerometer derived wind data showed that the MarTIM zonal winds were around 20ms^{-1} in the northern hemisphere region, compared to 74ms^{-1} from the data, and 6ms^{-1} compared to 34ms^{-1} in the southern hemisphere. However, the method of

deriving horizontal winds from the accelerometer has not undergone intensive peer review so its reliability is still in question. The comparisons with the NCAR MTGCM showed that the large scale thermospheric structures for the vertical and zonal winds compared well with MarTIM, with the vertical winds being of comparable magnitude. However the zonal wind speeds from MarTIM were around half those found in the NCAR MTGCM. An interesting feature of both the vertical and zonal MTGCM wind speedplots is the lower atmospheric structure. No comparable features appear in this region for the basic MarTIM runs, only in the tidal and MCD lower boundary plots do similar structures appear. Bougher et al, [7], has not made it clear whether tidal forcing was present for these MTGCM results. Further comparison was done with the MTGCM in chapter 5 to address the outstanding issues with the MTGCM middle atmosphere structure.

The effect of the IR heating and cooling on the zonal mean flow in MarTIM results in the main horizontal wind jets appearing at lower altitude pressure levels than for the EUV/UV only forcing MarTIM simulations. There is also an increase in the overall zonal mean horizontal wind speeds. This is consistent with the introduction of additional forcing in the middle atmosphere region. However, the horizontal wind speeds in the middle atmosphere region were still found to be too low. Tests performed on MarTIM's fixed lower boundary implied that non zero winds would be needed at the lower boundary in order to provide a significant background wind field which the IR heating could then accelerate. The next development step for MarTIM was then to assess the possible sources for physically realistic winds at the lower boundary and to effectively introduce them into the model. Self consistent lower boundary winds were provided by the (2,2) migrating tide (which also dissipates and provides additional momentum and energy into the thermospheric flow) and from the Mars Climate Database.

7.1.3 Effect of the (2,2) Tide on the Thermosphere

Chapter 5 examined the effect of introducing the (2,2) semi-diurnal migrating tide into MarTIM using terrestrial tidal theory. The effect on the zonal and vertical winds was compared to the NCAR MTGCM results and the basic MarTIM results. This showed that although there was not much change in the magnitudes of the vertical

winds, the zonal winds did increase slightly compared to the basic MarTIM simulation results. The magnitudes were still much lower than the MTGCM zonal winds however. The comparison in terms of the middle atmospheric structure in both the vertical and zonal winds was much improved. This confirms the suspicions outlined in the previous chapter that a form of tidal forcing was present in the MTGCM simulations. The differences in the wind magnitudes still imply that to match the MTGCM winds speeds additional energy and momentum sources need to be included in MarTIM simulations.

The effect of the (2,2) semi-diurnal migrating tide on the mean zonal flow was examined in section 5.5. This showed that the presence of a propagating tide in the atmosphere disturbed the geostrophic balance (where the Coriolis force is balanced by the pressure gradient) compared to the basic MarTIM simulations. The similarity of figures 5.6 and 5.7 at high altitudes imply that the (2,2) tide has mostly dissipated at these altitudes. The mechanism used to dissipate the tidal momentum is discussed in section 5.5.2. The dissipation timescales are of the order of velocity over the momentum equation terms. It is possible to say that the smaller the term at a given altitude the larger its associated dissipation timescale will be and so it will be less important in dissipating the tide at higher altitudes. Figure 5.7 demonstrates that in the polar regions, at all pressure levels, the horizontal advection and curvature terms play an important role in the dissipation of the momentum due to the tide in to the mean zonal flow. In the lower altitude pressure levels the vertical viscosity, Coriolis and the pressure gradient forces play important roles in tidal dissipation.

The zonal mean structure of the meridional and zonal winds is significantly altered by the presence of the tide. There is an increase in magnitude in the middle atmosphere. The change in structure seen in the middle atmosphere regions is explained by the breakdown of geostrophic balance. The meridional pressure gradients are no longer balanced by the Coriolis force and so the average meridional winds are no longer zero. The difference plots of the zonal mean horizontal winds have isolated the effects of the (2,2) tide on the mean zonal flow. A multicellular structure is seen in the meridional wind difference plot in the lower altitudes. This corresponds to the tidal velocity in the middle atmosphere. Above this the strong jet features, which dominate the upper atmosphere, demonstrate the effect of the dissipation of the tides

momentum into the mean zonal flow. Corresponding features are seen in the zonal wind difference plot. The main effect of the tidal momentum dissipating in the upper atmosphere are two westward jets close to the equatorial region.

The region in which the tide dissipates is confirmed when examining the amplitude of the (2,2) tide in the horizontal winds. The greatest changes in the mean zonal flow are shown to occur above the altitude of greatest tidal amplitude. This corresponds to the tide dissipating and depositing its momentum into the background flows of the atmosphere.

Corresponding to the changes in the zonal mean flow patterns induced by the tide, there are also changes in the zonal mean temperature patterns. In the upper atmosphere there is a mean temperature increase in the equatorial regions and a cooling at the poles. Comparing the magnitudes to the vertical wind difference it is possible to see how the altered circulation patterns in the winds, caused by the initial tidal perturbations, then the tidal dissipation, correlate with the temperature changes, through regions of adiabatic cooling from upwelling and compressional heating from downwelling vertical winds. The point to be noted though is that the change in temperature is only a few degrees K. So although the (2,2) tide does have an effect on the temperature structure in MarTIM it does not dominate.

In chapter 3 the fractional abundance of O in MarTIM was compared to Mariner 9 data. As the distribution over local time and latitude of the MarTIM results was quite different to the data it was thought that tidal perturbations may rectify this. What was found was that the introduction of the (2,2) semi-diurnal tide did have an effect on the distribution of the O fractional abundance, but not enough to produce a good match. Additional features such as planetary waves and gravity waves may need to be included in MarTIM to generate a greater variation in the O abundance, and a better comparison to the available data.

7.1.4 The Mars Climate Database Lower Boundary

Chapter 6 deals with the incorporation of the Mars Climate Database, version 3.1, as the lower boundary of MarTIM and the effect on the middle and upper atmosphere. The initial study involved comparing the MCD and the MarTIM+MCD zonal wind output in the overlap region of the two models (from 60km to around 120km). The

large scale structures in MarTIM+MCD initially diverge from those seen in the MCD, then converge again at the higher altitudes. The difference may be to do with the difference in dealing with IR heating and cooling. It is not clear from the literature if the MCD includes non-LTE IR heating and cooling, nor at what altitude they might start to dominate. These may be different in different models and thus the zonal wind patterns may be expected to differ too. This could also explain why the zonal wind patterns start to agree again at the higher altitudes. Here it appears the different models have similar IR heating and cooling again.

The effect of the MCD lower boundary on the model as a whole is significant. It introduces changes in the atmospheric flows that then cause changes in location of adiabatic heating and cooling and these in turn affect the temperature structures. The most obvious changes are seen in the vertical winds and the height variations across a pressure level. There is a large increase, especially in the middle atmosphere region, in the small scale structures observed in these parameters. Regions of upwelling now occur over the lower altitude regions of the pressure level and downwelling occurring over the higher altitude regions. This illustrates the effect height variation across a pressure level (determined mainly by topographic features) has on the vertical winds and consequently the atmospheric circulation. In the basic MarTIM simulations the height variation across a pressure level is determined by the energy sources and sinks in the atmosphere. With the introduction of the MCD lower boundary, the background height variation across a pressure level is not constant. The temperatures and horizontal wind speeds input are no longer constant at the lower boundary also. The structures and magnitudes seen in the MarTIM+MCD results are due to the interaction of the basic drivers of the model (EUV/UV/IR heating, IR cooling etc.) with the non constant background atmosphere. Hence at high altitudes the large scale wind structures are the same as for basic MarTIM simulations, where EUV/UV forcing dominates. There is an increase in the middle atmosphere wind speeds and structures. This confirms that for realistic winds speeds in this region, significant background winds, from the lower boundary, need to be present. IR forcing alone is not sufficient to accelerate the atmosphere to the expected velocities.

The effect on the magnitude and structure of the temperature distributions in the MarTIM+MCD output are also examined. There is a temperature increase over the

whole thermosphere and that the structure has altered significantly from that seen in the basic MarTIM output. With the addition of the IR heating and cooling in chapter 4 it was shown that the altered vertical winds were resulting in regions of adiabatic cooling and heating which changed the overall temperature structures. Something similar was evident in chapter 6 with the vertical winds having a much more complex small scale structure, being closely linked to the height variations, and so causing regions of adiabatic heating and cooling throughout the thermosphere, altering the temperature structures seen. This altered structure is further evident in the diurnal variations of the temperature across a thermospheric pressure level.

The influence of the MCD lower boundary on the zonal mean flow in MarTIM is also examined. An order of magnitude change of the meridional and zonal winds is found compared to the basic MarTIM results. The zonal mean winds in MarTIM+MCD simulations are up to fives times larger across the whole model than the basic MarTIM zonal mean winds. This result again underlines the importance of the MCD lower boundary on the middle and upper atmosphere regions. Looking at the zonal mean difference plots it is evident that the largest change in horizontal wind speeds occurs in the middle atmosphere region of the model. This is consistent with earlier results and again shows that the assumptions in the basic MarTIM simulations were not suitable for generating strong winds in the middle atmosphere. IR heating and cooling alone are not sufficient to force significant horizontal winds in this region. The lower boundary winds propagating from below are needed.

Comparisons with data from Mars Global Surveyor and Mars Pathfinder were performed. The Mars Pathfinder conditions were simulated and the temperatures compared to the data. It was found that there was only limited agreement between MarTIM+MCD and the data over a small altitude range. It was concluded that because the horizontal variation of the data was not accounted for in the comparative model profiles it was difficult to tell how reliable the comparison was. With the increase in zonal wind speeds in the middle atmosphere region of the model, comparisons with the data derived from the MGS accelerometer data were performed with this version of the model. What was found was that although the winds had increased there was still a discrepancy and they did not match the data from the northern and southern hemispheres exactly. It is possible that additional features need to be included in the

model, such as gravity waves or non-migrating tides, or the data has an unknown bias. The Mars Global Surveyor phase II aerobraking density dataset was used to compare to the MarTIM+MCD density output. At a constant altitude of 140km the density variation over a number of orbits was compared. They showed good agreement in terms of magnitudes. However the downward trend in the MGS inbound data was not reproduced by MarTIM+MCD and additional atmospheric features need to be included.

The development of MarTIM has highlighted the main thermospheric drivers. In the early work the response of the thermosphere to EUV/UV and IR solar radiation was shown. The seasonal and diurnal variations were explained, but horizontal wind speeds in the middle atmosphere were shown to be too low. The introduction of the (2,2) semi-diurnal migrating tide, resulted in significant changes to the mean zonal flow. A small increase in the middle atmosphere horizontal winds also occurred. It was the addition of the MCD lower boundary that had the largest effect on the thermosphere and middle atmosphere. Although high altitude thermospheric temperatures and winds were controlled by solar heating, effects from the lower atmosphere were still in evidence (e.g. the double peaked diurnal temperature variation). The middle atmospheric region was shown to have increased horizontal winds, as well as additional small scale structure. The results have illustrated that lower atmospheric effects on the thermosphere and middle atmosphere regions of MarTIM are very important, and cannot be neglected if realistic modelling studies of this region are to be undertaken.

The development of MarTIM, the coupling to the MCD and the results it has produced has lead to many possible directions for future development of MarTIM, these are discussed in the following section.

7.2 Future Work

The development and validation of the UCL Martian Thermosphere Ionosphere Model has provided a sound basis for further advanced studies. Areas for future work can be divided into three general categories;

- Effects of lower atmospheric structures on the Martian thermosphere and ionosphere

- Composition
- Effects of the solar wind and magnetic reconnection on the Martian neutral thermosphere and ionosphere

7.2.1 The Lower Boundary

This thesis has shown that the morphology and dynamics of the lower atmosphere has a significant effect on the thermosphere of Mars. Now that the response of a low dust Mars atmosphere has been studied, the MCD lower boundary can be used to introduce moderate and heavy dust storm effects into MarTIM. The solar heating of the dusty atmosphere causes the inflation of the lower atmosphere. This additional warming would modify the winds and effect the whole atmospheric structure, [14]. The prescnece of dust in the atmosphere will also affect the strength of the lower atmosphere tides and the zonal mean thermal and horizonral wind gradientsthat feed into MarTIM via the lower boundary. Recent work has shown that the density variations caused by dust storms are present in the region where the aerobraking of Mars Global Surveyor and Mars Odyssey occurred, [14]. Datasets exist, [73], [6], to validate the dusty atmosphere results. This work is the obvious next immediate stage of MarTIM development now that the effect of a basic MCD lower boundary has been demonstrated.

The MCD lower boundary could also be used to examine the effect of gravity waves on the thermosphere. Small scale variability can be activated in the MCD which is a gravity wave parameterisation, [20]. Most GCMS are not able to run at high enough vertical resolution for vertically propagating gravity waves to be modelled individually, [51], so a parameterisation is normally used. Activating this in the MCD will determine what effects would propagate into the upper atmosphere via the lower boundary,for example whether they would change the zonal mean flows in the middle atmosphere and the thermosphere as they break. Gravity wave parameterisation's have been used in other Martian GCMs and the drag force they create has been shown to strongly affect the wind fields and momentum balance in the middle atmosphere, [3], [20], [41]. The inclusion of gravity wave effects in MarTIM will further modify the structure in the middle atmosphere region.

The work presented in this thesis also showed the influence of the (2,2) semi-

diurnal migrating tide on the flows in the Martian atmosphere. However, analysis done on the MGS and Mars Odyssey aerobraking data has determined the presence of several longitudinal density structures. Initially they were identified as stationary (i.e. with respect to Mars' surface) planetary waves, [27], they are now attributed to non-migrating tides, [26], [1]. Non-migrating tides are longitude-dependant or non-sun synchronous tides. The diurnal Kelvin wave has been shown to strongly feature in the aerobraking data, [90], [26]. As these waves are present in the MCD, studies can be done to examine their influence on the thermosphere.

Inclusion of these features into MarTIM will determine the magnitude of their influence on the thermosphere and also improve the validation against the aerobraking data. The influence of these tides and waves on the ionosphere can also be determined, as there is evidence of tidal effects in some interpretations of the MGS radio science experiment, [12], [88].

7.2.2 Composition

Neutral Chemistry

The development of a full 3-D photochemistry MarTIM is a possibility. As outlined earlier though, this would entail further species to be added to MarTIM's chemical scheme. Other species, such as those that act as a catalyst for CO_2 production; OH, H_2O and H, would need to be incorporated. This would improve the detailed interaction between dynamics, radiation and chemistry in the modelled Martian thermosphere.

The Ionosphere

The ionospheric work in this thesis demonstrated good general agreement with data. It also highlighted several key areas for improvement. The inclusion of the solar2000 radiation scheme as a replacement for the current scheme would improve MarTIMs ability to reproduce day to day variations in the ionosphere, [86], [67]. Then one could, for example, compare the response of Earth's ionosphere and Mars' ionosphere to solar activity, [66]. Although the main study in this thesis involved comparisons of the upper altitude electron density peak with data, issues remain for the lower altitude peak, which was not as well reproduced. The solar2000 radiation scheme

includes new X-ray data from the SNOE satellite, [86]. This is penetrating radiation so its inclusion would effect the morphology of the lower peak. The other main area of concern was the higher than expected electron density at high altitudes. This is due to the assumption of photochemical equilibrium existing throughout MarTIM and the neglecting of any mass loss mechanisms at the top level. The inclusion of ion diffusion in MarTIM would result in a decrease in ionisation with altitude, [12], [63], and a resultant decrease in the electron density at high altitudes. This would bring the topside magnitudes of the electron density into better agreement with the MGS radio science data. The effect of incorporating a mass loss mechanism, such as solar wind interaction is discussed in the section below.

7.2.3 The Upper Boundary

Several improvements can be made to the upper boundary of MarTIM to help improve the accuracy of the results seen in this region. Increasing the number of scale-heights MarTIM uses (currently 17) will allow the region of the ionopause (around 300km) to be examined, [62]. The interaction of the solar wind on the Martian upper atmosphere is important and should ideally also be included. The solar wind interaction transfers momentum into the topside ionosphere, [61], and also strips ions away in an effect called sputtering, [18], [49]. Atmospheric sputtering occurs when ionised O^+ in the upper atmosphere is accelerated by the solar wind electromagnetic field and strikes the exobase, causing a cascade of collisions that results in the ejection of particles from the atmosphere, [43]. A Monte Carlo model is the most common way of modelling this effect precisely, [43]. However, for MarTIM, incorporating simple calculations of average loss rate at different altitudes would be a simple way of examining mass loss from the top of the Martian atmosphere and its effects on the composition. To include fully the solar wind interaction with MarTIMs upper boundary is not straightforward. Studies of the interaction at Mars have normally been performed using MHD models, [82]. The development of a 2D or even 3D MHD model at UCL would be a large undertaking. At best MarTIM would be able to provide the ionospheric structure for the MHD model, yet a direct coupling of the two would be a complex task and would most probably result in unfeasible computer simulation time. An alternative would be some sort of parameterisation of the ionospheric region and its dynamics. If an

MHD model is developed to study the effect of the solar wind on the Martian topside then the presence of the magnetic hotspots cannot be ignored. It has been shown that these crustal magnetic fields reconnect with the solar wind magnetic field and form "mini-magnetospheres", [74], [46]. These features are important not only because they cause the shape of the bow shock at Mars to become lumpy, [74], [82], but they also prevent direct heating of the atmosphere by the solar wind and affect the electron temperature, [46]. The effect of understanding the atmospheres/ionospheres response to these magnetic field reconnection areas is important if a global positioning satellite system was to be used on Mars, [66], and in the instance of humans reaching Mars, the implications on radio communications, [66].

There are many areas where MarTIM could help in characterising and understanding data from Mars missions. The recent plans put forward by NASA and ESA for further Mars exploration, with a final aim of a human walking on Mars, means that there will be future opportunities for data to be gathered and for predictions to be made using Mars atmosphere models. However, as Appendix A emphasises, even three GCMs run for the same conditions, cannot agree well on the magnitudes and structures of the various atmospheric parameters. A general conclusion of this thesis is that by understanding not only what features affect and control the structure of the Martian atmosphere, but how and why they are implemented in different GCMS can progress be made toward an accurate representation of the Martian thermosphere. The need for active intercomparison between research groups working on Martian thermospheric GCMS is as an important feature of development as data validation.

Appendix A

Intercomparison Workshop 2003

This section contains a range of plots that were produced for the intercomparison workshop in Granada, 2003. Each figure shows plots from MarTIM+MCD, MTGCM+AMES and the LMD GCM. They demonstrate the similarities and differences in key parameters between three surface to thermosphere Martian GCMs. There are different colour schemes used for the plots, for the LMD GCM and MTGCM the largest values are pink, moving through red, yellow and green to the smallest values which are represented by blue. The MarTIM plots use a rainbow graident, with red representing the largest values and violet the smallest values.

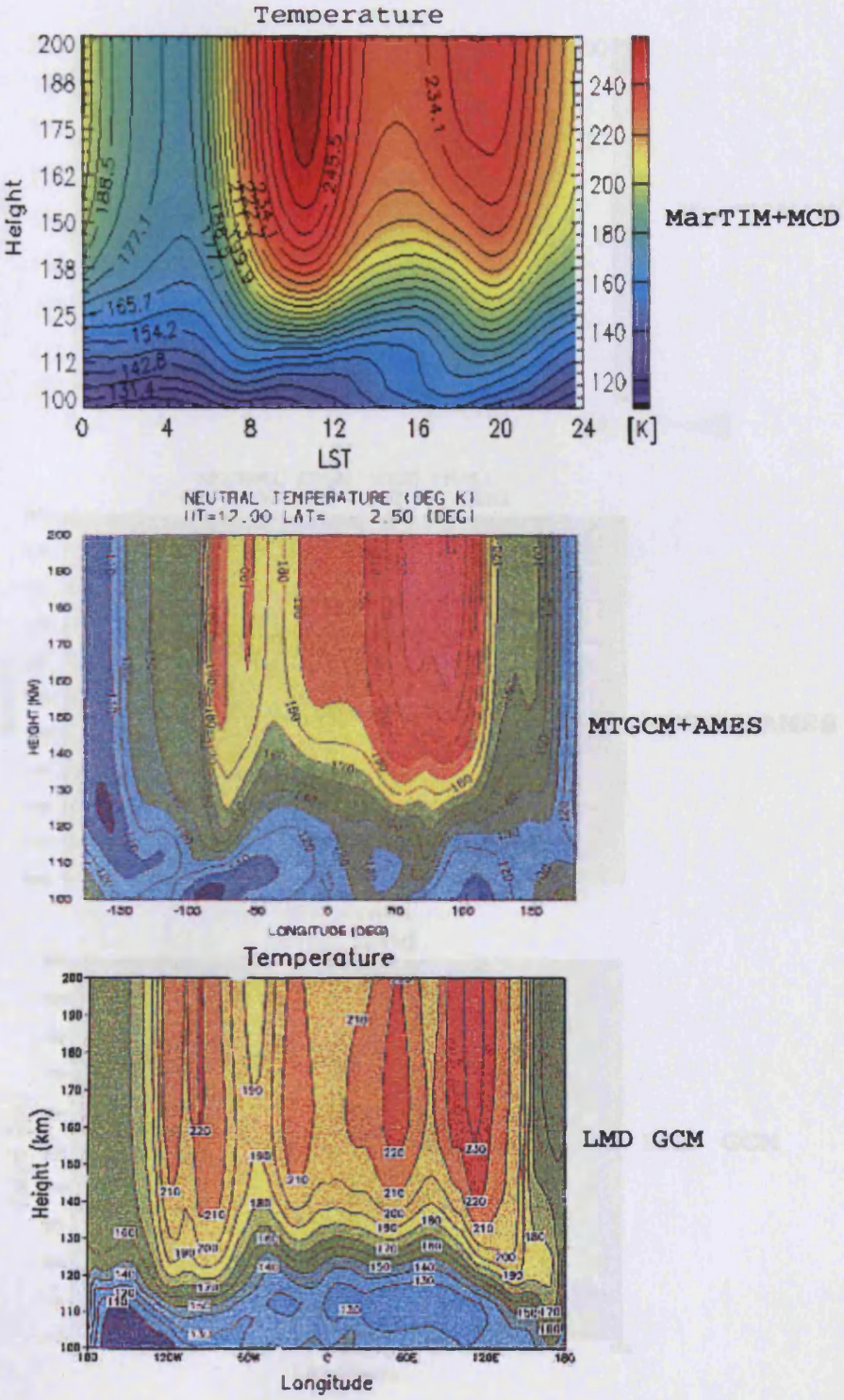

Figure A.1: Temperature in terms of longitude and altitude. MarTIM (top), MT-GCM+AMES (middle) and LMD-GCM (bottom)

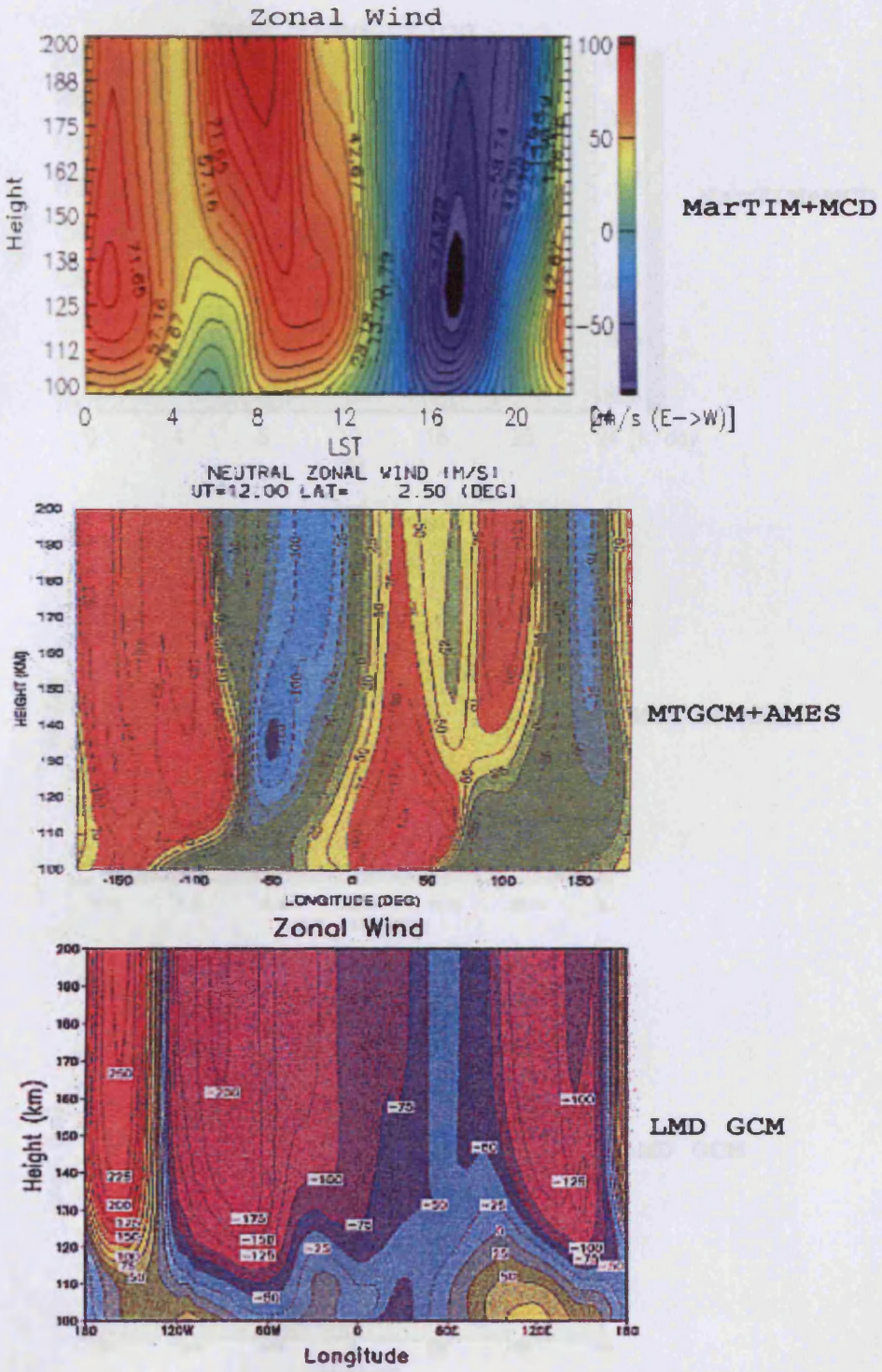

Figure A.2: Zonal wind (+ve eastward) in terms of longitude and altitude. MarTIM (top), MTGCM+AMES (middle) and LMD-GCM (bottom)

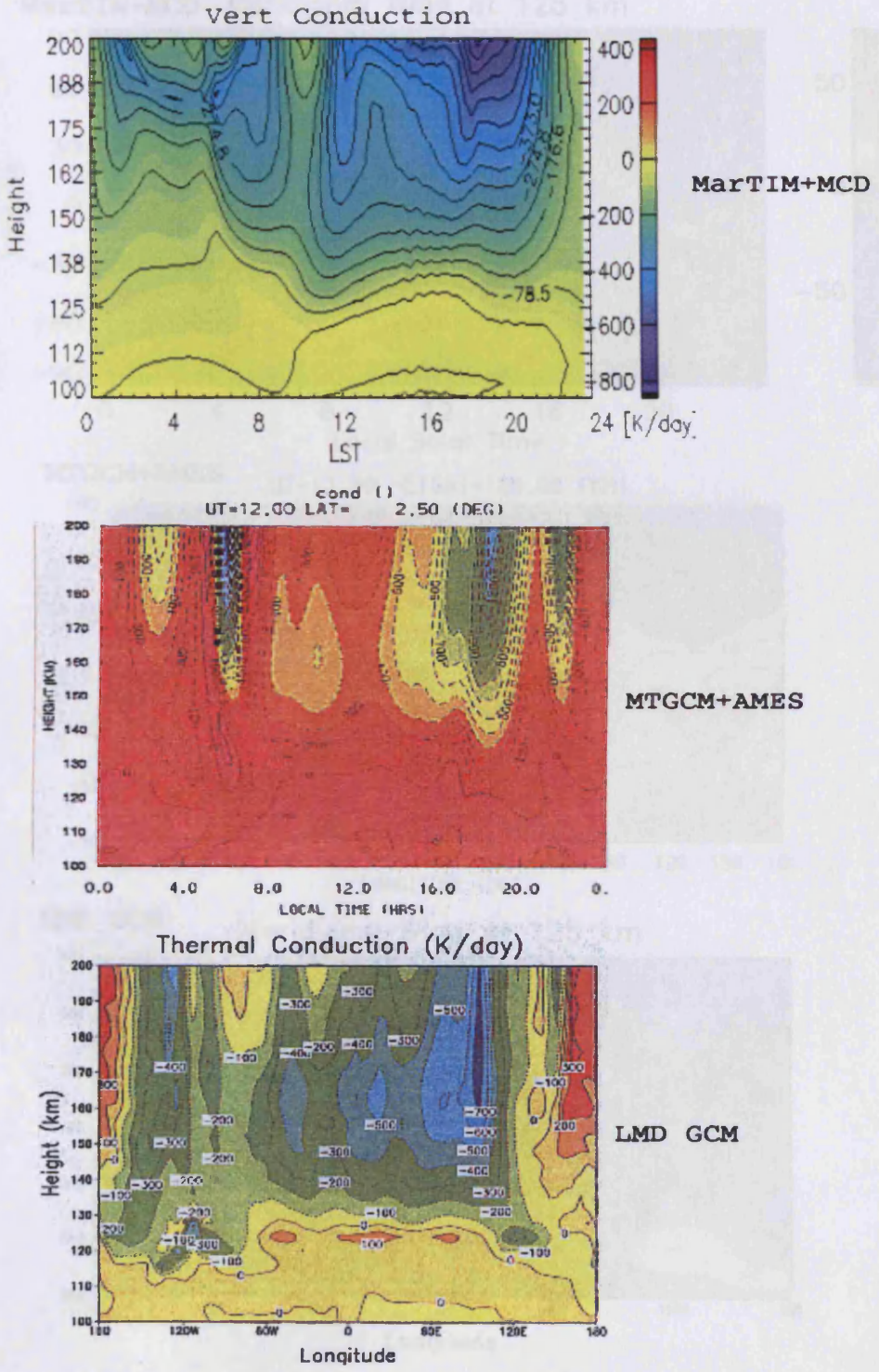

Figure A.3: Vertical conduction in terms of longitude and altitude. MarTIM (top), MT-GCM+AMES (middle) and LMD-GCM (bottom)

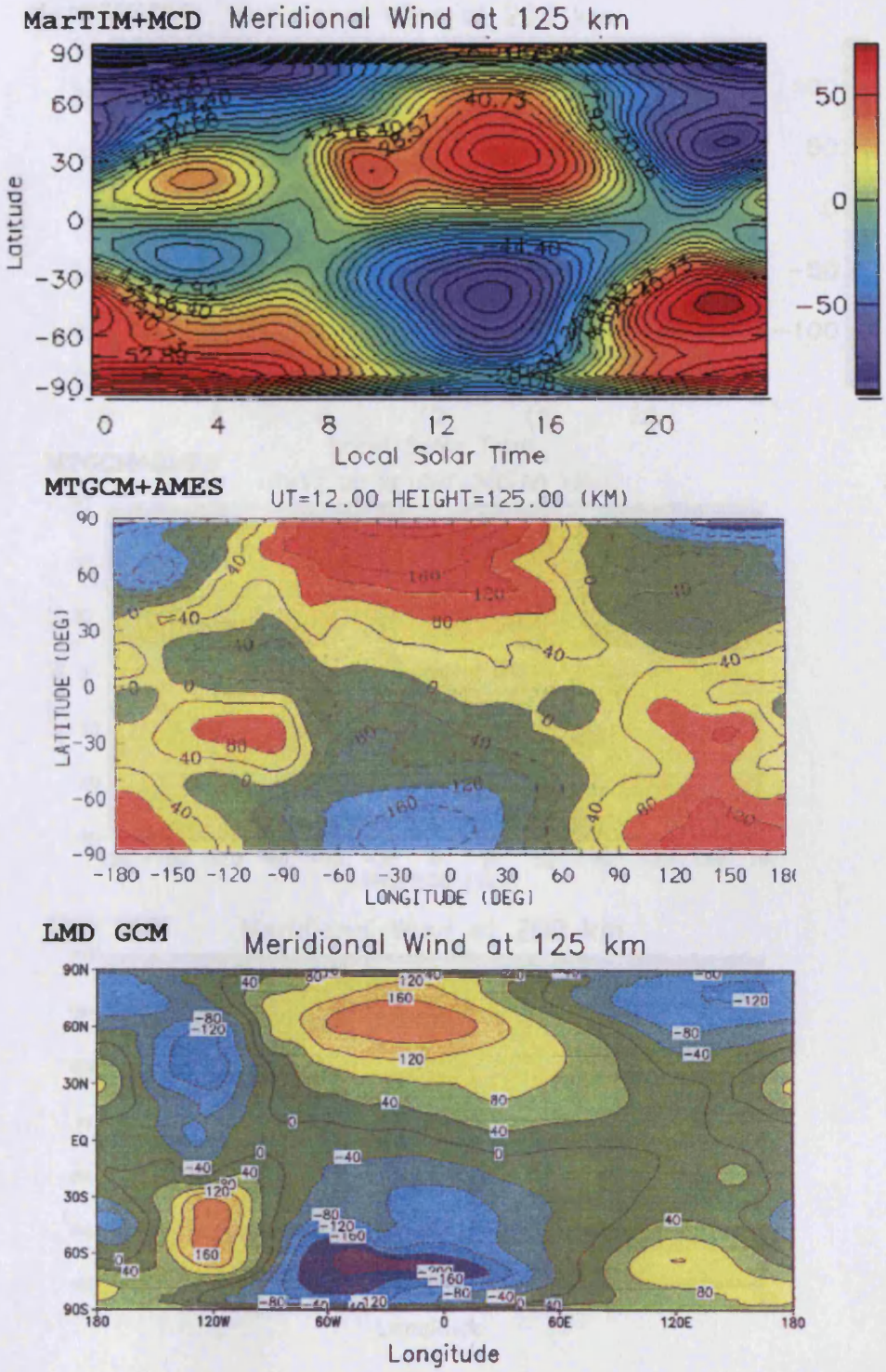

Figure A.4: Meridional wind (+ve northward) at 125km in terms of longitude and latitude. MarTIM (top), MTGCM+AMES (middle) and LMD-GCM (bottom)

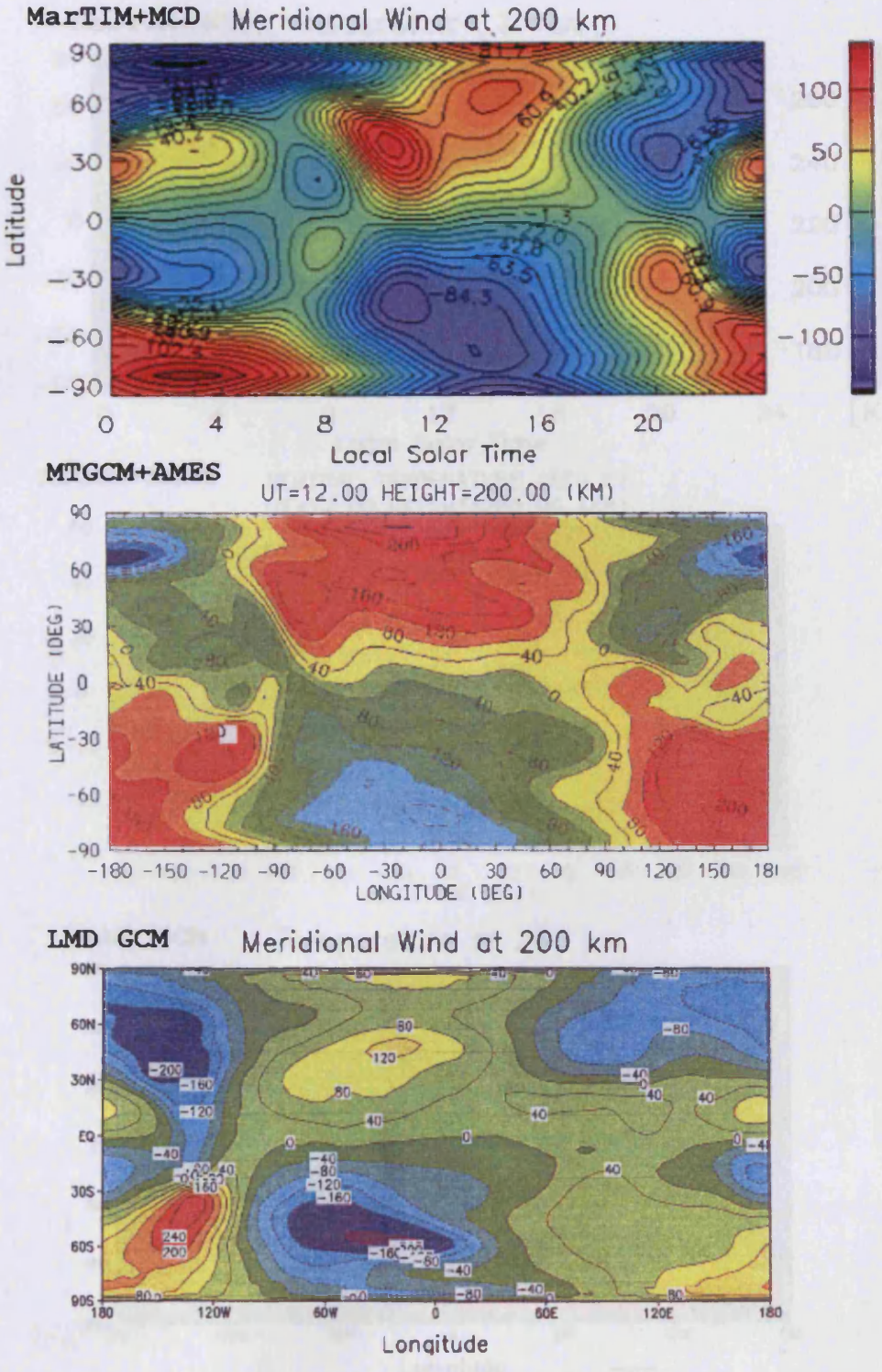

Figure A.5: Meridional wind (+ve northwardward) at 200km in terms of longitude and latitude. MarTIM (top), MTGCM+AMES (middle) and LMD-GCM (bottom)

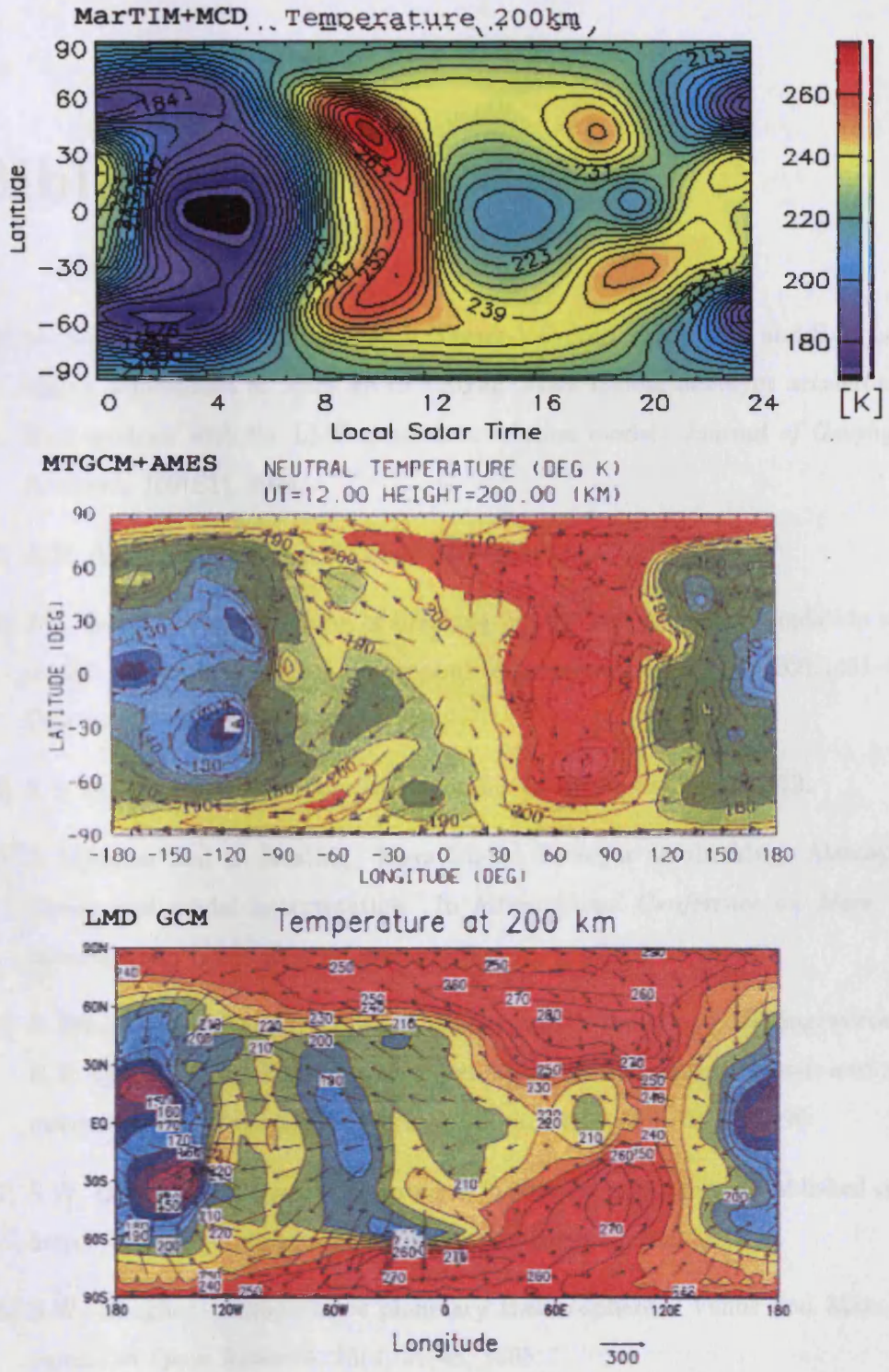

Figure A.6: Temperature at 200km in terms of longitude and latitude. MarTIM (top), MTGCM+AMES (middle) and LMD-GCM (bottom)

Bibliography

[1] M. Angelats i Coll, F Forget, M.A. Lopez-Valverde, P.L. Read, and S.R. Lewis. Upper atmosphere of Mars up to 120km: Mars Global Surveyor accelerometer data analysis with the LMD general circulation model. *Journal of Geophysical Research*, 109(E1), 2004.

[2] A.D. Aylward. Personnal Correspondence.

[3] J.R. Barnes. Possible effects of breaking gravity waves on the circulation of the middle atmosphere of Mars. *Journal of Geophysical Research*, 95(B2):1401–1421, February 1990.

[4] S.J. Bauer. *Physics of planetary ionospheres.* Springer-Verlag, 1973.

[5] S. Bougher and G. Keating. Mars Global Surveyor aerobraking: Atmospheric trends and model interpretation. In *International Conference on Mars.* Fifth International Conference on Mars, 1999.

[6] S. Bougher, G. Keating, R. Zurek, J. Murphy, R. Haberle, J. Hollingsworth, and R.T. Clancy. Mars Global Surveyor aerobraking: Atmospheric trends and model interpretation. *Advances in Space Research*, 23(11):1187–1197, 1999.

[7] S.W. Bougher. Comparative terrestrial planet thermospheres. Published online. http://data.engin.umich.edu/tgcmplanetsarchive/thermo.html.

[8] S.W. Bougher. Comparative planetary thermospheres: Venus and Mars. *Advances in Space Research*, 15(4):21–45, 1995.

[9] S.W. Bougher and R.E. Dickinson. Mars mesosphere and thermosphere 1: Global mean heat budget and thermal structure. *Journal of Geophysical Research*, 93(A7):7325–7337, July 1988.

[10] S.W. Bougher and R.E. Dickinson. Mars thermosphere 2: General circulation with coupled dynamics and composition. *Journal of Geophysical Research*, 95(B9):14811–14827, August 1990.

[11] S.W. Bougher, R.E. Dickinson, R.C. Ridley, and R.G. Roble. Venus mesosphere and thermosphere, three-dimensional general circulation with coupled dynamics and composition. *Icarus*, 73:545–573, 1988.

[12] S.W. Bougher, S. Engel, D. Hinson, and J. Forbes. Mars Global Surveyor radio science electron density profiles: Neutral atmosphere implications. *Geophysical Research Letters*, 28:3091–3094, 2001.

[13] S.W. Bougher, C.G. Fesen, E.C. Ridley, and R.W. Zurek. Mars mesosphere and thermosphere coupling: Semi-diurnal tides. *Journal of Geophysical Research*, 98(E2):3281–3295, February 1993.

[14] S.W. Bougher, J. Murphy, and R.M. Haberle. Dust storm impacts on the Mars upper atmosphere. *Advances in Space Research*, 19(8):1255–1260, 1997.

[15] S.W. Bougher, R.G. Roble, and T. Fuller-Rowell. *Atmospheres in the solar system: Comparative aeronomy*, volume 130, chapter Simulations of the upper atmospheres of the terrestrial planets, pages 261–288. American Geophysical Union, 2002.

[16] P.J Cattermole. *Mars: The mystery unfolds.* Oxford University Press, 2001.

[17] S. Chapman and R.S. Lindzen. *Atmospheric tides.* D.Reidel, 1970.

[18] E. Chassefiere and F. Leblanc. Mars atmospheric escape and evolution; interaction with the solar wind. *Planetary and Space Science*, 52(11):1039–1058, 2004.

[19] CNES, ESA, IAA, LMD, AOPP. *International Workshop: Mars atmosphere modelling and observations*, 2003.

[20] M. Collins, S.R. Lewis, and P.L. Read. Gravity wave drag in a global circulation model of the Martian atmosphere: Parameterisation and validation. *Advances in Space Research*, 19(8):1245–1254, 1997.

[21] D. Darling. *The universal book on astronomy.* Wiley and Sons, 2003.

[22] Instituto de Astrofisica de Andalucia. Online. http://www.iaa.csic.es.

[23] C.G. Fesen, R.E. Dickinson, and R.G. Roble. Simulation of the thermospheric tides with the National Center for Atmospheric Research Thermospheric General Circulation Model. *Journal of Geophysical Research*, 91:4471–4489, 1986.

[24] J. Forbes. *The upper mesosphere and lower thermosphere*, volume 87, chapter Tidal and planetary waves, pages 261–288. American Geophysical Union, 1994.

[25] J.M. Forbes. Tides in the middle and upper atmospheres of Mars and Venus. *Advances in Space Research*, 33:125–131, 2004.

[26] J.M. Forbes, S.W. Bridger, A.F.C.and Bougher, M.E. Hagan, J.L. Hollingsworth, G.M. Keating, and J. Murphy. Non-migrating tides in the thermosphere of Mars. *Journal of Geophysical Research*, 107(E11):5113–5120, 2002.

[27] J.M. Forbes and M.E. Hagan. Diurnal Kelvin wave in the atmosphere of Mars: Towards an understanding of "stationary" density structures observed by the MGS accelerometer. *Geophysical Research Letters*, 27:3563–3566, 2000.

[28] F. Forget. Discussions at EGS/AGU Meeting in Nice, France, 2003.

[29] F. Forget, F. Hourdin, R. Fournier, O. Hourdin, C.and Talagrand, M. Collins, S.R. Lewis, P.L. Read, and J. Huot. Improved general circulation models of the Martian atmosphere from the surface to above 80km. *Journal of Geophysical Research*, 104:24155–24176, 1999.

[30] J. Fox, P. Zhou, and S. Bougher. The Martian thermosphere/ionosphere at high and low solar activities. *Advances in Space Research*, 17(11):203–218, 1995.

[31] J.L. Fox and A. Dalgarno. Ionisation, luminosity and heating of the upper atmosphere of Mars. *Journal of Geophysical Research*, 84(A12):7315–7323, 1979.

[32] T. Fuller-Rowell. *A three dimensional, time dependant global model of the thermosphere.* PhD thesis, University of London, 1981.

[33] T. Fuller-Rowell and D Rees. Derivation of a conservation equation for mean molecular weight for a two-constituent gas within a three-dimensional, time de-

pendant model of the thermosphere. *Planetary and Space Science*, 31(10):1209–1222, 1983.

[34] R Haberle. *Encyclopedia of planetary sciences*, chapter M, pages 432–440. Chapman and Hall, 1997.

[35] S.A. Haider. Chemistry of the nightside ionosphere of Mars. *Journal of Geophysical Research*, 102(A1):407–416, 1997.

[36] W.B. Hanson, S. Sanatani, and D.R. Zuccaro. The Martian ionosphere as observed by the Viking retarding potential analysers. *Journal of Geophysical Research*, 1977.

[37] M. Harris. *Coupled mesosphere and thermosphere Earth model.* PhD thesis, University College London, 2001.

[38] W. Herschel. On the remarkable appearances at the polar regions of the planet Mars, the inclination of its axis, the position of its poles and spheroidal figure; with a few hints to its real diameter and atmosphere. *Philosophical Transactions of the Royal Society of London*, 74:233–273, 1784.

[39] S.S. Hough. On the application of harmonic analysis to the dynamical theory of the tides: Part 1 on Laplace's "Oscillations of the first species", and on the dynamics of oceans currents. *Philosophical Transactions of the Royal Society of London*, A:139–185, 1898.

[40] F. Hourdin. A new representation of the co_2 15μm band for a Martian general circulation model. *Journal of Geophysical Research*, 97:18319–18335, 1992.

[41] M.M. Joshi, B.N. Lawrence, and S.R. Lewis. Gravity wave drag in three-dimensional models of Mars. *Journal of Geophysical Research*, 100(E10):21235–21245, 1995.

[42] H. Kieffer, B. Jakosky, C. Snyder, and M. Matthews, editors. *Mars.* The University of Arizona Press, 1993.

[43] B Kopp. Loss of CO2 from the Martian atmosphere through sputtering. University of Chicago, 2001.

[44] V.A. Krasnopolosky. Photochemistry of the Martian atmosphere (mean conditions). *Icarus*, 101:313–332, 1993.

[45] V.A. Krasnopolosky. Mars photochemistry: Weak points and search for solutions. In *Sixth International Conference on Mars Proceedings*, 2003.

[46] A.M. Krymskii, T.K. Breus, N.F. Ness, D.P. Hinson, and D.I. Bojkov. Effect of crustal magnetic fields on or near terminator ionosphere at Mars. *Journal of Geophysical Research*, 108(A12):1431–1439, 2003.

[47] A. Kutepov. Discussions at EGS/AGU Meeting in Nice, France, 2003.

[48] A. Kutepov, O. Gusev, and V. Ogibalov. Solution of the non-lte problem for molecular gas in planetary atmospheres: Superiority of accelerated lambda iteration. *Journal of Quantative Spectrosopy and Radiative Transfer*, 60(2):199–220, 1998.

[49] F. Leblanc and R.E. Johnson. Sputtering of the Martian atmosphere by solar wind pickup ions. *Planetary and Space Science*, 49:645–656, 2001.

[50] F. Lefevre, S. Lebonnois, and F. Forget. A three dimensional photochemical transport model of the Martian atmosphere. In *Lunar and Planetary Science, 2003.* Lunar and Planetary Science XXXIV, 2003.

[51] S.R. Lewis, M. Collins, F. Forget, and Y. Wanherdrick. Mars Climate Database v3.1 - detailed design document. Technical report, University of Oxford, April 2001.

[52] S.R. Lewis, M. Collins, P.L. Read, F. Forget, F. Hourdin, R. Fournier, C. Hourdin, O. Talagrand, and J. Huot. A climate database for Mars. *Journal of Geophysical Research*, 104(E10):24177–24194, 1999.

[53] R.S. Lindzen. The application of terrestrial tidal theory to Venus and Mars. *Journal of the Atmospheric Sciences*, 27:536–549, July 1970.

[54] M. Lopez-Puertas and M. Lopez-Valverde. Radiative energy balance of co_2 non-lte ir emissions in the Martian atmosphere. *Icarus*, 114:113–129, 1995.

[55] M. Lopez-Puertas and F. Taylor. *Non-LTE radiative transfer in the atmosphere.* World Scientific, 2001.

[56] M Lopez-Valverde. Personnal correspondence.

[57] M. Lopez-Valverde. Non-local thermosdynamic equilibrium in general circulation models of the Martian atmosphere:1. *Journal of Geophysical Research*, 103(E7), July 1998.

[58] M. Lopez-Valverde and M. Lopez-Puertas. A non-local thermodynamic equilibrium radiative transfer model for infrared emissions in the atmosphere of Mars:1. *Journal of Geophysical Research*, 99(E6):13093–13115, June 1994.

[59] M. Lopez-Valverde and M. Lopez-Puertas. A non-local thermodynamic equilibrium radiative transfer model for infrared emissions in the atmosphere of Mars:2. *Journal of Geophysical Research*, 99(E6):13117–13132, June 1994.

[60] M. Lopez-Valverde and M. Lopez-Puertas. Co2 non-lte cooling rate at 15um and its parametrisation for the Mars atmosphere. Esa contract: Martian environment Models, Instituto de Astrofisica de Andalucia, Granada, Spain, 2001.

[61] R. Lundin, E.M. Dubinin, H. Koskinen, O. Norberg, N. Pissarenko, and S.W. Barabash. On the momentum transfer of the solar wind to the Martian topside ionosphere. *Geophysical Research Letters*, 18(6):1059–1062, 1991.

[62] K.K Mahajan and A.K. Dwivedi. Ionospheres of Venus and Mars: A comparative study. *Advances in Space Research*, 33(2):145–151, 2004.

[63] C. Martinis, J. Wilson, and M. Mendillo. Modelling day-to-day ionospheric variability on Mars. *Journal of Geophysical Research*, 108(A10):1383–1394, 2003.

[64] E.A. Mason and T.R. Marrero. The diffusion of atoms and molecules. *Advanced Atomic and Molecular Physics*, 6:155–232, 1970.

[65] M.B. McElroy and T.M. Donahue. Stability of the Martian atmosphere. *Science*, 177:986–988, 1972.

[66] M. Mendillo, X. Pi, S. Smith, C Martinis, J. Wilson, and D. Hinson. Ionospheric effects upon a satellite system at Mars. *Radio Science*, 39(RS2028):1–11, April 2004.

[67] M. Mendillo, S. Smith, J. Wroten, H. Rishbeth, and D. Hinson. Simultaneous ionospheric variability on earth and Mars. *Journal of Geophysical Research*, 108(A12):1432–1459, 2003.

[68] I. Mueller-Wodarg. The neutral atmosphere. Presentation Notes, 2002.

[69] I.C.F. Mueller-Wodarg. *Modelling perturbations through the mesopause in Earth's upper atmosphere.* PhD thesis, University of London, 1997.

[70] I.C.F. Mueller-Wodarg. The thermosphere of Titan simulated by a global three-dimensional time-dependent model. *Journal of Geophysical Research*, 105(A9):20833–20856, 2000.

[71] H. Nair. Photochemistry in the Martian atmosphere. *Icarus*, 111:124–150, 1994.

[72] J.P.L. NASA. Aerobraking information. Published online. http://marsprogram.jpl.nasa.gov/odyssey/mission/aerobraking.html.

[73] J.P.L. NASA. Nasa Mars rovers homepage. Published online. http://marsrovers.jpl.nasa.gov.

[74] N.F. Ness, M.H. Acuna, and J.E.P. Connerney. Effects of magnetic anomalies discovered at Mars on the structure of the Martian ionosphere and solar wind interaction as follows from radio science occultation experiments. *Journal of Geophysical Research*, 85(A7):15991–16004, 2000.

[75] A.O. Nier and M.B. McElroy. Structure of the neutral upper atmosphere of Mars. *Science*, 194:1298–1300, 1976.

[76] A.O. Nier and M.B. McElroy. Composition and structure of Mars upper atmosphere: Results from the neutral mass spectrometers on Viking 1 and 2. *Journal of Geophysical Research*, 82(28):4341–4349, 1977.

[77] B. Peters. A Martian thermosphere/ionosphere global circulation model. Master's thesis, University of London, 2001.

[78] M.H. Rees. *Physics and chemistry of the upper atmosphere.* CUP, 1989.

[79] H. Rishbeth and O.K. Garroitt. *Introduction to ionospheric physics.* Academic Press, 1969.

[80] H. Rishbeth and I.C.F. Mueller-Wodarg. Vertical circulation and thermospheric composition: A modelling study. *Annales Geophysicae*, 17:794–805, 1999.

[81] N.A. Savich and V.A. Samovol. The nighttime ionosphere of Mars from Mars 4 and Mars 5 dual frequency radio occultation measurements. *Space Research*, 16:1009–1011, 1976.

[82] H. Shinagawa and S.W. Bougher. A two-dimensional mhd model of the solar wind interaction with Mars. *Earth, Planetary and Space Science*, 51:55–60, 1999.

[83] Y Soobiah. Observations of magnetic anomaly signatures in mars express asperaels data. Talk given at the Young Persons Planetary Forum, October 2004.

[84] A.I.F. Stewart, M.J. Alexander, R.R. Meier, L.J. Paxton, S.W. Bougher, and C.G. Fesen. Atomic oxygen in the Martian thermosphere. *Journal of Geophysical Research*, 97(A1):91–102, 1991.

[85] MGS Radio Science Team. Public access to Mars Global Surveyor Radio Science data products. internet. http://nova.stanford.edu/projects/mgs/public.html.

[86] W.K. Tobiska, T. Woods, F. Eparvier, R. Viereck, L. Floyd, D. Bouwer, G. Rottman, and O.R. White. The solar2000 empirical solar irradiance model and forecast tool. *Journal of Atmospheres and Solar Terrestrial Physics*, 62:1233–1250, 2000.

[87] M.R. Torr and D.G. Torr. Ionisation frequencies for solar cycle 21: Revised. *Journal of Geophysical Research*, 90(A7):6675–6678, 1985.

[88] J.S. Wang and E. Nielsen. Evidence for topographic effects on the Martian ionosphere. *Planetary and Space Science*, 52:881–886, 2004.

[89] C. Winchester and D. Rees. Numerical models of the Martian coupled thermosphere and ionosphere. *Advances in Space Research*, 15(4):51–68, 1995.

[90] P. Withers. *Tides in the Martian atmosphere and other topics.* PhD thesis, University of Arizona, 2003.

[91] M.H.G. Zhang and J.G. Luhmann. Comparison of peak ionosphere pressures at Mars and Venus with incident solar wind dynamic pressure. *Journal of Geophysical Research*, 97(E1):1017–1021, 1992.

[92] M.H.G. Zhang, J.G. Luhmann, and A.J. Kliore. An observational study of the nightside ionosphere of Mars and Venus with radio occultation methods. *Journal of Geophysical Research*, 95(A10):17095–17102, 1990.

[93] R.W. Zurek. Diurnal tide in the Martian atmosphere. *Journal of Atmospheric Science*, 33, February 1976.